Measurement of Ingress through Gas Turbine Rim Seals

Carl Matthew Sangan

A thesis submitted for the degree of Doctor of Philosophy

University of Bath
Department of Mechanical Engineering
July 2011

~

Abstract

One of the most important problems facing gas turbine designers today is the ingestion of hot mainstream gases into the wheel-space between the turbine disc and its adjacent casing. A rim seal is fitted at the periphery and a superposed sealant flow is used to prevent ingress. The aim of this PhD research was to design a new rotor-stator testing facility, from which both flow physics and future heat transfer characteristics in relation to ingress could be measured and analysed, along with a detailed investigation into the sealing characteristics of turbine rim-seals there from. The rig was constructed as an engine representative model of a gas turbine wheel-space, from which data correlations could tentatively be scaled and applied to actual engine design.

The novel testing facility was designed in great detail for both sealing effectiveness research and to investigate the thermal effects of hot gas ingress; insight never previously achieved. An extensive commissioning process was undertaken to ensure that the correct, albeit benign, fluid-dynamic conditions were created inside the single stage turbine rig.

Effectiveness data are presented for single-clearance rim-seals in a variety of ingress conditions from which a fundamental understanding is developed for both rotationally-induced and externally-induced ingress. A newly developed orifice model is validated against the experimental data, resulting in theoretical predictions of the sealing effectiveness characteristics of various rim-seals. It is suggested that these predictions could be scaled to engine representative conditions where they could act as a future design tool for secondary air system engineers.

The theory is then extended to the application of double clearance-seal configurations, whereby the beneficial aspects are shown both theoretically and experimentally, leading on to the suggestion of a possible optimisation process resulting in an *ultimate* double seal. It is postulated that this would be the highest performance that can ever be achieved with a double clearance configuration.

For My Parents Who Gave Me
The Opportunity To Get This Far…

…And For My Wife In Supporting Me
In Overcoming The Final Hurdle

Acknowledgements

First and foremost I would like to thank Dr G.D. Lock, for his continued advice, support and encouragement. I would also like to extend my gratitude to him for giving me the opportunity to work on such a research project and for giving me the responsibility of constructing and running such an industrially relevant test facility.

Prof. J.M. Owen is also thanked for his passionate nature towards ingress research and unwavering technical advice throughout the development from his original sketches; many conversations and pieces of advice will stay with me throughout my career.

Dr. M. Wilson is also mentioned for his eagerness to follow the project and especially for the CFD input and support owing to his expertise in this area.

Technical acknowledgement is given to Roland Wiltshire, Paul Griffiths, Guy Brace, and especially Alan Jefferis for drawing on many years of experience in constructing these rigs, and imparting their advice on the component design and to Alan Jefferis in particular for fabricating all the in-house components.

The project sponsors, Siemens, and in particular, Kok Mun Tham, Vince Laurello, Oliver Schneider, John Hannis, and John Maltson are thanked for their technical input which has been invaluable. Todd Ebert from Florida Turbine Technologies (FTT) also assisted greatly in the project, especially with supporting FEA and CFD analysis.

Finally, a special thank you must be given to the Aero-Thermo Research team here at the University of Bath and especially the Gas Turbine Research group, without whose enthusiasm for the rig development as a whole, progress would not have been as successful and productive. My fellow postgraduates and journal co-authors Olly Pountney and Kunyuan Zhou were especially supportive and helped to make the work as enjoyable as it was rewarding.

Table of contents

Table of figures

Nomenclature

a	Speed of sound	S	Axial spacing between rotor and stator
A	Area	s_c	Seal clearance
b	Radius of seal	$s_{c,0}$	Radial seal-clearance for stationary case
c	Concentration	T	Temperature
c_p	Specific heat capacity	U	Bulk mean velocity of sealing flow $[= \frac{\dot{m}_0}{2\pi\rho b s_c}]$
C	Velocity relative to vane	V	Velocity relative to blade
$C_{d,e}$ $C_{d,i}$	Discharge coefficients for egress, ingress	V_r	Radial component of velocity
C_m	Free disc moment coefficient $[= M / {}^1/_2\rho\Omega^2 r^5]$	V_z	Axial component of velocity
C_p	Pressure coefficient $[= p_2 - \overline{p_2} / {}^1/_2\rho\Omega^2 b^2]$	V_ϕ	Tangential component of velocity
$C_{p,max}$	Pressure Coefficient $[= \Delta p / 0.5\rho W^2]$	V^*	Circumferential-average radial component of velocity through the seal-clearance
C_w	Non-dimensional flow-rate $[= \frac{\dot{m}}{\mu b}]$	W	Axial velocity in annulus
$C_{w,e}$ $C_{w,i}$	Values of C_w for egress, ingress	z	Axial distance
$C_{w,0}$	Non-dimensional sealing flow-rate	ΔC_p	Non-dimensional pressure difference $[= \Delta p / {}^1/_2\rho\Omega^2 b^2]$
$C_{w,min}$	Minimum value of $C_{w,0}$ to prevent ingress	Δp	External pressure difference $[= P_{2,max} - P_{2,min}]$
$C_{\beta 1}$	Modified internal swirl ratio $[= \beta_1^2/(1-r_1^2/r_2^2)]$	α	Vane angle
$C_{\beta 2}$	Modified external swirl ratio $[= \beta_2^2/(r_2^2/r_1^2-1)]$	β	Blade relative angle, swirl ratio $[= V_\phi / \Omega r]$
F	Centrifugal force	β_0	Blade relative angle at design
G	Axial gap ratio $[= S / b]$	Γ_c	Ratio of discharges coefficients $[= C_{d,i}/C_{d,e}]$
G_c	Seal-clearance ratio $[= S_c / b]$	Γ_p	Pressure parameter $[= C_p / C_{\beta 1}]$
$G_{c,crit}$	Critical seal-clearance ratio	Γ_T	Summation of Γ parameters
h	Local convective heat transfer coefficient	Γ_β	Swirl parameter $[= C_{\beta 1} / C_{\beta 2} \approx (\beta_2 / \beta_1)^2]$
i	Current	$\Gamma_{\Delta p}$	External pressure parameter $[= \Delta C_p / C_{\beta 1}]$
k	Thermal conductivity	δ	Radial growth of seal
K	Empirical constant	δ^*	Displacement thickness of boundary layer

L	Characteristic Length	ε	Sealing effectiveness [= $C_{w,0}/C_{w,e}$ = Φ_0/Φ_e]
$\dot{m}$	Mass flow-rate	ε_c	Concentration effectiveness [= $(c_s - c_a) / (c_0 - c_a)$]
M	Relative Mach number, moment	η	Double seal performance parameter
n	Number of data points	θ	Non-dimensional vane pitch
Nu_r	Local Nusselt number [$= hr/k_{air}$]	λ_T	Turbulent flow parameter [= $C_{w,0}/Re_\Phi^{0.8}$]
p	Absolute static pressure	μ	Dynamic viscosity
$\bar{p}$	Mean absolute static pressure over one vane pitch	ν	Kinematic viscosity [= μ / ρ]
P	Power	ρ	Density
P_{max}	Non-dimensional pressure parameter [$= 0.5 C_{p,max} Re_w^{\,2}$]	σ	Standard deviation, fitting error
P_T	Total Pressure	Φ	Non-dimensional sealing parameter [= $C_w / 2\pi G_c Re_\Phi$]
Q	Power requirement	Φ_e	Value of Φ when $C_w = C_{w,e}$
r	Radial co-ordinate	Φ_i	Value of Φ when $C_w = C_{w,i}$
R	Resistance	Φ_i*	Value of Φ_i when $\Phi_0 = 0$
R_s	Wire-mesh resistance	Φ_{min}	Value of Φ when $C_w = C_{w,min}$
Re_s	Axial-gap Reynolds number [$= \frac{\rho \Omega S^2}{\mu}$]	Φ_0	Value of Φ when $C_w = C_{w,0}$
Re_w	Axial Reynolds number [$= \frac{\rho W b}{\mu}$]	Ω	Angular velocity of rotating disc
Re_Φ	Rotational Reynolds number [$= \frac{\rho \Omega b^2}{\mu}$]		

Subscripts

a	Annulus	*o*	Superposed flow, zero rotation
ax	Axial-clearance seal, axial component of velocity	*rad*	Radial-clearance seal
CI	Combined ingress	*RI*	Rotationally-induced ingress
com	Combined ingress parameter	*s*	Stator
e	Egress	*1,2*	Locations in wheel-space and annulus, respectively
EI	Externally-induced ingress	*	Value when $C_{w,0} = 0$
i	Ingress	‹	Inner seal location

max	Maximum	^	Estimate value from theoretical curve
min	Minimum	+ / -	Upper and lower bounds of 95% confidence intervals

Abbreviations

ASME	American Society of Mechanical Engineers	EPSRC	Engineering and Physical Sciences Research Council
CFD	Computational Fluid Dynamics	HMA	Hot Main Annulus
CMA	Cold Main Annulus	OM	Orifice Model
DP	Design Point	TLC	Thermochromic Liquid Crystals

Chapter 1: Introduction

1.1 Birth of the jet engine

The earliest documented history of jet propulsion is to be found from Hero of Alexandria (circa AD 60), who developed the first reaction-type turbine. This basic steam turbine was produced initially as a toy; however it was inconceivably the start of man's fascination and onward development of such machines. Lock (2007) details a thorough breakdown of further advances gearing up to the turbojet revolution; pioneered by both Sir Frank Whittle, in England, and also independently by Hans von Ohain, in Germany.

The attraction of such a gas turbine for propulsion purposes, and what led the development drive, was the potentially large power output in relation to the weight and size of the engine concepts. It was whilst working as a flight cadet at RAF College Cranwell in 1928 that Whittle wrote his thesis entitled "Future Developments in Aircraft Design." As detailed in Meher-Homji (1998), Whittle, like many others, envisioned a piston engine driven compressor, blowing air over fuel jets and then subsequently exhausting this hot air through a propelling nozzle. However, it was not long until he realized that the pressure ratio across the compressor could be dramatically increased if the propeller was substituted by a turbine. Come the turn of 1930, Whittle filed a Patent for "Improvements in Aircraft Propulsion" (Fig. 1.1). The design featured a single-shaft turbojet; namely an axial-centrifugal compressor, a tubular combustor and a two-stage turbine.

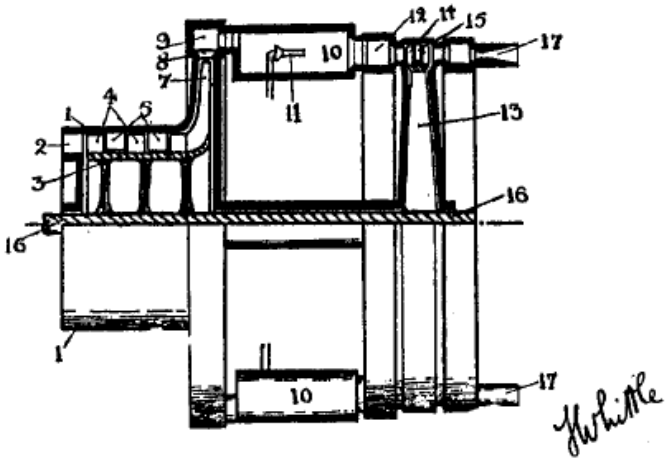

Figure 1.1 Frank Whittle's patent No. 347206 (Meher-Homji, 1998)

The development from idea to reality was not a smooth transition for Whittle's engine, as during his studies at Cambridge in 1935 the patent was left to expire due to an absence of onward financial backing. It was the opposition from Dr. Griffith, who worked at Britain's Air Ministry at

the time, that rendered the concept to be judged non-feasible and support for the £5 renewal fee was therefore rejected at his request. It was only by a great deal of determination on behalf of Whittle that he was able to launch Power Jets Ltd. in the spring of 1936, with start-up capital of merely £10,000 and appointing himself as Chief Engineer. April 12, 1937 saw the first test runs of Whittle's concept WU engine, however with problems arising and re-constructions necessary, it wasn't until 1940 that fully successful trials were held on the second generation engines termed, "W.1" and "W.2". By this point, the government had taken note and promised Power Jets Ltd. a contract to produce these engines in collaboration with Gloster Aircraft Company; to power the experimental E28/39 aircraft, and the then planned Gloster Meteor fighter, respectively (Fig. 1.2). Whittle's W1 engine gave flight to the first E28/39 on May 15, 1941, and it was this success that firmed up plans for the Meteor production. However, with concerns raised as to Whittle's ability to produce the desired engines on his own, the production rights were handed over to the Rover Company, which developed the W.2B to a certain extent before themselves being outsourced to Rolls-Royce - which finished the job. On June 12, 1943 the Gloster Meteor eventually took to the skies, powered by two Rolls Royce "Welland" turbojets – developed in their very essence from Whittles early designs. The engines in question were rated at only 1600 lb thrust, but nevertheless could propel the Meteor to speeds above 400 mph. The Welland engines would lead on to the Derwent and eventually the Nene and Tay turbojets, with Whittle's basic design features living on as his co-invention was developed and continues to be developed today.

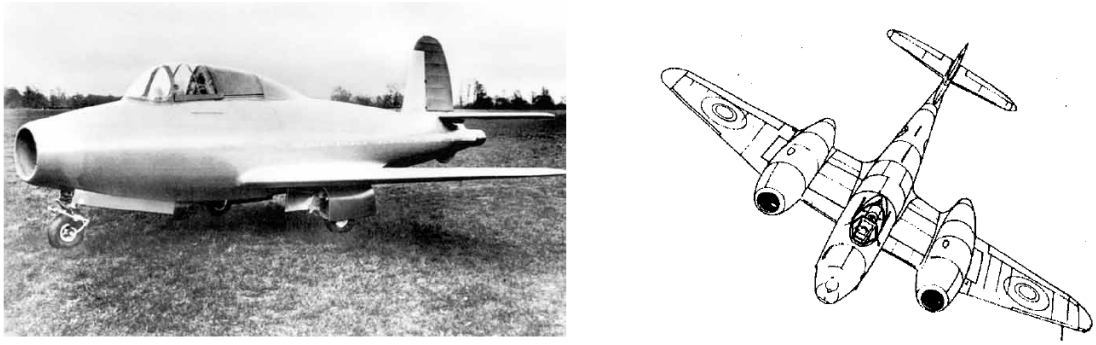

Figure 1.2 The experimental Gloster E28/39 and twin-engined Gloster Meteor fighter

On the other side of the development was Hans von Ohain, who developed his idea of a turbojet whilst studying for his doctorate at the University of Göttingen in 1934 (Meher-Homji and Prisell (2000)). Upon impressing his concepts upon the university faculty, his designs were supported on recommendation by Heinkel. Due to time constraints and the desire to construct a working prototype, von Ohain's first engine was developed using hydrogen as the fuel. The first engine, demonstrated to Heinkel in 1937, consisted of a back-to-back radial compressor and a radial inflow turbine (Fig. 1.3).

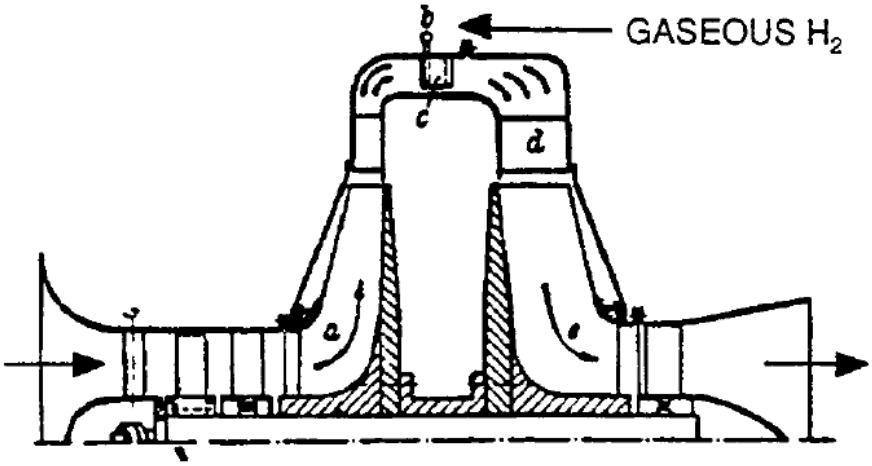

Figure 1.3 Ohain's prototype hydrogen engine (Meher-Homji and Prisell, 2000)

After impressing with his hydrogen engine, von Ohain received a promotion to head of aerospace propulsion at Heinkel, and there he developed his HeS3 and HeS8 engines, which would power the He 178 and twin engined He 280, respectively (Fig. 1.4). The first flight of the He 178 would go on to precede Whittle's first flight by twenty months.

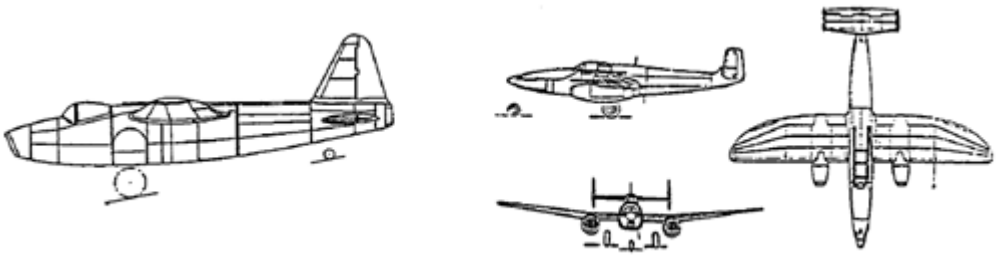

Figure 1.4 The Heinkel He 178 and twin-engined He 280 fighters

Von Ohain and Heinkel were to eventually have their contract for the He 280 cancelled in 1943 in favour of the alternative Jumo 004 turbojet, developed in collaboration between Junkers and BMW (Meher-Homji (1997)). This design would feature many of the same concepts and would become the world's first production turbojet and go on to power the Messerschmitt Me-262 (first flight July, 1941). The design featured an eight-stage compressor unit, six combustion chambers and a single-stage turbine (Fig. 1.5).

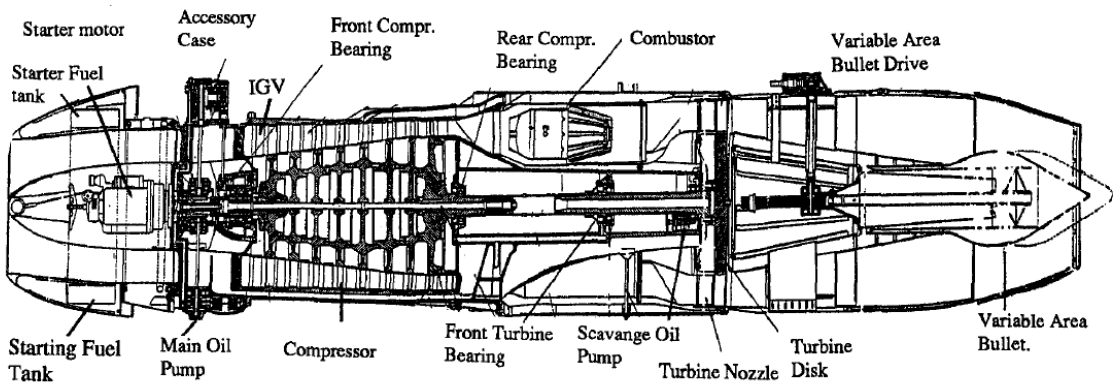

Figure 1.5 Cross section of the Jumo 004 turbojet (Meher-Homji, 1997)

Owing to the lack of high-temperature materials available at the time, the expected time between overhaul was 25 to 35 hours, rendering this engine acceptable for mission usage, however, leaving a lot to be desired in terms of civilian transport.

Whittle was awarded a knighthood for his efforts and proclaimed the "father of the jet engine." Von Ohain worked for the US government for a further 32 years in aerospace research. The work of these two men ignited the procession from these early designs towards the phenomenal advancements seen today in gas turbine roles the world over. They will both forever be remembered as the men who started it all.

1.2 Gas turbine engines

A gas turbine works on the principle of a rotary engine extracting energy from a flow of combustion gas. The three main features of a basic gas turbine are an upstream compressor coupled to a downstream turbine, with a combustion chamber situated between the two. The inflow air is compressed before entry into the combustion chamber, at which point it is mixed with injected fuel and ignited. During the ignition process the gas flow experiences increases in temperature and velocity, allowing this now high energy flow to be expelled through a diverging nozzle over the turbine blades; which in turn drive the compressor stages. An example variation of these fluid conditions throughout the working cycle is detailed in Fig. 1.6 for an axial-flow turbojet. Considering the flux of momentum across the gas turbine, and the increase in fluid velocity caused by the ignition and expansion processes, the force supplied to cause this resulting acceleration will be very large. Working on the principle of Newton's third law, a force equal in magnitude but opposite in direction will act on the gas turbine; this is known as the net thrust of the engine.

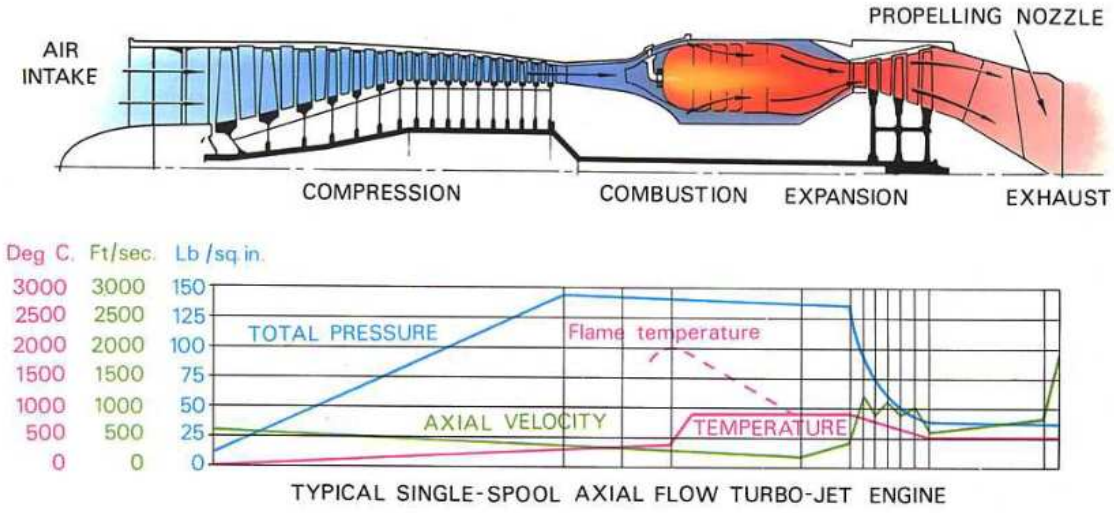

Figure 1.6 Pressure, temperature and velocity variation in a turbojet (Rolls-Royce (1996))

Gas turbines can be described thermodynamically by the ideal Brayton cycle, in which an isentropic compression (A-B) is followed by an isobaric combustion (B-C) and then finally an isentropic expansion (C-D). This cycle, whilst useful for basic understanding, falls someway short of the actual workings of the engine in which friction and turbulence will cause changes in entropy resulting in nonisentropic compression and expansion. Losses in the combustion process are also expected, with the operating cycle for a simple gas turbine shown in Fig. 1.7; which also highlights the difference between idealistic and real cycles, shown in black and red, respectively.

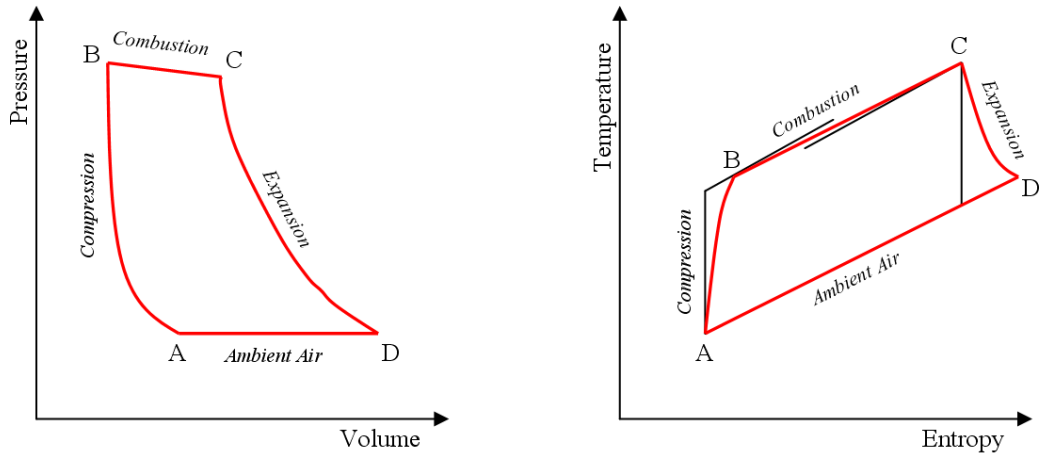

Figure 1.7 Operating cycles for a simple gas turbine

Uses for the gas turbine have been vast, owing largely to the very high power-to-weight-ratio and relatively few number of moving parts to fail in the design. One of the most

important uses for the concept is aircraft propulsion, discussed in depth by Cumpsty (1997). However, other employments are to be found as turboshaft engines for helicopters, microturbines for power distribution, powering naval vessels and more recently as natural gas burners for electricity generation. So whether on land, sea or air the development of the gas turbine continues to evolve, and research in this field is as active as ever.

1.3 Evolution of cooling technology

With new and very rapid technological advances in both the aerospace and industrial sectors, further increases in gas turbine performance are of paramount importance. The competitive nature of gas turbine design has forced an increase in expected turbine entry temperatures, engine pressure ratios and hence cooling technologies of both the blades and discs. With the reduction in specific fuel consumption a key driver in modern turbine design, overall pressure ratios (OPR) have risen, which in turn has led to an increased turbine entry temperature (TET).

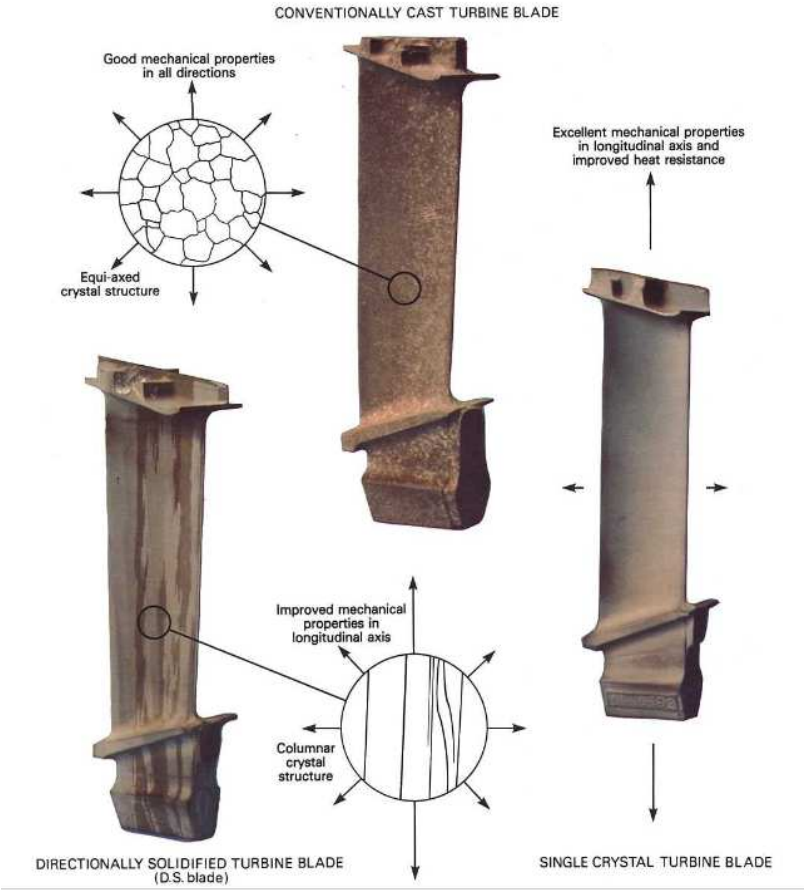

Figure 1.8 Various turbine blade crystal structures (Rolls-Royce, 1996)

The TET has come a long way from the 1050 K of the Whittle W1 engine and is now frequently found to be around 1800 K. This is evidently above the melting point of the turbine components and hence effective cooling systems are employed. As found with any cyclical heat engine, these higher combustion temperatures result in incrementally greater efficiencies; thus considerable engineering hours are spent in fine tuning these complex, and in some cases rotating, cooling systems to make these TET advancements possible.

The first advancements were found in turbine blade materials which have been modified completely since the 1940's. Early engines featured high temperature steel forgings; however these were quickly phased out in favour of cast alloys which provided better creep and fatigue properties. These first blades consisted of equ-axed crystals lying in all directions, however, the process of directional solidification was then developed which allowed for the crystal structure to become aligned along the blade length (Fig. 1.8), which helped to improve the blades' resistance to creep. Even further improvements were made when companies started to produce blades grown from a single crystal, thus removing the slip planes that existed in earlier blades. Contemporary blades are manufactured in this way and now include a thermal barrier coating, which further aides the cause.

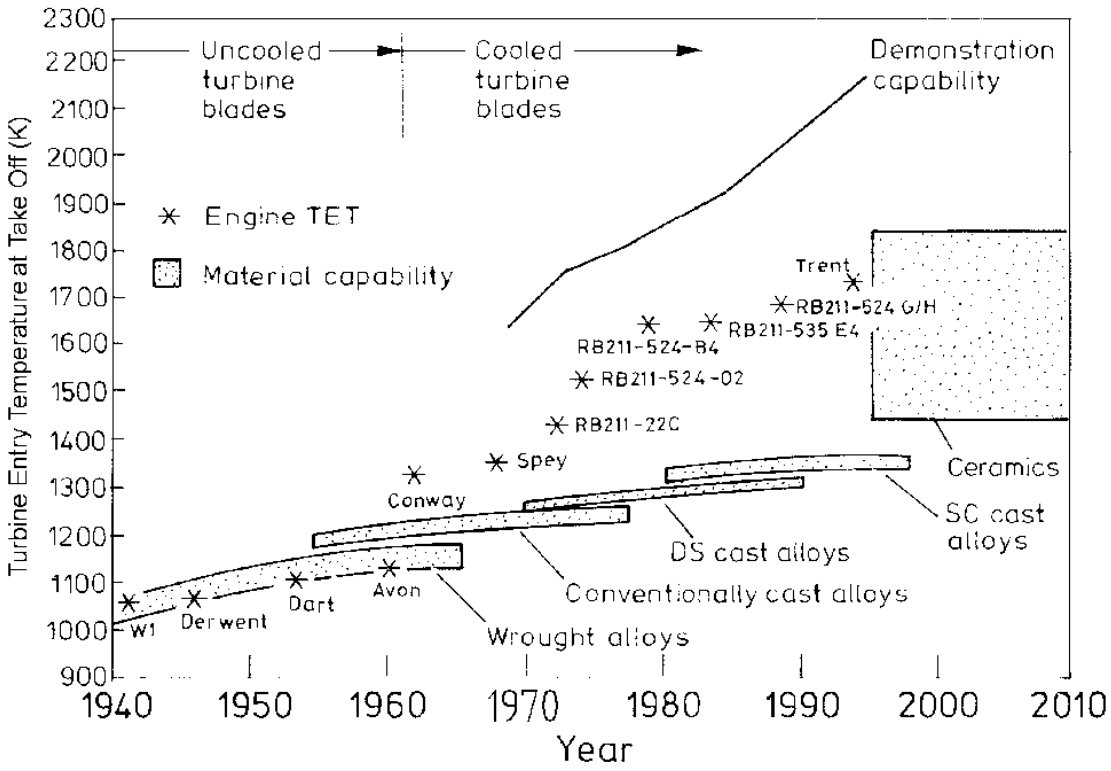

Figure 1.9 Chronological turbine entry temperature improvements at take-off condition (Cumpsty, 1997)

Improvements in material technology contribute to the rise in TET's only in combination with the influence of engine cooling systems. The Rolls-Royce Conway was the first production

engine to use single-pass, internal-blade cooling, shown in a chronological Rolls-Royce TET improvement chart (Fig. 1.9).

The development of these internal cooling passages is complex, with current designs featuring intricate labyrinths of internal passages through which coolant flows over ribs and fins to cool the blade interior, before exiting through tiny surface holes creating a protective air film to cool the blade exterior (Figure. 1.10).

Improvements in engine cooling performance increase the lifetime of turbine components and also reduce the amount of cooling air bled from the compressor stages, which can be as high as 20% of the core flow. Reducing this cooling percentage is paramount if a high propulsive efficiency is to be maintained; however it is also essential to maintain the structural integrity of the critical components within the engine.

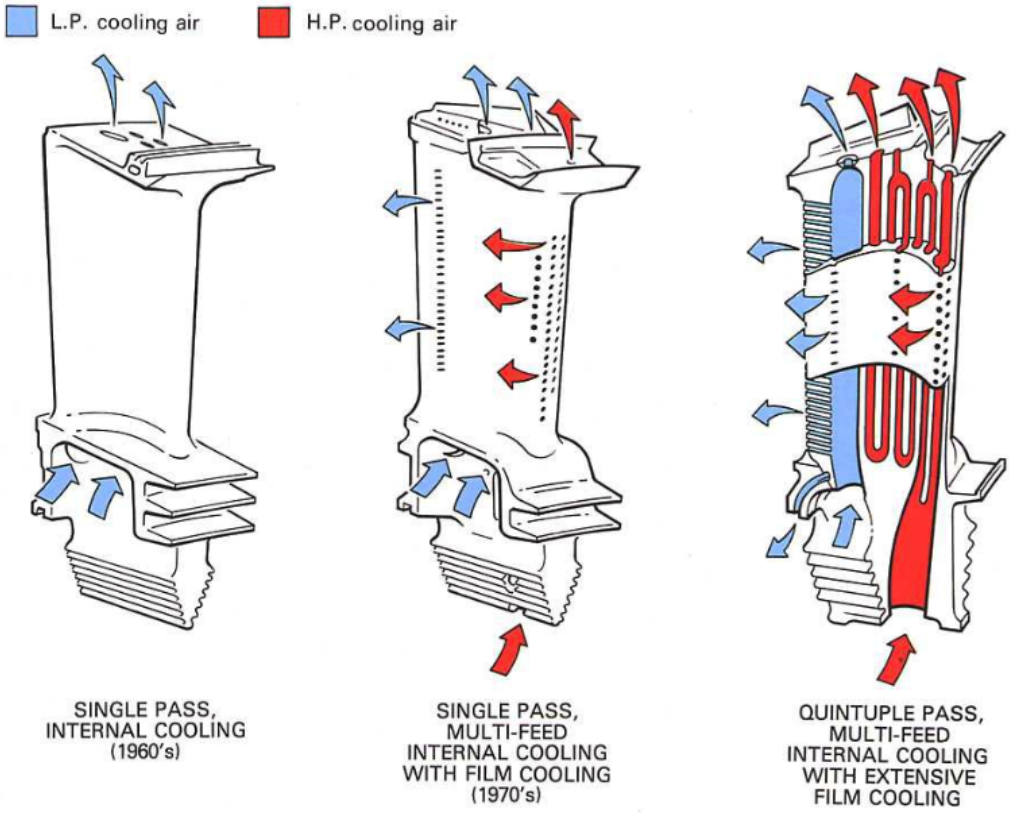

Figure 1.10 The development of turbine blade cooling (Rolls-Royce, 1996)

As documented, much work has been conducted into the cooling of engine components, with the use of new alloys, ceramic materials and effective blade cooling techniques found to be highly beneficial. However, in order to continue to advance the trend in engine cooling performance, much research now focuses on the disc cooling procedure. The heat transfer between air in the cavities and the adjacent discs governs temperature gradients throughout the engine cycle.

The thermal stresses caused by alternating expansion and contraction of the turbine discs are a major component of the total stress determining the disc's cycle life.

The above leads to the problem of gas turbine ingress, whereby hot mainstream gas can be ingested into the wheel-space between the turbine discs and adjacent casing. The use of compressed air to seal the wheel-space in an efficient way is a key problem faced by internal air systems engineers. An engine representative diagram highlighting the highly complex nature of gas turbine cooling systems is included as Fig. 1.11.

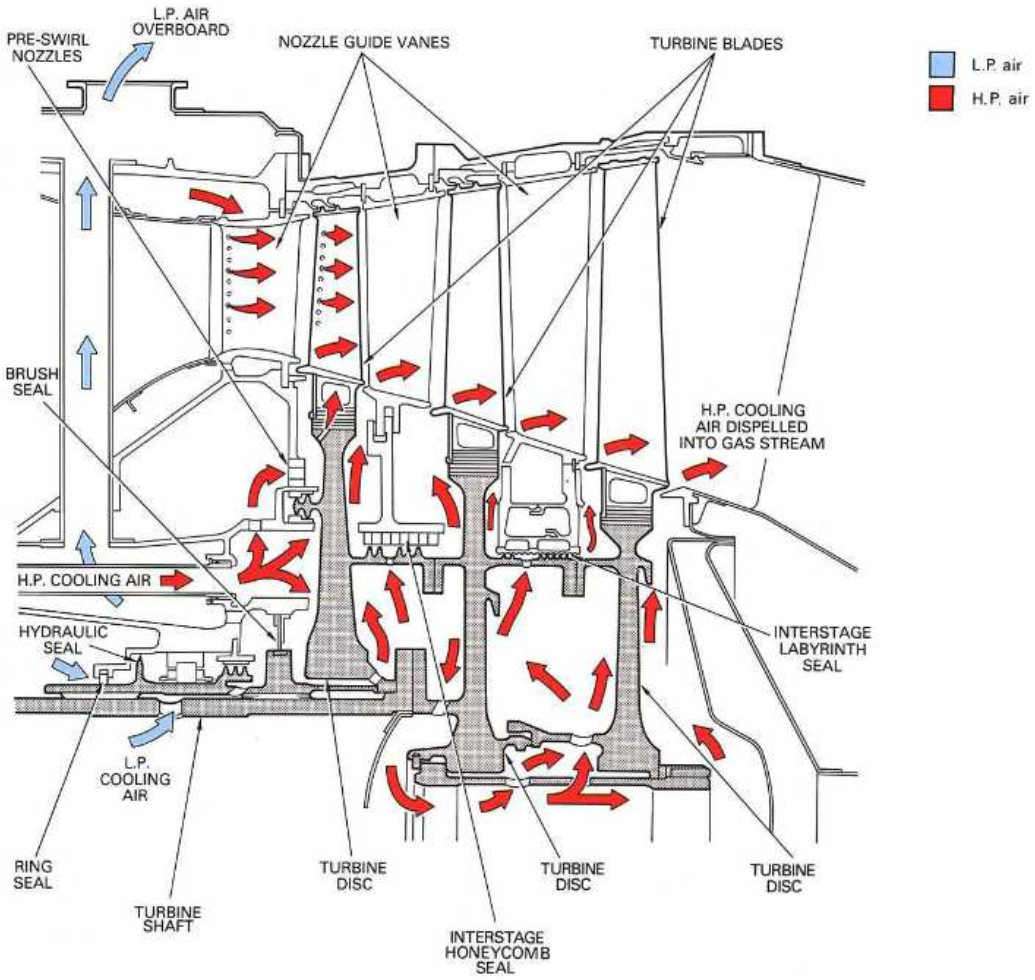

Figure 1.11 Internal air system for a gas turbine (Rolls-Royce, 1996)

The internal air system can be simplified to distinguish those coolant paths related directly to the prevention of mainstream gas ingestion into the wheel-space between the rotor and stator discs. A single stage model of this concept is shown as Fig. 1.12, where it can be seen that a rim seal is fitted at the periphery between the adjacent discs, and that a sealant flow is used to reduce the ingress into the wheel-space.

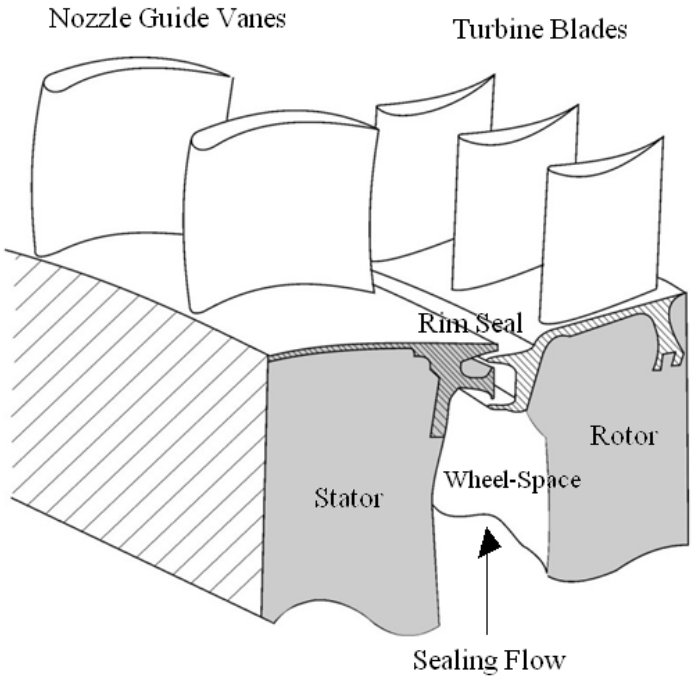

Figure 1.12 Schematic model of the sealant air used to combat mainstream gas ingestion

The sealing balance is key to effective and efficient cooling of the discs. If the sealant flow is excessive, *i.e.* more than the minimum required to cool the discs, then the amount of coolant air bled from the compressor discharge is unwarranted, and the associated reduction in propulsive efficiency is detrimental to the engine performance. This performance penalty would mean the turbine is uncompetitive in a world economy dominated by increasing fuel costs. In contrast, if the sealant flow is insufficient, then overheating of the rim seal and cavity is possible causing potentially catastrophic damage to the turbine.

The aim of the internal air system is therefore to either purge the cavity, thus preventing mainstream ingestion, or at minimum to dilute the hot ingested gas to achieve an acceptable disc temperature. The ingress problem is considered to be one of the most important of the gas turbine cooling problems and thus a great deal of international research is concerned with acceptable design criteria for future turbine production. There is a growing trend to utilise computing power to run highly complex 3D unsteady CFD codes, which require validation. Careful experimental research is therefore unavoidable, with engine test rigs and simplified engine models still vital to the understanding of these complex flows, whilst offering engine designers simpler ways of predicting these inescapable and potentially catastrophic effects.

1.4 Thesis aims

The aim of this PhD research is to design a new rotor-stator testing facility, from which both the fluid dynamics and heat transfer characteristics of ingress can be measured and analysed. The test facility will allow for a detailed investigation into the sealing characteristics of various turbine rim-seal configurations. The rig will be constructed as an engine representative model of a gas turbine wheel-space, from which data correlations could tentatively be scaled and applied to actual engine design.

The University of Bath has extensive experience with thermochromic liquid crystals (TLC) and the rig will be specifically designed to accommodate this experimental technique. This novel approach would enable, for the first time, the thermal effects of ingress inside the wheel-space to be visualised and measured and for heat transfer data to be acquired on the rotor surface. It is hoped that the experimental measurements will provide fundamental insight into the ingress problem and inform improvements in future internal air system designs.

The main experimental aim of this thesis is to measure the sealing characteristics of a series of generic rim-seal geometries, which will inform the design of Siemens proprietary seals. The rig data will also be used to validate a simple "orifice model," which will allow the engine designer to estimate the effect of ingress without the need for extensive initial research. The rig will therefore be designed to both accommodate optical access to TLC, as well as containing sufficient instrumentation to gather data to support the orifice model.

The design and manufacturing program is documented in this thesis, along with the procedure for the commissioning of the facility. An extensive range of seal effectiveness measurements aimed at the validation of the orifice model will be presented, culminating in an investigation into the characteristics of double seals and the proposition of an *ultimate* seal. The experimental heat transfer will form no part of this thesis; this will appear in a subsequent thesis from the University of Bath.

1.5 Project funding

The research described here is part of a programme jointly funded by the UK Engineering and Physical Sciences Research Council, Siemens Fossil Power Generation and Siemens Oil & Gas. This research was funded by EPSRC grant EP/G069107/1

1.6 Thesis overview

Chapter 1 has given an introduction to the historical development of gas turbines, the theoretical concepts applied in their use and the improvement and problems involved in the cooling technology required to design them.

Chapter 2 presents a comprehensive literature review describing the design of previous ingress rigs and the theoretical models developed from them. All ingestion regimes are considered in turn and their applicability to the current work is explained.

Chapter 3 derives the salient equations from the orifice model, used to support the experimental measurements. The orifice model developed by Professor J.M. Owen is extended to formulate the explicit effectiveness equations for comparing with the experimental data.

Chapter 4 describes the design of the new gas turbine facility constructed at the University of Bath. The rig is developed from early principles and documented through to commissioning.

Chapter 5: Experimental data for rim-seals are presented for a series of conditions under the Externally-Induced (EI) ingestion regime. The data are shown to agree well with the orifice model theory and highlight the benefits of using the new parameters derived from the theoretical model.

Chapter 6: Experimental data for rim-seals are presented for a series of conditions under the Rotationally-Induced (RI) ingestion regime. The data is again shown to be predicted well by the effectiveness equations. The fluid dynamics inside the rotor-stator cavity is discussed in terms of the radial variation of sealing effectiveness on the stator wall.

Chapter 7: The performance characteristics of double rim-seals are investigated, highlighting the protection that an inner seal can provide to the inner wheel-space by containing the hot gas ingress within an intermediate annulus formed between the two seal clearances. The concept of an *ultimate* seal is also considered, along with the optimisation procedure required to attain it.

1.7 Publications

The following publications were produced over the duration of research documented in this thesis: Sangan *et al.* (2011a), Sangan *et al.* (2011b) and Sangan *et al.* (2011c). Whilst the two ASME conference papers form the main body of discussion reported in this thesis, Sangan *et al.* (2011c) was conducted as a precursor to the heat transfer design work and as such is included as Appendix E. It is expected that the contents of Chapter 7 will form the basis for future publications.

Sangan, C. M., O. J. Pountney, K. Zhou, M. Wilson, J. M. Owen and G. D. Lock (2011a). Experimental Measurements of Ingestion through Turbine Rim Seals. Part 1: Externally-Induced Ingress. ASME Paper GT2011-45310. To Appear in ASME Journal Turbomach.

Sangan, C. M., O. J. Pountney, K. Zhou, M. Wilson, J. M. Owen and G. D. Lock (2011b). Experimental Measurements of Ingestion through Turbine Rim Seals. Part 2: Rotationally-Induced Ingress. ASME Paper GT2011-45313.

Sangan, C. M., K. Zhou, K. Litherland, R. Lam and G. D. Lock (2011c). "Thermal imaging as flow visualization for gas-turbine film cooling." Proceedings of the Institution of Mechanical Engineers, Part G: Journal of Aerospace Engineering, 225(**4**): pp 417-431.

An invention disclosure document has been submitted, which is expected to form the basis of a Siemens patent application. The document covers the design of an optimised double rim-seal which was developed over the course of this research program.

Owen, J. M., G. D. Lock, C. M. Sangan, K.-M. Tham, C.-P. Lee and V. P. Laurello (2011). Finned Rim Seal for Gas Turbine. Siemens Invention Disclosure, Siemens Orlando, **2011E10442US.**

Chapter 2: Literature review

Rotating flow governs the fluid dynamics of turbine disc cooling. These highly complex flows are found to be 3D and can be unsteady. Of particular interest to this field are those flows found in the compressor and turbine stages of the engine, along with the internal cooling systems required for them to function. These internal air systems are used to prevent mainstream gas ingestion into the disc cavities, as well as providing cooling air for the turbine blades and vanes. In practice it is uneconomical to provide design criteria for these systems using full size gas turbine replicas, and consequently this research is often conducted using small-scale models and test rigs. From these experiments, accurate results can be used to derive design criteria that can be scaled to engine conditions, often with the use of theoretical models. The experimental work also serves to validate CFD codes which can then be used with greater conviction to assist the production of new and more efficient engines in the future.

Important work in the area of gas turbine ingestion has been published at academic centres worldwide, with the University of Bath rig documented in this thesis joining this active research field; an entire session is devoted annually to ingress at the American Society of Mechanical Engineers (ASME) Gas Turbine Expo. Test rigs at the Universities of Sussex, Arizona State and Aachen, to name a few, have already contributed greatly to the research since initial work began in the 1970s.

A detailed and well received overview of both experimental and theoretical literature related to a wider study of rotating flows has been compiled by Owen and Rogers (1989) and Owen and Rogers (1995). This chapter will give a brief introduction to the fluid dynamics found in rotating systems, moving on to a more detailed look at the theory behind the physical mechanics of ingestion. A detailed review of previous and current research into this field will be presented, with emphasis on rig design, experimental conclusions and the theoretical models developed from them. A short review of experimental procedure for heat transfer measurements will be given to disclose the reasons behind many of the design decisions documented in the design chapter of this thesis.

2.1 Single disc rotating in free space

As a precursor to discussing the complex flow that occurs in rotor-stator systems, it is beneficial to look at a simple disc spinning in free air. The disc will be of radius b, and rotates about the z-axis with angular velocity Ω (Fig. 2.1).

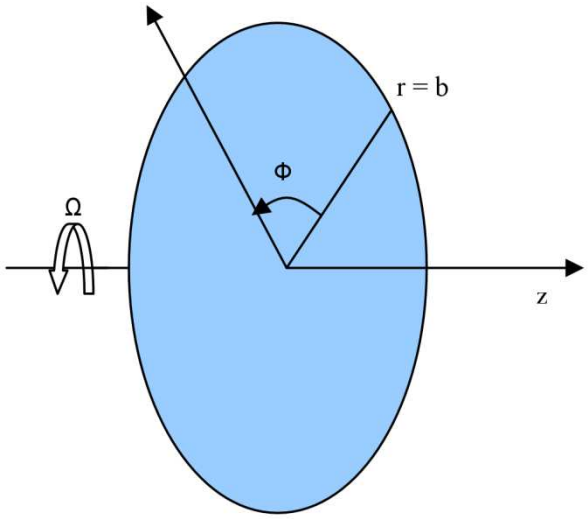

Figure 2.1 Co-ordinates for a rotating disc in free air

Boundary layers will develop on either side of the disc, with a maximum tangential velocity component ($V_\phi = \Omega r$) at the disc surface, falling in each case to zero in the free-stream outside the boundary layer. When the disc rotates the centrifugal forces will cause the fluid within the boundary layer to flow radially outwards. Since the radial velocity component will be zero on both the disc surface and in the free-stream, external fluid will become entrained axially into the disc boundary layer. The flow pumped by a rotating disc is often referred to as the "free-disc entrainment rate" or the "free disc pumping effect".

Inside the boundary layer, the flow may be laminar or turbulent, whereby the determining parameter is the local rotational Reynolds number (Eq. 2.1).

$$Re_\Phi = \frac{\Omega r^2}{\nu} \qquad \text{(Equation 2.1)}$$

For all values of Ω the flow is usually laminar near the rotation axis, however, for large values of Ω, the flow may become turbulent with increasing radius, featuring a transition region between the two.

2.2 Rotor-stator system without superposed flow

A common gas turbine configuration consists of a rotating disc situated adjacent to a stationary casing. This can be suitably modelled by considering the fluid dynamics between a rotating disc and a stationary disc, termed the rotor and stator, respectively. A rotor-stator system is

defined as a rotating disc of diameter, *b*, rotating at a distance *S* from a stationary disc of similar diameter, as shown as Fig. 2.2.

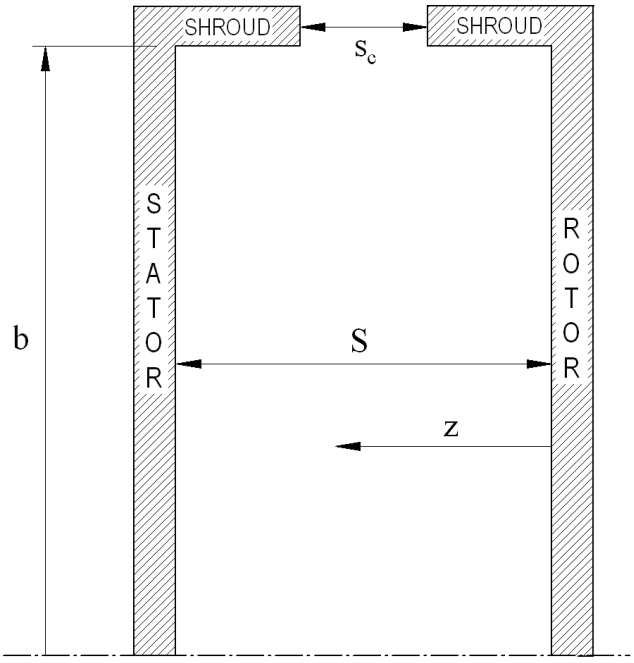

Figure 2.2 Generic rotor-stator configuration

Two initial models were proposed for the flow between rotating and stationary discs, with the first being Batchelor-type flow. Batchelor (1951) suggested that there would be a core of fluid between the two discs that would rotate with an angular velocity of magnitude between zero and Ω. This implied that two boundary layers would exist; one on the rotor identical to that on a free disc and a second on the stator. The stator boundary layer would contain a radial inflow of fluid into the cavity, with an efflux of fluid from the boundary layer into the rotating core. The core flow would then become entrained on the rotor boundary layer and out of the system.

Stewartson (1953) proposed an alternative model, where he suggested that a boundary layer existed on the rotor disc, analogous to the free disc theory. He used computations and basic experiments to suggest that the tangential component of velocity is reduced from Ω*r* on the rotor surface to zero away from it at the stator surface. He therefore concluded that no boundary layer was necessary on the stator and that no core rotation existed.

It has now been shown experimentally that the flow between a rotating and stationary disc is of Batchelor type, whereas the free disc setup is similar to the Stewartson type. Theoretical streamline patterns for the two flow types are shown diagrammatically as Fig. 2.3. It was further investigated and shown by Picha and Eckert (1958) that when the discs were open to the

atmosphere, no significant core rotation occurs, however when the discs were surrounded by a shroud (as is typical of rotor-stator systems) then core rotation did indeed exist.

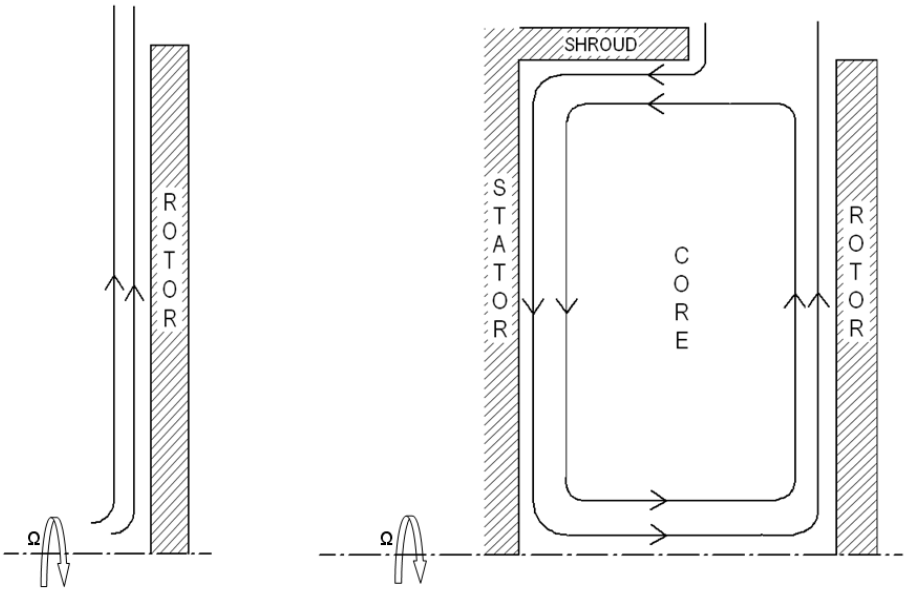

Figure 2.3 Rotating flow patterns for both a free-disc (left) and a simple rotor-stator system (right)

The existence of such a core flow was shown by Chen *et al.* (1996) who used laser-doppler anemometry (LDA) to investigate the radial and tangential velocity components in a simple rotor-stator system with a stationary shroud. The experiments were conducted with no superposed flow-rate and results were taken across the wheel-space. (Here z is the axial distance from the rotor-side as shown in Fig. 2.2). The flow structure was found to be a turbulent form of Batchelor flow, with a radial outflow on the rotor (z/S = 0), a radial inflow on the stator (z/S = 1) and with an inviscid rotating core between these boundary layers (Fig. 2.4).

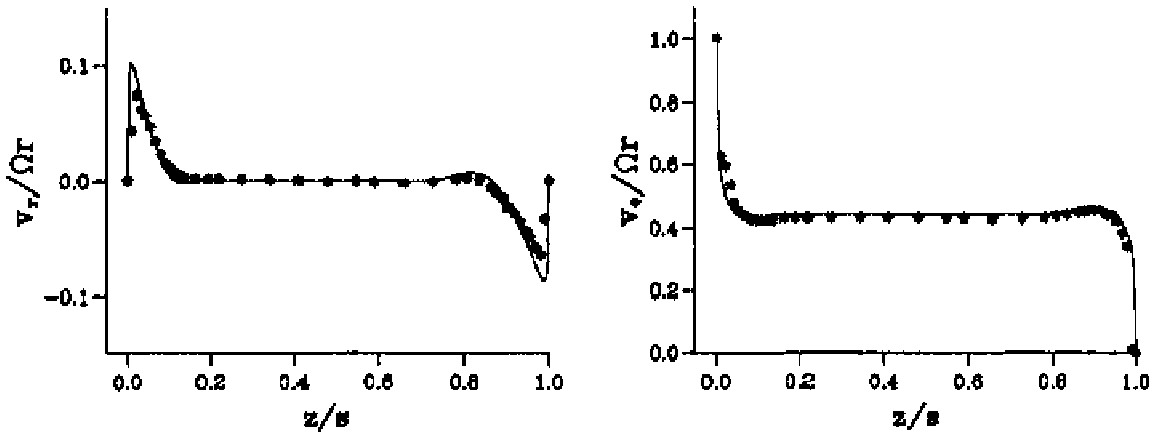

Figure 2.4 Radial and tangential velocity profiles across a rotor-stator wheel-space (Chen *et al.* (1996))

The component of radial velocity is shown to be zero on both the discs and in the core, owing to the viscous forces near the disc surfaces and the Coriolis forces in the core, respectively.

The turbulent flow structure inside a rotating cavity depends mainly on two non-dimensional parameters, provided that separate boundary layers exist on either disc: the swirl ratio (Eq. 2.2) and the turbulent flow parameter (Eq. 2.3); this is discussed in detail by Owen and Rogers (1989). The swirl ratio is defined as the ratio of the tangential velocity component inside the rotating core to the angular velocity of the rotor at equal radii

$$\beta = \frac{V_\phi}{\Omega r} \qquad \text{(Equation 2.2)}$$

The turbulent flow parameter combines the rotational Reynolds number and the non-dimensional flow-rate, both defined in the nomenclature and measurable under experiment.

$$\lambda_T = C_w {Re_\Phi}^{-0.8} \qquad \text{(Equation 2.3)}$$

Again, it must be emphasized that this hypothesis is only true in the case of Batchelor-type flow where an inviscid rotating core exists between two separated boundary layers.

2.3 Flow regimes in a rotor-stator cavity

If a simple rotor-stator system is considered without a superposed flow and with variable axial clearance between the rotor and stator, a gap Reynolds number, Re_S, can be defined (Eq. 2.4) with axial spacing, S.

$$Re_s = \frac{\Omega S^2}{\nu} \qquad \text{(Equation 2.4)}$$

When Re_s is large, a boundary layer will feature on at least one of the discs, with a rotating and inviscid core formed between them. When Re_s is small, Couette flow will occur in which viscous-dominated flow will fill the entire disc cavity. The flow may still be laminar or turbulent irrespective of Re_s. Daily and Nece (1960) experimented with a rotor-stator cavity and proposed four flow-regimes based on the above theory, shown graphically as Fig. 2.5. The flow regimes are dependent on the rotational Reynolds number, Re_Φ, and the axial gap ratio, $G = S/b$.

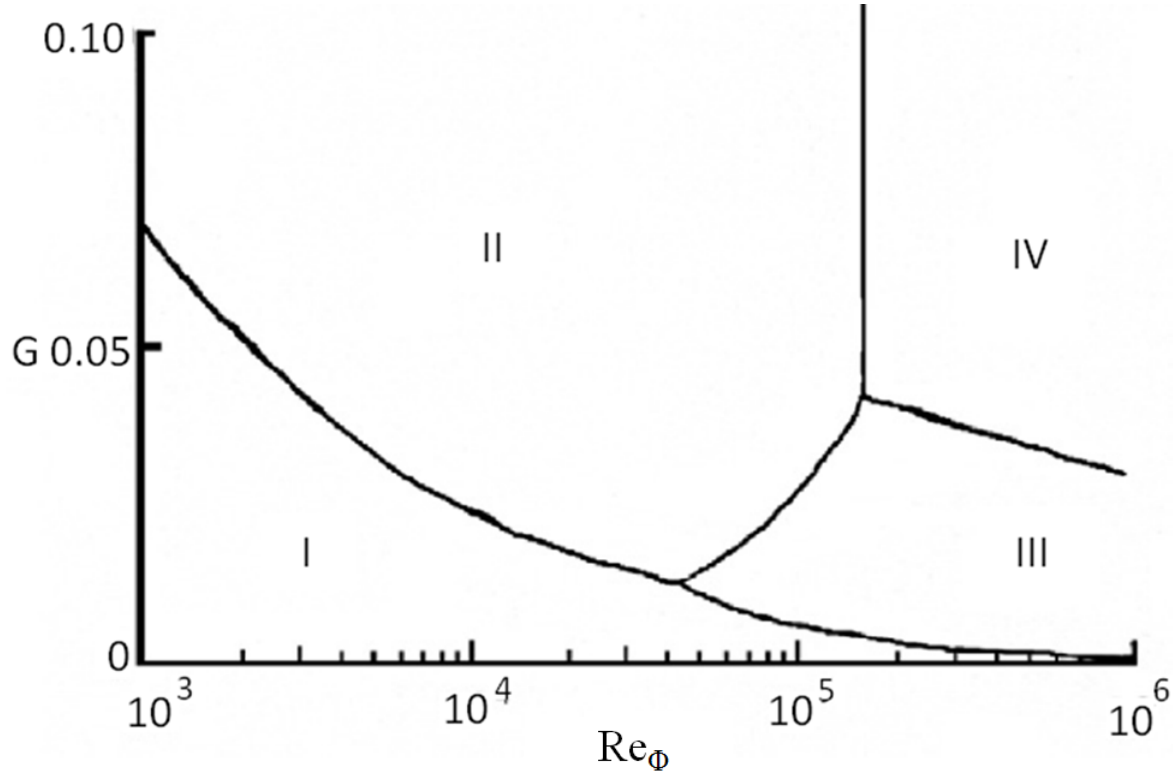

Figure 2.5 Flow regimes (Daily and Nece (1960))

- Regime I: Laminar flow for narrow spacing (low values of G). Flow will be of a Couette type with merged boundary layers on the rotor and stator. For a constant rotational Reynolds number, the frictional heating on the rotor will decrease with an increase in G.
- Regime II: Laminar flow for larger values of G and low Re_Φ. The flow will feature a boundary layer on both the rotor and stator, but now with a rotating core in between the two discs. The stator reduces the core rotation and hence the frictional heating of the rotor disc below that of a free disc. However, as G increases still further, the stator effects will reduce thus increasing the frictional rotor heating again. In fact for $G > 0.1$ the stator will have no effect and the frictional heating will be analogous to that of a free-disc.
- Regime III: Turbulent flow for narrow spacing, similar in nature to Regime I.
- Regime IV: Turbulent flow for larger spacing, similar in nature to Regime II.

Empirical correlations can be used to determine critical gap ratios for minimising unnecessary rotor heating, which could be detrimental to the lifetime of the engine components.

2.4 Rotor-stator system with superposed flow

Gas turbine ingress occurs when hot gas from the mainstream gas path is ingested into the wheel-space between the rotor and stator discs. Various rim seal geometries have been utilised at the disc periphery, along with a superposed sealant flow, in order to minimise this ingress. If too much sealant flow is used, then there is a detrimental effect on the engine efficiency, whereas too little can lead to overheating and thus damage the discs and blade roots. A balance therefore exists which must be optimised by the designer to avoid any unnecessary performance penalties. CFD codes have recently been able to compute such flows, although engine designers are naturally reluctant to accept these results without experimental validation. This has led to a great deal of research related to predicting ingress.

The physical mechanics governing ingress are 3D and unsteady. However, simple mathematical orifice models have been used to estimate the ingress behaviour. In order to support the derivation of these orifice models, work has been conducted into engine-representative rotor-stator rig geometries, where the fluid dynamics can be simulated and examined. A common setup is that of a one-stage "rotor-stator system," where a single rotating disc is positioned adjacent to a stationary disc; a wheel-space is formed between the discs.

The streamlines expected for a rotor-stator system with a superposed sealant flow are shown as Fig. 2.6. Ingress will occur when the pressure in the mainstream flow near the rim seal is higher than in the wheel-space. The ingested air then flows radially inwards, travelling down the stator boundary layer, before being taken axially across the inviscid rotating core. The flow is then entrained into the rotor boundary layer and is mixed with a superposed sealant flow, which enters the system through the centre of the stator disc. This integrated sealant and ingress flow then exits the wheel-space through the seal clearance.

For a rotor-stator system with a superposed flow-rate, the flow conditions not only depend on the rotational Reynolds number, Re_Φ, and the axial gap ratio, G, but additionally on the non-dimensional superposed flow-rate, C_w (Eq. 2.5).

$$C_w = \frac{\dot{m}}{\mu b} \qquad \text{(Equation 2.5)}$$

The flow regimes detailed in Section 2.3 will be similar for cases with a superposed flow, however, Owen and Rogers (1989) suggested that premature transition from laminar to turbulent flow may exist at lower Re_Φ.

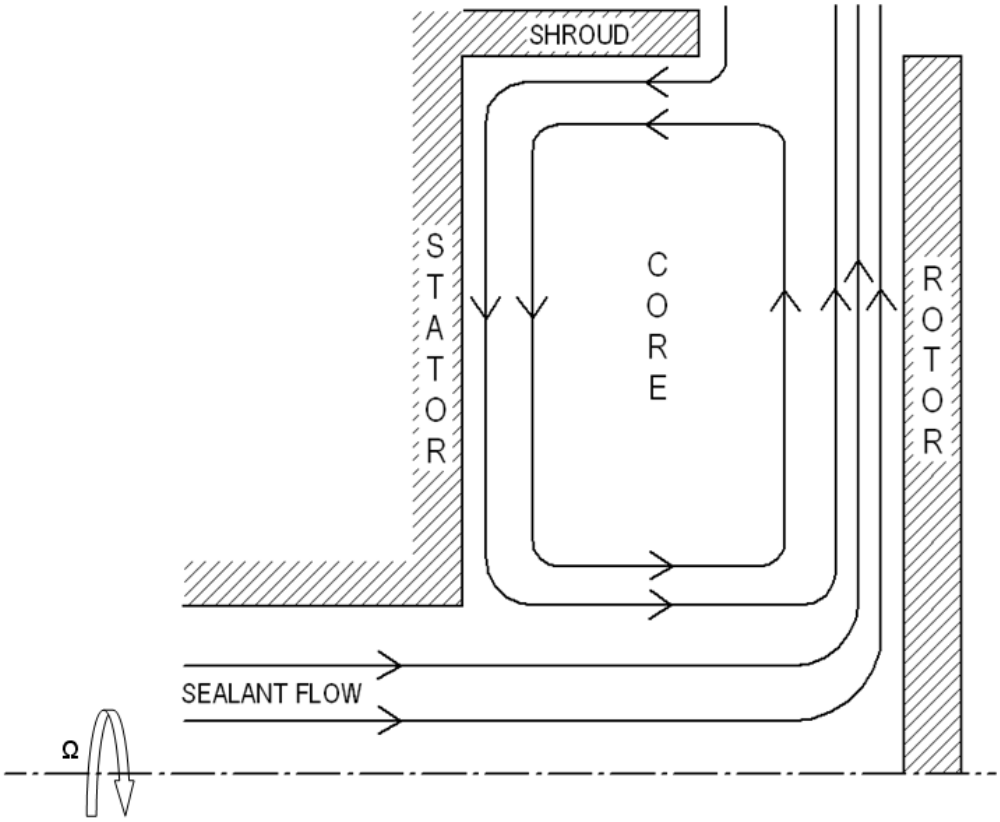

Figure 2.6 Rotating flow patterns for a rotor-stator system with a superposed flow
(Based on the CFD described in Zhou *et al.* (2011b))

2.5 Ingress research and development of mathematical models

In order to document the development of ingress research, it is desirable to split the review into four predominantly chronological sections. The early work featured rotationally-induced ingress for the most part, before moving on to externally-induced ingress. A combined-ingress regime has also been investigated where the effects of disc rotation and the external flow field are both experienced, with neither being the dominant effect. In addition to experimental work, simple mathematical models have also been developed to predict ingress without the need for experimentation. These so called "orifice models" will also be considered.

2.5.1 Rotationally-induced (RI) ingress

Rotationally-induced ingress is analogous to the disc-pumping effect of Batchelor-type flow between a rotating and stationary disc. Among the first to present results using such a simple rotor-stator system were Bayley and Owen (1970), who employed a radial flow of sealant air that

was discharged through an axial-clearance seal into the atmosphere. Due to the rotation of their rig (Fig. 2.7), the pressure inside the wheel-space was sub-atmospheric and thus ingested air could be drawn into the system. The disc was 30 inches in diameter, and positioned adjacent to a shrouded stator disc with a variable three inch cavity width. The rotor was spun to 4500 rpm during the experiments.

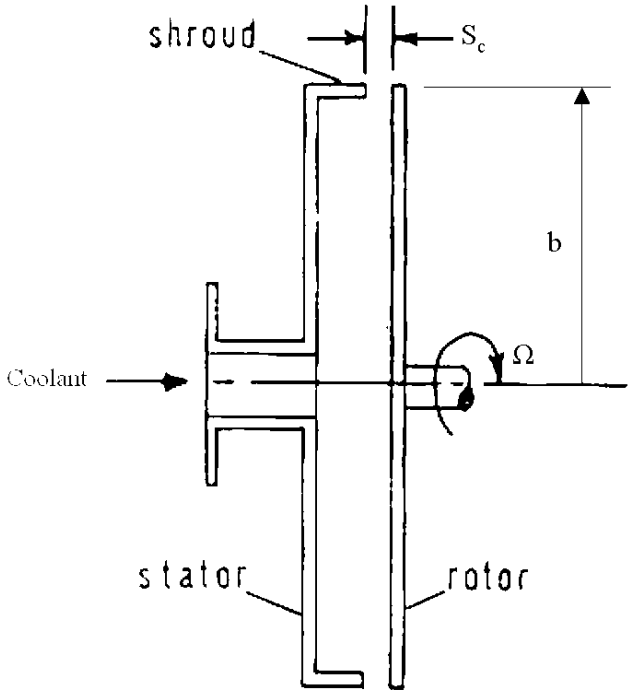

Figure 2.7 Experimental rig model (Bayley and Owen (1970))

Bayley and Owen experimented with increasing the radial flow-rate, causing the wheel-space pressure to increase and hence reducing the ingested air. At suitably high radial flow-rates, ingress did not occur, and the system was said to be "sealed." These experiments were an extension of previous work by the authors in which an identically designed but unshrouded and hence less-realistic system was tested. The fluid dynamics of this system are discussed by Bayley and Owen (1969), however, their latter work was to be far more applicable to practical turbine and hence more beneficial conclusions were drawn.

The study investigated the minimum superposed flow rate required to prevent the static pressure on the stator-side becoming sub-atmospheric, *i.e.* to seal the system. Figure 2.8 shows the effect of shroud clearance on the minimum mass flow-rate to prevent ingress ($C_{w,min}$). It can be seen that the shroud clearance ratio (G_c) is the controlling parameter and that there is little effect of the gap ratio (G). This ties in with the Stewartson and Batchelor-type analysis explained in Section 2.2, whereby G will only have an effect when G and G_c are of comparable size.

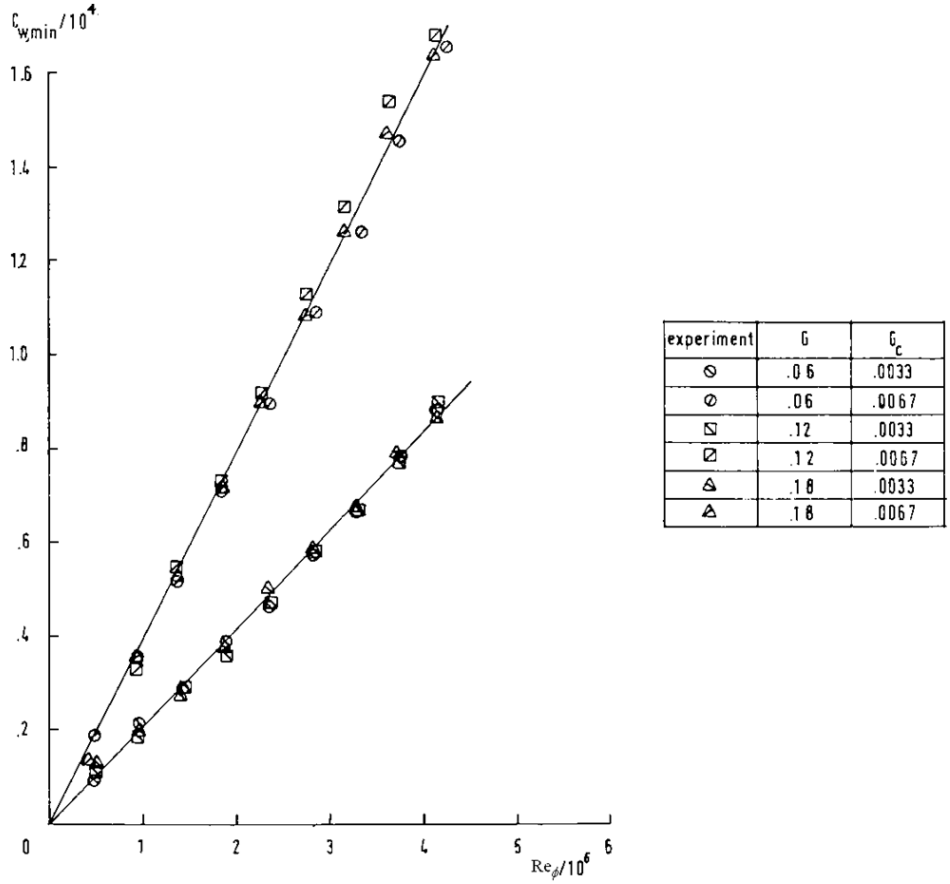

Figure 2.8 Variation of $C_{w,min}$ with Re_Φ for various G and G_c (Bayley and Owen (1970))

Using a number of dimensionless parameters and the correlation from Fig. 2.8, they were able to propose a sealing criterion with the seal clearance modelled as a simple orifice. It was subsequently proposed that the minimum non-dimensional flow-rate to prevent ingress occurring was proportional to the rotational Reynolds number and the seal clearance ratio, according to Eq. 2.6.

$$C_{w,min} = 0.61 G_c Re_\Phi \quad \text{(Equation 2.6)}$$

That is when $C_w \geq C_{w,min}$ ingress could not occur.

Phadke and Owen (1983) performed further research, again using a simple rotor-stator system, but this time with peripheral seal variation. One axial and four radial configurations were tested (Fig. 2.9), using a pressure criterion as the key ingress indicator.

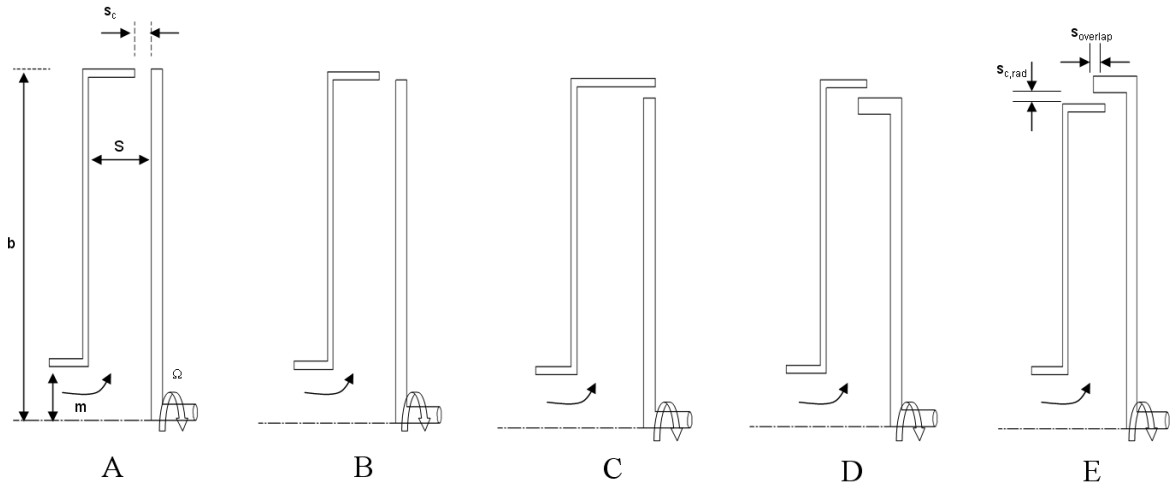

Figure 2.9 Schematic diagram of rotor-stator seal configurations (Adapted from Phadke and Owen (1983))

A pressure inversion effect occurred for radial overlap seals featuring the stator overlapping the rotor (*e.g.* seals C and D). The expected monotonic decrease in pressure on the stator wall with Re_Φ found with axial seals was not present in these cases and as C_w was increased, the configurations in question began to exhibit an unexpected *increase* in pressure with Re_Φ. The "pressure inversion" effect was attributed to the flow entrained near the rotor impinging on the stator face and forming a high-pressure region. It can be seen in Fig. 2.10 that the radial overlapping seals require less sealant flow to prevent ingress and therefore the pressure inversion effects were seen to be beneficial.

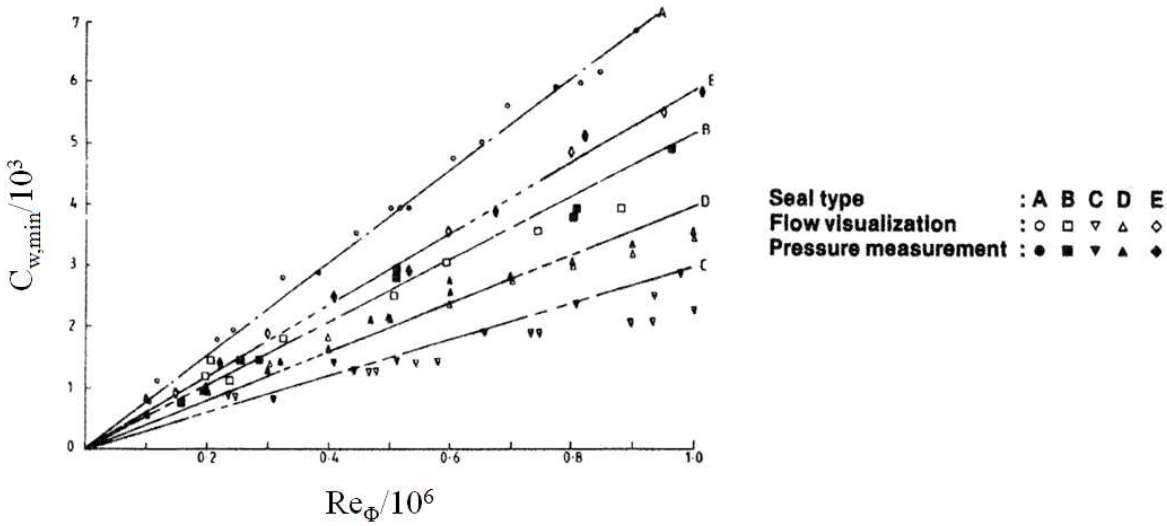

Figure 2.10 Variation of $C_{w,min}$ with Re_Φ based on flow visualisation and the pressure criterion for the five seals (Phadke and Owen (1983))

Following on from the early RI work, Graber *et al.* (1987), and later Daniels *et al.* (1992), used carbon dioxide concentration measurements to determine a cooling effectiveness, again for various seal geometries. This concept of cooling effectiveness was a new way of determining the beneficial aspect of adding more sealant flow. Their rig constituted a rotor-stator system with the addition of an external annulus. Experiments were performed with two swirl ratios in the annulus, however it has been recently suggested by Owen (2009a) that, due to the axial flow being small and with no reported evidence of circumferential pressure variation in the annulus, the external flow would have been quasi-axisymmetric and that the ingress will have occurred in the rotationally-induced regime.

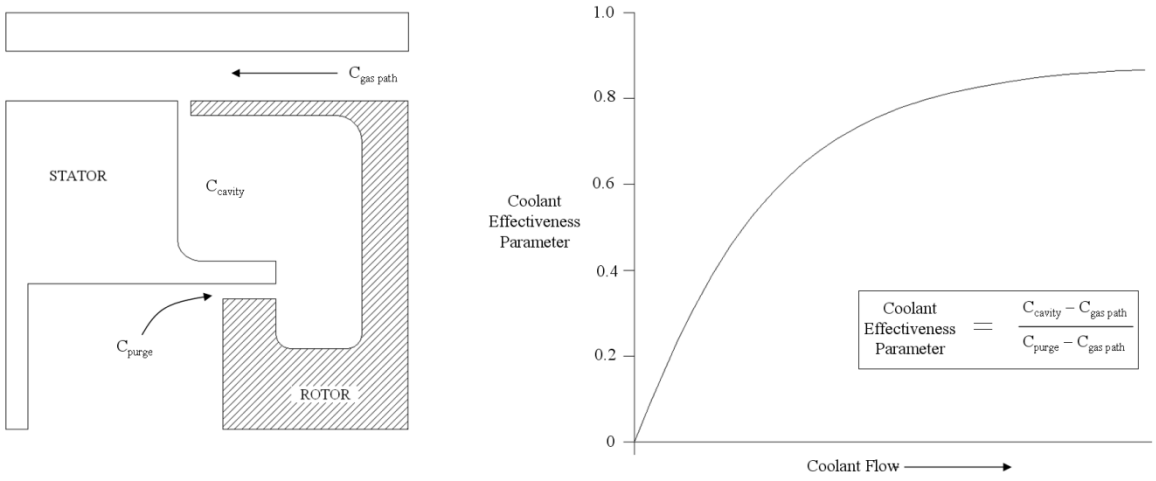

Figure 2.11 Definition of cooling effectiveness (Adapted from Graber *et al.* (1987))

Effectiveness measurements were made at various sealant flow rates, constructing effectiveness curves similar to the typical shape profile shown in Fig. 2.11. For a typical seal, 80% effectiveness was achieved at half of the coolant flow required to seal at 99% effectiveness.

The rim seals featured in most gas turbines are not designed to completely prevent ingestion into the cavity. Acceptable rim seal temperatures can often be achieved with sealant flow-rates less than the no ingestion amount. This principle is important in ingress research, where the effectiveness performance of seals is scrutinised at all flow-rate levels.

Graber *et al.* (1987) tested a selection of seal configurations (Fig. 2.12), with the effectiveness data in reasonable agreement with that of Phadke and Owen (1983). The results indicated that the constant of proportionality in Eq. 2.6 was not constant for all seal configurations. The cooling effectiveness characteristics of Config.3 compared to Config.4 showed a beneficial aspect of increasing the radial overlap dimension, whilst Config.2 outperformed both featuring a tighter radial clearance. Both these design features were suggested as ways of reducing the purge flow-rate whilst achieving the same cooling effectiveness.

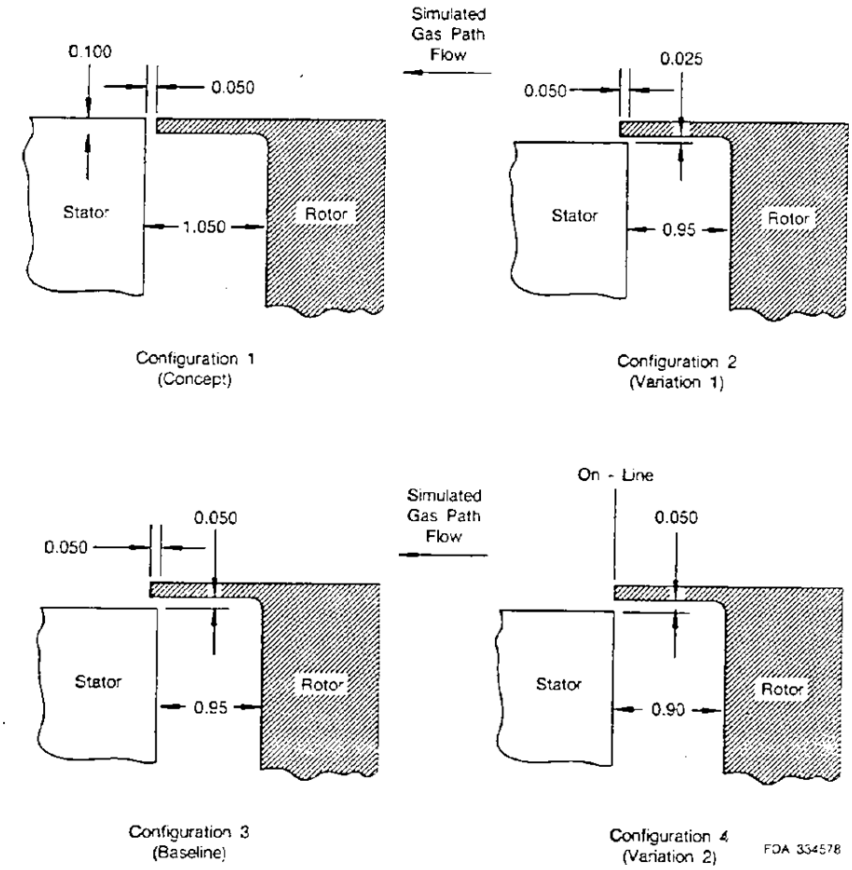

Figure 2.12 Rim seal configurations (dimensions in inches) (Graber *et al.* (1987))

Phadke and Owen (1988a) expanded on their earlier work by suggesting that a rotating core at the centre of the wheel-space rotates at the speed necessary to satisfy the conservation of both momentum and mass. Rotation of the core would create a radial pressure gradient towards the clearance seal, and thus if there is a gap between the shroud and rotor, fluid would be pumped out of the system. The ingress air is then drawn into the system as compensation for the outflow. Their superposed flow was intended to pressurise the wheel-space and hence prevent ingress.

Further tests were conducted with a rotor-stator rig in a quiescent environment with no external flow. An expanded selection of seal geometries from that of Phadke and Owen (1983) were investigated, and among others, featured slotted clearances and a double axial seal. Three techniques were applied to determine ingress: smoke injected flow visualisation, concentration measurements and velocity measurements.

The tested configurations are shown as Fig. 2.13 featuring the flow pattern representations taken from the flow visualisation studies. For all configurations, the sealant flow entered axially, impinged on the rotor and then flowed outwards as a radial wall jet. Seals 4 and 5 exhibited the same pressure inversion effects seen by Phadke and Owen (1983), where above a certain flow-rate the pressure near the seal actually increased with Re_Φ. This effect was explained by the 'impinging

jet phenomenon,' where the jet forms a circular "curtain" of fluid that increases the pressure and helps to prevent ingress.

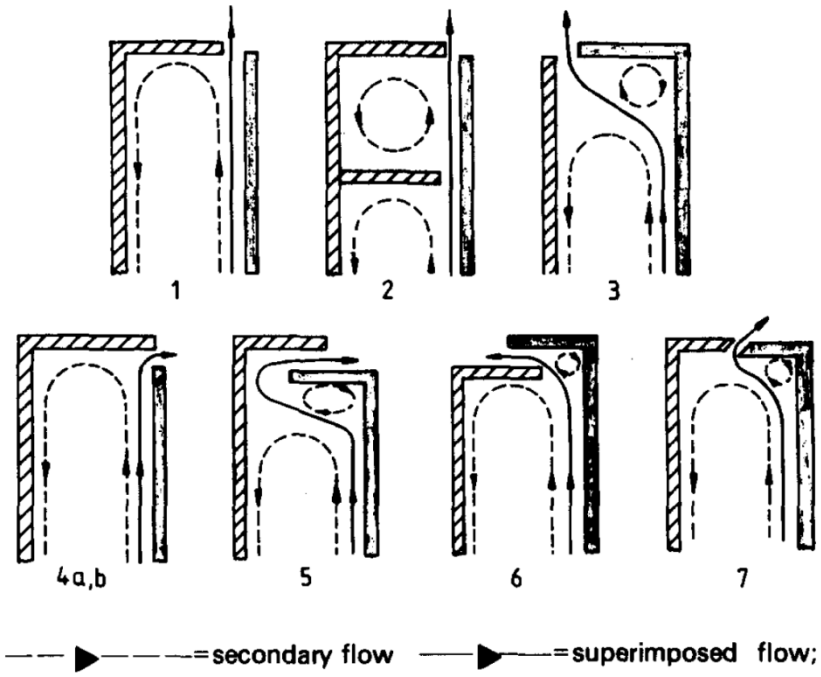

Figure 2.13 Representation of flow patterns for the seven seal outlets (Phadke and Owen (1988a))

Pressure measurements suggested that for a given value of C_w, there is a critical value of Re_Φ where the wheel-space pressure changes from positive to negative relative to the pressure in the annulus; after which ingress occurs. It was also proposed that according to von Kármán (1921), any core rotation will be suppressed when C_w is equal to the free disc entrainment rate, and thus at this point radial inflow on the stator will be prevented. It was shown that for a quiescent environment, the amount of ingested fluid is proportional to Re_Φ, G_c and a decreasing C_w. The effect of G_c was fully analysed using flow visualisation, with Fig. 2.14 showing the results for an axial clearance seal (Seal Configuration 1).

The seals were ranked, with the radial seals all outperforming the axial seal as previously suggested in earlier work. The work confirmed however, that for all tested seals, the superposed sealant flow-rate necessary to prevent the ingress of external air still increased with both the rotational speed of the rig and the seal clearance itself. The authors concurred with Bayley and Owen (1970) and found linear variations of $C_{w,min}$ with Re_Φ for all configurations, with the axial-clearance seal case shown in Fig. 2.14.

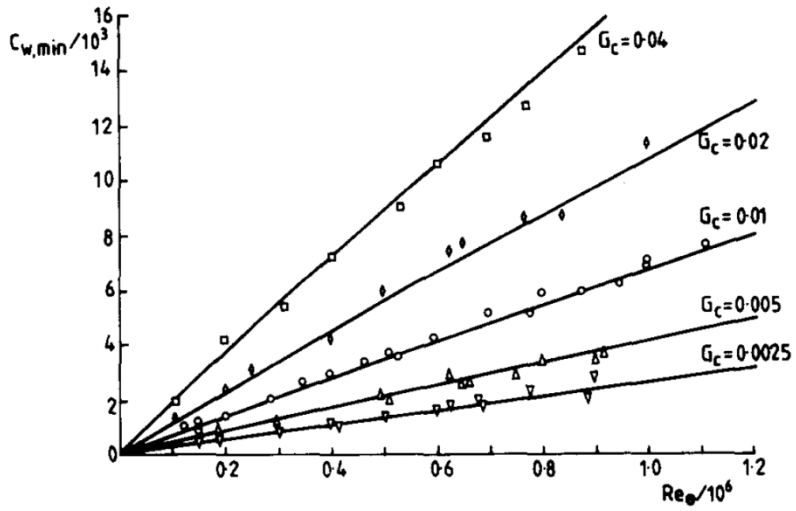

Figure 2.14 The Effect of G_c on the variation of $C_{w,min}$ with Re_Φ (Phadke and Owen (1988a))

Chew (1991) aimed to develop a theoretical model for ingress, using available experimental data. The model worked by linking the boundary layer flow inside the wheel-space to the seal, which was treated as an orifice. Chew was able to examine the Phadke and Owen work and attempted to replicate the minimum sealing flows required for similar seal configurations. Questions were raised over the experimental error present in this work, however using the empirical constants from Phadke (1982), the theory showed agreement with the findings of Graber *et al*.. It was hoped that the integral momentum solution developed for the flow between two discs would provide a basis from which to develop more elaborate models.

Chew *et al.* (1992) re-examined the model a year later in the light of new data from Dadkhah *et al.* (1992). Measurements of static pressure, gas concentration and total pressure were made in a new test facility at the University of Sussex with the capability of external flow. Dadkhah *et al.* used a nominally axis-symmetric external flow without vanes or blades which featured two radial seals, one downstream and one upstream of the rotor. With the two seals angled at different directions to the mainstream they were able to conclude that the mainstream flow was having an effect on the estimates of $C_{w,min}$. This, along with work by Abe *et al.* (1979) and Phadke and Owen (1988a) were among the first to suggest that as well as rotationally-induced ingress caused by free-disc pumping, there may also be an externally-induced regime.

2.5.2 Externally-induced (EI) ingress

Abe *et al.* (1979) designed a rig which featured vanes inside a mainstream annulus. Twenty-seven vanes were positioned upstream of the seal clearance and turned the flow by 50°. A rotor-stator system was constructed featuring variable mainstream and coolant flows and utilising oil paint flow visualisation, velocity probes, stator-side static pressure taps and propane concentration measurements as instrumentation. Various seal geometries were tested including axial clearances and a variety of hook seals (Fig. 2.15).

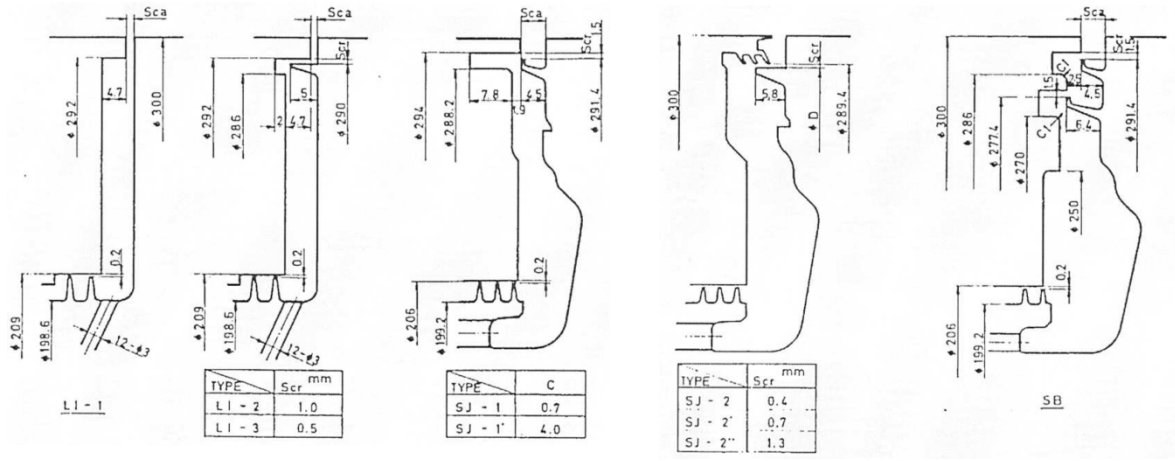

Figure 2.15 Seal testing geometries (dimensions in mm)(Abe *et al.* (1979))

Cooling air was measured on the rotor disc with mainstream flow (ingress) entering on the stator side for shrouds L1-2 and L1-3 (See Fig. 2.15). Static pressures inside the wheel-space became increasingly non-axisymmetric as cooling air and the disc speed increased. It was postulated that the non-axisymmetry of the main flow caused by the vanes was affecting the pressure distribution inside the wheel-space. This formed the basis of externally-induced ingress in which it was implied that ingress could be dominated by the external flow in the annulus, not solely from the rotation of the disc as previously thought.

Abe *et al.* found that alterations in the disc speed had a negligible affect on the ingestion of mainstream flow. This was one of the first times that the Bayley and Owen (1970) correlation had been questioned; in fact it was suggested that for all experiments where asymmetric external conditions were used the correlation would underestimate the ingress produced. From this point onward, research has turned to investigate the addition of vanes, and eventually blades, and their effects on externally-induced ingress caused by these associated pressure asymmetries.

Phadke and Owen (1988b) and Phadke and Owen (1988c) investigated ingress in the presence of a quasi-axisymmetric external flow. This research was important in understanding externally-induced ingress. The rig developed for this purpose utilised a peripheral shroud clamped between two aluminium discs with an external suction fan, as shown in Fig. 2.16. It must be noted that no vanes or blades were present in the external annulus, however the circumferential pressure asymmetry was created by blocking off sections of the annulus with mesh.

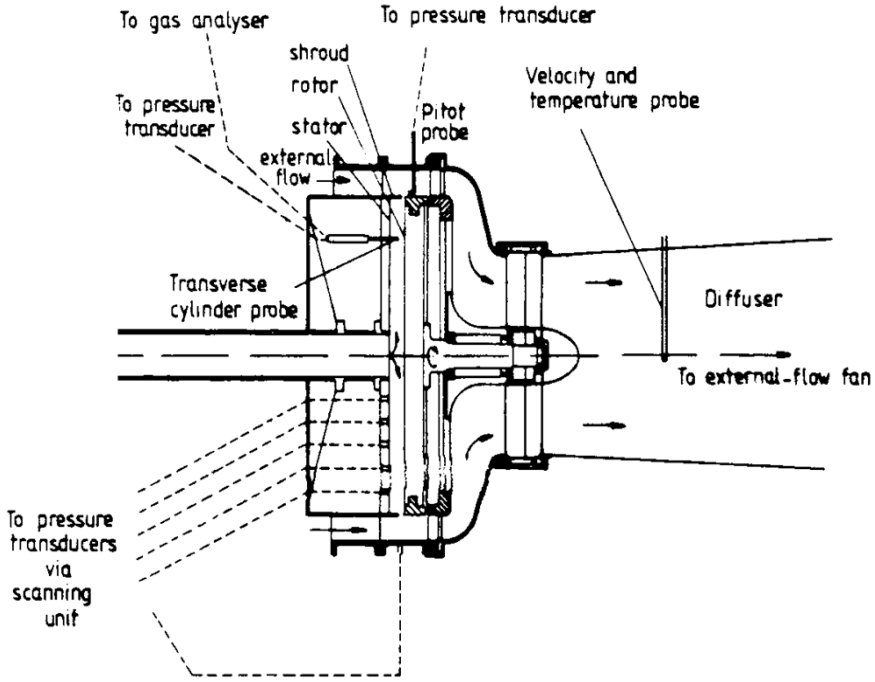

Figure 2.16 Schematic of external-flow rig (Phadke and Owen (1988b))

Phadke and Owen used a pressure criterion to determine whether the wheel-space was sealed, as well as flow visualisation and concentration measurements to quantify the ingress. The flow visualisation technique used smoke in the external flow, which could be drawn into the wheel-space when ingress occurred; the concentration method used nitrous oxide which was injected into the sealant flow, allowing a gas analyser to record dilution effects.

As sections of the external flow were blocked with meshes, it was possible to produce an asymmetric flow even without rotation of the disc. $C_{w,min}$ was shown to be proportional to the axial flow Reynolds number (Re_w) when the disc was stationary, shown in Fig. 2.17. At this point, however, whether this was due to the external flow directly, or more accurately the external pressure-asymmetry, was indistinguishable. Furthermore, Fig. 2.17 shows that as the clearance gap ratio (G_c) is increased, the extent of the ingress also increases.

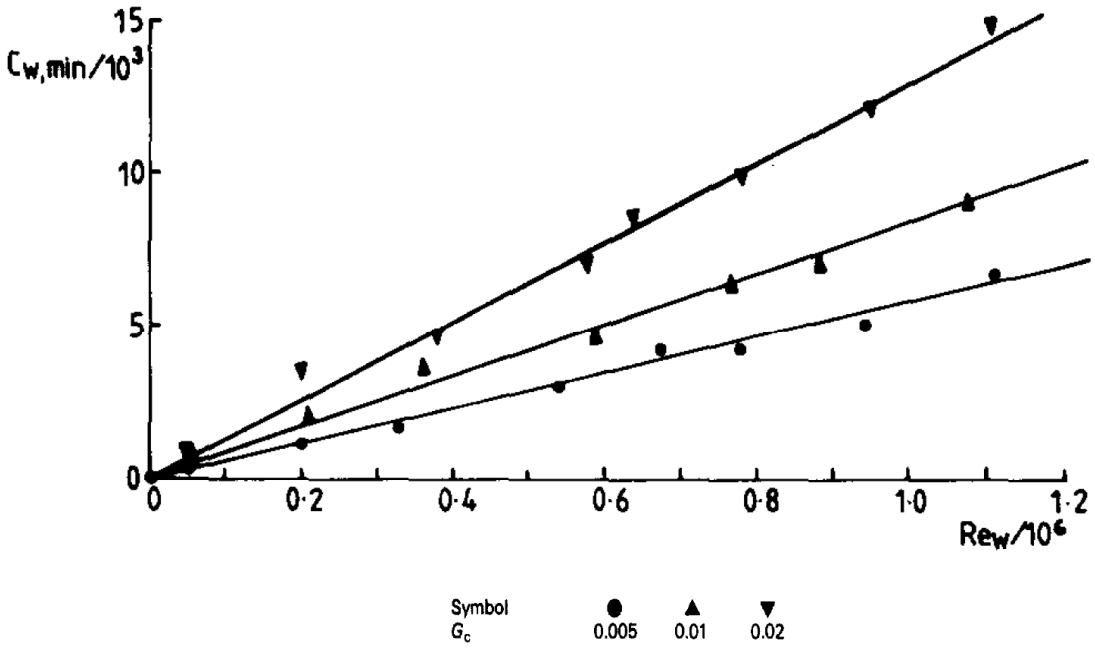

Figure 2.17 Effect of G_c on the variation of $C_{w,min}$ with Re_w (Phadke and Owen (1988b))

Tests were also conducted for varying rotational speeds in addition to variation of the external flow-rate. Figure 2.18 shows the variation of $C_{w,min}$ for one seal clearance ratio ($G_c = 0.01$). It was clearly shown that two regimes of ingress existed: a rotationally induced regime at small values of Re_w/Re_Φ and an externally induced regime at large values of Re_w/Re_Φ. It can be seen in Fig. 2.18 that in the rotationally-induced regime, where $Re_w \rightarrow 0$, $C_{w,min}$ increased with Re_Φ, *i.e.*, $C_{w,min} \propto Re_\Phi$. Contrastingly, in the externally-induced regime, where Re_w is large, non-axisymmetric external flow occurs and $C_{w,min}$ is independent of Re_Φ, but increases with Re_w, *i.e.*, $C_{w,min} \propto Re_w$. It is also apparent that at intermediate values of Re_w a corresponding minimum occurs.

Phadke and Owen (1988c) aimed to determine whether the externally-induced ingress regime was dominated by the pressure asymmetry or the mainstream flow-rate itself. Different combinations of honeycomb meshes were used to create altered pressure asymmetries without changing the external flow-rate. Figure 2.19 shows the results of this investigation, which concluded that externally induced ingress is dominated by the pressure asymmetry and not the external flow-rate.

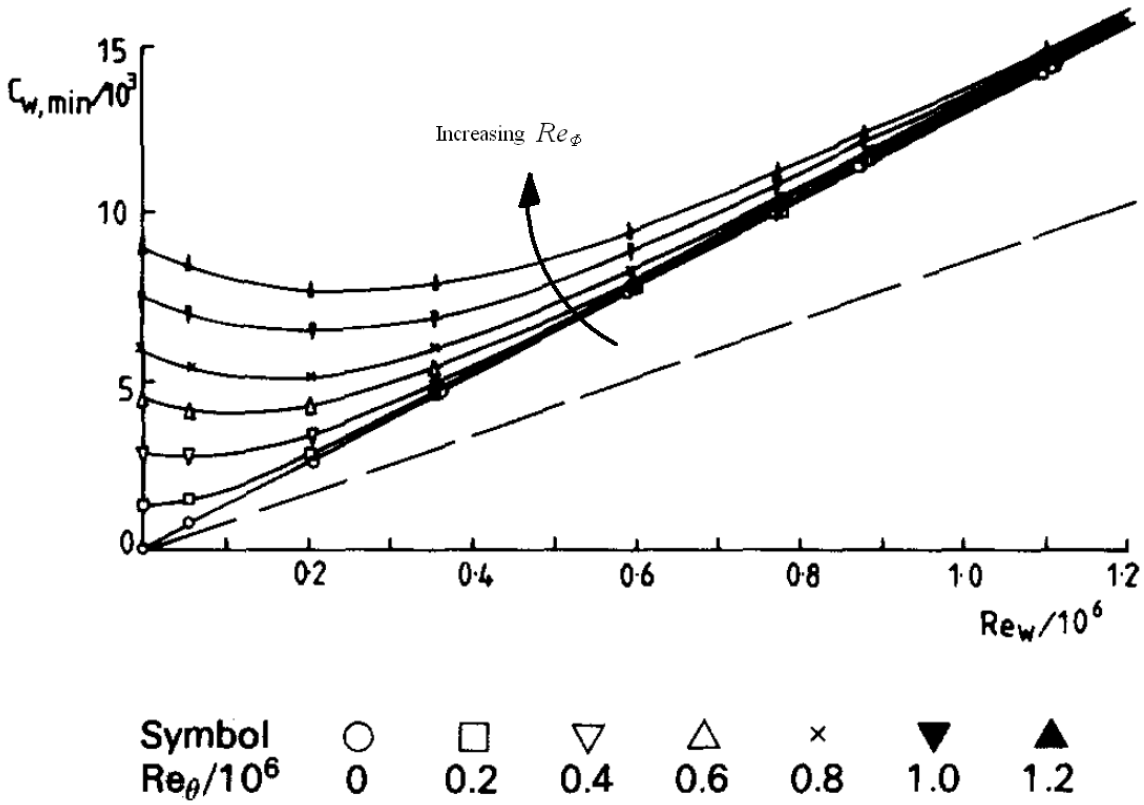

Figure 2.18 The effect of Re_Φ on the variation of $C_{w,min}$ with Re_w (Phadke and Owen (1988c))

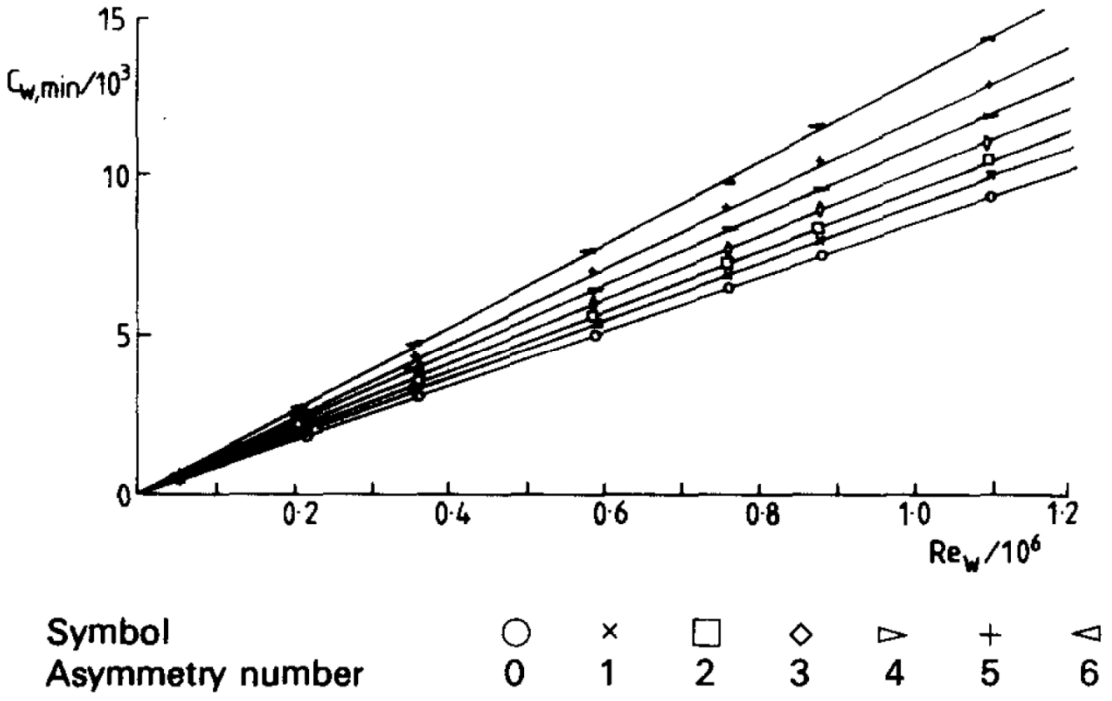

Figure 2.19 Variation of $C_{w,min}$ with Re_w for the different pressure asymmetries (Phadke and Owen (1988c))

With the discovery of this new externally-induced ingress regime, tests were conducted to investigate the effect of seal geometry. As with previous work, a selection of axial and radial-clearance seal configurations were examined, with the results featured in Phadke and Owen (1988b). The results were plotted as $C_{w,min}$ versus a volumetric flow-rate parameter, shown in Fig. 2.20. The flow-rate parameter was derived from the driving pressure across the seal, with area $2\pi rs_c$, and which was attributed a discharge coefficient. It was found that for all tested seals, the data collapsed onto a single line. Phadke and Owen were then able to correlate this result and produce an equation for externally–induced ingress (Eq. 2.7).

$$C_{w,min} = 2\pi K G_c P_{max}^{\frac{1}{2}} \qquad \text{(Equation 2.7)}$$

where

$$P_{max} = 0.5 C_{p,max} Re_w^{\,2} \qquad \text{(Equation 2.8)}$$

$C_{p,max}$ is a non-dimensional pressure difference from the external annulus, caused by the non-axisymmetric external flow, and K is an empirical constant. It can therefore be seen that P_{max} is a controlling parameter in this model and it was implied that this would play a dominant role in determining the quantity of externally-induced ingress.

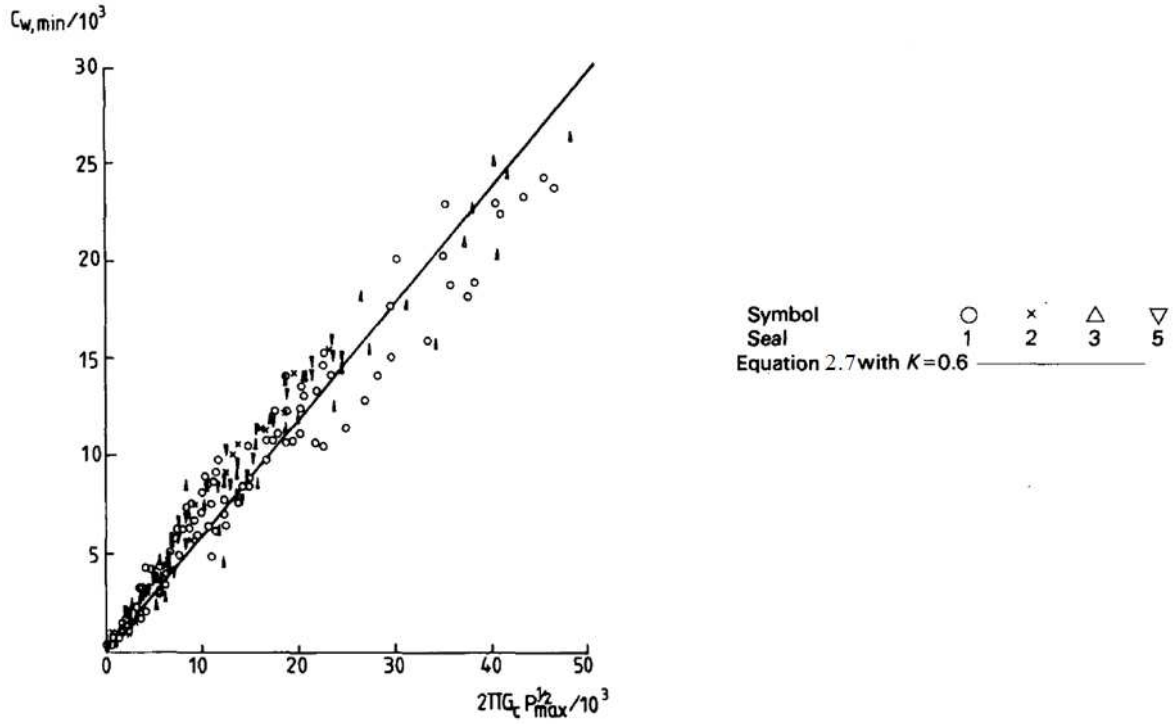

Figure 2.20 Variation of $C_{w,min}$ with $2\pi K G_c P_{max}^{\,2}$ (Phadke and Owen (1988c))

At this point in the research, it was postulated that by using the Bayley and Owen (1970) correlation for RI ingress and the Phadke and Owen (1988) correlation for EI ingress, a conservative design would be one that assumes a $C_{w,min}$ greater than that predicted for both regimes. This proposal was later supported by Khilnani and Bhavnani (2001), who made their own concentration and pressure measurements in a rotor-stator system with sealant and external flow. They produced results in corroboration with Phadke and Owen (Fig. 2.21).

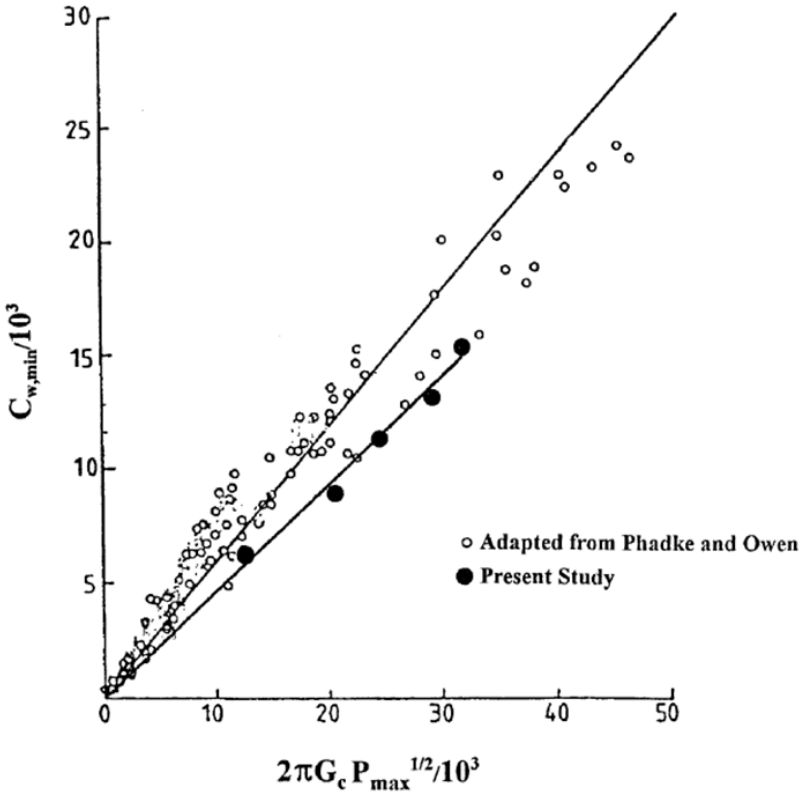

Figure 2.21 Comparison with Phadke and Owen correlation (Khilnani and Bhavnani (2001))

The Phadke and Owen (1988) three part paper also investigated the effects of a double axial-clearance seal. It was suggested that a double seal is important for EI ingress, as the outer cavity acts as a buffer volume, thus reducing ingress to the inner wheel-space. The pressure asymmetry was seen to attenuate inside the outer cavity as shown in Fig. 2.22, where $C_{w,min}$ for the outer seal is larger than that for the inner seal.

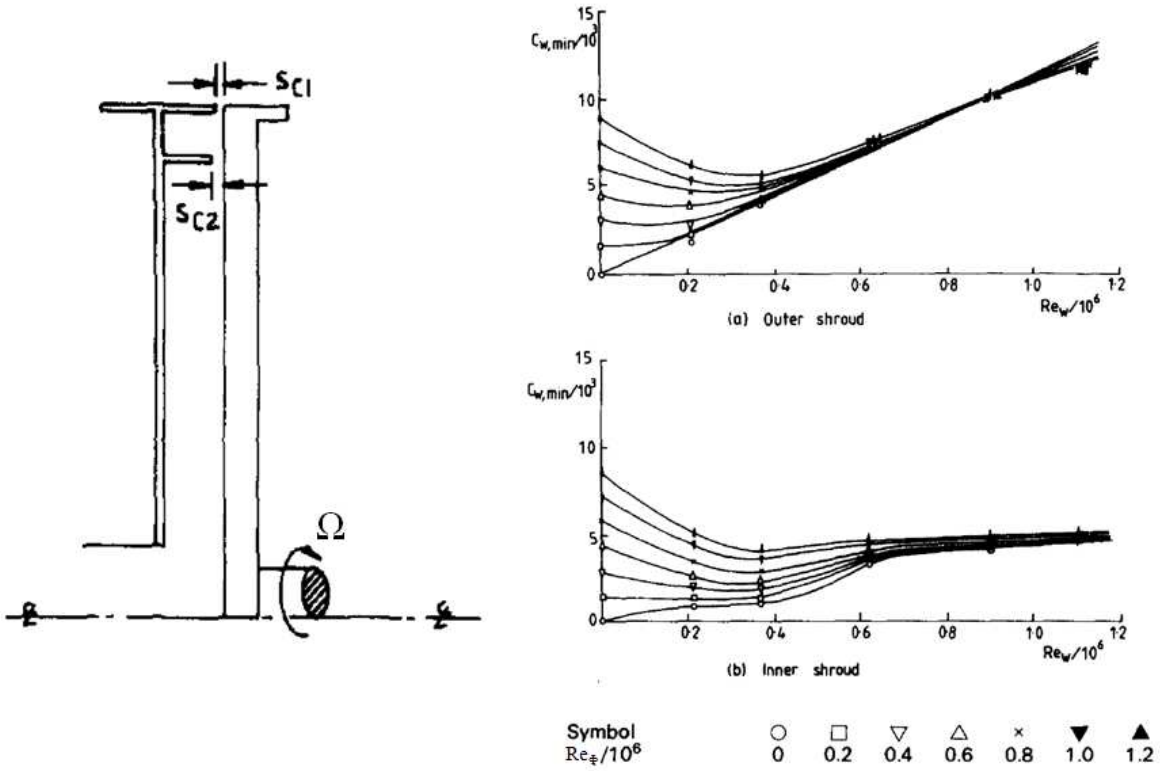

Figure 2.22 Effect of a double axial-clearance seal on EI ingress (Adapted from Phadke and Owen (1988c))

Hamabe and Ishida (1992) then continued the trend of investigating EI ingress caused by non-axisymmetric external flows. They suggested that whilst many papers had assessed the minimum sealant flow-rate required to prevent ingress, few had estimated the ingress flow-rate itself, or considered the shape of the external pressure profile. A rotor-stator rig featuring nozzles in the external annulus was used to create non-axisymmetric flow. Concentration taps were used to produce effectiveness plots, similar to previous work. Twenty-four static pressure taps were used to measure the external pressure non-axisymmetry in the form of non-dimensional pressure coefficients.

In order to account for the pressure differential driving ingress, it was necessary to integrate the circumferential pressure profile. A model developed a year earlier by Hamabe and Ishida (1991) was expanded to model this circumferential pressure profile as different common functions (step function, *sine*-wave and saw-tooth distribution), which were integrated and compared to the experimental data profile. Despite none of the common functions providing perfect agreement with the actual integrated data, it was found that the saw-tooth model gave the best prediction. It was suggested, however, that any accurate estimation of effectiveness must take the precise pressure distribution into account as even small differences in the approximated profile affected the effectiveness values considerably.

Chew *et al.* (1994) extended their work at Sussex from the rig of Dadkhah *et al.* (1992) to investigate external flows with upstream nozzles present in the annulus. Their orifice model performed less well than that of Hamabe and Ishida in terms of predicting sealing effectiveness, however measurements of a rim-seal discharge coefficient, C_d, showed similar trends. Discharge coefficients were measured with a stationary rotor disc, showing a monotonic decrease in the discharge coefficient for outflow, $C_{d,e}$,with increasing external flow-rate. For inflow, the discharge coefficient, $C_{d,i}$,reached a minimum at a particular sealant-to-mainstream flow ratio, above which it increased with mainstream flow-rate.

Green and Turner (1994) were the first to use a fully equipped rotor-stator system, featuring 18 vanes and 32 blades. Using a simple axial clearance configuration they compared four different external flow setups (Fig. 2.23). It was shown that the no external flow condition produced the least ingestion and the condition with just the vanes present (*i.e.* no blades) produced the most ingestion. Surprisingly, the full stage case (*i.e.* blades and vanes) showed a reduction in the ingested flow, closer to the RI (no external flow) case. It was suggested that the rotor blades must have had a smoothing effect on the vane pressure asymmetry, thus lessening the pressure magnitudes.

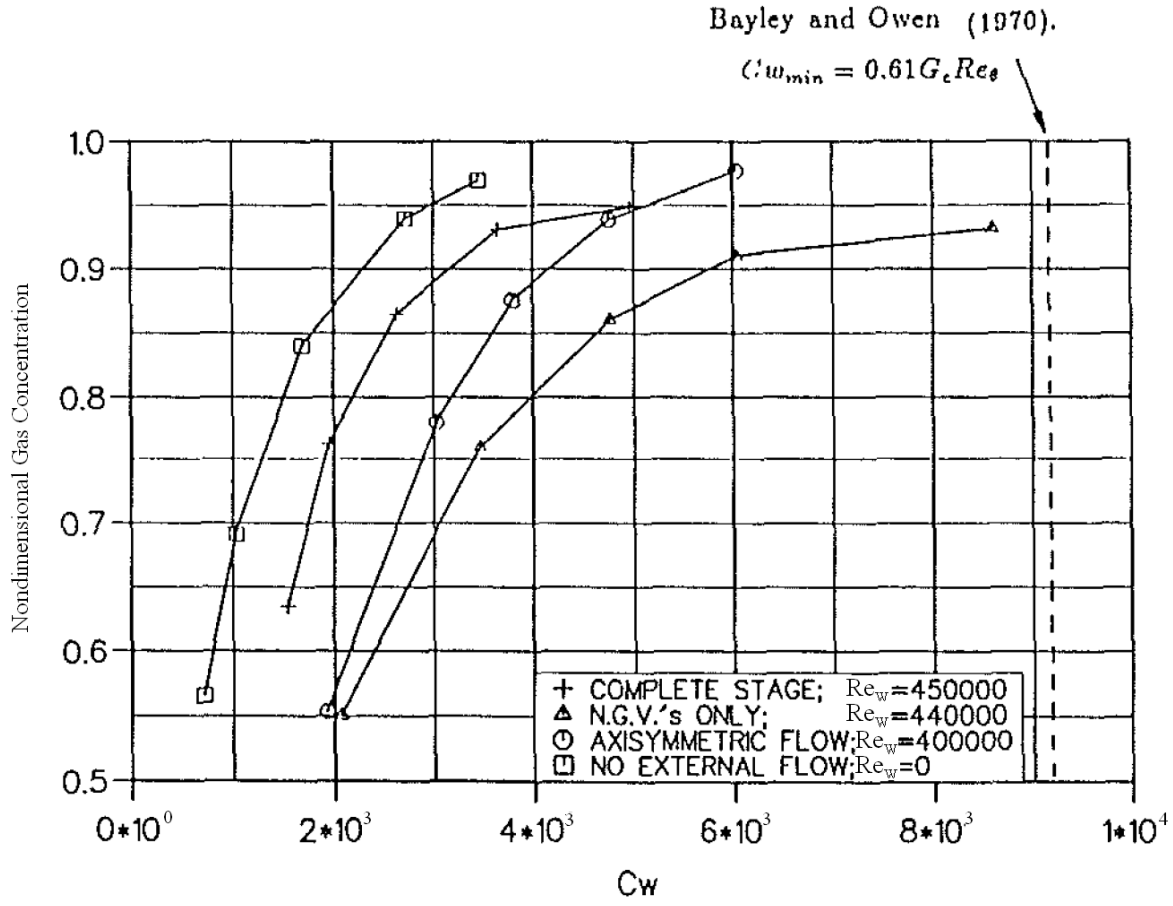

Figure 2.23 Variation of sealing effectiveness with non-dimensional coolant flow-rate for four external flow conditions (Green and Turner (1994))

Experiments by Bohn *et al.* (1995) further suggested that the blades and vanes in the external annulus causing the pressure asymmetry had a governing role in producing ingress. Their experimental work used a rotor-stator system with variable positioned vanes and without blades. It was shown that the ingestion into the wheel-space increased as the vanes were moved closer to the rim seal. This was caused by the circumferential distribution of pressure produced by the vanes decaying axially downstream, and therefore being most prominent when the vanes were positioned closer to the rim seal. Using Laser Doppler Velocimetry (LDV) at engine conditions, they also showed experimentally that ingress can occur not only on the stator but also on the rotor side of the wheel-space under certain conditions.

Bohn and Wolff (2003) modelled a turbine stage in an altered experimental rig with both a single row of vanes and single row of blades. Four seal configurations were investigated using gas concentration measurements, in each case producing an effectiveness curve with variation in C_w. The authors compared their data with that collected by Phadke and Owen (1988) and found a new correlation for $C_{w,min}$. This involved the non-dimensional flow-rate to prevent ingress being expressed as Eq. 2.9:

$$C_{w,min} = K * 2\pi * G_c * \sqrt{\frac{1}{2} C_{p,max}} * Re_w \qquad \text{(Equation 2.9)}$$

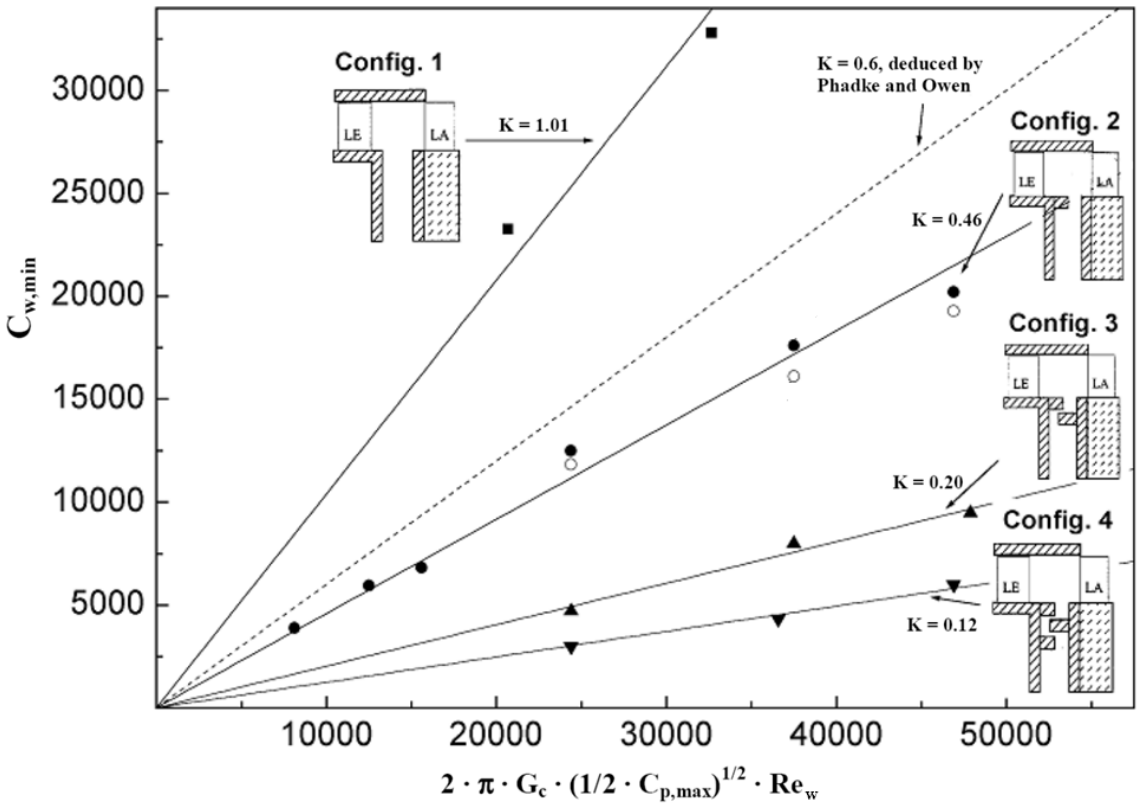

Figure 2.24 Comparison of the different $C_{w,min}$ of four sealing configurations (Bohn and Wolff (2003))

Graphical relationships were produced for all four seal geometries using Eq. 2.9 and it was shown that they had similar linear distributions to those predicted by Phadke and Owen; however the previous estimate for the empirical constant, K, was deemed conservative (Fig. 2.24). It was suggested by Bohn and Wolff that to produce accurate estimations of $C_{w,min}$ for different seal geometries, an empirical constant, K, should be found experimentally for each seal configuration.

Further studies by Bohn *et al.* (2003) on the same experimental rig went on to suggest that high pressure directly in front of the blade leading edge causes a maximum ingestion effect at these points. LDV measurements confirmed that the hot gas ingestion increased when the blades passed the stator wakes compared to when the blades pass through the main stator passage region. Many velocity profiles at differing radial positions are included in the paper illustrating this effect.

More recently, Bohn *et al.* (2006) compared an axial and radial seal configuration using a full rotor-stator stage (*i.e.* with vanes and blades). A comprehensive analysis of 115 pressure/concentration points was taken inside the rig using Scani-valve setups. A strong effect of rim seal configuration was found on the sealing efficiency. The radial seal was shown to out-perform the axial seal (*i.e.* less sealant flow was required to purge the wheel-space).

Johnson *et al.* (2006) were able to estimate cooling effectiveness using a theoretical model, where the seal clearance was treated as an orifice. Time-dependent pressure distributions were used on the turbine hub, along with a discharge coefficient assigned to the seal clearance. Previous model estimations had used the time-averaged pressure distribution downstream of the vanes, however the Johnson *et al*. model used two-dimensional time-dependent CFD calculations. This enabled the model to take into account the wake from the vanes and the bow-wave associated with the blades in order to more accurately calculate the pressure-driven ingress. The model was developed to relate the gas path ingestion flow rate to the circumferential pressure fields at the seal location. A lumped C_d discharge parameter was used for both ingress and egress, where C_d was a function of the seal geometry and could vary from 0 to 1 depending on configuration. Johnson *et al*. used the velocity ratio $V^*/\Omega b$ for their correlation with the cooling effectiveness, ε, where V^* is the circumferential-average radial component of velocity through the seal clearance. It was shown that $V^*/\Omega b$ is proportional to the non-dimensional sealing parameter $C_{w,min}$.

In order to evaluate their estimates, the model was compared to experimental results produced by Bohn *et al.* (2003), whose rig consisted of a turbine stage with 16 vanes and 32 blades. The orifice model showed good agreement with the data of Bohn *et al.*, and converged with a discharge coefficient (C_d) of 0.4. Figure 2.25 illustrates the relationship between the model and the experimental data.

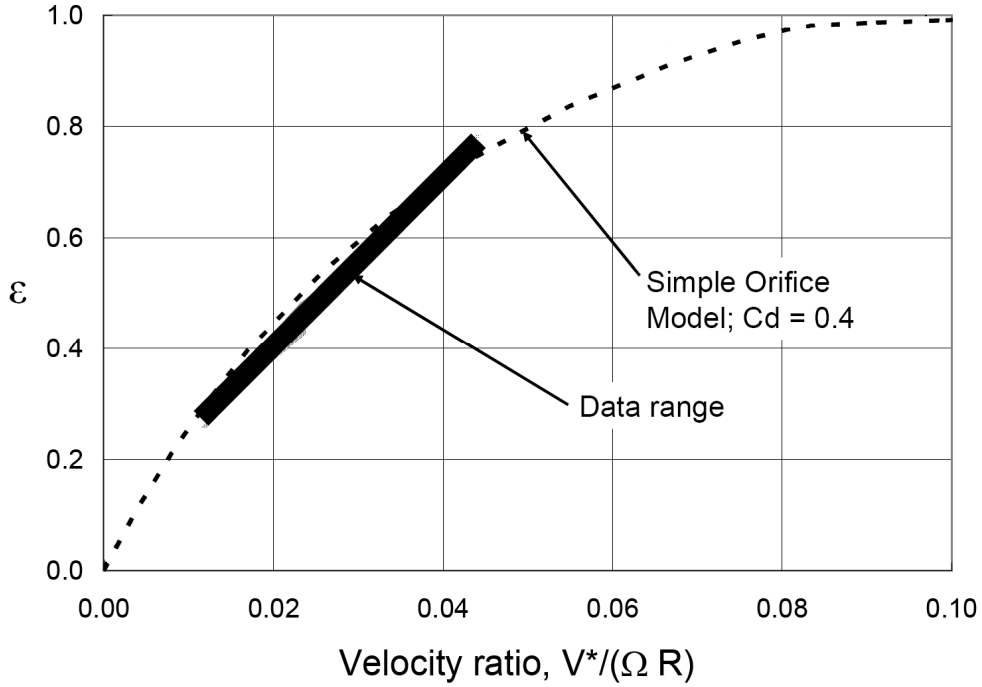

Figure 2.25 Comparison of orifice model (dashed-line) with data for blade-vane2 experiment (Adapted from Johnson et al. (2006))

The effect of varying the spacing between the vane trailing edge and blade leading edge was also examined. A close-spaced and far-spaced setup were used in which it was concluded that the effect of aerofoil pressure variations were more important for close-spaced turbines. The fluctuation of pressure in the annulus (hence the driving potential for ingress) was reduced for the case where the spacing between the vanes and blades was decreased. The far-spaced case exhibited far less magnitude of external pressure fluctuation and thus the driving pressure for ingress was less. The effect of altering the vane and blade spacing was concurrent with earlier work by Dring *et al.* (1982) that had also suggested that by increasing the axial spacing the driving potential for ingress was significantly reduced.

Most previous orifice models had used ingestion mechanisms such as those set out by Johnson *et al*. (1994) and Wang *et al.* (2006) and used one lumped discharge coefficient for both ingress and egress across a seal. Recently, Johnson *et al.* (2008) adapted their orifice model to incorporate two discharge coefficients: one for ingress ($C_{d,i}$) and another for egress ($C_{d,e}$). Other alterations included the addition of a radial momentum term to account for swirl effects in the seal mixing region. This work showed improved seal characterisation over the previous one-discharge-coefficient models, with the new model schematic shown as Fig. 2.26. Using experimental results from Arizona State University (ASU), data were well predicted by the orifice model with discharge coefficient values of $C_{d,e} = 0.27$ and $C_{d,i} = 0.2$. It was concluded that the new model was better able to characterise seals with a wider range of configurations.

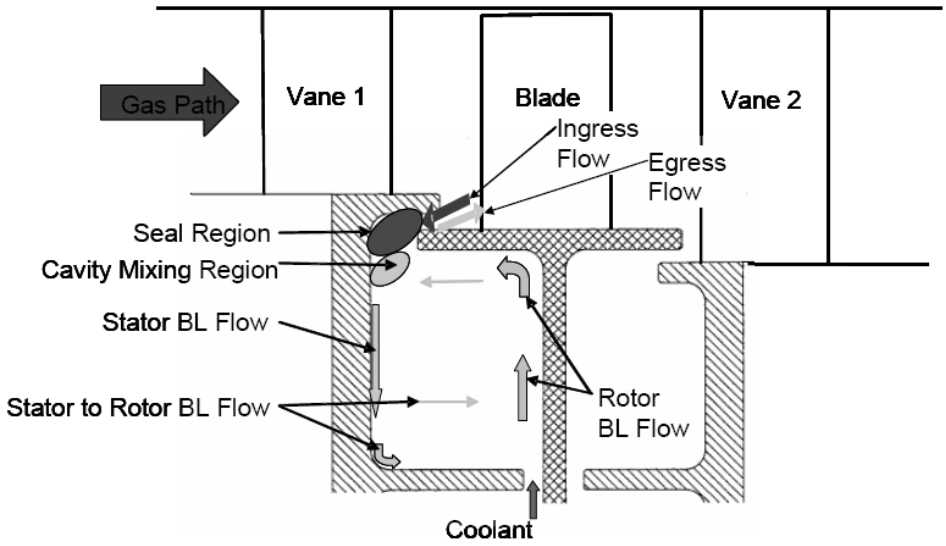

Figure 2.26 Schematic of rim cavity model (Johnson et al. (2008))

CFD computations have also been used to varying success, however, difficulties have arisen in computing unsteady three dimensional flows. Computational studies, such as that of Cao *et al.* (2004) have shown that the swirling ingress effects will destabilise the rotating flow inside the wheel-space causing instabilities in CFD. Among others, such as Gentilhomme *et al.* (2003), who attempted to extend the orifice theory by adding inertial effects into CFD codes to reasonable effect, only highlights the need for experimental validation if CFD codes are to provide gas turbine engineers with an appropriate design tool for future turbines.

2.5.3 Development of an orifice model at the University of Bath

Most recently, and a key driver for the current University of Bath research programme, is the validation of a new orifice model proposed by Owen (2009a) and Owen (2009b). The model aims to predict the sealing effectiveness for rotationally-induced, externally-induced and combined ingress (where the effects of both rotational speed and the external flow are significant).

The theoretical model is based on a stream tube flow from a source to a sink, via a small orifice. This orifice is attributed a pair of discharge coefficients (one for ingress and another for egress), and by using the analytical/numerical solutions from Owen (2009a) and Owen (2009b) the mass flow-rates can be estimated; in principle giving an ingress and egress approximation.

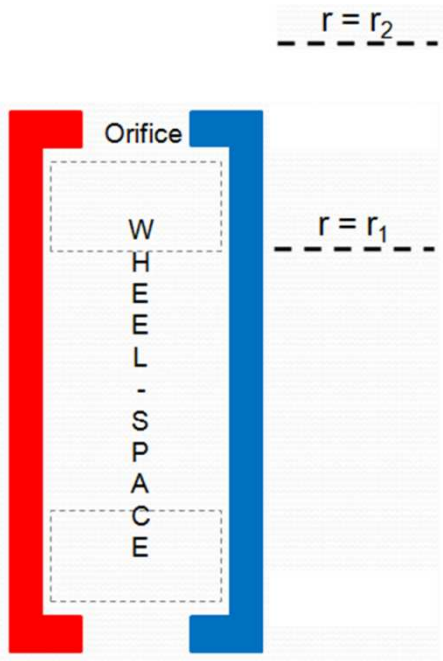

ASSOCIATED FLOW PRINCIPLES

- The principle of the orifice model is that air flows in a stream tube from a source to a sink, via a small orifice. The velocity in the orifice is much greater than the source.
- For egress, the source is assumed to be in the wheel-space, radially inwards of the mixing region at $r = r_1$, with the sink assumed to be radially outwards of the rim seal at $r = r_2$.
- For Ingress, the fluid is assumed to enter from a quiescent source at $r = r_2$ and to flow into the wheel-space at $r = r_1$.
- The mass flow-rates are calculated by assuming that the flow is inviscid, and a discharge coefficient is used to account for viscid effects.

Figure 2.27 A generic wheel-space model and the flow principles associated with the orifice model

Owen (2009a) described the development of the theoretical model for the case of rotationally-induced ingress (*i.e.* in an absence of external flow). The analytical expressions developed from the model use a similar two-discharge coefficient system to Johnson *et al.* (2008) and when solved for incompressible flow, produced near-perfect agreement with the earlier work of Graber *et al.* (1987).

Owen (2009b) then expanded the model for externally-induced and combined-ingress cases. The external ingress case was solved analytically/numerically for incompressible flow and again produced fine agreement with the published data of Johnson *et al.* (2006). The combined-ingress regime was also investigated with theoretical expressions developed. Flow conditions in

this region are such that neither RI or EI ingress dominate and the ingress was said to occur in a transition regime between the two asymptotes (Fig. 2.28). The RI and EI asymptotes are formulated from expressions developed in the orifice model, with $\Gamma_{\Delta p}$ an external pressure parameter.

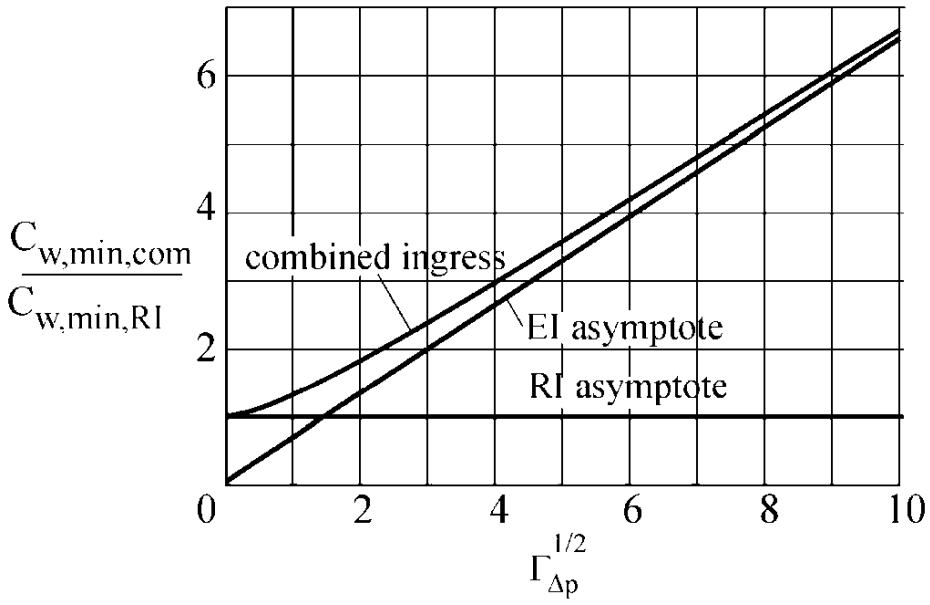

Figure 2.28 The combined ingress approximation (Owen (2009b))

Owen postulated that the CI regime may be of great importance to engine designers as it may occur especially in the case of double seals, where the outer clearance may be externally induced, however, the inner clearance may be governed by rotationally-induced ingress.

The orifice model was further developed for the externally-induced regime in Owen *et al.* (2010a), where different external pressure profiles were used to investigate the sensitivity of the profile shape to the predicted outcome. Saw-tooth and *cosine* approximations were used for the circumferential external pressure profile, as well as integrating the fitted-profile used in Johnson *et al.* (2006). The analysis was conducted in order to see if an appropriate assumption could be used to simplify the orifice equations for swirling flow developed in Owen (2009). Figure 2.29 shows the sealing effectiveness characteristics predicted by the orifice model using the different external pressure profiles; the sealing flow-rate was quantified using a new non-dimensional sealing parameter: $\Phi_0 = C_{w,0} / 2\pi G_c Re_\Phi$.

Earlier findings were reinforced that suggested that EI ingress is caused by the *magnitude* of the peak-to-trough circumferential difference of pressure in the annulus, with the shape of the distribution of secondary importance. The saw-tooth assumption was shown to produce reasonably accurate analytical fits to the Johnson *et al.* data without requiring the numerical solutions developed from the fitted or *cosine* profiles. The so-called '*saw-tooth model*' then allowed for a

simple equation to be developed, linking the sealing effectiveness, ε, to a form of the non-dimensional sealing parameter, Φ_0.

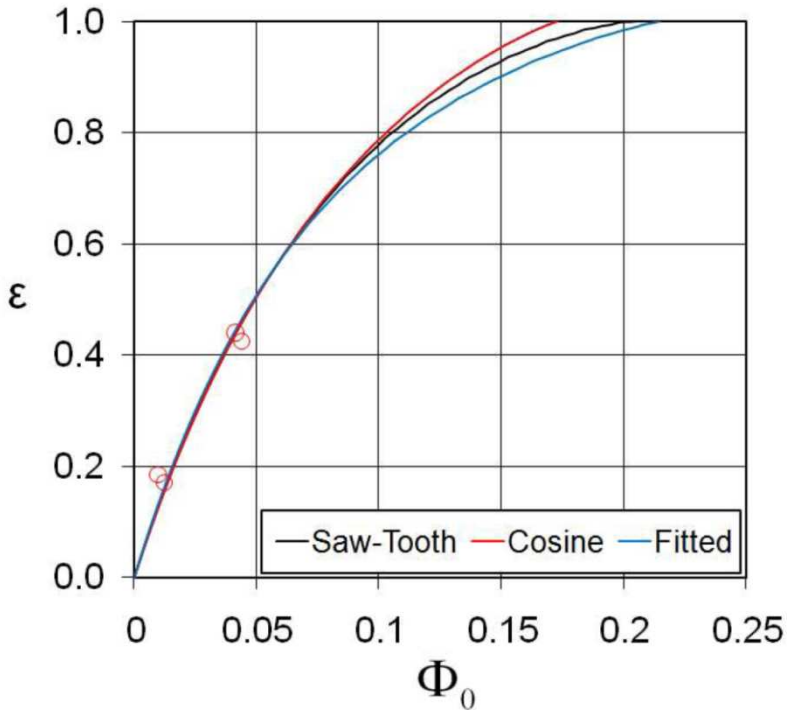

Figure 2.29 Variation of the sealing effectiveness with Φ_0 (Owen *et al.* (2010a))

The saw-tooth approximation was also applied to the combined-ingress case in Owen *et al.* (2010b). The early data of Phadke and Owen (1988c) was predicted with reasonably good agreement using a variable discharge-coefficient.

2.6 Use of thermochromic liquid crystals in research

The measurement of temperature using thermochromic liquid crystal (TLC) is well established and has been employed for nearly forty years, with the first recorded literature published by Klein (1968). The rig has been designed to accommodate TLC and a brief introduction is given below.

The TLC technique is an optical and non-intrusive method, with the crystals being commercially available in the form of sprayable slurry. The experimental section is first coated in a matt black paint before the crystal slurry is diluted and applied to the desired surface using an airbrush. These crystals selectively reflect light, with the wavelength of the reflected light being directly proportional to the temperature of the liquid crystal. In order to use the crystal technique

quantitatively, an *in situ* calibration is required in which the perceived colour of the crystals is related to their temperature. The TLC response is usually defined in terms of hue. Hue varies monotonically with the temperature of the crystal (within a temperature range), allowing the crystals to map a heated surface. An account detailing this basic calibration procedure is given by Smith *et al.* (2001). It is also suggested that a more complex calibration procedure is undertaken in order to minimise the errors associated with crystal research. Multiple calibrations for effects such as hysteresis (Anderson and Baughn (2004)), film thickness and light intensity (Roth and Anderson (2007)), and viewing angle, measurement noise and ageing (Wiberg and Lior (2004)), are all recommended depending on the situation.

2.6.1 Experimental results using TLC

Roy *et al.* (2001) were able to use TLC to measure the distribution of convective heat transfer coefficient on a rotor disc surface. The rig consisted of a model rotor-stator cavity, with both mainstream and sealant flow, and also allowed them to record the fluid temperature distribution. Ingress experiments were performed, however it must be noted that due to both flows being equal in temperature, no ingestion temperature effects could be monitored on either the local temperatures or the Nusselt number on the disc. The rig featured 52 blades and 59 vanes, along with TLC applied to the rotor on top of an epoxy base-layer. Core air temperature measurements were taken at five radial locations using thermocouples.

Bunker *et al.* (1992a) and Bunker *et al.* (1992b) also used TLC to estimate the radial distribution of convective heat transfer coefficient on a rotor disc in a rotor-stator cavity. They used a heat balance to estimate the mean temperature radial profile, and from this they derived the heat transfer coefficients. Their calculations however, did not take into account the rotation of the core fluid inside the cavity.

2.6.2 Novelty of proposed rig design for heat transfer

At present there has been no measurements of the thermal effects of ingress in a rotating-disc system. The gas turbine research group at the University of Bath has much experience in the use of TLC applied to rotating disc systems. Kakade *et al.* (2009a,b) and (2011) provide successful measurements of heat transfer coefficient on a pre-swirl rig, and the experience gained from this work will be used to aid in the design of the new ingress rig.

A slow-transient technique using TLC was developed to estimate the local heat transfer coefficients on the rotating disc (Newton *et al.* (2003); Owen *et al.* (2003); Yan and Owen (2002); Kingsley-Rowe *et al.* (2005)). The transient technique involves mesh heaters in order to heat the flow, along with optical access to the area coated with TLC. In order to record the TLC colour response, the region is illuminated by an off-axis stroboscopic light synchronised with the speed of the rotor disc. A CCD camera is used to digitally record the results. An analytical solution of Fourier's equation is used to measure the distribution of heat transfer coefficient. This successful technique has been re-employed on the new rig.

Chapter 3: Theoretical orifice model

The orifice model established at the University of Bath has been validated using the experimental data presented in this thesis. The development of the orifice model is not a principal part of this thesis, yet a prerequisite understanding of the validation process is essential; whilst also forming a basis from which to derive the *effectiveness* equations that are fundamental in the theoretical estimation of experimental results.

The orifice equations for swirling flow are based on an 'orifice ring' shown in Fig. 3.1. Egress and ingress flows can occur through the elemental areas δA_e and δA_i, respectively, which in summation are equal to the axial-clearance area of the seal, δA_c. Egress flows through a stream-tube from inside the wheel-space, where the pressure is p_1, and emerges in the external annulus where the pressure is p_2. The reverse applies to the ingress flow, which begins in the annulus and emerges inside the wheel-space.

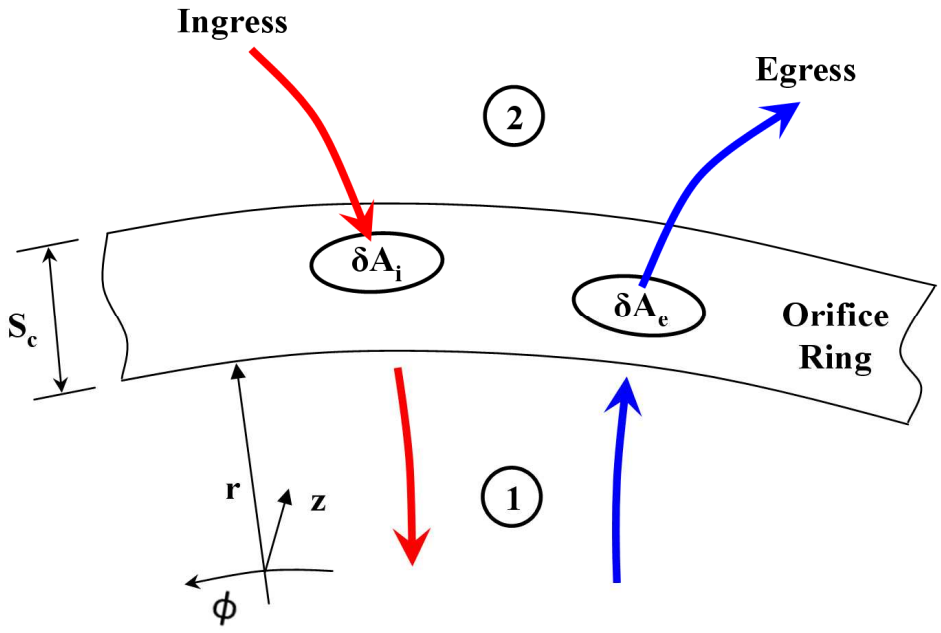

Figure 3.1 Orifice ring

The analysis assumes the flow is inviscid, with a continuity of mass and energy for each of the stream-tubes for both egress and ingress. A discontinuity of pressure is applied across the orifice ring. The conservation of angular momentum is also applied, so that free-vortex flow occurs with rV_ϕ a constant. It is assumed that $(r_2\text{-}r_1) / r_1 << 1$ and that $V_{r,1}^2 << V_{r,2}^2$ for egress and *vice*

versa for ingress. In order to account for the effects of viscosity, empirical discharge coefficients are included.

For inviscid flow through a stream-tube, Bernoulli's equation (Eq. 3.1) is valid with constant total pressure.

$$p_1 + \frac{1}{2}\rho {U_1}^2 = p_2 + \frac{1}{2}\rho {U_2}^2 \qquad \text{(Equation 3.1)}$$

For egress flow it is assumed that $V_{z,1}^2, V_{r,1}^2 << V_{\phi,1}^2$, $r_2 V_{\phi,2} = r_1 V_{\phi,1}$ and $U_2^2 \approx V_{r,2}^2 + V_{\phi,2}^2$, so that Eq. 3.1 can be re-written as Eq. 3.2, where $V_{r,e}$ has been used in place of $V_{r,2}$.

$$V_{r,e} = \left\{ 2\frac{(p_1 - p_2)}{\rho} + {V_{\phi,1}}^2 \left(1 - \left(\frac{r_1}{r_2}\right)^2\right)\right\}^{1/2} \qquad \text{(Equation 3.2)}$$

For ingress, the equivalent equation is

$$V_{r,i} = \left\{ 2\frac{(p_2 - p_1)}{\rho} - {V_{\phi,2}}^2 \left(\left(\frac{r_2}{r_1}\right)^2 - 1\right)\right\}^{1/2} \qquad \text{(Equation 3.3)}$$

At this point, it is pertinent to introduce the swirl ratio, β, where

$$\beta = \frac{V_\phi}{\Omega b} \qquad \text{(Equation 3.4)}$$

Equations 3.2 and 3.3 can now be re-written as Eqs 3.5 and 3.6, respectively, with both being valid for EI and RI ingestion.

$$\frac{V_{r,e}}{\Omega b} = \left\{ 2\frac{(p_1 - p_2)}{\rho \Omega^2 b^2} + {\beta_1}^2 \left(1 - \left(\frac{r_1}{r_2}\right)^2\right)\right\}^{1/2} \qquad \text{(Equation 3.5)}$$

$$\frac{V_{r,i}}{\Omega b} = \left\{ 2\frac{(p_2 - p_1)}{\rho \Omega^2 b^2} - {\beta_2}^2 \left(\left(\frac{r_2}{r_1}\right)^2 - 1\right)\right\}^{1/2} \qquad \text{(Equation 3.6)}$$

In order to simplify the analysis, three non-dimensional coefficients can then introduced as defined in Eq. 3.7.

$$C_p = \frac{p_2 - p_1}{\frac{1}{2}\rho \Omega^2 b^2}, \qquad C_{\beta 1} = {\beta_1}^2 \left(1 - \frac{{r_1}^2}{{r_2}^2}\right), \qquad C_{\beta 2} = {\beta_2}^2 \left(\frac{{r_2}^2}{{r_1}^2} - 1\right) \qquad \text{(Equation 3.7)}$$

Separate discharge coefficients are introduced for egress and ingress, $C_{d,e}$ and $C_{d,i}$. These are defined as the ratios of the real to inviscid flow in the stream tubes, resulting in Eqs 3.8 and 3.9, when $C_{\beta 1} \geq C_p$ and $C_p \geq C_{\beta 2}$, respectively:

$$\frac{V_{r,e}}{\Omega b} = C_{d,e}\sqrt{C_{\beta 1} - C_p} \quad \text{(Equation 3.8)}$$

$$\frac{V_{r,i}}{\Omega b} = C_{d,i}\sqrt{C_p - C_{\beta 2}} \quad \text{(Equation 3.9)}$$

The mass flow rates for egress and ingress can be calculated by integrating the velocity across the seal clearance:

$$\dot{m}_e = \rho \int_{A_e} V_{r,e} dA_e \qquad \text{and} \qquad \dot{m}_\iota = \rho \int_{A_i} V_{r,i} dA_i \quad \text{(Equation 3.10)}$$

Conservation of mass is used to define the superposed mass flow rate (Eq. 3.11), from which it is possible to define the sealing effectiveness, ε (Eq. 3.12). Here, $\varepsilon = 1$ when no ingress occurs and $\varepsilon = 0$ when the sealant flow is zero. The sealing effectiveness is the most primary parameter used to quantify and rank seal performance.

$$\dot{m}_0 = \dot{m}_e - \dot{m}_\iota \quad \text{(Equation 3.11)}$$

$$\varepsilon = 1 - \frac{\dot{m}_\iota}{\dot{m}_e} = 1 - \frac{C_{w,i}}{C_{w,e}} = \frac{C_{w,0}}{C_{w,e}} \quad \text{(Equation 3.12)}$$

where the non-dimensional flow-rate, $C_w = \dot{m}/\mu b$.

Owen (2009a,b) provide a derivation of the swirling orifice equations and solve them for compressible and incompressible steady 1D flow, including an alternate definition from the radial momentum equation for a rotating fluid. The advantage of the incompressible equations is that they can be solved analytically. The resulting solutions are simple enough to provide a quantitative estimation of the seal performance without the need for numerical solvers. The reader is directed to Owen (2009a,b) and Owen *et al.* (2010a,b) for details of the derivation of the orifice equations.

3.1 Solution of the incompressible orifice equations

In order to simplify the resulting solutions, it is sagacious to introduce a further set of non-dimensional terminology. A non-dimensional sealing parameter, Φ, is used to quantify the flow-rates, and although it appears to contain viscous terms, the parameter in fact reduces to an inertial definition as shown in Eq. 3.13:

$$\Phi = \frac{C_w}{2\pi G_c Re_\Phi} = \frac{U}{\Omega b} \quad \text{(Equation 3.13)}$$

Here U is the bulk-mean radial velocity through the seal clearance.

Using the same subscript notation for egress, ingress and for sealant flow, the flow parameters for each then become Φ_e, Φ_i and Φ_0, respectively. Φ_{min} is defined as the value of ϕ_0 when the ingress is zero (Eq. 3.14).

$$\Phi_{min} = \frac{C_{w,min}}{2\pi G_c Re_\Phi} = \frac{U_{min}}{\Omega b} \quad \text{(Equation 3.14)}$$

The continuity equation and the definition of sealing effectiveness are then analogous to Eqs 3.11 and 3.12:

$$\Phi_0 = \Phi_e - \Phi_i \quad \text{(Equation 3.15)}$$

$$\varepsilon = 1 - \frac{\Phi_i}{\Phi_e} = \frac{\Phi_0}{\Phi_e} = \frac{\Phi_0}{\Phi_0 + \Phi_i} \quad \text{(Equation 3.16)}$$

when $\Phi_0 < \Phi_{min}$

Although the effectiveness is a convenient parameter, the designer wants to know how much hot gas actually enters the wheel-space when $\Phi_0 < \Phi_{min}$. This involves calculating the ingress parameter, Φ_i, where from Eq. 3.16:

$$\frac{\Phi_i}{\Phi_0} = \varepsilon^{-1} - 1 \quad \text{(Equation 3.17)}$$

Two other convenient parameters are the ratio of the discharge coefficients, Γ_c, and the non-dimensional pressure difference in the turbine annulus, ΔC_p, which acts as the driving potential for EI ingress.

$$\Gamma_c = \frac{C_{d,i}}{C_{d,e}} \quad \text{(Equation 3.18)}$$

$$\Delta C_p = \frac{\Delta p}{\frac{1}{2}\rho\Omega^2 b^2} \quad \text{(Equation 3.19)}$$

where Δp is the time-average peak-to-trough static pressure difference in the turbine annulus.

The direct analytical solutions for both RI and EI ingestion are shown in detail by Owen (2009a,b) and only the solved equations are presented here.

3.1.1 Effectiveness equation for RI ingestion

For the case of RI ingestion, and neglecting external swirl, it was shown in Owen (2009a) that

$$\Phi_{min,RI} = C_{d,e} C_{\beta 1}{}^{\frac{1}{2}} \qquad \text{(Equation 3.20)}$$

Where $C_{\beta 1}$ is the modified internal swirl ratio.

From Appendix B of Owen (2009a), the following equations govern the flow associated with RI ingress. These equations have been manipulated to form the explicit effectiveness equations (Sangan *et al.* (2011b)) which become the important theoretical expressions from the orifice model which are validated by the experimental work.

$$\frac{\Phi_e}{\Phi_{min,RI}} = \frac{1-\Gamma_p}{\Gamma_T} \qquad \text{(Equation 3.21)}$$

$$\frac{\Phi_i}{\Phi_{min,RI}} = \frac{\Gamma_c{}^2 \Gamma_p}{\Gamma_T} \qquad \text{(Equation 3.22)}$$

and

$$\frac{\Phi_0}{\Phi_{min,RI}} = \frac{\Phi_e - \Phi_i}{\Phi_{min,RI}} = \frac{1-\Gamma_p\left(1+\Gamma_c{}^2\right)}{\Gamma_T} \qquad \text{(Equation 3.23)}$$

where

$$\Gamma_c = \frac{C_{d,i}}{C_{d,e}} \qquad \Gamma_p = \frac{C_p}{C_{\beta 1}} \qquad \Gamma_T = \left[\left(1-\Gamma_p\right)^{\frac{1}{2}} + \Gamma_c \Gamma_p{}^{\frac{1}{2}}\right] \qquad \text{(Equation 3.24)}$$

Using Eqs 3.21 and 3.22, it follows that

$$\varepsilon = 1 - \frac{\Phi_i}{\Phi_e} = \frac{1-\Gamma_p\left(1+\Gamma_c{}^2\right)}{1-\Gamma_p} \qquad \text{(Equation 3.25)}$$

Eq 3.25 can be rearranged to give

$$\Gamma_p = \frac{1-\varepsilon}{(1-\varepsilon)+\Gamma_c{}^2} \qquad \text{(Equation 3.26)}$$

Using Eq 3.26 to eliminate Γ_p from Eq 3.23, it follows that for $\Phi_0 \leq \Phi_{min,RI}$

$$\frac{\Phi_0}{\Phi_{min,RI}} = \frac{\varepsilon}{\left[1+(1-\varepsilon)^{\frac{1}{2}}\right]\left[1+\Gamma_c^{-2}(1-\varepsilon)\right]^{\frac{1}{2}}} \quad \text{(Equation 3.27)}$$

Thus for $\Phi_0 > \Phi_{min,RI}$, the effectiveness will be unity.

As derived here, Eq 3.27 will be referred to as the *RI effectiveness equation*.

3.1.2 Ingested flow-rate for RI ingestion

The sealing effectiveness is a useful parameter, which is usually determined from concentration measurements in an experimental rig. However, it is also useful for the engine designer to be able to estimate Φ_i, the non-dimensional flow-rate of air that enters the wheel-space when $\Phi_0 < \Phi_{min}$.

From Eq 3.16

$$\varepsilon = \frac{\Phi_0}{\Phi_{e,RI}} = \frac{\Phi_0}{\Phi_0+\Phi_{i,RI}} \quad \text{(Equation 3.28)}$$

and following on through Eq 3.17

$$\frac{\Phi_{i,RI}}{\Phi_0} = \varepsilon^{-1} - 1 \quad \text{(Equation 3.29)}$$

As

$$\frac{\Phi_{i,RI}}{\Phi_{min,RI}} = \frac{\Phi_{i,RI}}{\Phi_0}\frac{\Phi_0}{\Phi_{min,RI}} \quad \text{(Equation 3.30)}$$

it follows from Eqs 3.27 and 3.29 that

$$\Phi_{i,RI} = \Phi_{min,RI}\frac{1-\varepsilon}{\left[1+(1-\varepsilon)^{\frac{1}{2}}\right]\left[1+\Gamma_c^{-2}(1-\varepsilon)\right]^{\frac{1}{2}}} \quad \text{(Equation 3.31)}$$

In the limit $\Phi_0 = 0$, where $\varepsilon = 0$, Eq 3.31 reduces to

$$\Phi_{i,RI}{}^{*} = \Phi_{min,RI}\frac{1}{2\left[1+\Gamma_c^{-2}\right]^{\frac{1}{2}}} \quad \text{(Equation 3.32)}$$

where * signifies that $\Phi_0 = 0$. Eq 3.32 gives the maximum non-dimensional flow-rate that can be ingested into the wheel-space.

Figure 3.2 shows the variation of ε, Φ_e and Φ_i with Φ_0 according to the above equations assuming $\Gamma_c = 1$. It can be seen that for $\Gamma_c = 1$, $\Phi_{i,RI}^*/\Phi_{min,RI} = 0.35$; meaning that at its worst case, only 35% of the flow required to seal the system could be ingested into the wheel-space.

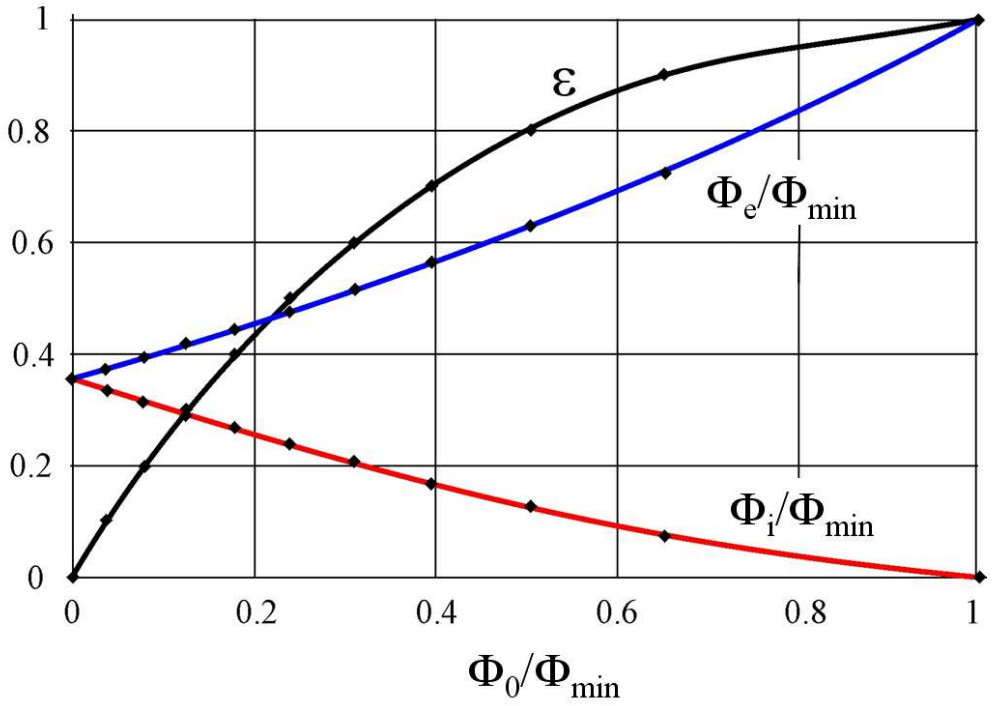

Figure 3.2 Theoretical variation of ε, Φ_e and Φ_i with Φ_0 for RI ingress with $\Gamma_c = 1$

3.1.3 Effectiveness equation for EI ingestion

For the case of EI ingestion, a linear 'saw-tooth model' was used to approximate the time-average circumferential pressure distribution in the external annulus. Figure 3.3 illustrates this modelling assumption, where the pressure is plotted graphically over a nondimensional vane-pitch, θ. For ingress to occur, the pressure in the annulus, p_2, must be greater than the wheel-space pressure, p_1; egress will occur *vice versa*.

The advantage of using a saw-tooth approximation is that the orifice equations can be solved analytically. Other pressure profiles, *e.g. cosine* functions or exact experimental fits require a numerical solution. The saw-tooth model was shown to produce reasonable results for both experimental and CFD data, and a *cosine* approximation was shown not to be significantly more accurate (Owen *et al.* (2010a)).

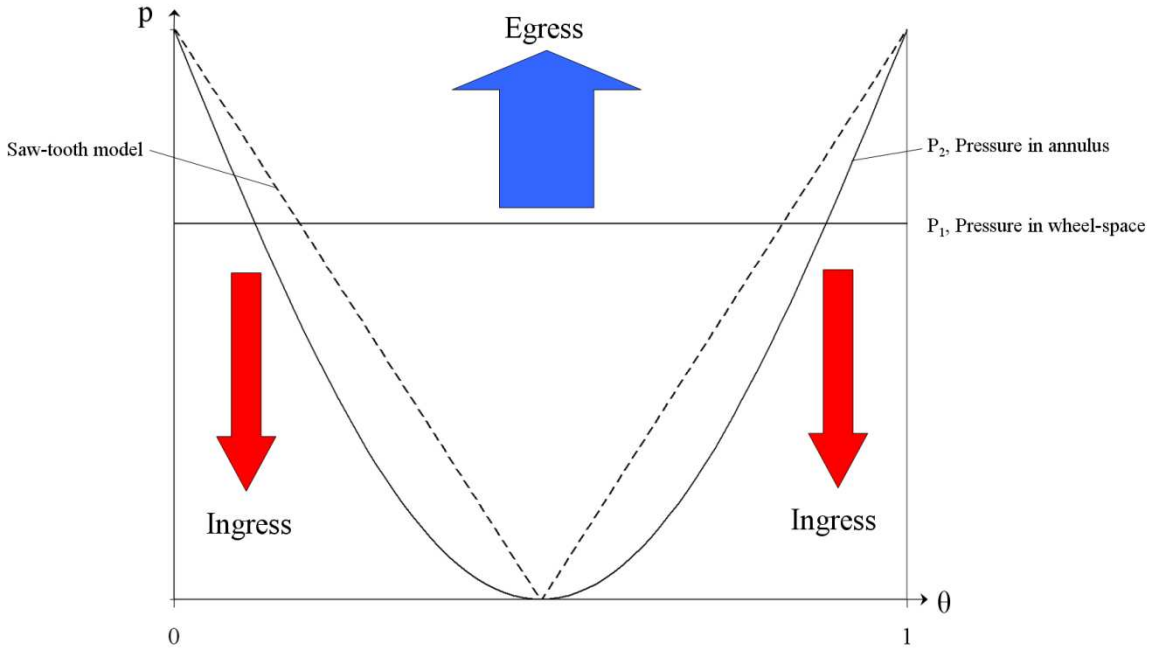

Figure 3.3 Saw-tooth model for EI ingestion (adapted from Owen (2010))

Owen (2009b) solved the orifice equations analytically for EI ingress using the saw-tooth assumption, so that

$$\Phi_{min,EI} = \frac{2}{3} C_{d,e} \Delta C_p^{\frac{1}{2}} \qquad \text{(Equation 3.33)}$$

Owen (2009b) shows that the following equations govern the sealing parameters associated with EI ingress. These equations were manipulated to form the explicit effectiveness equation for EI ingestion (Sangan *et al.* (2011b)) which is the form used for validation against experimental data in this thesis.

With reference to Figure 3.3, a normalised axisymmetric pressure parameter, g, is defined in the wheel-space, as

$$g = \frac{p_1 - p_{2,min}}{\Delta p} \qquad \text{(Equation 3.34)}$$

where Δp is the time-average peak-to-trough static pressure difference in the annulus.

The orifice model solutions for the ratio of non-dimensional sealing parameter (Eq. 3.35) and resulting sealing effectiveness (Eq. 3.36) are stated in terms of g in Owen (2009b).

$$\frac{\Phi_0}{\Phi_{min,EI}} = g^{\frac{3}{2}} - \Gamma_c (1-g)^{\frac{3}{2}} \qquad \text{(Equation 3.35)}$$

and

$$\varepsilon = 1 - \Gamma_c \left[\frac{1-g}{g}\right]^{\frac{3}{2}} \quad \text{(Equation 3.36)}$$

Eq.3.36 can be rearranged to give

$$g = \frac{1}{\left[\frac{1-\varepsilon}{\Gamma_c}\right]^{\frac{2}{3}}+1} \quad \text{(Equation 3.37)}$$

Thus by eliminating g from Eqs 3.35, it can be shown that for $\Phi_0 < \Phi_{min,EI}$

$$\frac{\Phi_0}{\Phi_{min,EI}} = \frac{\varepsilon}{\left[1+\Gamma_c^{-\frac{2}{3}}(1-\varepsilon)^{\frac{2}{3}}\right]^{\frac{3}{2}}} \quad \text{(Equation 3.38)}$$

Thus for $\Phi_0 > \Phi_{min,EI}$, the effectiveness will be unity.

Eq 3.38 will be referred to as the *EI effectiveness equation*.

The variation of ε with Φ_0 for the EI regime will be qualitatively similar in shape to RI ingestion when $\Gamma_c = 1$ (Figure 3.2). Figure 3.4 shows the effect of varying Γ_c on the shape of the EI effectiveness curves. It can be seen that Γ_c affects the gradient of the produced curves.

It can be seen from Eq. 3.38 that the variation of ε with Φ_0 depends only on the two parameters $\Phi_{min,EI}$ and Γ_c, meaning that the EI effectiveness equation has essentially uncoupled ingress from its driving force, the external pressure coefficient, ΔC_p (Eq. 3.19). However, Eq. 3.33 shows the relationship between $\Phi_{min,EI}$ and ΔC_p. For mathematical consistency in this relationship, a set of very restrictive conditions must be met with regard to the measurement location of ΔC_p (Owen 2010a). It is suggested that measurements of $\Phi_{min,EI}$ at rig conditions might be extrapolated to determine $\Phi_{min,EI}$ at engine conditions using Eq. 3.33, but care must be made in selecting the position in the annulus that ΔC_p is measured or calculated. The extrapolation is beyond the scope of this thesis (along with combating compressibility issues); a current EPSRC Knowledge Transfer Partnership exists between the University of Bath and Siemens to test this important concept.

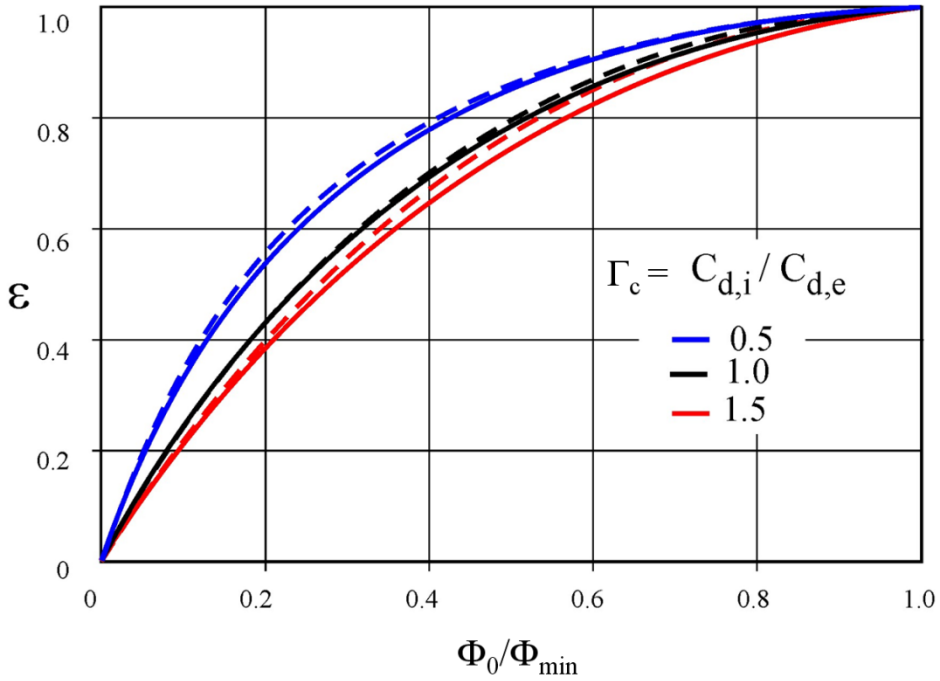

Figure 3.4 Theoretical effect of Γ_c on variation of ε with Φ_0/Φ_{min}.
Solid line is EI ingress; broken line is RI ingress.

3.1.4 Ingested flow-rate for EI ingestion

The sealing effectiveness is a useful parameter, which is usually determined from concentration measurements in an experimental rig. As with RI, it is also useful for the engine designer to be able to estimate Φ_i, the non-dimensional flow-rate of air that enters the wheel-space when $\Phi_0 < \Phi_{min}$ for the EI regime.

From Eq 3.16

$$\varepsilon = \frac{\Phi_0}{\Phi_{e,EI}} = \frac{\Phi_0}{\Phi_0+\Phi_{i,EI}} \qquad \text{(Equation 3.39)}$$

and following on from Eq 3.17

$$\frac{\Phi_{i,EI}}{\Phi_0} = \varepsilon^{-1} - 1 \qquad \text{(Equation 3.40)}$$

Also, as

$$\frac{\Phi_{i,EI}}{\Phi_{min,EI}} = \frac{\Phi_{i,EI}}{\Phi_0}\frac{\Phi_0}{\Phi_{min,EI}} \qquad \text{(Equation 3.41)}$$

it follows from Eqs 3.38 and 3.40 that

$$\Phi_{i,EI} = \Phi_{min,EI} \frac{1-\varepsilon}{\left[1+\Gamma_c^{-\frac{2}{3}}(1-\varepsilon)^{\frac{2}{3}}\right]^{\frac{3}{2}}} \quad \text{(Equation 3.42)}$$

In the limit $\Phi_0 = 0$, where $\varepsilon = 0$ and Eq. 3.42 reduces to

$$\Phi_{i,EI}^{*} = \Phi_{min,EI} \frac{1}{\left[1+\Gamma_c^{-\frac{2}{3}}\right]^{\frac{3}{2}}} \quad \text{(Equation 3.43)}$$

where * denotes the case where $\Phi_0 = 0$. Eq 3.43 gives the maximum non-dimensional flow-rate that can be ingested into the wheel-space.

3.2 Statistical fitting of the effectiveness equations

The effectiveness equations for RI (Eq. 3.27) and EI (Eq. 3.38) both contain two empirical constants, Φ_{min} and Γ_c. A method has been developed using maximum likelihood estimation, where the effectiveness equations can be fitted to experimental data by optimising the two constants (Zhou *et al.* (2011a)). The technique has been further developed to include confidence limits in the fitting procedure and to quantify the fitting error. It has been shown that the number of experimental data points, n, must be greater or equal to 16 in order for the confidence limits associated with the predicted values to capture the true values in over 90% of cases. This has repercussions in terms of the experiments and is why fitting will be limited to data sets of 16 experimental points or over.

The theoretical fits will be discussed in latter chapters along with optimised empirical constants and confidence limits. The fitting method will form no further part of this work. The interested reader is directed towards Zhou *et al.* (2011a) and for an understanding of maximum likelihood programming in 'R' to Wood (2006).

3.3 Determining the orifice model parameters experimentally

The method of statistically fitting data discussed in Section 3.2 requires experimental measurements of sealing effectiveness, ε, with the variation in non-dimensional sealing parameter,

Φ_0. It is common practice to determine a sealing effectiveness, ε_c, based on gas concentration measurements:

$$\varepsilon_c = \frac{c_s - c_a}{c_0 - c_a} \quad \text{(Equation 3.44)}$$

Concentration measurements in the *seeded* sealant flow at inlet to the system, main annulus flow and at determined points on the stator surface are notated by the symbols c_0, c_a and c_s, respectively. It follows from Eq. 3.17 that the non-dimensional ingress parameter can be determined experimentally from

$$\Phi_i = \Phi_0 \left(\frac{c_0 - c_s}{c_s - c_a}\right) \quad \text{(Equation 3.45)}$$

The non-dimensional sealing parameter, Φ_0, can be varied, with the sealing effectiveness measured at each instance, allowing the creation of a set of data which can quantify the sealing characteristics of a particular rim-seal configuration. Enough different sealant-flow levels must be tested in order to satisfy the minimum number of data points for the statistical fitting method. This will generate a theoretical prediction of Φ_{min} and Γ_c, with the former parameter allowing seal performance to be ranked.

One additional parameter that will be important for scaling the measurements of Φ_{min} to engine-representative conditions is the non-dimensional pressure difference in the turbine annulus, ΔC_p - see Eq. 3.33. In order to assess an appropriate measurement location, data was acquired at two locations in the turbine annulus. The instrumentation associated with this will be discussed in Section. 4.7.2.

Chapter 4: Design of a gas turbine testing facility for ingestion research

This chapter describes the design and construction of a new research facility which experimentally models hot gas ingestion into the wheel-space of an axial turbine stage. The design was influenced by the requirement of collecting data to support the theoretical models described in Chapter 3 and the use of TLC applied areas for heat transfer measurements. Measurements of CO_2 gas concentration in the rim seal region and inside the wheel-space quantified the sealing effectiveness of various rim seal geometries. Another important consideration was the measurement of the external driving pressure; an orifice model requirement.

The project proposal for Siemens[1] required the design of two annulus air supply configurations for the rig, which were to be constructed and fitted sequentially during the testing schedule. The requirement for heat transfer tests featured a heated main annulus flow, whereas the gas concentration measurements would only require a simpler cold annulus flow. These two configurations are termed the hot main annulus (HMA) and cold main annulus (CMA), respectively. The CMA design would feature a feed system which supplied cold air to the annulus test section with a high degree of axissymmetry, whereas the HMA would use a system featuring integrated mesh heater units to heat the external flow temperature for a transient experiment.

Initial calculations were conducted to assess the running conditions for the rig; these included mass-flows, disc speeds, and vane and blade angles. In conjunction with Siemens, the test section design (based on the engine geometry) was modelled in CAD. Manufacture preceded an extensive commissioning of the CMA configuration. This chapter will document the design, fabrication and commissioning process as a precursor to the testing programme which will be described in subsequent chapters.

4.1 Conceptual design of the rig

The rig featured a single axial turbine stage, where a stator and rotor created a contained wheel-space. Sealant flow entered through the centre of the stator disc and flowed radially-outward through the wheel-space, emerging through a rim-seal into an external annulus. It was expected that a volute would collect the external flow at stage exit.

Schematic diagrams were created for the HMA and CMA configurations. A schematic of the former is shown in Fig. 4.1. This configuration featured an external-flow split into four inlet

[1] SIEMENS Fossil Power Generation and SIEMENS Oil & Gas

pipes. Each pipe contained a mesh heater that raises the temperature of the annulus flow, before each pipe feeds a quarter of a duct which forms a transition from a rectangular to annular geometry.

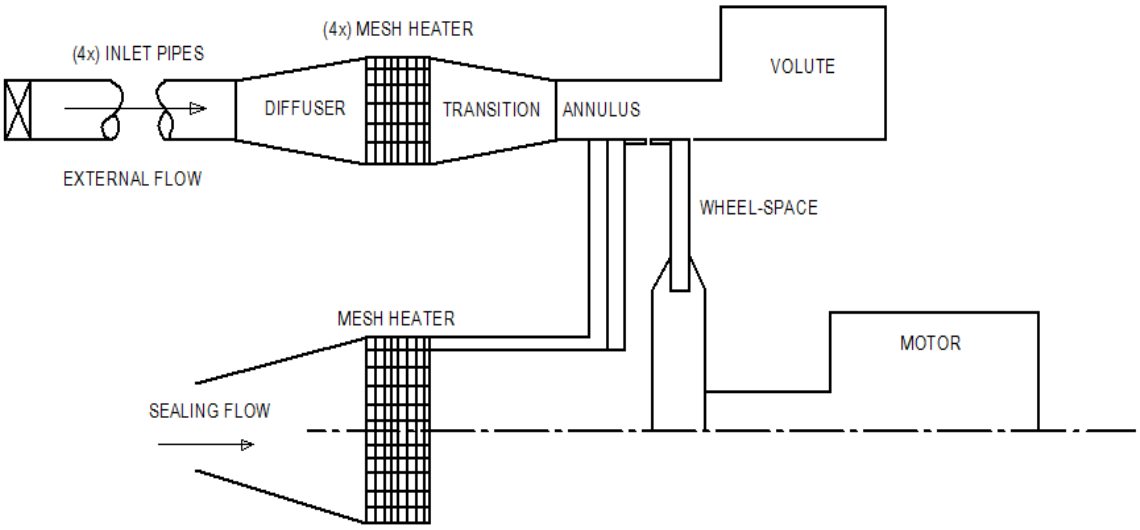

Figure 4.1 Schematic of the proposed rig layout for the HMA

The alternate CMA concept (Fig. 4.2) featured one inlet tube per vane, fed through a contracting plenum chamber into the annular test section. This provided axissymmetric flow, without the complicated and unorthodox ducting required by the HMA. In order for the flow to be fed into the inlet pipes, a radial diffuser formed the transition between that and the laboratory supply pipe.

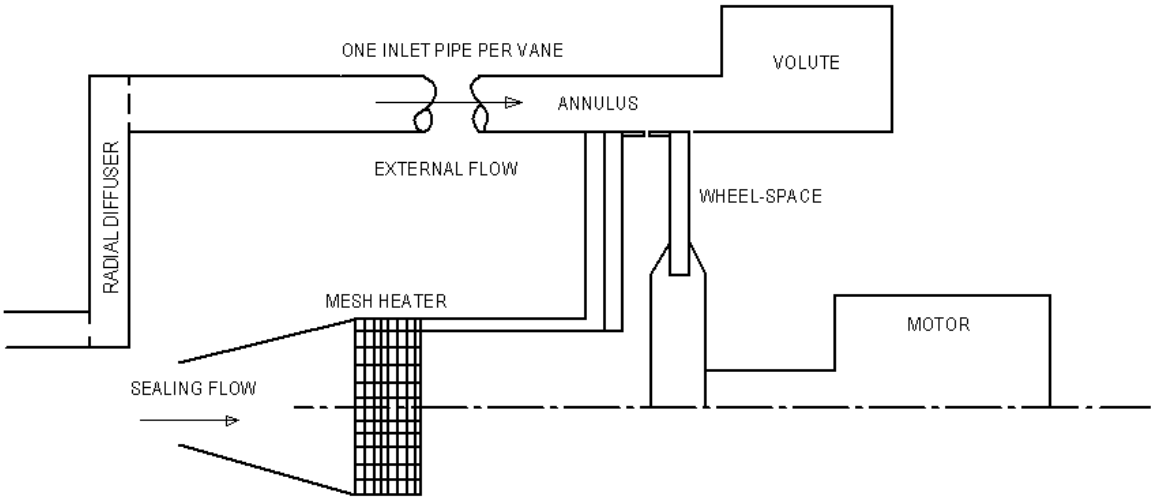

Figure 4.2 Schematic of the proposed rig layout for the CMA

As the rotor-stator section remained unchanged with either feed system, the two systems were interchangeable without major overhaul on the test section.

4.1.1 Design point calculations

The rig was designed with three generic design points at 2000, 3000 and 3500 rpm. The design points corresponded to the expected external pressure fields predicted by Siemens who ran pre-design CFD codes to establish expected operating conditions. Siemens provided the geometry of the vane. Symmetric blades were used as there was no means of dissipating any power generated by loaded blades.

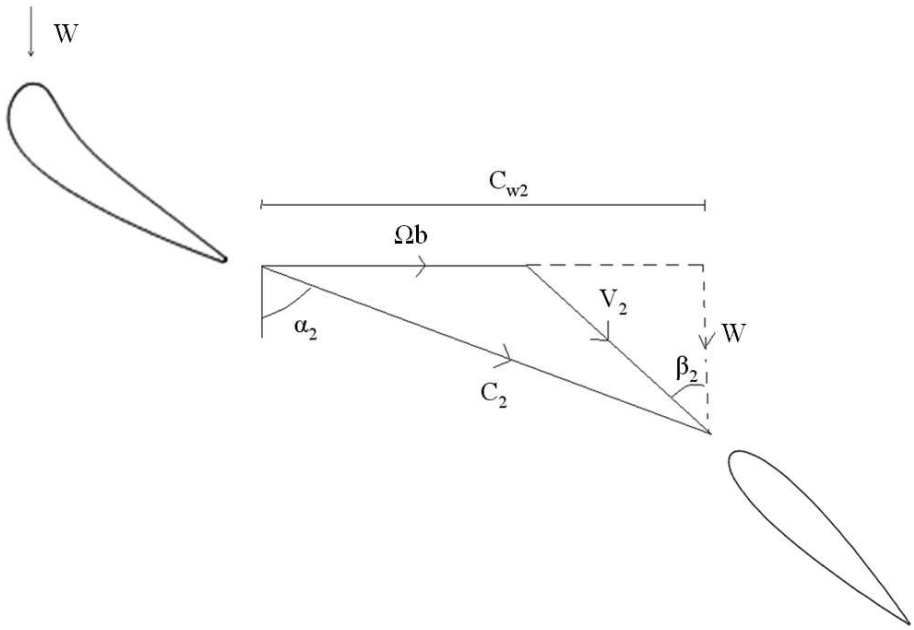

Figure 4.3 Generic vane-blade velocity triangles

In order to keep the symmetric blades unloaded, the CFD analysis predicted that the velocity triangles required a blade inlet angle of 56.7° on design. Although not engine representative, these un-turned blades still created the unsteady pressure distribution over the seal clearance. The three design points each have a specific annulus mass flow (or axial component of velocity, *W*) which was dependant on disc speed. The velocity triangles are shown in Fig. 4.3. Each design point has geometrically similar velocity triangles. This allowed a variation in Re_Φ for the same non-dimensional driving potential in the annulus. The theoretical model has predicted that the non-dimensional sealing parameter, Φ_0, should accommodate for the variation in Re_Φ and eliminate this variable for when ranking seals.

The design points were calculated for an annulus height (*h*) of 10 mm and at a blade platform inner-radius (*b*) of 0.19 m. The annulus height was set at 10 mm in order to achieve

sufficient flow velocities inside the annulus; acceptable annulus Mach numbers were a limiting factor.

The initial design point assumptions were stipulated as follows:

- In line with current engine design trends, an initial estimate of the chord to pitch ratio was set at one (Chord/Pitch = 1)
- The number of blades must be greater than the number of vanes ($N_{blades} > N_{vanes}$)

The air flow through the rotor-stator section was modelled using isentropic gas relationships and by applying the conservation of mass. All velocity triangle components were calculated. The conditions for the three design points (DP) are shown in Table 4.1.

Two key non-dimensional modelling parameters in terms of achieving the appropriate fluid dynamics are the axial Reynolds number (Eq. 4.1) and rotational Reynolds number (Eq. 4.2), also shown in Table 4.1. The rotational variant will be the more important of the two, being extensively encountered in problems involving rotating viscous flow. The magnitude of Re_Φ in the rig was made as large as possible given the restraints of the design. Typically 5 x $10^5 < Re_\Phi <$ 9.7 x 10^5.To ensure turbulent flow, Re_Φ should be greater than 3 x 10^5 (Theodorsen and Regier (1944)). A typical engine Re_Φ would be in the order of 10^7 and the difference in Re_Φ must be taken into consideration when scaling the data from the rig to the engine. The important scaling parameter is the compressibility of the flow in the annulus. For the rig the Mach number in the annulus was less than 0.4.

$$Re_w = \frac{Wb}{\nu} \qquad \text{(Equation 4.1)}$$

where:
- Re_w is the axial Reynolds number in the annulus
- W is the bulk-mean axial velocity in the annulus
- b is blade platform inner-radius
- ν is the kinematic viscosity of air

$$Re_\Phi = \frac{\Omega b^2}{\nu} \qquad \text{(Equation. 4.2)}$$

where:
- Re_Φ is the rotational Reynolds number
- Ω is the angular speed of the disc
- b is blade platform inner-radius
- ν is the kinematic viscosity of air

Calculated Parameter	**2000 rpm DP**	**3000 rpm DP**	**3500 rpm DP**
Vane Exit Angle (α_2)	73.5^o		
Blade Inlet Angle (β_2)	56.7^o		
Rotational Velocity Component (Ωb)	39.8 m/s	59.7 m/s	69.6 m/s
Axial Velocity Component (W)	21.5 m/s	32.2 m/s	37.6 m/s
Vane Exit Velocity (C_2)	75.5 m/s	113.3 m/s	132.2 m/s
Annular Blade Area ($A_{annulus}$)	$0.01256\ m^2$		
External Mass Flow Rate ($\dot{m}_{external}$)	0.34 kg/s	0.51 kg/s	0.60 kg/s
Axial-Flow Reynolds Number (Re_w)	2.86×10^5	4.40×10^5	5.21×10^5
Rotational Reynolds Number (Re_Φ)	5.32×10^5	8.17×10^5	9.68×10^5
Re_w/Re_Φ	0.538	0.538	0.538
Vane Exit Mach Number (M)	0.225	0.339	0.398

Table 4.1 Design point parameters

It should be noted that although Re_Φ is an order of magnitude below that found in most engines, Owen and Rogers (1989) have shown that, for rotating flow, the turbulent flow structure in the boundary layers is principally governed by the turbulent flow parameter, λ_T , and depends only weakly on Re_Φ. Hence the flow structure in the rig is considered to be representative of that found in the cooling systems of engines.

4.1.2 Technical feasibility of the design

It was possible to assess the power required to run the rig, and calculate entrainment coefficients, as well as the power requirements to heat the external flow in the case of the HMA design. The calculations are shown in Appendix A, with a summary of all calculated parameters presented in Table 4.2. The mass-flow entrained by a free-dive gives a conservative estimate of the sealant flow-rate levels that may be required to purge the wheels-space under experiment. The power to drive the disc, sealant flow-rates and mesh heater power are all within the viable limits of the laboratory.

Calculated Parameter	2000 rpm DP	3000 rpm DP	3500 rpm DP
Entrainment Coefficient (C_w)	8.38 x 10^3	1.18 x 10^4	1.35 x 10^4
Free Disc Moment Coefficient (C_m)	5.64 x 10^{-3}	5.21 x 10^{-3}	5.05 x 10^{-3}
Mass Flow Entrained if a Free Disc	0.027 kg/s	0.038 kg/s	0.044 kg/s
Power Required to Drive Disc	15 W	48 W	74 W
Mesh Heater Power Required for HMA	17 kW	26 kW	30 kW

Table 4.2 Technical parameters for rig design

It was important to assess the size of the rig to ensure it could be situated within the limited confines of the gas-dynamics laboratory. This involved creating a plan-view schematic and an assessment of the rig geometry, the required mounting and connected pipe-work. The base plate on which the associated motor and bearing unit would be situated was taken from an previously existing rig (Kakade *et al.* (2011). A sizing procedure based on the larger HMA variant was conducted based on pipe inlet lengths (ISO 5167-2:2003) and basic component breakdown (Fig. 4.4).

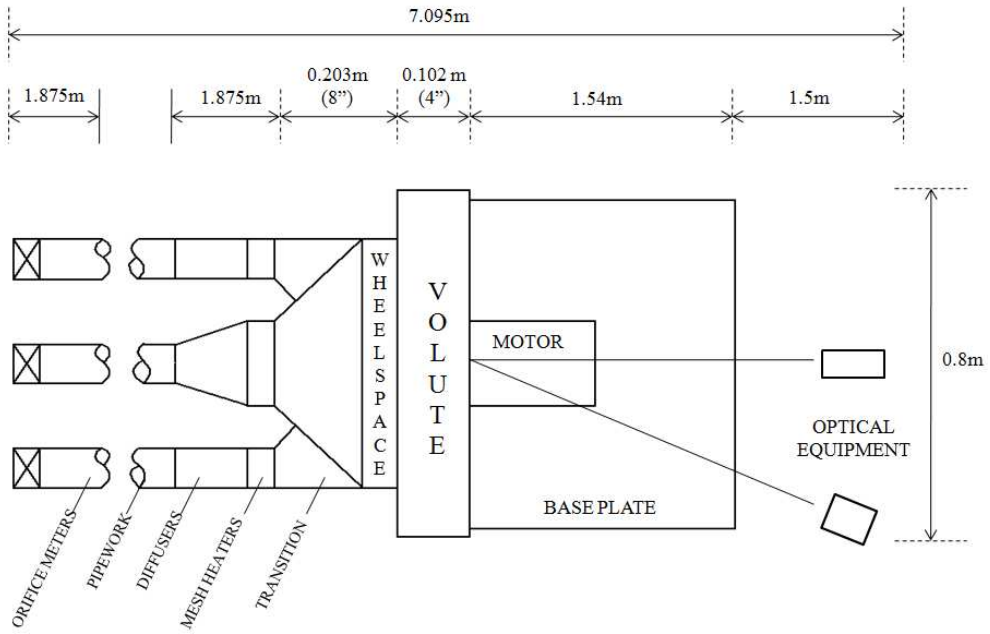

Figure 4.4 Initial rig sizing

From Fig. 4.4 it was decided that the existing gas dynamics cell could house either inlet configuration (HMA or CMA) and that a secondary control room would be constructed adjacent to

the cell to house the computer and control systems. Both the external and sealant flow-rates require accurate measurements, so orifice meters were critical and located in the pipe-work occupying both rooms, allowing sufficient flow-development lengths. Figure 4.5 shows a schematic overview of the pipe-work design spanning the two rooms. Note the inclusion of two orifice meters fitted on the near wall, each designed and fabricated to the European Standard EN ISO 5167-2 (2003), one for the 2 inch and one for the 4 inch pipes which would convey the sealant and external flows, respectively. Each of the flows was controlled by a Kinetrol unit (pneumatically controlled actuator valve) with electrical signal control and a built in fail-safe component. The two pipes adjoined to form a co-axial inlet to the rig for feeding into the test section.

Figure 4.5 also shows the schematic design of a gas injection system, featuring a selection of calibration gases supplied to a gas analyser in the test cell, where provisions for sealant flow seeding were also considered.

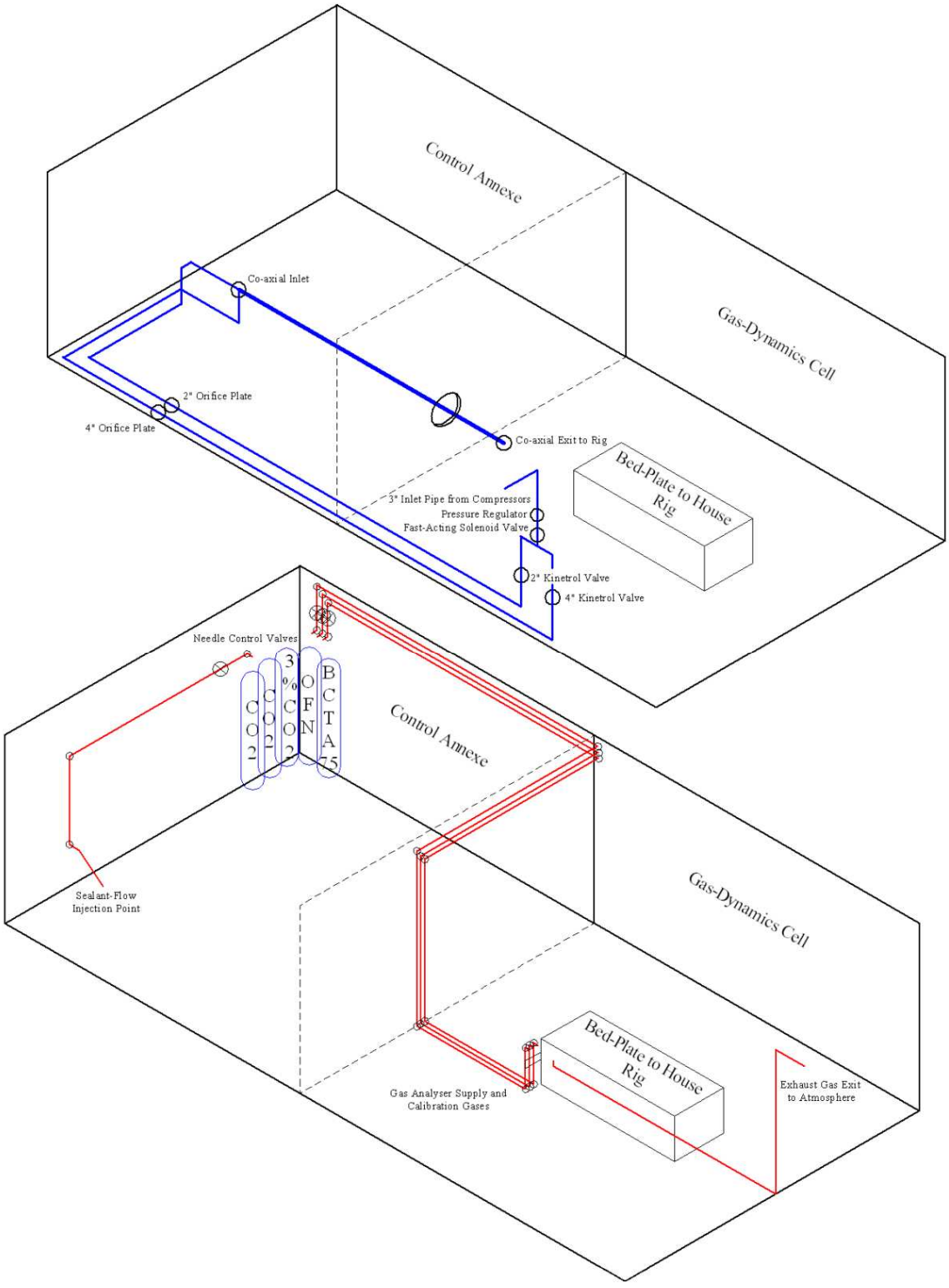

Figure 4.5 Service schematics of the gas dynamics facility (blue: compressed air supply; red: gas injection system)

In summary, the laboratory was transformed to house the new gas ingestion rig with the development work of the facility described as follows:

- Extension of room to incorporate a remote running annexe.
- Complete pipe-work overhaul including significant installation of the new pipes.
- Electrical re-fit of motor system and foundations laid for inclusion of large power supply for heating external flow.
- Installation of valve control system for balancing all flows into and out of the test facility.
- Fitting of a gas injection system for seeding flows.
- Safety procedure developed with automated emergency shut-down.
- Control logic and instrumentation discussed in Section 4.7.

The author produced the facility design and supervised the construction process. Appendix. B contains a selection of photographs highlighting the construction of the test facility.

4.2 Design of rotor-stator section

This section will discuss the final design of the rotor-stator section, a process which was iterative. The working section featured a simple rotor-stator geometry, with a sealant flow inlet through the centre of the stator. The rotor was connected through a base hub to a motor unit, with various rim seals fitted to the wheel-space periphery. The final design is shown as Fig. 4.6, which identifies the different materials. The design features will be discussed in Sections 4.2.1-3.

The design featured a stator disc constructed from polycarbonate, backed with an aluminium plate for support. Sealant flow pipe-work was flanged on to the stator back-face and, due to the potentially high temperature flows, coated with Rohacell 51 (a high strength insulating foam). The stator platform was manufactured from an aluminium ring containing clearance holes through which the vanes were attached to tapped holes in the polycarbonate disc.

The rotor was also polycarbonate, restrained by an aluminium blade platform featuring integral blade attachment holes and interior seal attachment points. The aluminium platform was constructed from high strength aerospace grade aluminium (T7075-T6) to contain the centrifugal growth of the enclosed polycarbonate rotor disc. The rotor disc itself was restrained by three Nitrile O-rings which acted to impose a restoring force upon the disc. The constraining hub was manufactured from aluminium and hollowed into a bell-shape, which helped to reduce the mass in the rotor. A clamping piece was used to constrain the rotor disc, which was also coated in Rohacell 51 to avoid the aluminium components becoming heat sinks during the heat transfer tests. The rotor hub was mounted to a drive-shaft through an air-cooled bearing, with 0.25 mm shims located up against a shoulder to allow for axial movement of the rotor.

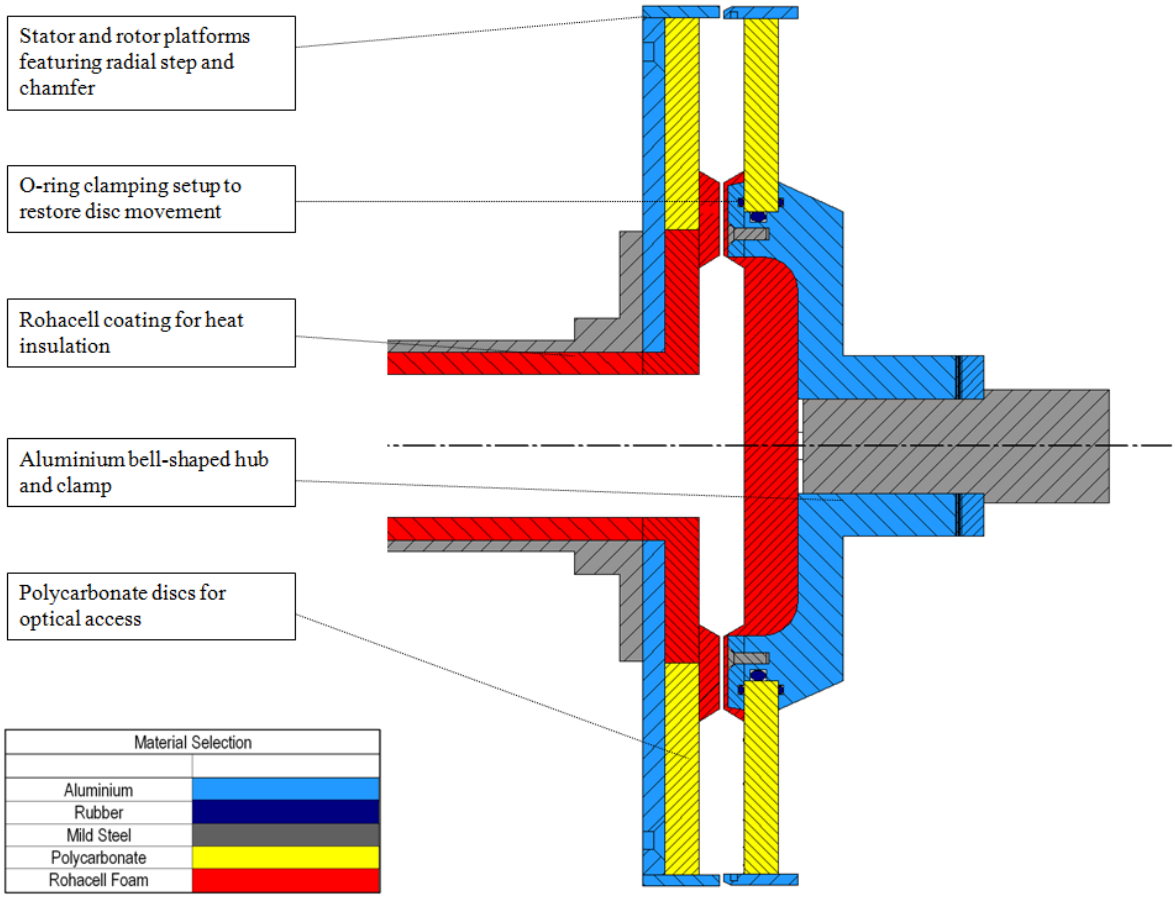

Figure 4.6 Rotor-stator design

The datum setup included a simple axial seal at the wheel-space periphery, along with an inner seal mid-way down the cavity designed to ensure turbulent Couette flow into the outer wheel-space, with appropriate swirl. This formed the baseline test case, from which more complicated seal configurations could be compared.

4.2.1 Platform design and structural analysis

The stator platform was made from 5 mm industrial aluminium, whereas the rotor blade platform was made from an aerospace-grade aluminium. The reasoning behind this is that the polycarbonate rotor disc expands under rotation, and thus the rotor platform, with its high strength, helps to reduce the growth of the rotor disc while reducing the internal stresses in the disc. The rotor platform featured a bonded interference fit with the rotor disc, and acted as a platform to which the blades were attached.

The datum seal used a 2 mm axial gap located midway between the vane trailing edge and the blade leading edge. The reasoning for this being that the ingress at this point will neither be

dominated by either the vane pressure distribution, nor the bow-wave effect from the downstream rotor blades. Figure 4.7 shows the relative position of the axial clearance. The decaying vane pressure distribution and the blade bow-wave effect are shown illustratively in red and blue, respectively. The influence of the vane and blade effects and the relative position of the clearance has been documented by Bohn *et al.* (1995).

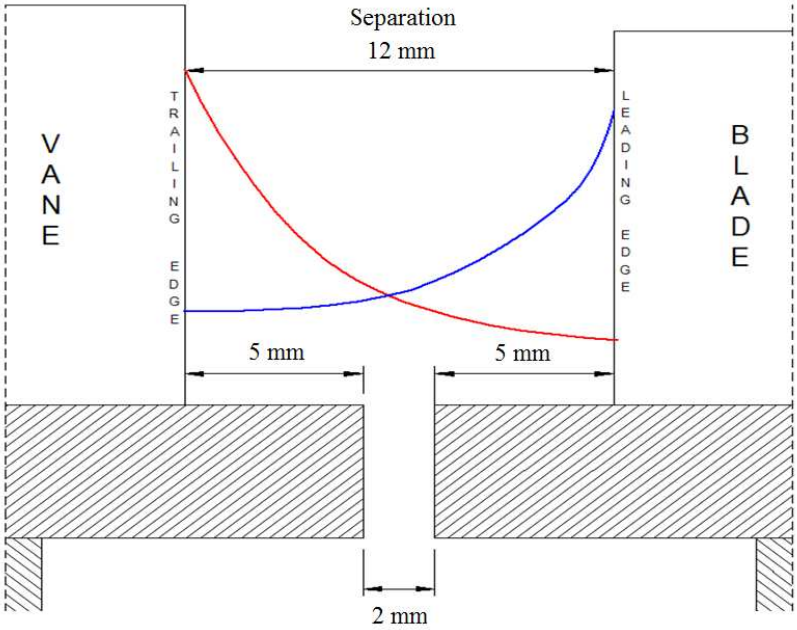

Figure 4.7 Axial clearance location in the centre of the wheel-space cavity

The experimental research programme required an alteration of the axial seal-clearance. It was specified by Siemens that the axial seal clearance should vary as $1.5 < s_c < 3.5$ mm ($0.007 < G_c < 0.016$), being achieved from relative movement of the rotor by ±1mm about the 2.5 mm mean seal clearance. Spacers were used on the rotor shaft to increment the axial displacement on the entire rotor and hub assembly.

Another design driver for the wheel-space periphery was the impingement of mainstream flow onto the rotor platform, which was to be avoided. The centrifugal growth of the rotor disc under rotation exacerbated the situation, and a radial step was suggested between the stator and rotor platforms. Figure 4.8 shows the flow expected with and without impingement, which could occur in the absence of a radial step.

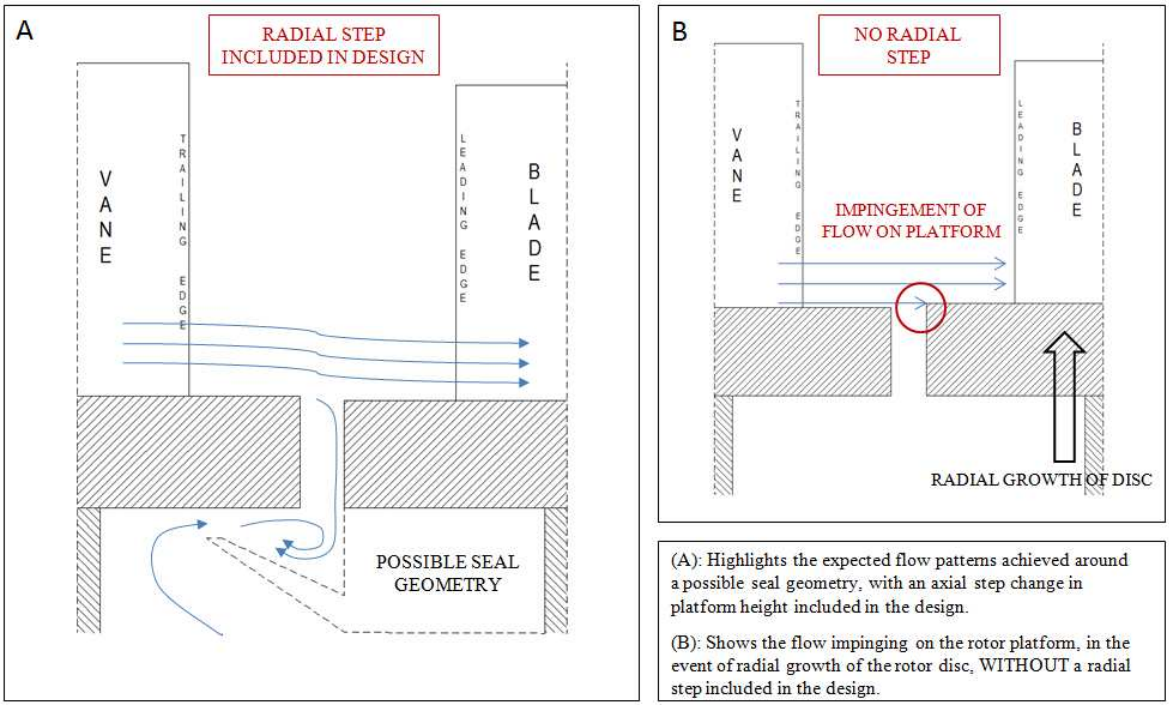

Figure 4.8 Effect of a radial step on flow impingement

In order to design the required radial step, the radial growth of the disc was predicted using the method of Morley (1954). The problem used a polycarbonate disc constrained by an aluminium ring with pre-determined radii and material properties, along with appropriate boundary conditions (Fig. 4.9). The calculations were made for the maximum motor speed of 6000 rpm as an upper bound.

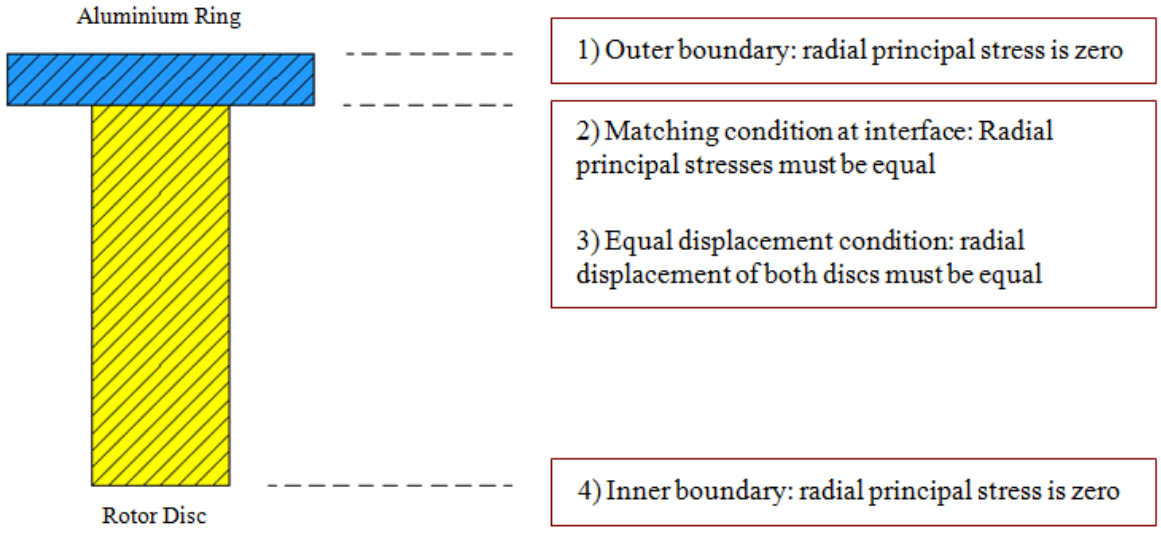

Figure 4.9 Growth and stress estimation for rotor disc

The method is based on the solution of a pair of material constants, produced using the set of four boundary (or "matching") conditions. These constants are then recycled to compute the radial displacements at any given radius. The disc-matching process for the growth of the two materials was solved and predicted a radial growth of the aluminium ring of 0.33 mm at 6000 rpm.

With an estimated rotor platform growth of 0.33 mm, and with a radial step-down still desirable in the rotating case, the radial step height was fixed at 0.4 mm in the stationary setup. An additional 30^{o} chamfer (1/3 depth) was included at the leading edge of the rotor platform to better resemble engine geometries used by Siemens. Figure 4.10 shows the change in step height and addition of the chamfer for the stationary design.

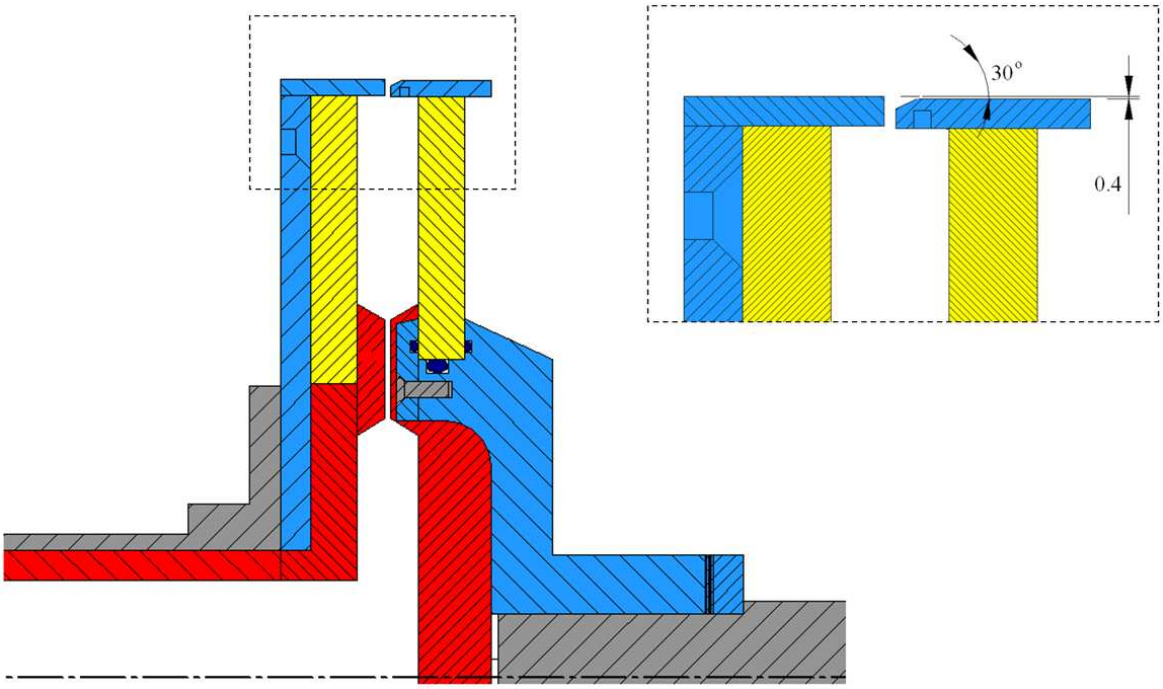

Figure 4.10 Radial step and chamfer on rotor platform

The maximum hoop stress in the aluminium rotor platform was estimated to be 114 MPa at 6000 rpm, which whilst below the yield stress of the aluminium 7075 T6 selected for this purpose, also required testing for fatigue failure (see Section 4.2.3).

4.2.2 Wheel-space geometry

The dimensions of the wheel-space were based on the need for optical access while also targeting actual engine ratios specified by Siemens (Fig. 4.11 highlights the variables available for optimisation).

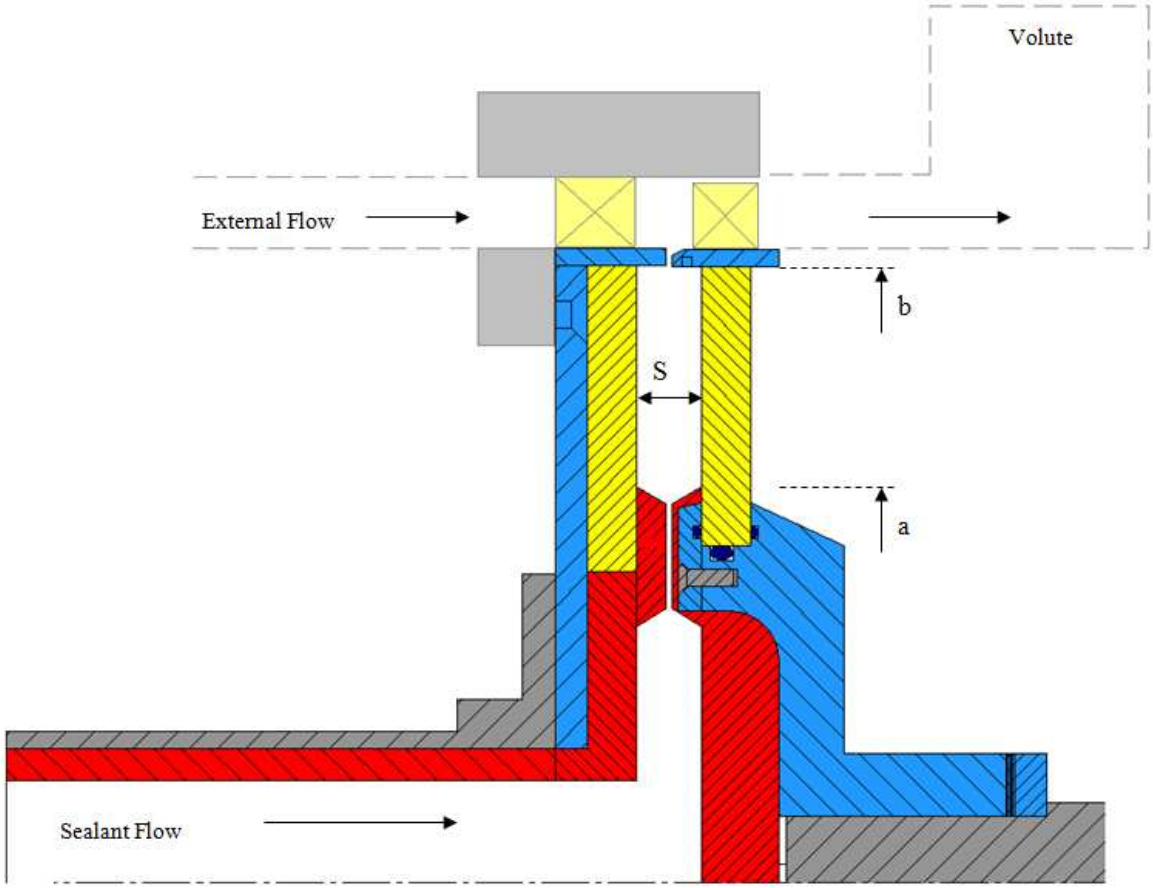

Figure 4.11 Variables available for cavity optimisation. Where "*S*" is the cavity width, "*a*" is the cavity inner radius and "*b*" is the cavity outer radius.)

The first important dimension was that of the *optical access ratio*, given by Eq. 4.3:

$$Optical\ Access\ Ratio = \frac{a}{b} \qquad \text{(Equation 4.3)}$$

A second dimension, the *cavity aspect ratio*, also had to be considered. It was decided that the rotor clamp extrusion would provide an appropriate entrance to the cavity, with the cavity aspect ratio given by Eq. 4.4:

$$Cavity\ Aspect\ Ratio = \frac{(b-a)}{S} \qquad \text{(Equation 4.4)}$$

Optimisation of Eq. 4.3 was important to allow sufficient optical access to the test section. It was also critical to ensure that the cavity width, *S*, was large enough to allow separate boundary layers to form on the rotor and stator. Using confidential Siemens ratios, the wheel-space

dimensions were matched to give an optimised cavity aspect ratio of 3.45 and an equivalent optical aspect ratio of 0.64. The dimensions are shown in Fig. 4.12.

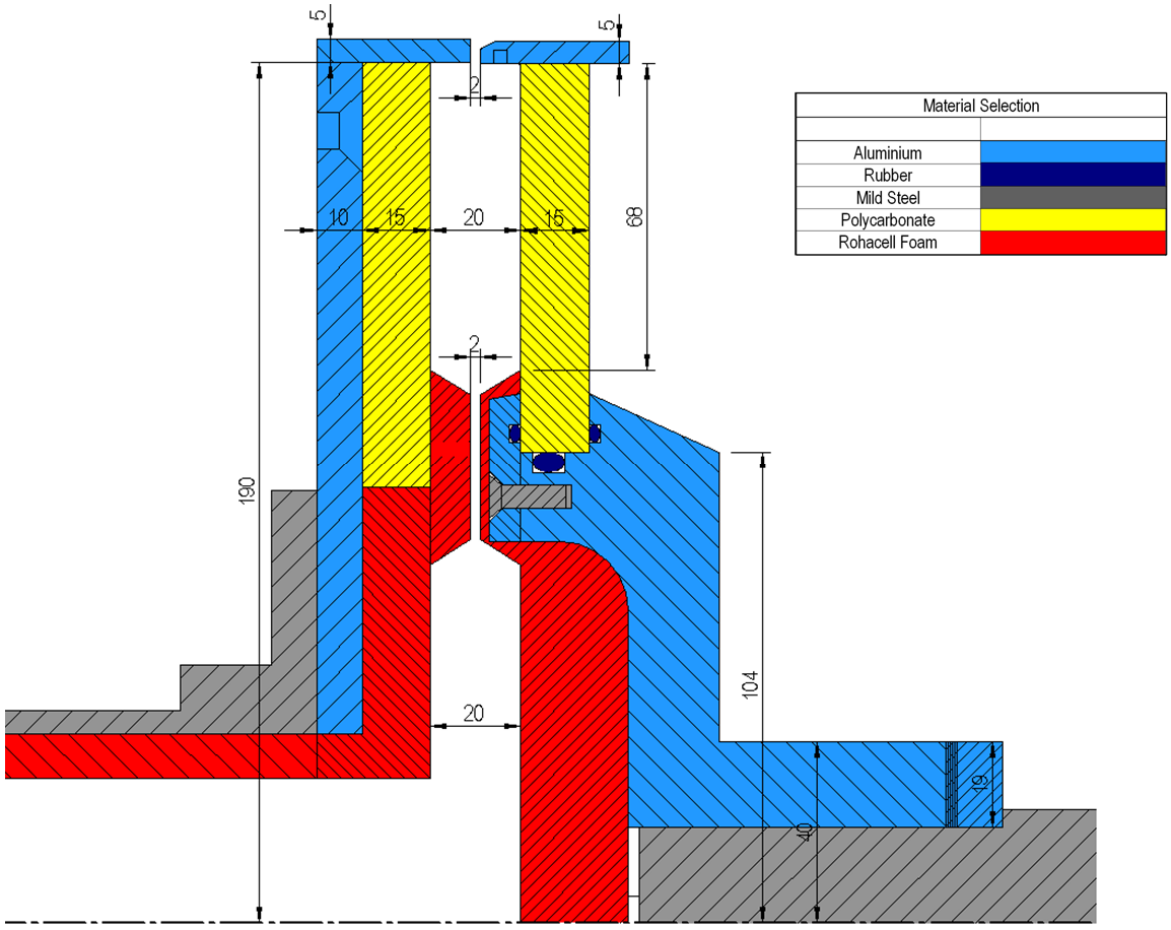

Figure 4.12 Dimensioned rotor-stator setup (all dimensions in mm)

An inner seal was used to ensure the correct flow conditions inside the cavity. This ensured that the sealing flow entered the wheel-space with the correct degree of swirl. This inner seal was optimised to produce turbulent Couette flow into the cavity, and the size of the clearance was determined according to the critical values specified by Daily and Nece (1960). For turbulent Couette flow to occur, the flow needs to reside in Regime III (Fig. 2.5), with the maximum clearance ratio corresponding to

$$G_{Crit} = 0.402 Re_{\Phi}^{\frac{-3}{16}} \quad \text{(Equation 4.5)}$$

By taking the rotational Reynolds number at the radial height of 0.122 m (corresponding to the inner seal), the critical clearance, S_{crit} = 4.19 mm. An inner clearance of approximately half this

value at the datum setup (2 mm) ensures turbulent Couette flow at the inner seal over the full range of axial seal clearances ($1.5 < s_c < 3.5$ mm).

The flow through this inner seal will consist of two components: a radial Poiseuille[2] flow and a tangential Couette[3] flow. It is assumed that the radial component is negligible and therefore the tangential component is dominant, providing a swirl ratio of 0.5 in the cavity. This condition is desirable as it resembles the typical engine conditions specified by Siemens.

4.2.3 Material selection

To conclude the rotor-stator design, a brief discussion of material choice is now presented. A Rohacell lining was used on the stator and rotor: Rohacell is a lightweight, insulating foam making it a perfect lining material for components downstream of the mesh heaters. The rotor and stator discs were manufactured from polycarbonate for optical accessibility, with 10 mm aluminium backing for rigidity on the stator. The rotor disc was clamped using an aluminium hub, which connected to the bearing unit associated with the motor. A 5 mm aluminium vane platform was used. A 5 mm aluminium blade platform with aluminium 7075 T6 was chosen for the rotor. All pipe-work and flanges were manufactured from steel.

The aluminium blade platform is one of the most structurally critical rig components, and was extensively tested to ensure operating safety. A flat-plate model was subjected to tensile and low-cycle fatigue testing prior to manufacture. Of particular concern was the maximum hoop stress calculated in Section 4.2.1, where it was essential to ensure that a sufficient safety factor was associated with the yield stress of the material. This would have indeed been the case with lower strength aluminium alloys such as 1050A or 2014A which were used to construct the stator hub. The 0.2% proof stress of higher strength alloys were compared to the previously calculated circumferential stresses. A high specification aerospace grade alloy (Al 7075 T6) was found to have acceptable properties, while at the same time be easily obtainable. The 0.2% proof stress of Al 7075 T6 is 505 MPa, compared to the estimated maximum 114 MPa experienced by the rotor platform under rotation, giving a safety factor of 4.5. The inclusion of 2 mm tapped holes from which the blade attachment would occur was expected to raise this stress level by a factor of up to three, rendering an estimated safety factor closer to two (including stress raisers).

With the material deemed safe under pure tensile failure, concerns also existed regarding the low-cycle fatigue performance. The material was thought to be especially vulnerable surrounding the tapped holes, where it was suggested that plastic regions could form leading to

[2] Poiseuille flow refers to a viscous and incompressible flow through a constant circular cross-section that is substantially longer than its diameter
[3] Couette flow refers to the flow of a viscous fluid in the space between two parallel plates, one of which is moving relative to the other

potential failure. A fatigue test was scheduled, requiring a full scale model of the blade platform to be constructed and tested. The replica was a 5 mm aluminium plate, dimensioned to scale, including the chamfer and three pairs of 2 mm holes. Due to the expense of the higher grade aluminium alloy (Al 7075 T6), a more modest Al 6082 T6 was selected for the model. Whilst it is characteristically suggested that the fatigue properties of this slightly more modest alloy would be marginally worse than the aerospace grade, it was suggested that upon passing the fatigue test it was reasonable to assume that the higher strength variant would also be a capable option.

In order to simulate the appropriate loading, the maximum stress was to be applied cyclically (simulating a single running test of the rig). A stress of 114 MPa applied over the platform area required a simulated tensile force of 18.81 kN using a Standard R–Ratio of 0.1, and giving a cyclical distribution about a mean 10.35 kN +/- 8.46 kN. Electronically controlled jaws were used to produce the load, cycling at 3 Hz up to 5000 cycles, where it was arbitrarily judged that the rig would never exceed this number of running cycles. Figure 4.13 details the experiment length and shows no resultant shift in loading – highlighting the absence of any permanent deformation. It was also of note that after the conclusion of the experiment, no aesthetic damage was noticeable.

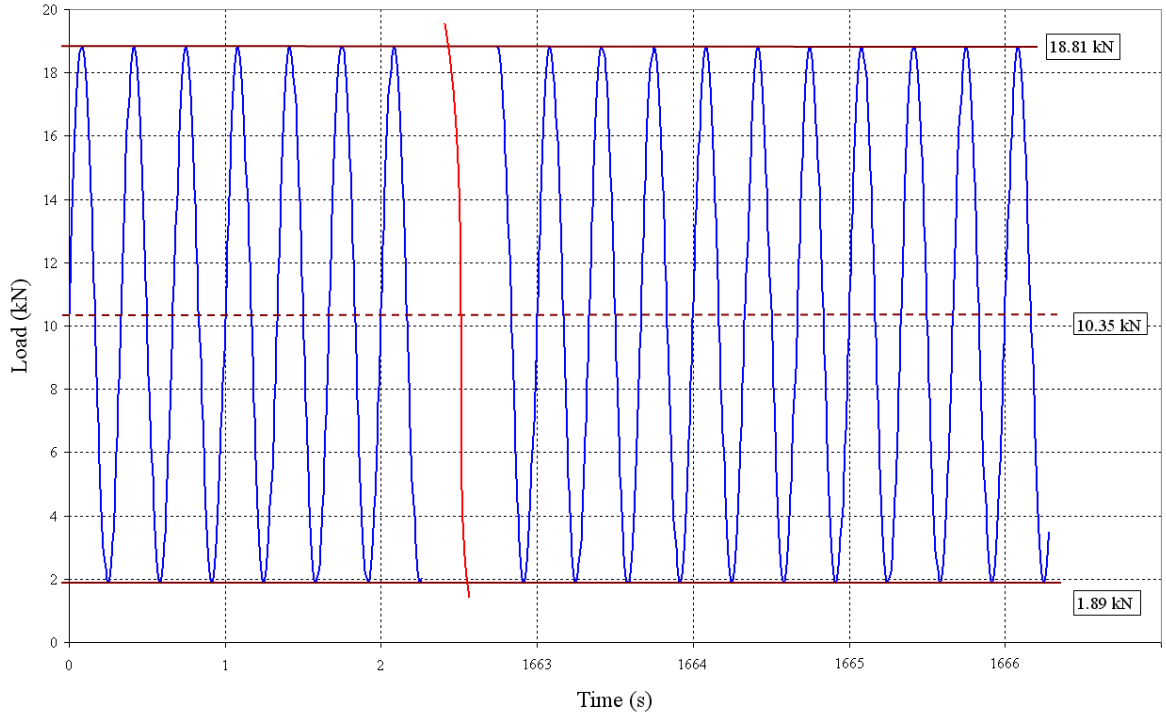

Figure 4.13 Low-cycle fatigue test to 5000 cycles

Aerospace-grade aluminium alloy (T7075 T6) was shown to be sufficient with regards to its tensile and fatigue properties, and thus it was selected as the rotor platform material.

4.3 Vane and blade configuration

In order to discuss the vane and blade setup, it is first essential to define all nomenclature associated with the corresponding velocity triangles. For this purpose, a set of velocity component triangles are included as Fig. 4.14, with all velocities and angles defined.

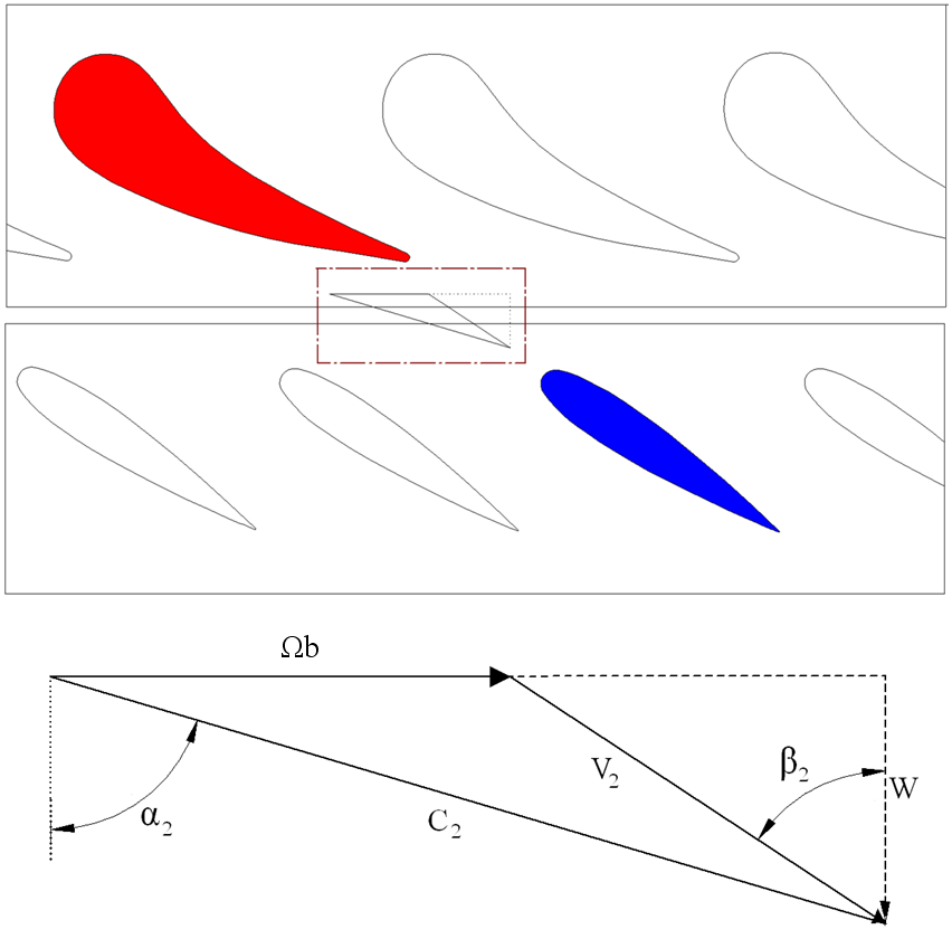

Figure 4.14 Velocity triangle defining all vectors and angles

Angle β_2 is the blade inlet angle (in the rotating frame), with the vane turning angle defined as "$\alpha_2 - \alpha_1$." The airflow leaves the vane with velocity C_2, at an angle α_2 (stationary frame), which is equivalent to velocity V_2 at an angle β_2 relative to the rotating blade.

A few assumptions were made to simplify the velocity triangles to those illustrated in Fig. 4.14:

- The flow is assumed to enter the vane stage with a purely axial velocity component. The vane inlet angle, α_1, is equal to zero, where W is the constant axial flow component.

- Symmetric blades were used as there was no means of dissipating any power generated by loaded blades.

The symmetric NACA 0018 blades still generated an unsteady pressure distribution at the seal clearance, with the ingress effects not substantially altered without the inclusion of a turned blade; a hypothesis verified by Siemens CFD. The vane turning angle (α_2) was 73.5°, whilst the blade inlet angle (β_2) for zero loading was determined as 56.7° after a more thorough viscid CFD analysis also conducted by Siemens. The full velocity triangle components at all design points were calculate and are shown as Table 4.3. It must be noted that these approximations are inviscid. The vane-blade co-ordinate system was developed with a 12 mm separation between the two (Fig. 4.15).

Velocity Triangle Parameter	**2000 rpm DP**	**3000 rpm DP**	**3500 rpm DP**
Vane Exit Angle (α_2)	73.5°		
Blade Inlet Angle (β_2)	56.7°		
Rotational Velocity Component (Ωb)	39.8 m/s	59.7 m/s	69.6 m/s
Axial Velocity Component (W)	21.5 m/s	32.2 m/s	37.6 m/s
Vane Exit Velocity (C_2)	75.5 m/s	113.3 m/s	132.2 m/s
Blade Inlet Velocity (V_2)	39.1 m/s	58.6 m/s	68.4 m/s

Table 4.3 Velocity triangles parameters

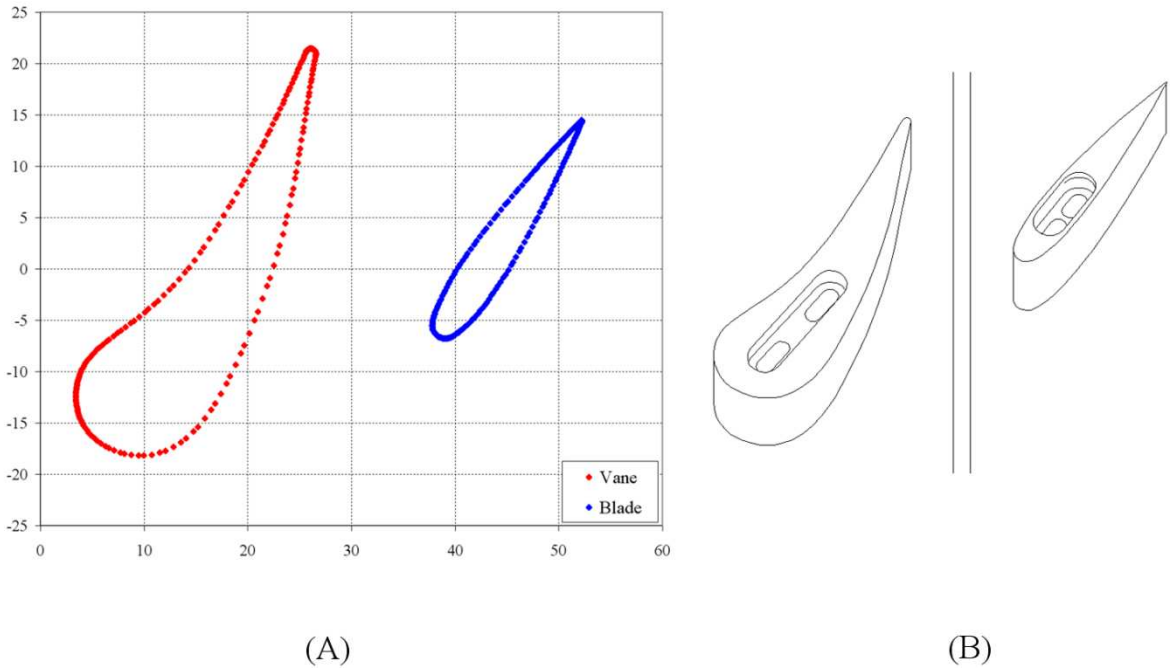

Figure 4.15 Vane and blade profiles: (A) Co-ordinate geometries, (B) Representative modelling

4.3.1 Vane and blade quantity & scaling

To determine the number of vanes and blades required for the rig, it was necessary to match the ratio of the vane-blade separation gap to the vane and blade true chords, with an engine representative equivalent. Figure 4.16 highlights the definitions used in the formulation of the ratio.

The chord of the vanes/blades also depended on the number of each used. The vane/blade number was applied circumferentially around the disc providing the pitch, which was subsequently converted to a chord using a supplied pitch/chord ratio. Engine representative pitch to true-chord ratios for the vanes and blades were provided by Siemens as 0.880 and 0.950, respectively.

In order to model the engine conditions, "a separation-gap to true-chord ratio" was calculated for a range of possible blade and vane numbers. This provided a range of possible ratios, with the closest ratio to actual engine setup being selected, along with its constituent vane and blade numbers. The effect of vane and blade number is shown graphically as Fig. 4.17.

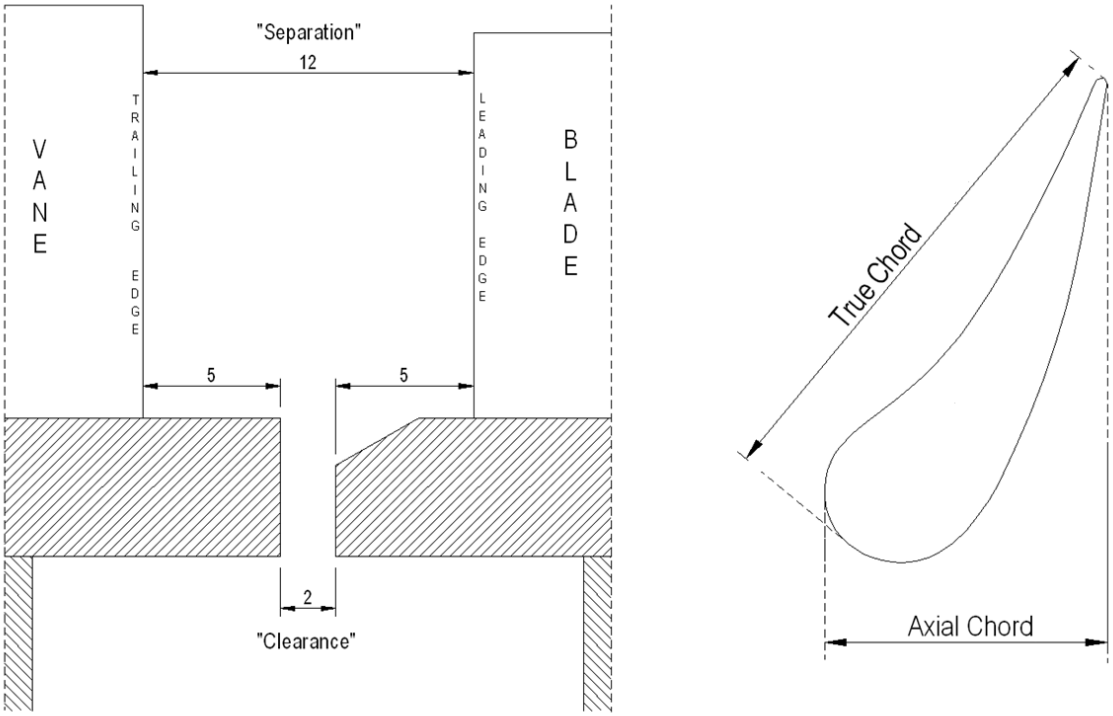

Figure 4.16 Vane and blade nomenclature

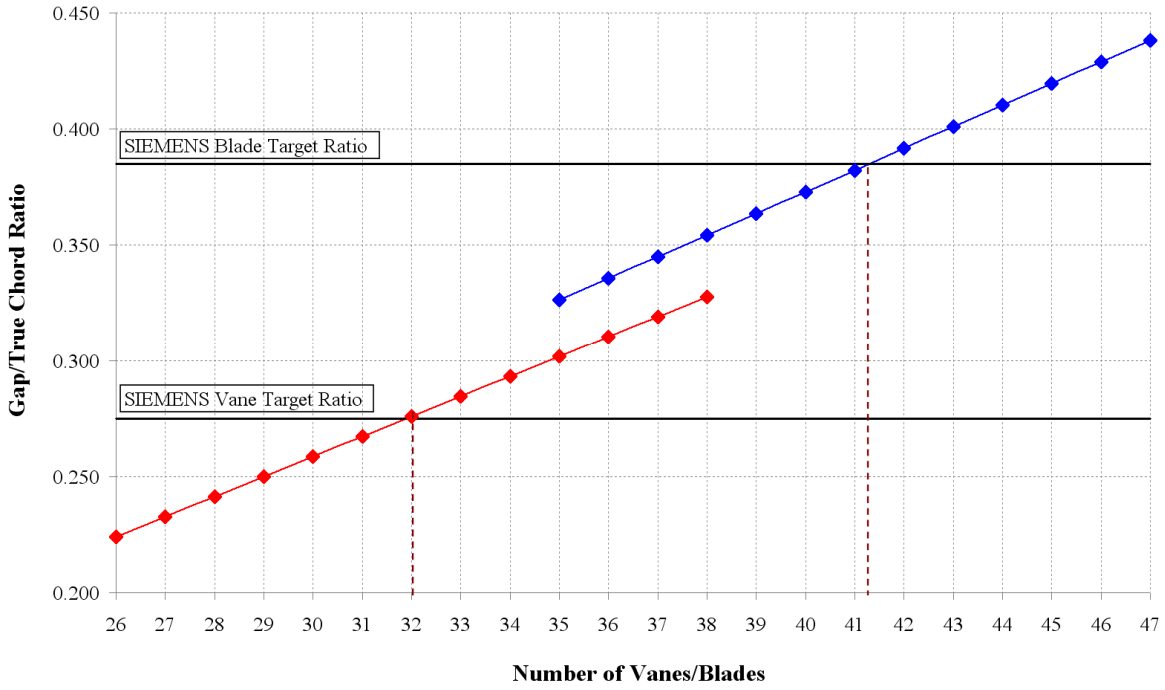

Figure 4.17 Effect of number of vanes and blades upon gap to true-chord ratio (Vane #'s in red, blade #'s in blue)

The engine representative ratios were 0.275 and 0.385 for the vanes and blades, respectively. Matching these ratios suggested that the rig should model 32 vanes and 41 blades. The 41 blade number is preferential as a prime number of blades reduces the likelihood of hitting resonant frequencies when in operation. Using the pitch to chord ratios supplied by Siemens, the true chords of the vane and blades were then calculated to be 43.51 mm and 31.39 mm, respectively.

4.3.2 Material selection for the vanes and blades

The vanes and blades were fabricated from a nylon based polymer, with each component being laser sintered by means of rapid-prototyping. The lightweight nature of nylon is beneficial, as well as it's insulating properties effectively eliminating experimental heat transfer issues. The components were each joined to the platform with a pair of M2 screws located in tapped holes underneath each unit.

Structural tests were conducted to look at the tensile failure of the restraining screws, as well as their fatigue properties. The equivalent weight of both the screws and blades were calculated for the maximum possible 6000 rpm rotational case. The centrifugal force under rotation (F) for an average blade weight of 1.14 g was estimated using Eq. 4.6 and was calculated as 8.93

kgf per blade. Upon taking an average 0.25 g mass for each screw, a blade and pair of screws produced a centrifugal force totalling 12.84 kgf per unit assembly.

$$F = \frac{m\Omega^2 r}{g} \qquad \text{(Equation 4.6)}$$

where:
- m is the stationary mass
- Ω is the angular speed of the disc
- g is the gravitational constant
- r is the radius of attachment

An aluminium specimen was produced featuring a pair of tapped M2 screws, which were failed under pure tension in an Instron machine. Figure 4.18 shows that the screws did not fail until a load of approximately 50 kgf, a safety factor of four.

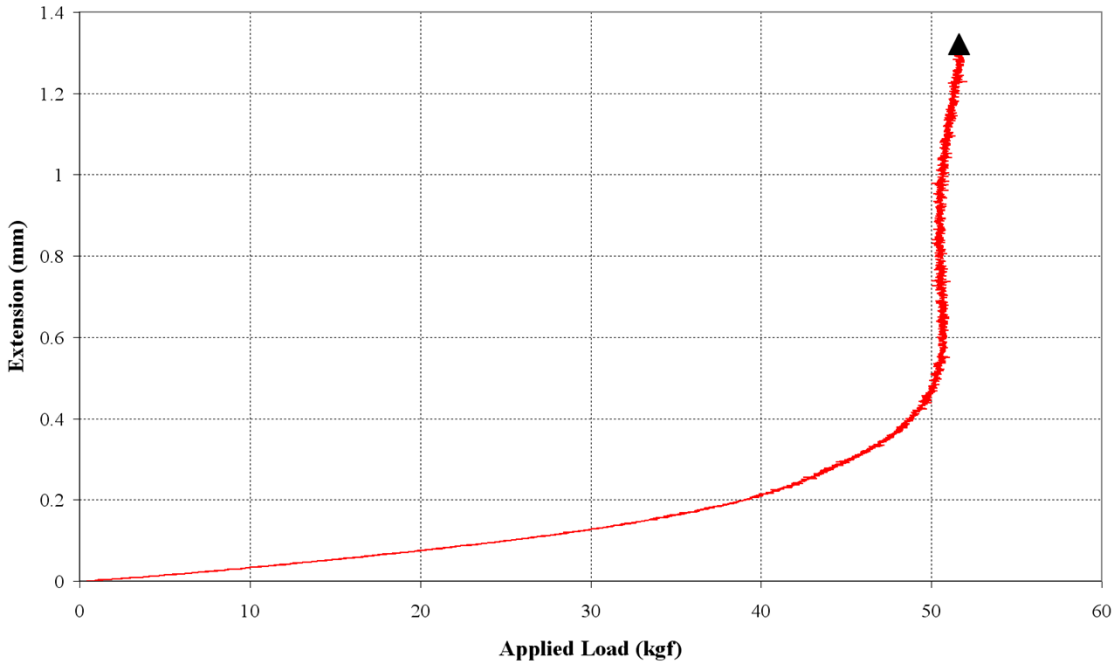

Figure 4.18 Tensile failure of blade attachment screws

A second sample was tested for low-cycle fatigue failure at the 12.84 kgf calculated load. The screws held firm up until the experiment ended at 20,000 cycles, at which point no further cycles were deemed neccessary. It was concluded from the two material tests that the validity of the nylon blade attachment procedure was a safe and practical process.

When assembling the rotor, 100 blades were manufactured and weighed. The weight distribution was shown to have a mean of 1.14 grams (Fig. 4.19), with the 41 blades of least deviation chosen for rotor attachment.

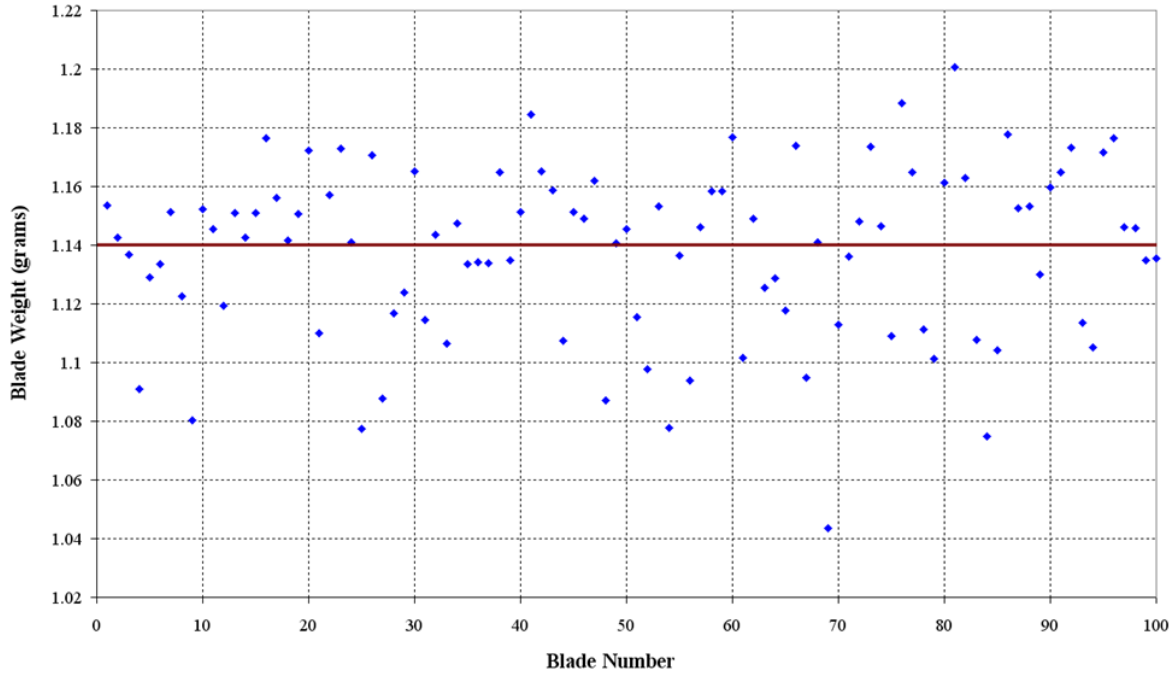

Figure 4.19 Blade weight distribution

4.3.3 Physical modelling of vane and blades

The vane and blades were modelled in order to be exported via parasolid documents for rapid-prototyping. Figure 4.20 shows the vane and blade set-up modelled in three dimensions. The vanes bridged the entire 10 mm annulus height, however the blades were 9.5 mm in height to allow for a tip clearance to the rotor housing.

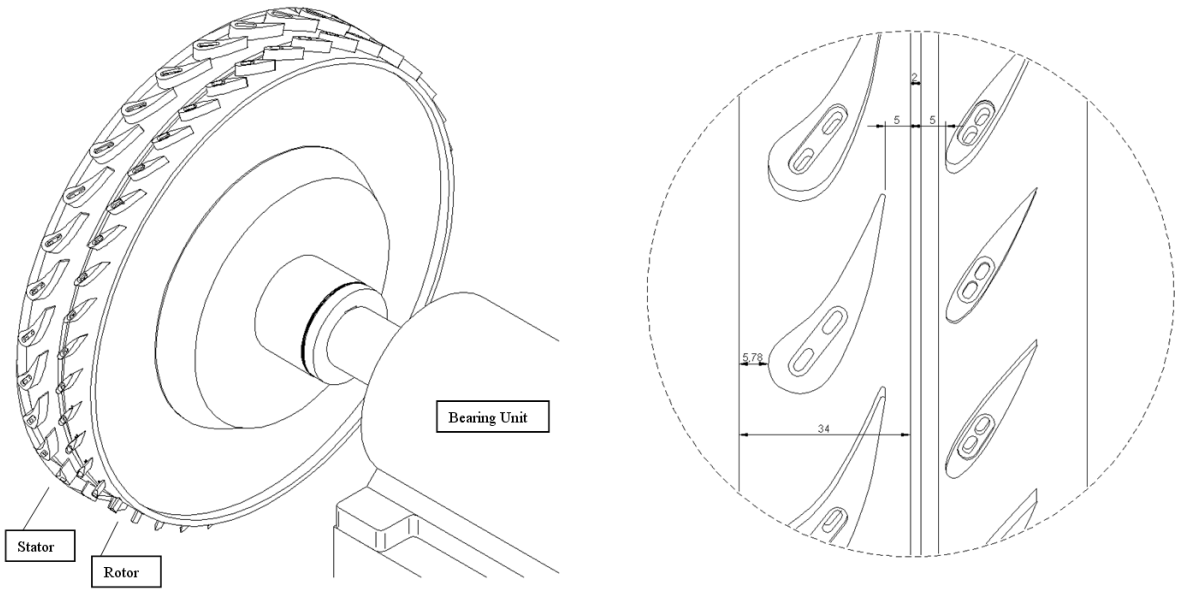

Figure 4.20 Vane and blade models attached to rotor-stator section

A selection of photographs of the facility development are compiled as Appendix.D, including views of the vane and blade geometries.

One final concern with the vane and blade design was that of the annulus height that they were to be contained in. With the annulus height set at 10 mm, it was deemed necessary to investigate any potential problems this would have on the blockage factor associated with the boundary layer composition in the annulus. In order to model the boundary layers, the annulus was treated as a pair of adjacent flat plates, on which equally developed turbulent boundary layers would grow. The length of the plates were taken to be the estimated curve-linear length of the vane channel (52 mm) and the free-stream velocity was taken to be the vane exit velocity (C_2).The seventh power law for turbulent boundary layer thickness was used, along with an estimate for displacement thickness, δ^* (White (1994)). The boundary layer analysis was conducted for all design points, however as expected, the 2000 rpm case with a lower flow-rate produced a thicker boundary layer.

The ratio of the boundary layer thicknesses compared to the annulus area is termed the *blockage factor* and defined in Eq. 4.7. The extent of the expected blockage factor determined how much of the ingestion would come from inside the boundary layer flow and not from the annulus flow-path.

$$Blockage\ Factor\ = \frac{(2\delta^*)}{h} \qquad \text{(Equation 4.7)}$$

where:
- δ^* is the displacement thickness of the boundary layer
- h is the annulus height
- "$2x$" is due to the boundary layer occurring on either side of the annulus

The blockage factor for the 2000 rpm case was found to be 3.47%, which was felt to be an acceptable value. It is therefore suggested that a substantial amount of the mainstream gas ingestion would in fact come from the mainstream flow and not all from the boundary layer as was the concern.

4.4 Design of a collecting system

In order to use the high flow quantities of heated air desirable for the HMA, a substantial collecting system was designed to transition the exit flow from the mainstream annulus into a three-inch pipe that exited the laboratory. The design was based on a linearly expanding volute, which also acted to regain some of the pressure drop across the vanes and blades. The expansion

was implemented into the radial plane to ensure sufficient optical access still existed for TLC research on the rotor disc. At the same time, enough strength was built into the system to allow for the pressure at the working section to be backed up to atmospheric conditions if necessary. This would minimise any sideways pressure loading on the rotor disc at running conditions and would be achieved by backing up the flow pressure with the use of an electronically controlled pneumatic actuator valve. The volute was fabricated from Nylon via a rapid-prototype procedure, and built from linearly expanding cross-sections. Four 90° sections were designed with mating flanges at each end, with an exit transition leading to a 3" exit pipe from the largest quarter.

The main difficulty associated with positioning the volute was ensuring unobstructed optical access for the TLC research. The linear volume expansion existed radially, away from the optical disc area. The complete concept is shown in Fig. 4.21.

Rotor displacement due to the difference in pressure between the wheel-space (p_1) and outside the rig (p_{atm}) was to be avoided as it would affect the running clearances. To avoid relatively large displacements of the rotor disc, it was desirable to ensure that p_1 was as close to p_{atm} as possible. A computer controlled actuator valve was located on the volute exit pipe, with a static pressure point taken at p_2 to provide positive feedback.

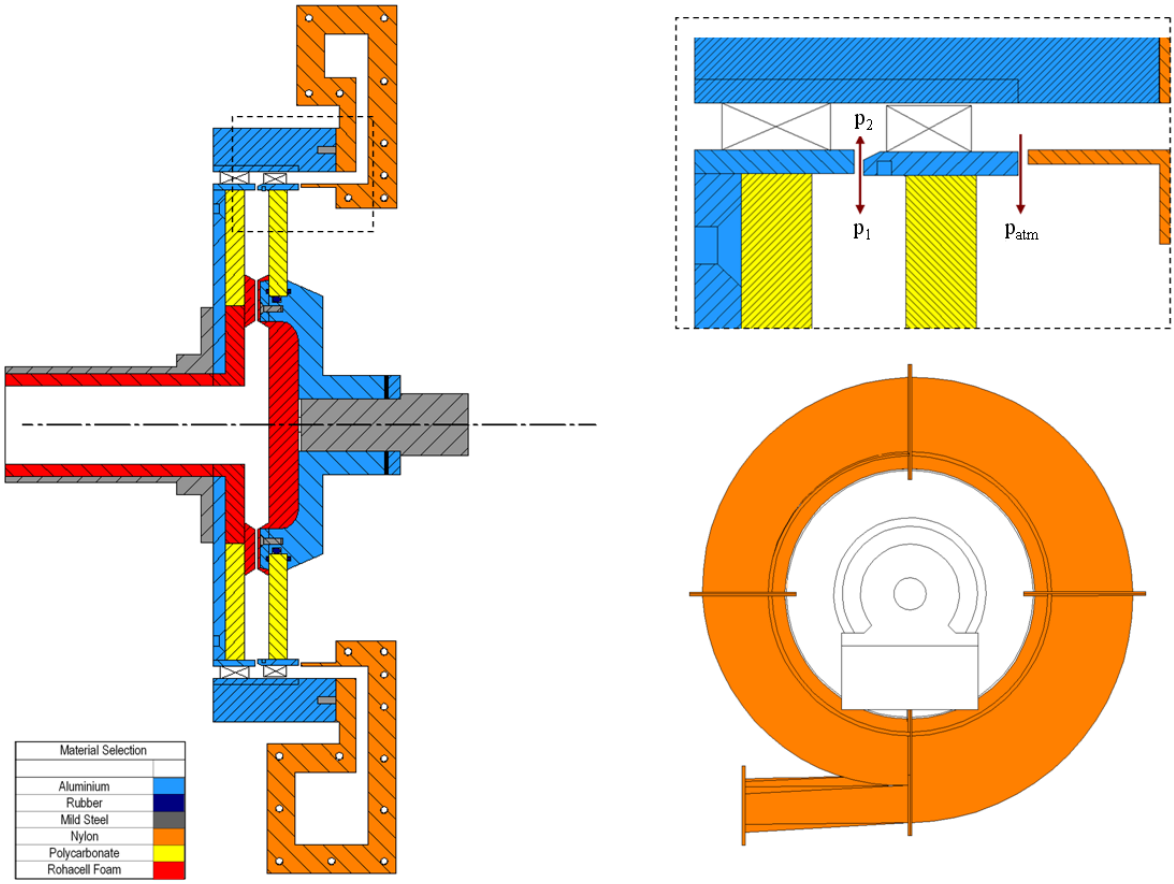

Figure 4.21 Volute location and linear expansion concept

4.4.1 Ensuring optical access to the working section

To allow the use of TLC inside the wheel-space, it was essential that the viewing characteristics be acceptable. A split section view allowed the optical viewing angles to be acquired. Figure 4.22 shows this section with the corresponding strobe angle available to the rotor disc (at the disc mid-radius height). It is apparent that the volute flanges have been overlooked as they appear only at 90 degree locations and therefore do not affect viewing angles.

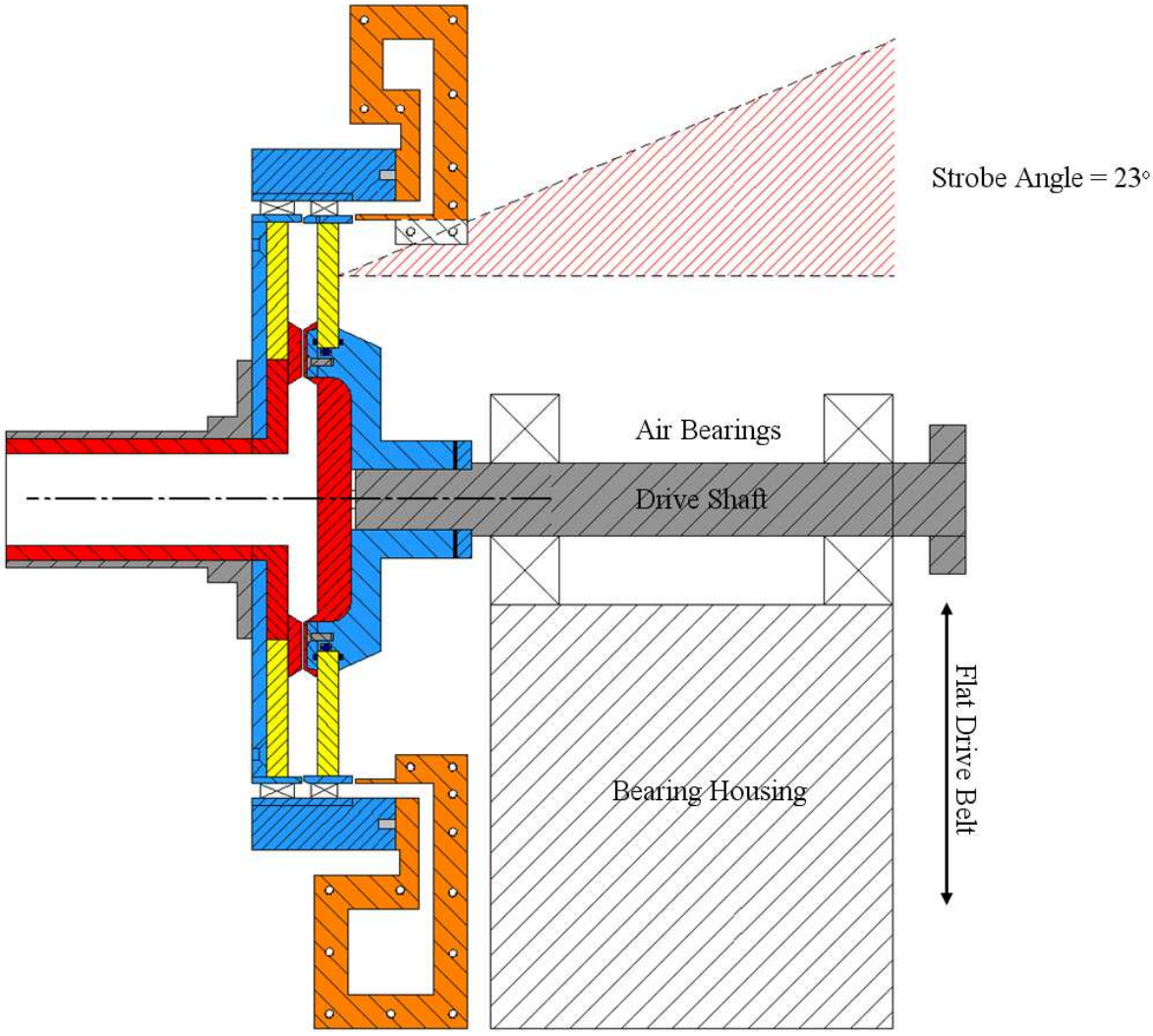

Figure 4.22 Optical access angles and location of rotor-stator assembly

From knowledge gained from a previous pre-swirl rig at the University of Bath (Kakade *et al.* (2011)), the optimum strobe-lighting angle is 20-30°, rendering an angle of 23° perfectly adequate.

4.4.2 Locating the rig and volute collector

Extensive consideration was given to the location of the volute in respect to mounting the rig. The largest part of the volute was located at floor level so that the pipe-work could be taken out easily on the base of the laboratory. The proposed location of the rig and volute is shown in Fig. 4.22, with the rotor hub connected to an air-cooled bearing unit atop an immovable base plate. The volute was fixed to an aluminium housing annulus surrounding the vanes and blades. The drive shaft protruded through the bearing unit and was connected to an electric motor mounted underneath the base-plate via a flat belt. Figure 4.22 shows that no reduction in optical access was caused by the bearing attachment, and that due to the bearing sizing, the whole rig and bearing unit were attached to a level base-plate below it.

In order to ensure safe operation of the rig, a safety guard was designed and enclosed the full working section and volute so as, in the unlikely event of a failure, any debris would be contained. The guard was fabricated from 5 mm plate steel, with a schematic layout and the installed unit shown as Fig. 4.23.

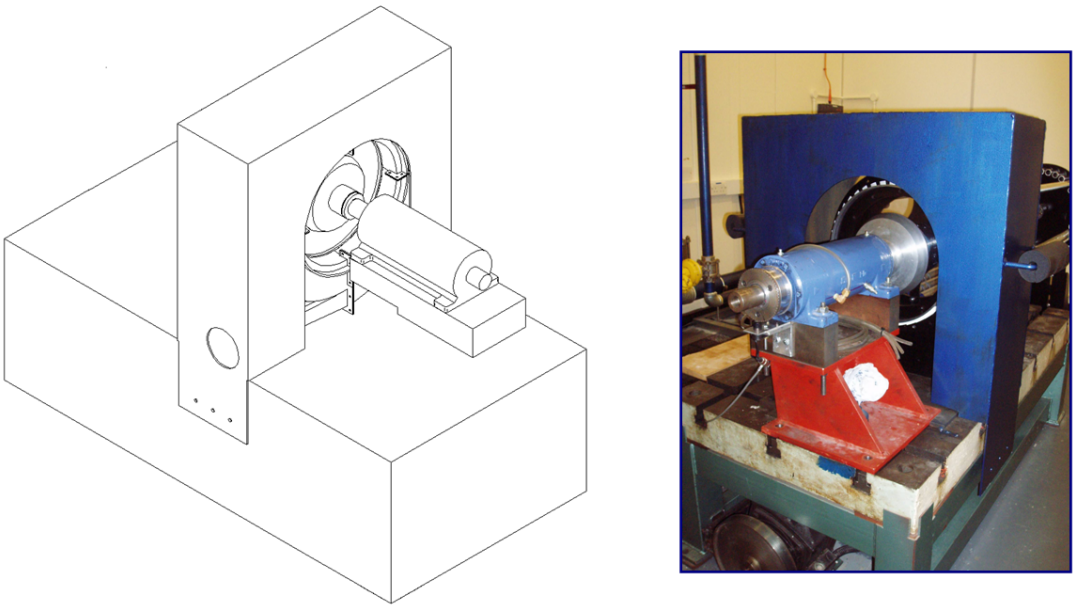

Figure 4.23 Safety guard to enclose volute and working section

4.5 Design of HMA and CMA feed systems

The following section outlines the individual component design upstream of the rotor-stator section. As discussed in Section 4.1, an HMA configuration featured a heated external flow,

whereas an alternate CMA featured a simpler feed system without the need for heated flow. These configurations will be considered in Sections 4.5.1-2.

4.5.1 Hot mainstream annulus (HMA)

The HMA configuration featured four quarter sections feeding the mainstream annulus. This minimised the flow-rates through each heater, which could cause bowing of the meshes. Four inlet diffusers passed air through four mesh heaters, from which the sections converged into a quarter-annular slot. These complex material geometries were one of the main reasons behind using a simpler CMA configuration for the first experimental program when heated external flows were not required. To aid onward discussion of the HMA, a schematic key is included as Fig. 4.24.

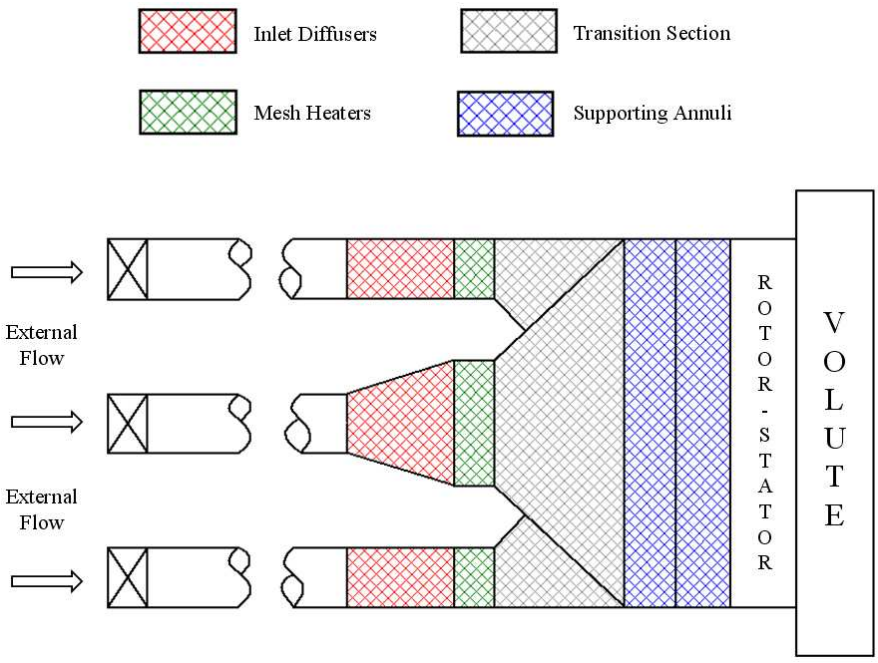

Figure 4.24 Component key for HMA configuration

4.5.1.1 Mesh heater design

In order to provide the step change in temperature required for the transient heat transfer technique set out in Section.2.6, four mesh heaters were required along the external flow paths. Each heated a quarter of the total external flow. Design calculations were conducted using Ireland *et al.* (1996) for a mesh heater design using a warp and weft wire arrangement, held between two brass terminal bars. The heating unit was housed in a Tufnol insulating frame and installed over the

desired flow path. A current was passed through the heater for a limited period with the heat produced being transferred from the wires to the air-flow, providing a step change in air temperature. The heaters tailored for this rig design were based on a maximum known flow velocity from the previously existing pre-swirl rig of Kakade *et al.* (2011).

The external mesh heaters were sized, based on the balanced velocity triangles for the maximum 6000 rpm motor speed. By following the process described in Section 4.1.1, it can be shown that the balanced external flow rate at 6000 rpm is 1.1 kg/s. The mesh heater design calculations based on Ireland *et al.* (1996) are compiled as Appendix C, with a summary given as Table. 4.4.

Mesh Heater Design Parameter	**Calculated Value**
Mesh Dimensions	120 mm x 112 mm
Power Required for 50^{o}C Temperature Rise	55.0 kW
Power Required from each Heater	13.8 kW
Mesh Resistance	0.0643 Ω
Current Supply Required	463 Amps

Table 4.4 Mesh heater design parameters

A 500 amp source was required for each of the heater units. The mesh heaters were modelled as shown in Fig. 4.25.

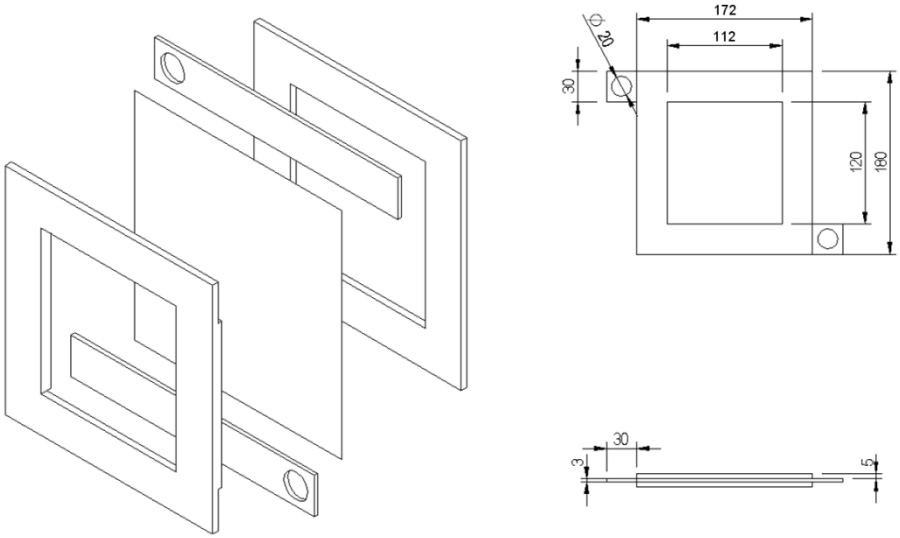

Figure 4.25 Mesh heater geometry

4.5.1.2 Transition section design

The transition section provided connection between the four rectangular mesh heaters and the annulus required for input to the mainstream annulus (see Fig. 4.24). This complex section was designed from mild sheet steel and insulated with 5 mm Rohacell lining. As it was imperative that the section not induce flow separation, the use of an unorthodox geometry was required.

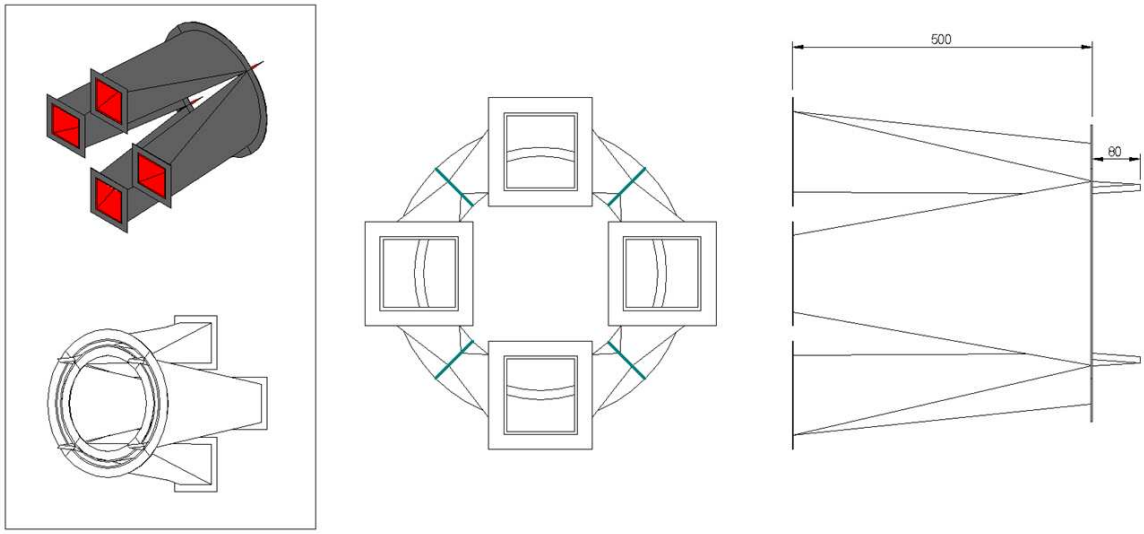

Figure 4.26 Mesh heater to annular transition geometry

The unit was manufactured from four individual rectangular to quarter-annular sections and then welded into the complete *transition unit*. Flanges were included at both ends of the section to allow joining with the annulus at one end and the heater frames at the other. Figure 4.26 shows the geometric proposal for the individual quarter annulus components.

In order for flow separation to be prevented, the combined diffusing angle must generally be less or equal to 10^{o} for a standard diffuser. In this unorthodox section, the combined diffusing angle was approximately 16^{o}, however the section featured both an expansion and contraction in perpendicular planes. The issue of flow separation was therefore avoided as the accelerating flow caused by the contraction was sufficient to keep the flow attached in the expansion plane. The section dimensions were calculated from basic trigonometry, with the radial geometry mirroring that of the rotor-stator section for onward connection.

It is apparent in Fig. 4.26 that Rohacell "spikes" were included and located over the welded joints in order to promote smooth flow transition over these anomalous regions. These spikes were housed in attached annuli; themselves in addition sandwiching a gauze to smooth any remaining flow discrepancies and promote concentricity of the flow path.

4.5.1.3 Complete HMA configuration

The rig design in its HMA configuration is shown as isometric, exploded and flow-path schematics as Figs 4.27, 4.28 and 4.29, respectively.

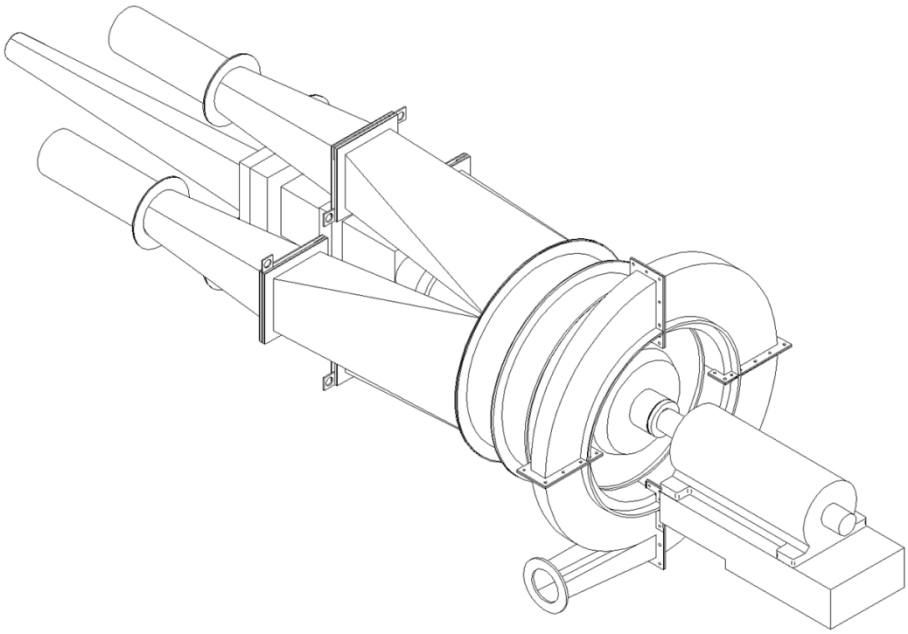

Figure 4.27 Isometric view of HMA configuration

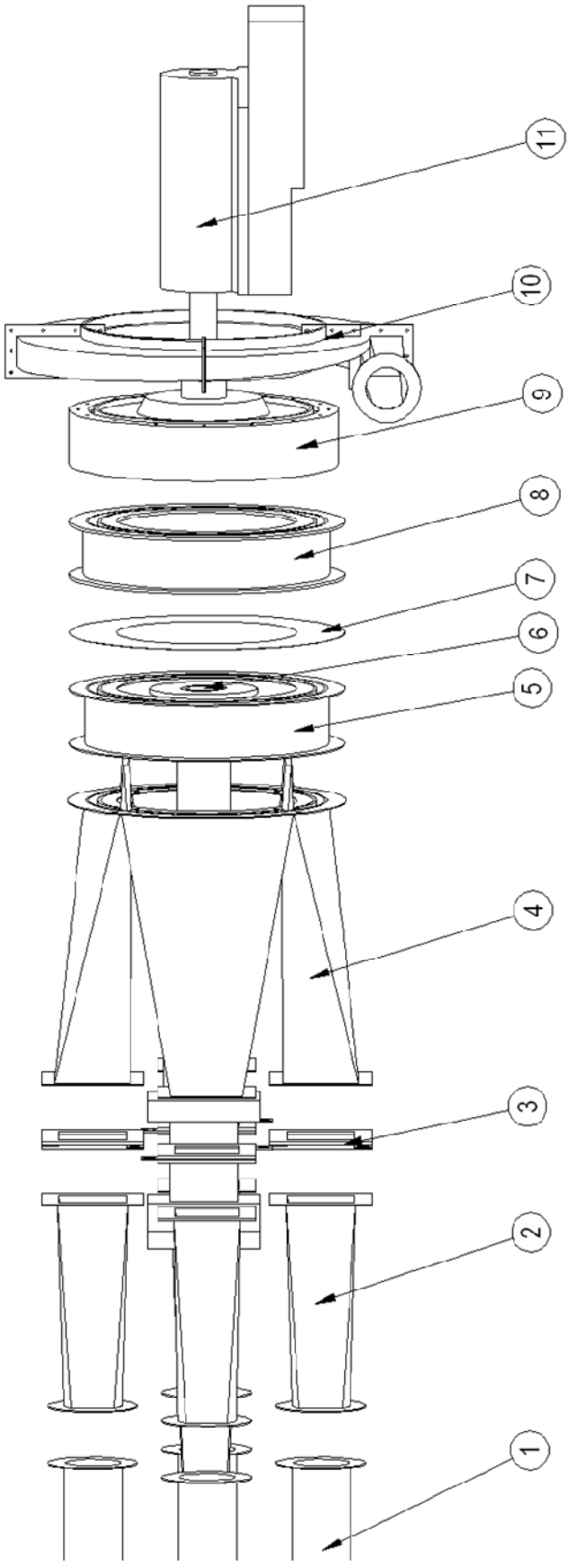

HMA Rig Components	
(Component Number)	Component Description
(1)	Inlet Pipes
(2)	Diffuser Sections
(3)	Mesh Heaters
(4)	Annular Transition
(5)	Annulus A
(6)	Sealant Flow Pipes
(7)	Gauze
(8)	Annulus B
(9)	Housing Annulus
(10)	Volute
(11)	Bearing Unit

Figure 4.28 Exploded component model of HMA configuration

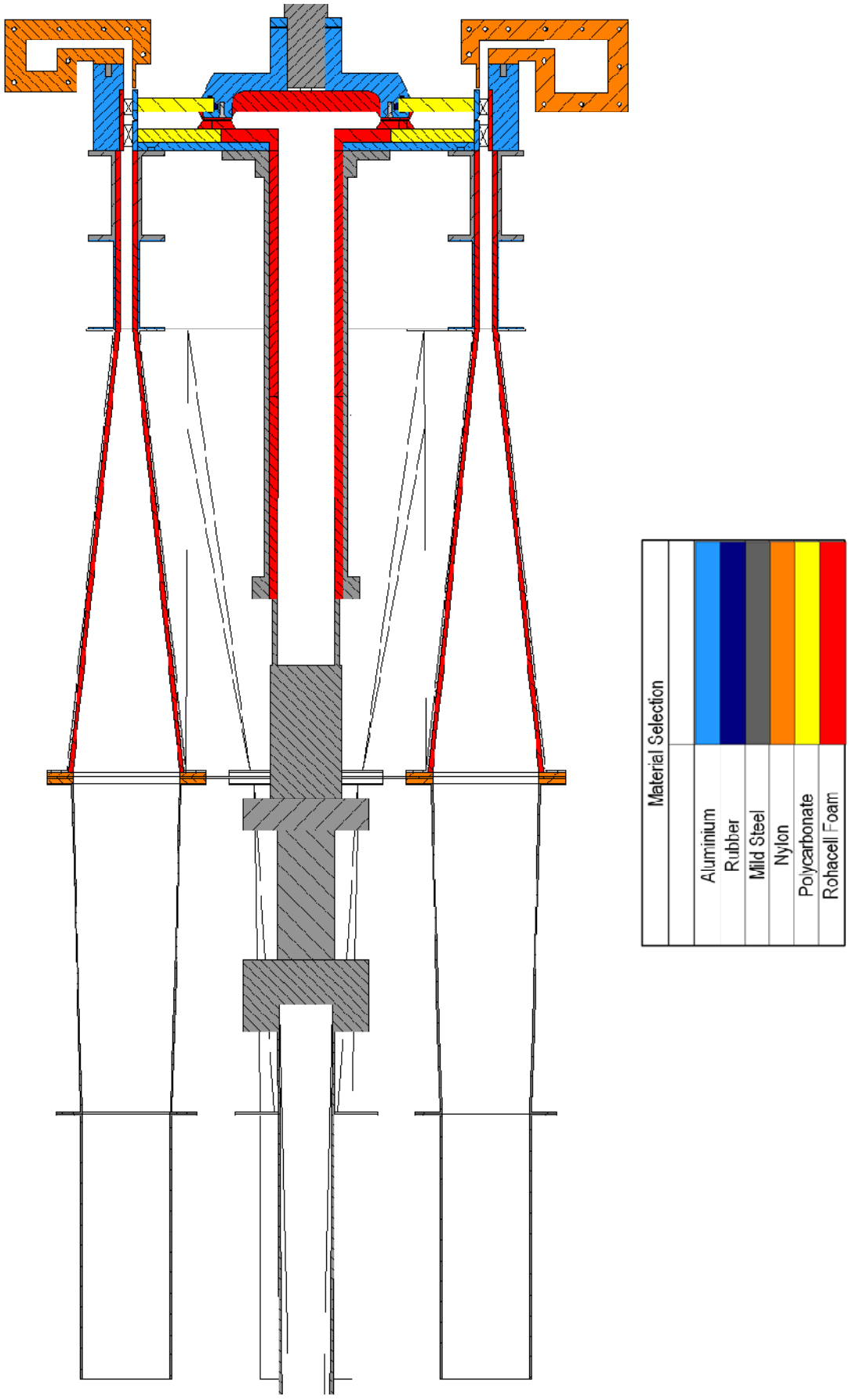

Figure 4.29 Flow-path section view of HMA configuration

4.5.2 Cold mainstream annulus (CMA)

The CMA featured thirty-two inlet pipes feeding individual vanes inside the mainstream annulus. The laboratory air was supplied through a coaxial pipe that contained a 2" pipe flowing through the centre and feeding the sealant flow, and a 4" external pipe around it supplying the mainstream flow. The mainstream flow was fed into a radial diffuser and expanded radially outward to feed the thirty-two feed pipes. At the downstream end of the thirty-two feed pipes, a simple contracting transition piece connected to the 10 mm mainstream annulus. No mesh heaters were required for this design and hence no external power-supply either, allowing for the CMA configuration to be fabricated in a lesser time period - beneficial in commissioning the rig on schedule. A schematic key is included as Fig. 4.30 from which to aid onward discussion.

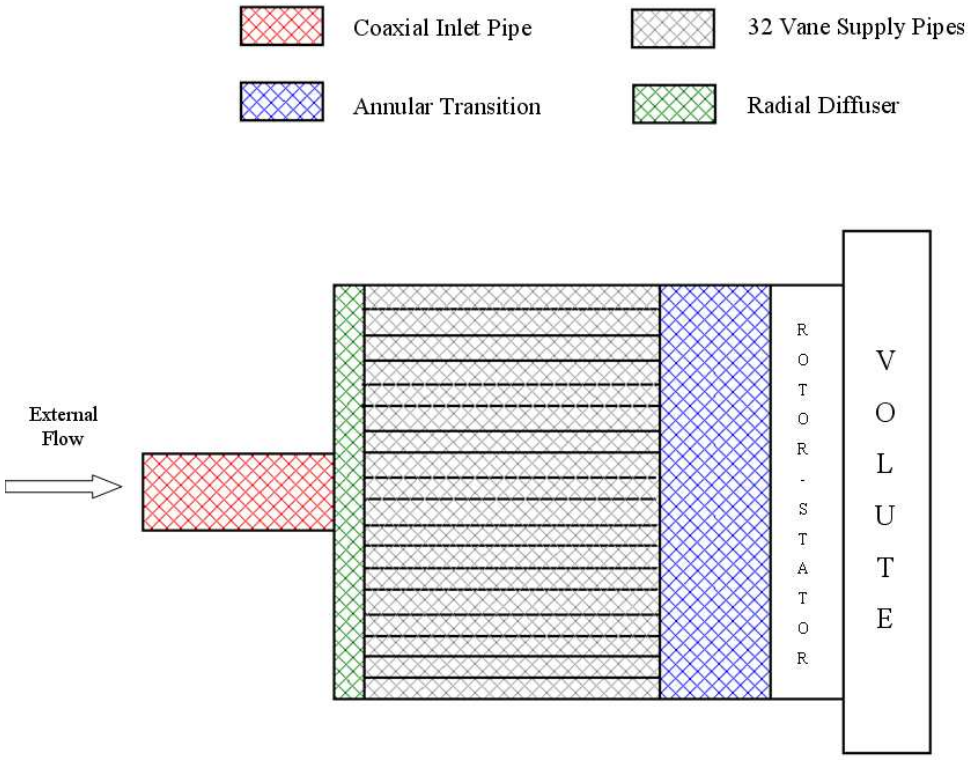

Figure 4.30 Component key for CMA configuration

4.5.2.1 Radial diffuser and inlet pipes

The radial diffuser consisted of two parallel steel plates at a 15 mm separation from each other, with a ring welded around the two to form an enclosed space (Fig. 4.31). The coaxial inlet pipe was flanged on to the centre of the diffuser back-face and provided flow which was turned 90 degrees radially outwards on contact with the front wall. The flow expanded radially outward and

was collected into 32 equally spaced stub pipes. The pressure axisymmetry was ensured by measuring 16 static pressures around the circumference in-line with alternate exit pipes.

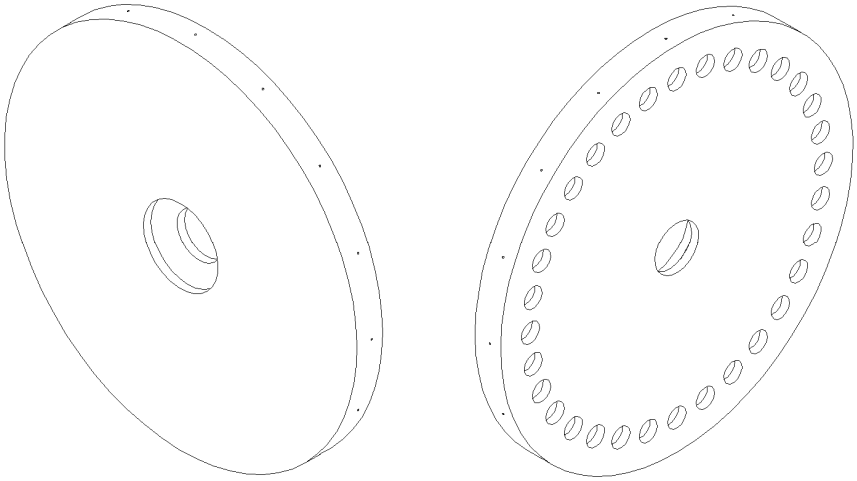

Figure 4.31 Radial diffuser geometry

The stub pipes leaving the radial diffuser were connected to corresponding stub pipes on the downstream annular transition section via 1.7 m long aluminium pipes. The pipes were connected to each stub pipe via a hosing sleeve located by two jubilee clips. This was desirable in order to have removable piping, allowing access to the instrumentation behind the stator. The annular transition section received all 32 pipes and contracted to form a 10 mm annulus which flanged directly on to the rotor-stator section. The annular transition section is shown as Fig. 4.32. The pipe connection process is shown in Fig. 4.33, where the section view is taken through the radial diffuser.

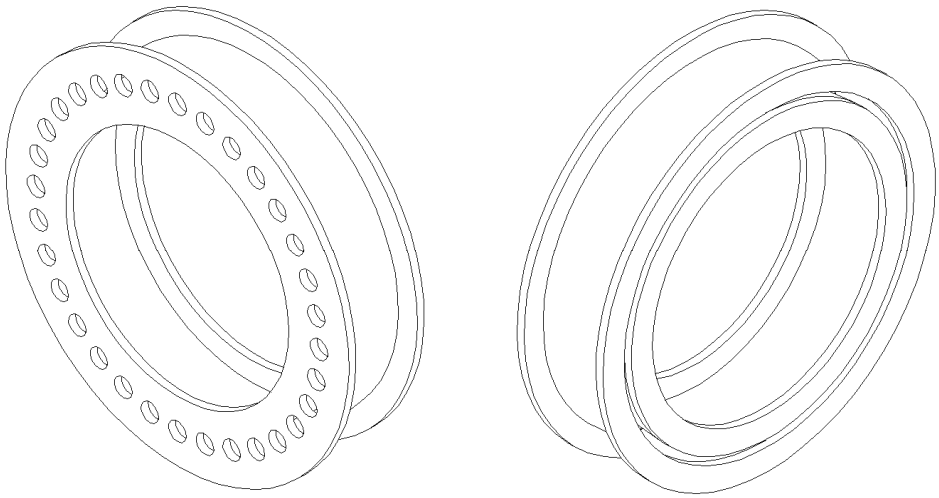

Figure 4.32 Transition section from 32 inlet pipes to working annulus

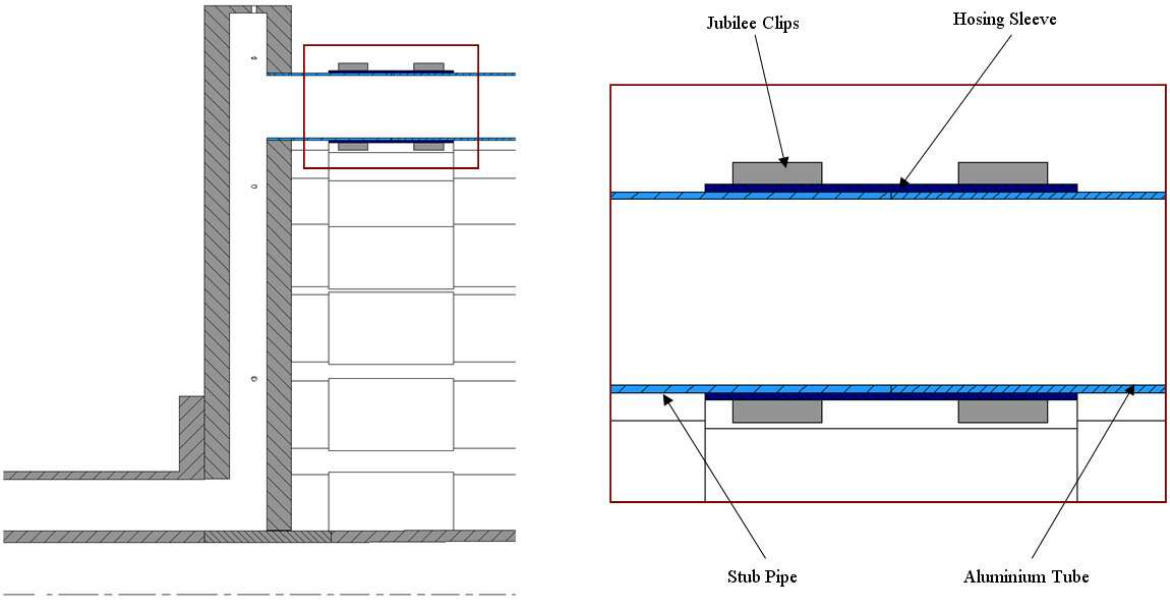

Figure 4.33 CMA inlet pipe attachment process

4.5.2.2 Complete CMA configuration

The rig design in its CMA configuration is shown as isometric, exploded and flow-path schematics as Figs 4.34, 4.35 and 4.36, respectively.

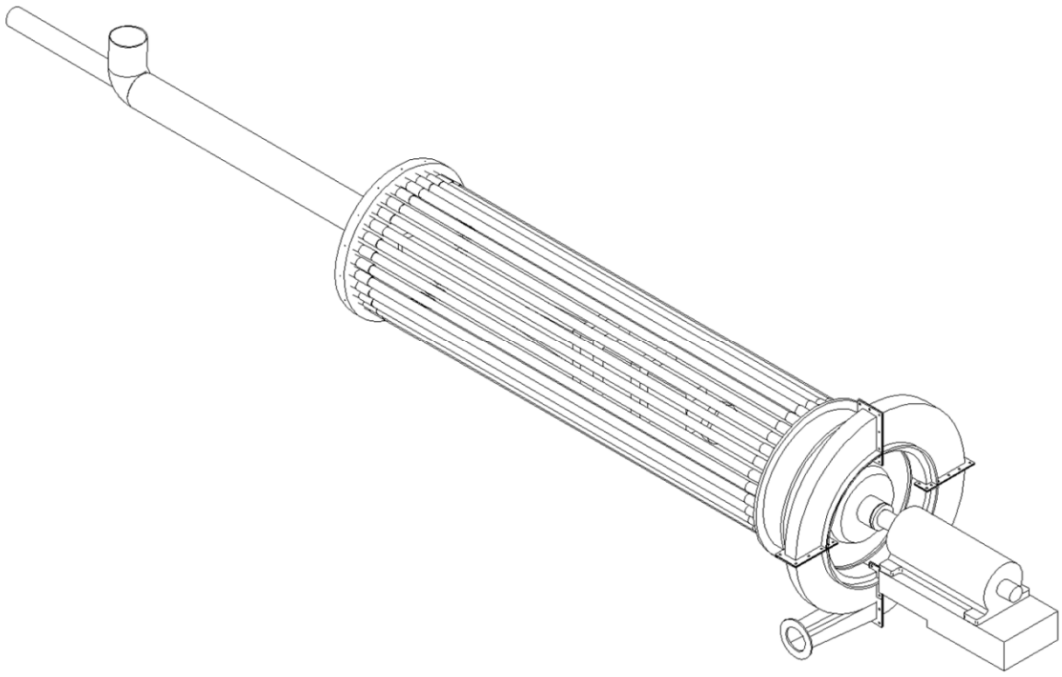

Figure 4.34 Isometric view of CMA configuration

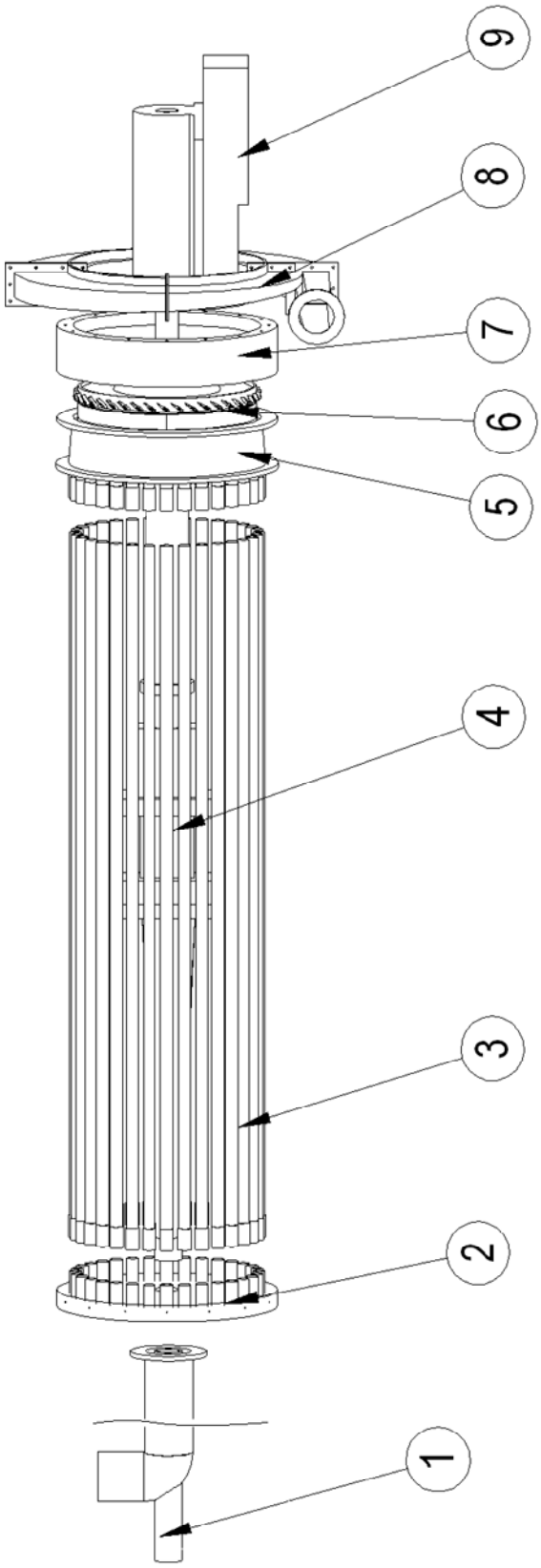

CMA Rig Components	
(Component Number)	Component Description
(1)	Coaxial Inlet Pipe
(2)	Radial Diffuser
(3)	32 Inlet Pipes
(4)	Central Flow Pipe
(5)	Annular Transition
(6)	Rotor-Stator Section
(7)	Housing Annulus
(8)	Volute
(9)	Bearing Unit

Figure 4.35 Exploded component model of CMA configuration

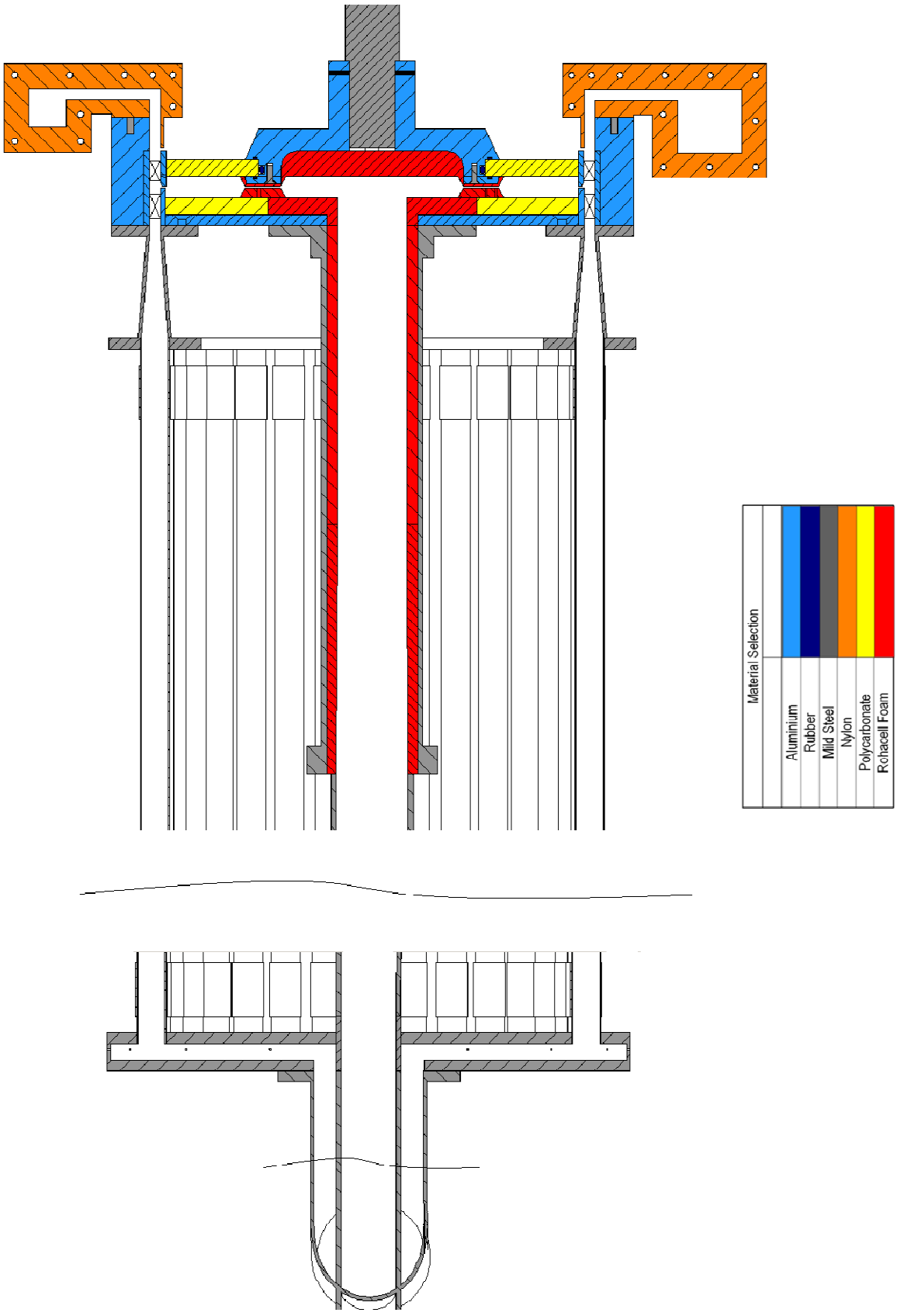

Figure 4.36 Flow-path section view of CMA configuration

4.6 Interchangeable rim-seals

In order to investigate the performance of different seal geometries, a modular method of changing the rim-seal inserts was required. A set of eight tapped M3 holes were designed into the underside of the rotor platform to locate any seal attachments, whereas a temporary adhesive bond was used for any stator attachments. A combination of either, or both, inserts was therefore viable to create rim seal configurations at the wheel-space periphery.

4.6.1 Generic seal geometries

The datum case was an axial clearance seal, where the rotor and stator platforms formed either side of the seal. This created the simplest geometry, forming a baseline against which other generic seals could be compared. The axial clearance seal is shown along with salient dimensions as Fig. 4.37.

From the datum case, three additional generic seals were developed, modelling simplified geometries often found in current engine designs. It was hoped that these generic seals would aid in understanding the fluid dynamics occurring inside the wheel-space using publishable and non-specific geometries, whilst being supported by the orifice model described in Chapter 3. Experience regarding the physical use of the theoretical model was to be developed, so that when Siemens' company proprietary seals were tested, more time could be dedicated to understanding the performance of the seals and not on the fundamentals.

The further generic seals featured a simple radial lip seal, a radial-axial combination and a double axial seal, referred to as Generics 2, 3 and 4, respectively. Generic seals 3 and 4 are double seal variants, where two separate clearances form an intermediate annulus between them. The proposed generic seal designs exhibited a range of seal clearance combinations and allowed for a comprehensive study and seal ranking procedure to occur. All four generic seals that formed the experimental programme detailed in this thesis are shown schematically as Fig. 4.37.

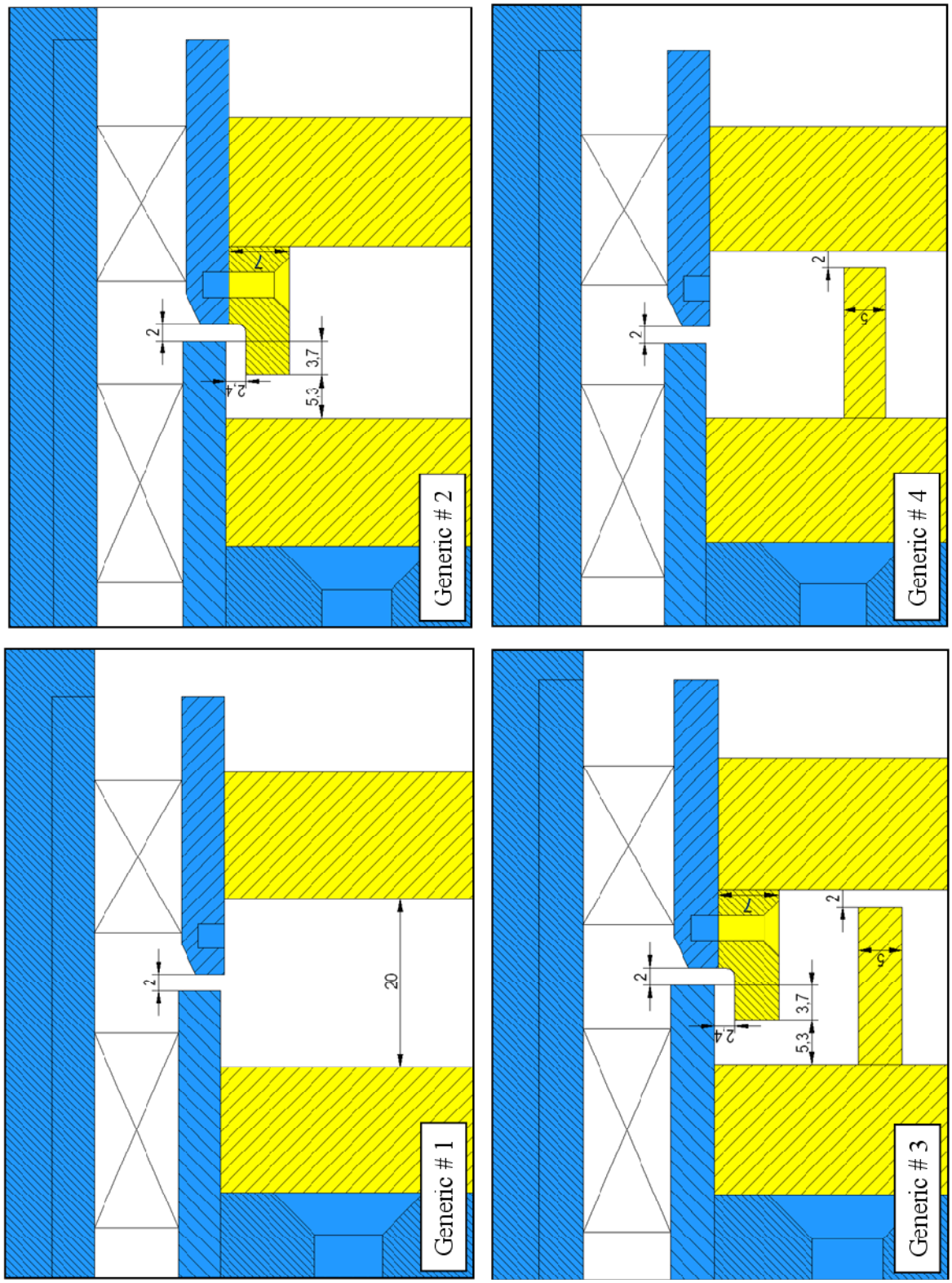

Figure 4.37 Generic seal configurations (Aluminium is shown in blue, polycarbonate is shown in yellow)

4.6.2 Siemens' exotic seal geometries

Siemens will propose a series of company proprietary seals which it considers to be beneficial over the generic concepts, developed with knowledge acquired over the experimental programme discussed in this thesis. The company wishes to quantify performance in order to assess whether the new, and more complex, geometries are cost-effective ways of improving its secondary air systems design for use in future engines.

4.7 Instrumentation and control

A suitable instrumentation layout was imperative to ensure available and accessible measurement locations. In this section, TLC position and all other additional instrumentation will be described in terms of its selection, function and location for both the concentration work described in this thesis and the future heat transfer studies. The control logic and computer software used to control the rig will also be discussed.

4.7.1 Wheel-space instrumentation

The majority of instrumentation was located inside the rotor-stator wheel-space and will now be described, assigned a number and its position shown schematically on a stator disc plan-view in Fig. 4.38.

① Static pressure tapings were taken through the stator casing to record the radial static pressure distribution inside the wheel-space. These were set at particular radial locations (with an emphasis on the outermost positions), with the tapings being connected via polyurethane tubing to a Scani-valve and calibrated pressure transducer.

② Total pressure probes were used in-line with alternate radial static pressure taps to allow for measurements of tangential velocity to be acquired inside the wheel-space.

③ Static pressure taps were included at an angular phase shift to the main radial line of pressure taps to check effects of the vane periodicity (plus a quarter phase).

④ Static pressure taps were included at an angular phase shift to the main radial line of pressure taps to check effects of the vane periodicity (minus a quarter phase).

⑤ Concentration probes were located inside the wheel-space. Carbon dioxide was injected into the sealant flow, at which point if ingress occured, a dilution in concentration would be traceable. A gas analyser measured the CO_2 concentration in parts per million and gave an indication of the amount of ingress occurring.

⑥ Fast-response thermocouple probes were used to acquire additional temperature data with which to complement the TLC results. The thermocouples were built in-house with 10 micron wire beads fitted inside a ceramic head.

⑦ Segments of the rotating and stationary discs were coated with TLC. The coated polycarbonate stator disc allowed for measurement of stationary adiabatic-wall temperatures, whereas the rotor disc coating yielded adiabatic-wall temperatures for the rotating surfaces. The crystal data produced two-dimensional thermal effectiveness maps.

⑧ A second TLC segment.

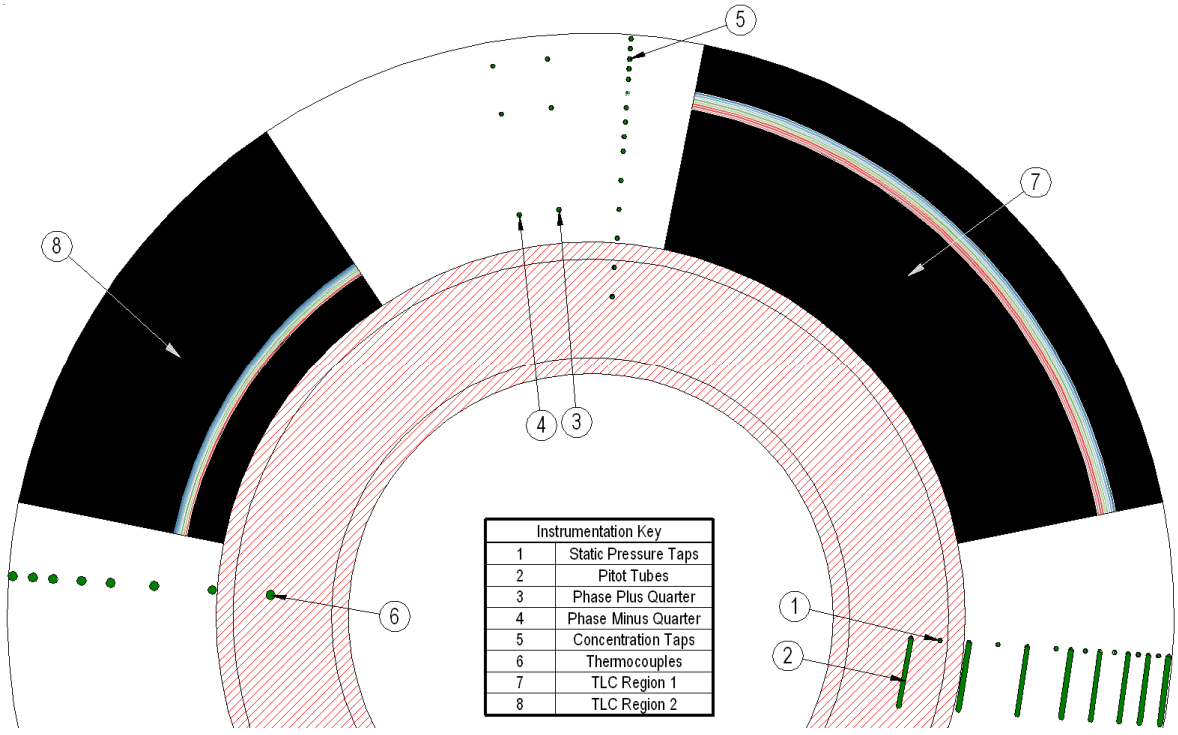

Figure 4.38 Wheel-space instrumentation key

All pressure and concentration taps were fabricated from 1.65 OD hypodermic tubing and fitted flush with the stator disc surface. Scani-valve units were fastened to the side of the rig's bed-plate and acted to step through each pressure reading for connection to a pressure transducer. The concentration taps were read by a duel channel infra-red absorption gas analyser.

Although not part of the experimental programme discussed in this thesis, consideration was given nonetheless to the heat transfer instrumentation. TLC measurements were taken using

Hallcrest crystals of two bands: a 30 degree and 40 degree crystal. The crystals were applied to both the stator and rotor faces.

4.7.1.1 Universal instrumentation for all seal configurations

The generic seal concepts (Section. 4.6.1) required the use of a stator attachment. It was therefore necessary to ensure that a universal instrumentation layout existed that had sufficient unobstructed components when the seal insert was attached. The stator attachment from Generic seals 3 and 4 was overlaid to show the universal nature of the arrangement, where the insert (shown in blue) slots in between key instrumentation. A stator overlay (in plan-view) for the seal attachment in question is shown as Fig. 4.39, with inactive instrumentation highlighted in block red.

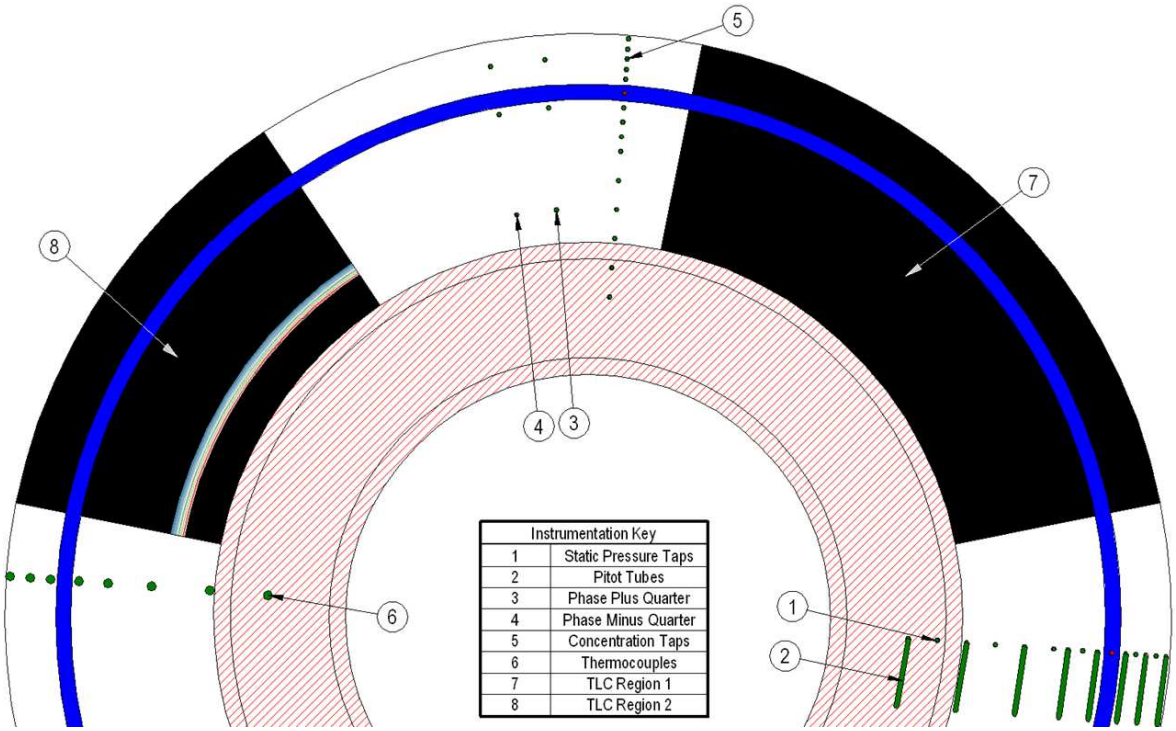

Figure 4.39 Active wheel-space instrumentation with stator attachment

4.7.2 Working annulus instrumentation

Key to determining externally-induced ingress is measurement of the non-dimensional pressure difference in the external annulus. The local mass flux between the annulus and wheel-space is determined by the local difference between the pressure in the wheel-space (p_1) and the corresponding pressure in the external annulus (p_2). The pressure in the external annulus is known to vary circumferentially with a non-axisymmetric pressure distribution; causing areas of ingress and areas of egress (Fig. 4.40). The "local" pressures were therefore required over a vane pitch in order to capture this '*driving potential*' for ingress to occur.

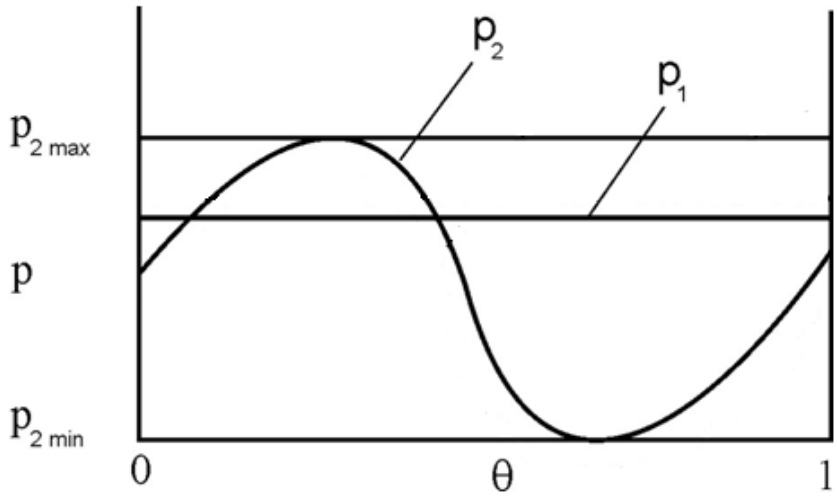

Figure 4.40 Non-axisymmetric pressure distribution in the external flow annulus, shown as a function of position over a vane pitch

The non-dimensional pressure difference (ΔC_p) is defined in Eq. 3.19, and had to be measured on the ingress rig. The distribution was measured using a string of static pressure taps over a vane pitch, thus forming a complete cycle. In order to investigate the magnitude of the driving pressures at different locations, the static pressure distribution was measured at both the vane hub and the annulus outer diameter (OD) with multiple sets of 15 taps over chosen vane pitches. The first set of taps were situated on the vane platform, 2.5 mm aft of the vane trailing edge. The second set of taps were located at the annulus OD at the mid-point of the axial seal-clearance. These are shown diagrammatically in Fig. 4.41, with the vane hub and annulus OD taps shown in indigo and red, respectively.

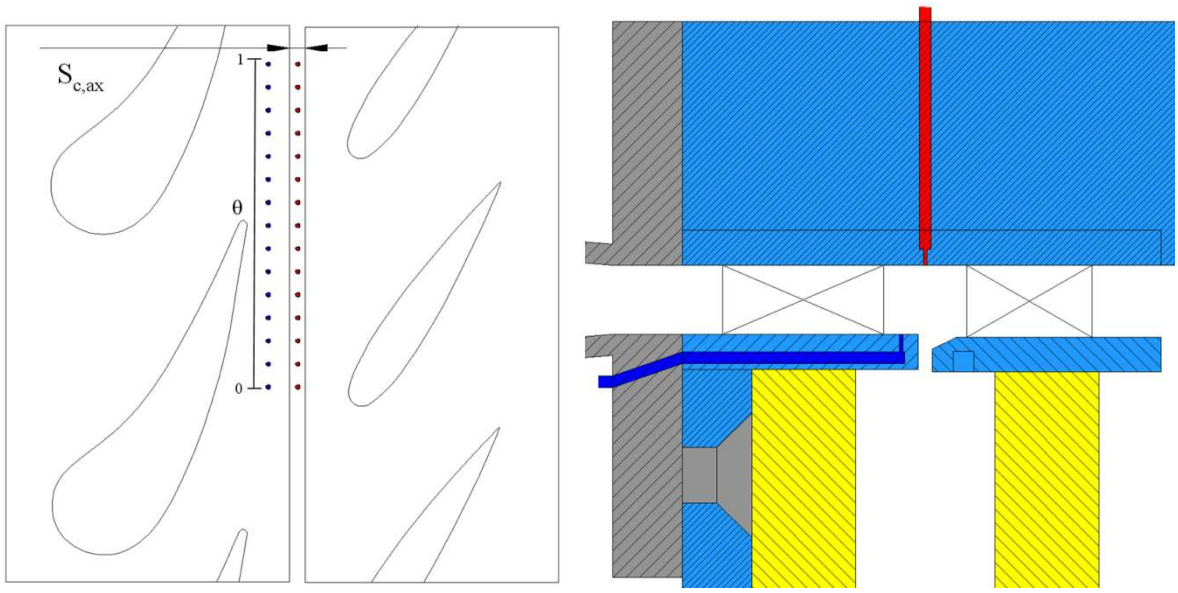

Figure 4.41 Instrumentation taps in the mainstream annulus

In order to quantify the circumferential asymmetry around the annulus, the set of 15 static pressure taps on the vane hub (shown in indigo) were located over four different vane pitches at 90° locations around the azimuth. This allowed for four pressure distributions to be recorded and the percentage axissymmetry to be quantified.

All the instrumentation taps in the mainstream annulus were again connected to an additional Scani-valve unit and calibrated pressure transducer. It should be noted that the 15 taps over a single vane pitch (θ) were designed so that the first and last positions were a duplicate. This enabled the repeatability over different channels to be checked.

4.7.3 Global system instrumentation

Instrumentation was employed to monitor the safe and efficient running of the test facility, while also monitoring the flow-rates supplied to it. These will be discussed in reference to their function during the testing programme.

To ensure that the rotor operated safely inside its casing under rotation, the displacements were constantly monitored in both the axial and radial planes, relative to the stationary clearances. Eddy-current displacement transducers were mounted inside the casing to monitor the axial deflection and radial growth of the rotor disc. The radial transducer was installed radially through the annulus housing and positioned downstream of the blades. The axial transducer was located in a bracket off of the bearing unit pointing axially backward onto the downstream rotor platform edge.

In order to ascertain the running clearances of the seals under rotation, the seal tip radial growths were measured in a free disc environment before the turbine casing and stator were introduced. The rotor was spun in free-air with a laser transducer focussed on the seal tip. The seal tip-growth at the design point disc speeds was recorded, allowing for the experimental running clearances to be known.

A laser reflection probe was mounted onto the bearing unit, focussed on the rotor shaft. A piece of reflective tape was positioned on the shaft, allowing the number of reflections received back by the laser transducer to indicate the speed in rpm. Through a signal processing box, the disc speed in rpm allowed for the strobe light to be synchronised to the disc speed as required for heat transfer experiments.

Orifice plates were used to measure the flows in both the external and sealant flow pipes. The plates were manufactured to ISO 5167-2:2003 for fluid flow in closed conduits, with the designated static pressure and thermocouples probes included in the pipe-work as set out in the standard. These taps were connected to individual pressure differential transducers, allowing for continuous data acquisition. The orifice plate calculations were solved numerically every second using a Newton-Raphson solver, allowing for live flow-rate indicators on screen when tuning the rig to design conditions.

4.7.4 Control logic

In order to run the rig, a complex control system was devised and written using LABVIEW. The system was based on a tabbed visual interface, where the rig could be tuned to design point conditions, before any or all of the instrumentation would acquire data.

The most important module was the "tuning tab" where visual indicators of external and sealant mass flow-rates, disc speed and running clearances were shown at one second increments. This allowed for the rig to be aerodynamically balanced without any substantial loads on the rotor blades. Once at the design condition, all flow-condition parameters were written to file, and the system requested which instrumentation to run. Concentration gas-analysers and multiple Scani-valve units could be selected and a multitude of acquisition options varied, for example recording time lengths, settling times and pressure ranges. After the desired data was recorded at that fluid-dynamic condition, the control system allowed the rig to be re-tuned to a different rotational speed, external or purge mass flow-rate.

A substantial amount of time was spent commissioning the control system so that all fluid-dynamic conditions could be created and investigated without manually entering the test cell. The

manual controls and dials were therefore located in the control annexe and could vary all flow-rates, speeds and gas injection remotely.

An important aspect of the control system was safety shutdown, where the rig was sequentially brought to rest in the event of failure. Although the pneumatic actuator valves were purchased with an in-built fail-safe mode, a fast-acting solenoid valve was placed at entry to the laboratory. The disc motor and acquisition equipment were also brought to rest via a single termination button.

4.7.5 Dynamic balancing of the rotor disc

To ensure that the rotor disc was dynamically balanced to turbine specification, the planar vibrations were analysed as the rotor was spun in free-air. Figure 4.42 shows the horizontal and vertical vibration components with variation in disc speed. Using vibration sensors fitted to the bearing assembly, the disc was found to be sufficiently manufactured within turbine specification and required no further dynamic balancing.

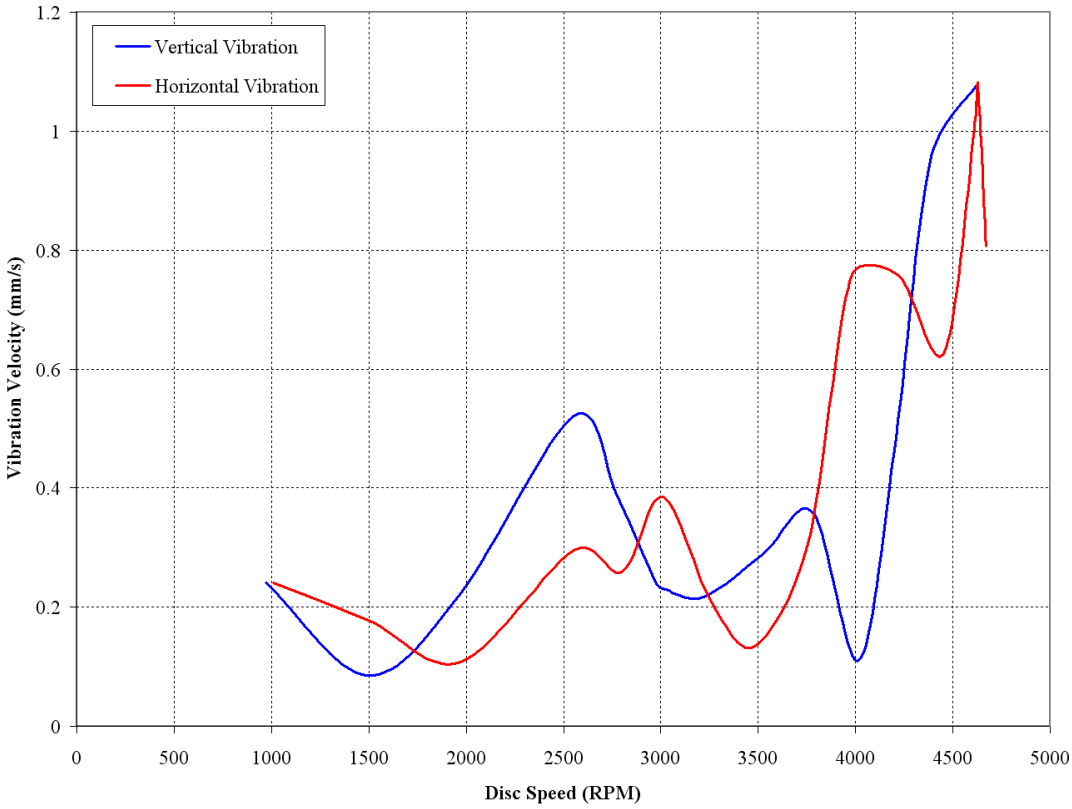

Figure 4.42 Dynamic balancing of the rotor disc

Chapter 5: Externally-induced ingress

This chapter describes how the new experimental facility was used to model externally-induced ingress, with an investigation assessing the performance of two single-clearance rim seals (Generics 1 & 2) in terms of sealing effectiveness. Measurements of CO_2 gas concentration in the rim seal region and inside the wheel-space were used to determine the variation of ε_c, the sealing effectiveness based on concentration, with Φ_o. The variation of pressure in the annulus, which governs the externally-induced ingestion, was obtained from steady pressure measurements on the platform downstream of the vanes and at the outer casing near the rim seal. The distribution of swirl inside the wheel-space was also measured to assess the fluid dynamic conditions.

The measurements provide data to validate CFD codes and provide insight into the physical phenomena governing hot gas ingestion. Furthermore, the effectiveness equations, developed from the orifice model for ingress described in Section 3.1.3, were used to correlate the experimental data. In principle, and within the limits of dimensional similitude, these models could be used to extrapolate the measurements of sealing effectiveness made on the experimental rig at one set of operating conditions to an engine operating at another set of conditions.

Chapter 6 of this thesis will describe an experimental investigation of ingress where there is no main-stream flow and consequently no circumferential variation of external pressure in the annulus. Owen (2009a) described this axisymmetric type of ingestion as rotationally-induced (RI) ingress. Unlike EI ingress, where the pressure differences in the main gas path govern ingestion, RI ingress occurs when the effects of rotation in the wheel-space are important. In gas turbines, EI ingress is usually the controlling mechanism for ingestion. However, in double rim seals the circumferential variation in pressure is attenuated in the annular space between the two seals. If the annular space is large enough to damp out the pressure asymmetry, EI ingress can dominate for the outer seal and RI ingress can dominate for the inner one. Double rim-seal geometries are discussed in Chapter 7.

5.1 EI ingress revisited

EI ingress was discussed in Section 2.5.2. This phenomenon is explained further here. Flow past stationary vanes and rotating blades in a turbine annulus creates an unsteady 3D variation of pressure radially outward of the rim seal, as illustrated in Fig. 5.1. The effective time-average peak-to-trough pressure difference comprises separate components produced by the vanes and blades. These vane and blade effects attenuate with distance from the trailing and leading edges respectively.

Ingress and egress occur through those parts of the seal clearance where the external pressure is higher (marked + in Fig. 5.1) and lower (marked -), respectively, than that in the wheel-space. This non-axisymmetric type of ingestion is the dominant mechanism of ingress in gas turbines and Owen (2009b) defined this as *externally-induced* (EI) ingress.

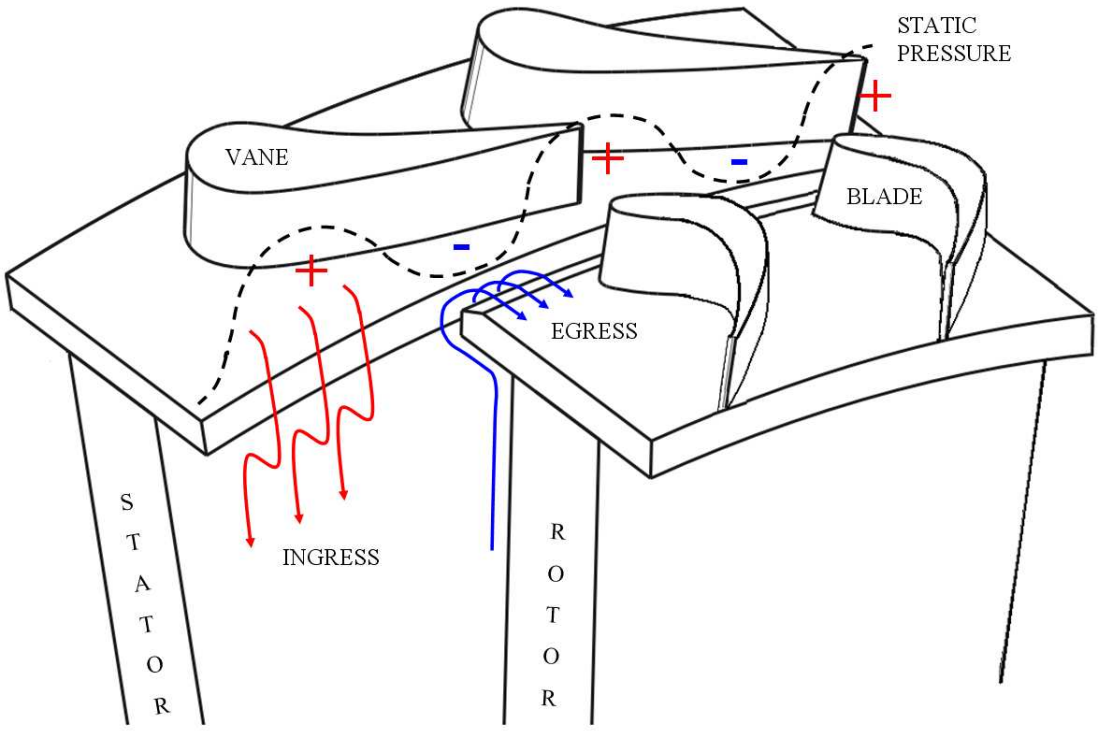

Figure 5.1 Variation of static pressure in a turbine annulus. (red arrows indicate hot-gas ingress and blue cooler egress; corresponding to regions of high and low pressure with respect to the wheel-space, respectively)

Numerous factors influence the degree of ingestion into the wheel-space: the vane and blade geometries and their axial spacing; the Mach and Reynolds numbers of the flow in the annulus; the configuration of the rim seal and its location relative to the vanes and blades; and the non-dimensional sealing flow parameter, Φ_o.

Figure 5.2a shows a simplified axisymmetric diagram of ingress and egress through an axial-clearance rim seal. Cool sealing air enters the wheel-space and fills a source region at low radius. This flow is entrained into the boundary layer on the rotating disc, which thickens with increasing radius, before it is ejected into the turbine annulus. There is a mixing region near the outer radius of the cavity, where hot gas ingested from the annulus mixes with the recirculating flow in the wheel-space. The ingested gas is transported in the boundary layer on the stator which (in contrast to that on the rotor) loses mass as the fluid moves radially inwards over the stator surface. Thus there is axial migration of fluid, through a core region, from the stator to the rotor boundary layer. Consequently the average temperature of the rotor boundary layer increases with radius but the temperature on the stator is approximately constant. The core region is diminished in

size, and pushed to higher radius (see Fig. 5.2b), as the superimposed sealing flow rate increases to Φ_{min}, the value of Φ_o necessary to prevent ingress.

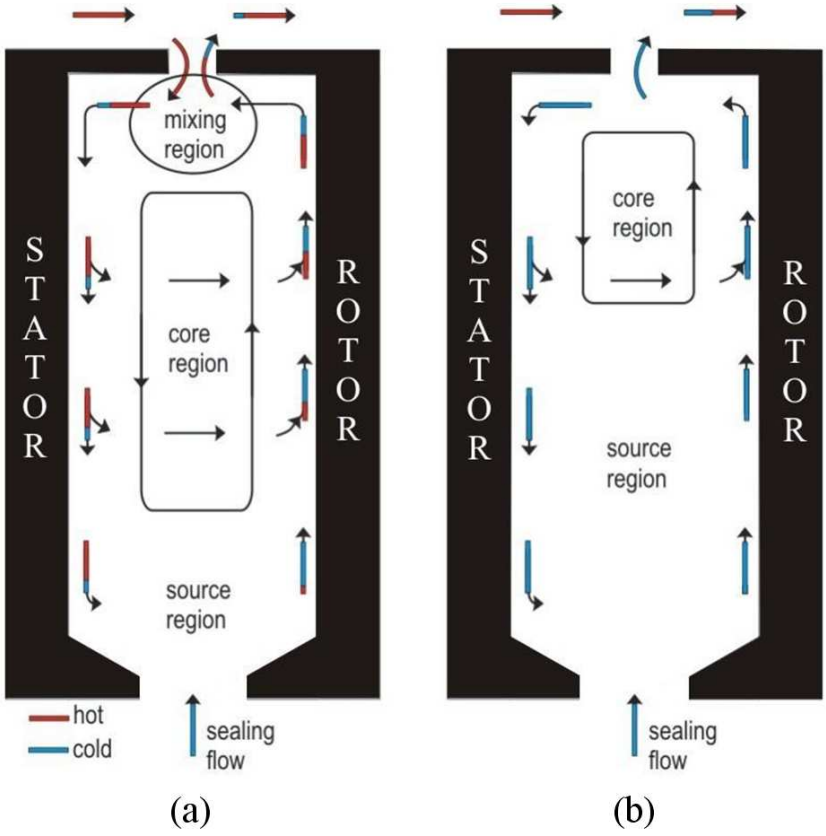

Figure 5.2 Simplified diagram of ingress and egress (a) $\Phi_0 < \Phi_{min}$ (b) $\Phi_0 = \Phi_{min}$

The experiments measure the concentration at 15 radial locations on the stator. The concentration distribution along the stator is expected to be approximately constant for fully mixed-out flow, where no additional fluid is added to the stator boundary layer inboard of the mixing region.

5.2 Commissioning the experimental facility

This section describes the rig variant used for the experimental programme documented in this thesis, along with the associated commissioning process.

5.2.1 Experimental rig variant

The CMA configuration was used for all experiments. The rotor-stator and main annulus feed system was as described in Sections 4.2 and 4.5.2, respectively. While commissioning the facility, it was found that the pressure in the working section was approximately atmospheric, negating the requirement for the volute and collecting system during this programme. The collection system was therefore removed and the air was simply expelled to the laboratory. In order to prevent the room becoming pressurised as the mass-flow filled the space, a variable speed extractor fan was fitted to the lab wall. The fan was calibrated to remove an equal quantity of air to that flowing though the turbine stage.

The test section of the facility is shown in Fig. 5.3. Compressed air entered the mainstream annulus of the stage through a convergent transition section fed from 32 circular pipes, each of 25.4 mm diameter, some of which are shown in Fig. 5.3.The upstream end of each pipe was connected to a radial diffuser (not shown in the figure) where the delivery pressure to each pipe was measured to be equal within +/- 5%. The vanes and blades were secured to aluminium platforms which form the periphery of the stator and rotor, respectively, with stationary components shown in red and rotating components in blue.

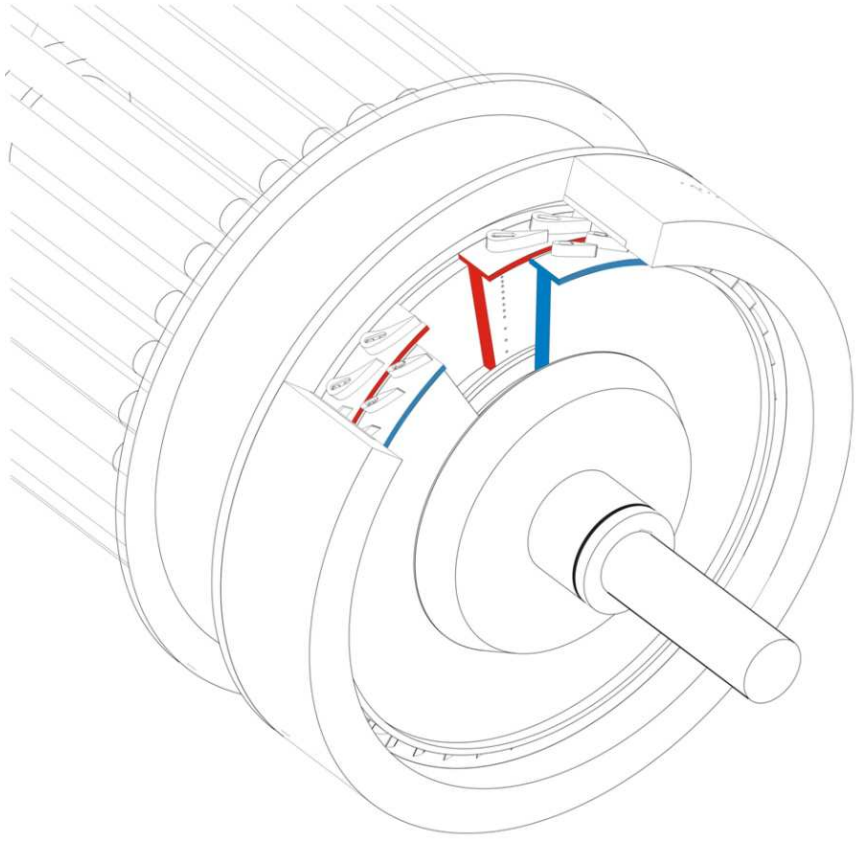

Figure 5.3 Rig test section showing turbine stage

Sealing air was introduced into the wheel-space at a low radius through an inner seal. To measure the degree of ingestion, this sealing flow was seeded with a carbon dioxide tracer gas. The concentration of CO_2 was monitored at the entrance to the wheel-space, c_0, and in the unseeded upstream flow through the annulus, c_a. The variation of concentration c_s with radius ($0.55 < r/b < 0.993$) along the stator disc in the wheel-space was determined by sampling through 15 tubes of diameter 1.65 mm (discussed in Section 4.7.1). These tubes (or taps) are illustrated in Fig. 5.3 and gas is drawn by a pump which led the samples to an infra-red gas analyser.

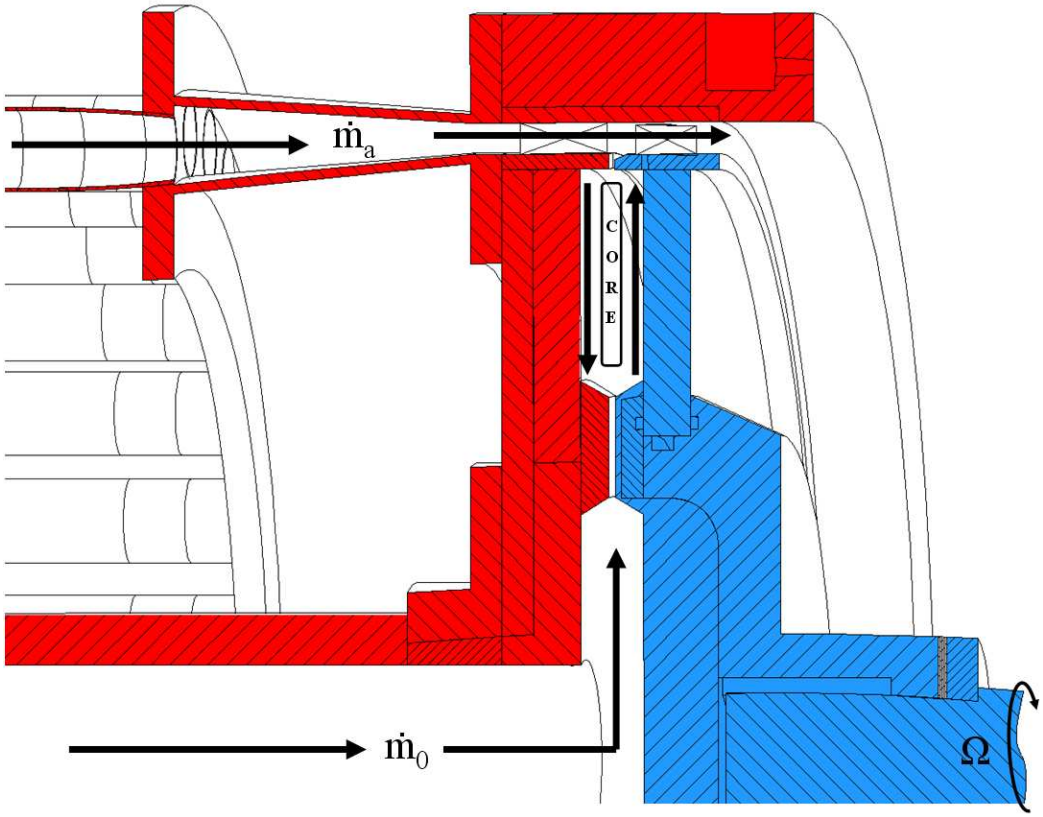

Figure 5.4 Rig test section showing sealing and mainstream flows (red, stationary; blue, rotating)

The definition of gas-concentration effectiveness, ε_c and ingress parameter were given as Eqs 3.44 and 3.45, respectively, and were determined experimentally. As discussed in Section. 5.1 with reference to Fig. 5.2, the value of ε_c is expected to be relatively insensitive to the radial location on the stator. This is shown to be the case in Section. 6.2, and thus the rim-seal effectiveness reported here is based on data collected at $r/b = 0.958$.

Concentration measurements were made using a Signal Group 9000MGA multi-gas analyzer, applying an infra-red filter-correlation technique to calculate seed-gas concentration level. The measurements of concentration are time averaged and made within a combined uncertainty of +/- 1.5% of the measured value. The analyzer was calibrated using an alpha-grade

pure N_2 as zero-gas and a 3% CO_2 in N_2 as the span-gas, acting as start and end points for the linear calibration, respectively. The sealant mass flow-rate in which the CO_2 seed is injected was measured to within +/- 3% uncertainty using the aforementioned orifice plate.

The effectiveness, ε, used in the orifice model (Eq. 3.39) is based on the convection of fluid created by pressure differences. In the mass-transfer equation, concentration differences in the fluid create diffusion and mixing, which are additional to the convection of fluid calculated by the orifice model. Consequently, the two definitions of effectiveness are similar but are not generally equivalent. Despite this, it is usual to match the measured and theoretical results by implicitly assuming that they are equivalent, which will be applied when fitting the theoretical effectiveness equations to the experimental data.

Two different single-clearance rim seals were investigated. These are shown diagrammatically in Fig. 5.5 with geometric details (static and under rotation) given in Table 5.1. The vane and blade platforms at the periphery of the parallel stator and rotor discs form a simple axial-clearance seal (Generic 1, Fig. 5.5a). The generic radial-clearance seal (Generic 2) shown in Fig. 5.5b features an identical geometry at the periphery of the stationary disc, with an axial overlap from a seal lip positioned at a lower radius on the rotating disc.

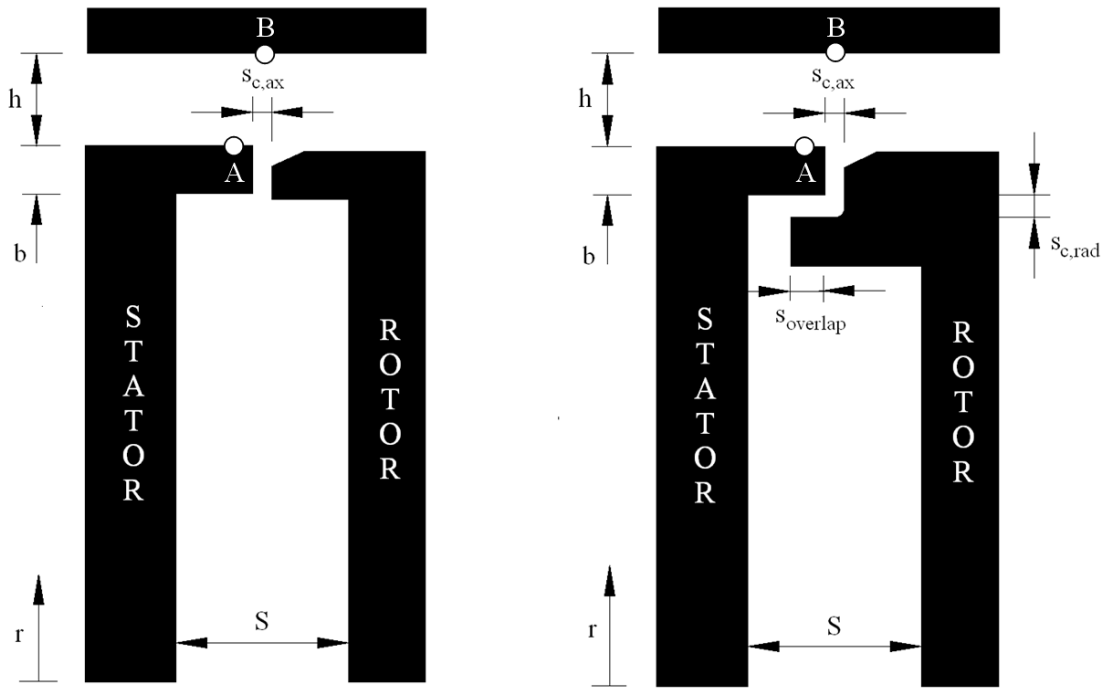

Figure 5.5 (a) Left – simple axial-clearance seal (Generic 1), (b) Right – radial-clearance seal (Generic 2)

Displacement transducers were used to measure the axial deflection of the disc. The axial clearance of the seal was found to increase slightly when under rotation and when sealing flow

pressurised the wheel-space, but at the maximum value of $\Phi_o = 0.38$ tested the variation in $s_{c,ax}$ was < 8% of the clearance. Displacement transducers were also used to measure the radial growth of the disc, rotor platform and radial-clearance seal under rotation, from which the operating seal clearances were determined.

Geometric Symbol	Axial-Clearance Seal	Radial-Clearance Seal
h	10.0 mm	
b	190 mm	
S	20.0 mm	
$s_{c,ax}$	2.00 mm	
$G_{c,ax}$	0.0105	
$s_{overlap}$	-	3.70 mm
$s_{c,rad,0}$ (0 rpm)	-	2.40 mm
$G_{c,rad,0}$ (0 rpm)	-	0.0126
$G_{c,rad}$ (2000 rpm)	-	0.0124
$G_{c,rad}$ (3000 rpm)	-	0.0121
$G_{c,rad}$ (3500 rpm)	-	0.0119

Table 5.1Geometric properties for both seal configurations

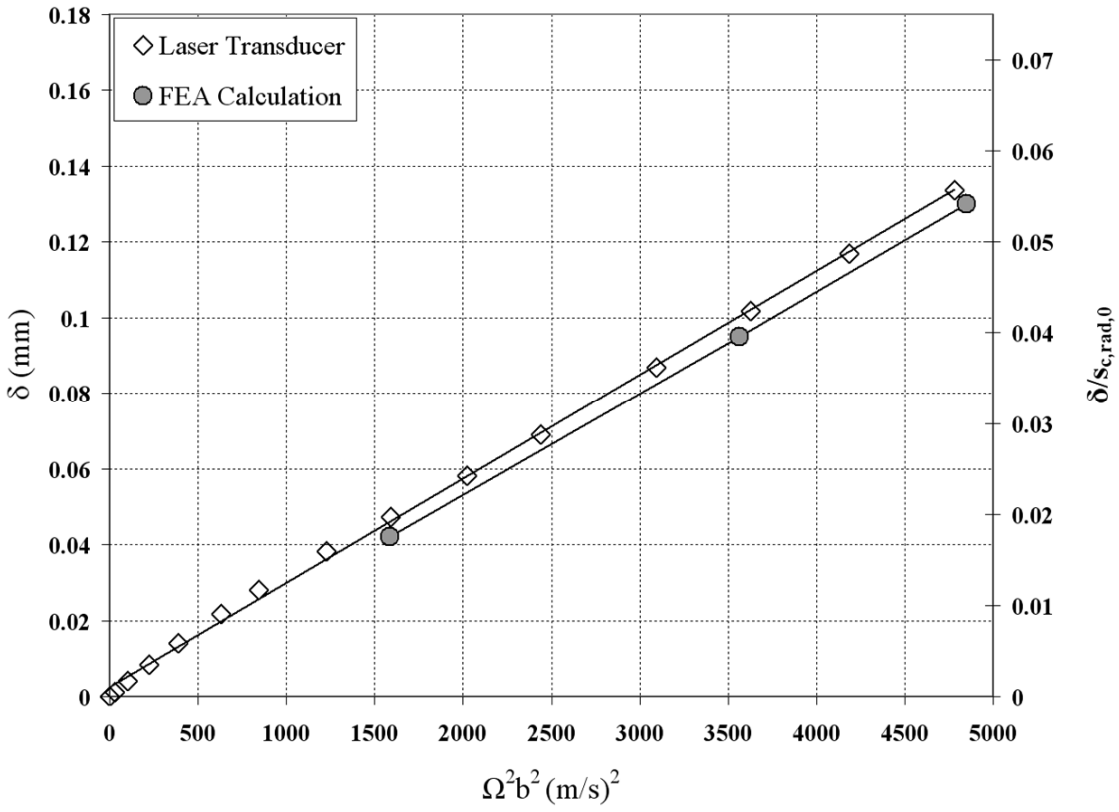

Figure 5.6 Radial displacement of radial-clearance seal measured at the seal-tip

Figure 5.6 shows the variation of $\delta = s_{c,rad} - s_{c,rad,0}$ and $\delta / s_{c,rad,0}$ with $\Omega^2 b^2$. Here $s_{c,rad,0}$ is the radial clearance at zero rotation and Ωb is the rotational speed of the disc. The radial clearance is seen to decrease linearly with the square of the disc speed, with $\delta / s_{c,rad,0} < 6\%$ at the maximum speed tested, and the value of $G_{c,rad}$ varied by approximately 4% as the disc speed increased from 2000-3500 RPM (see Table 5.1). Also shown in the figure are finite element analysis (FEA) calculations which agree well with the measurements.

The vanes and blades in the annulus produced a flow structure representative of those found in engines, albeit at lower Reynolds and Mach numbers. Figure 5.7 shows the geometry of the generic vanes and blades with the axial distance between the vane trailing edge and the blade leading edge being 12 mm (or 0.52 vane axial chords). The centre line of the 2 mm seal gap was equidistant between the vane and blade.

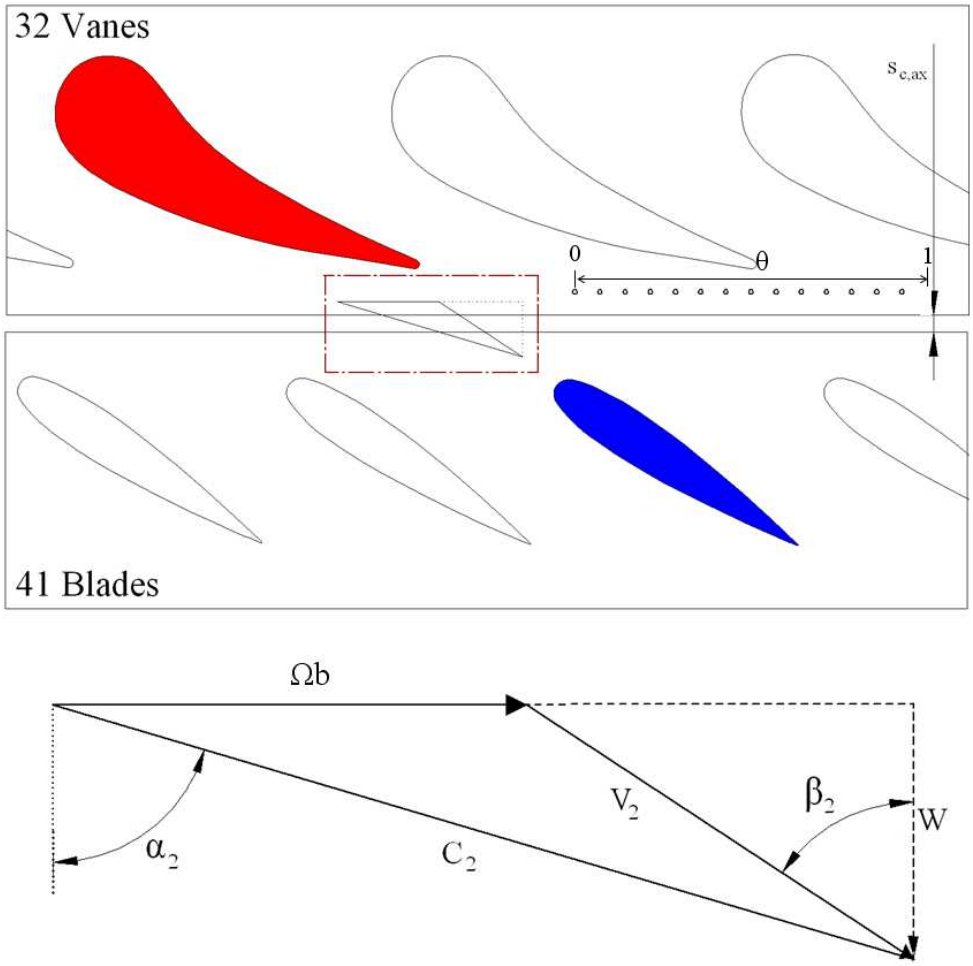

Figure 5.7 Vane and blade setup and associated flow angles

The circumferential variation of static pressure was determined from 15 taps (each 0.5 mm diameter) arranged across one vane pitch, as illustrated in Fig. 5.7; these taps were located in the

vane platform 2.5 mm downstream of the vane trailing edge (location A) and in the outer casing above the centre-line of the seal clearance (location B), as marked in Fig. 5.5. Data was averaged over four vane pitches.

The flow exiting the vanes is virtually incompressible and near atmospheric pressure; the density, ρ, speed of sound, a, and air viscosity, μ, were determined from the static temperature and pressure measured inside the wheel-space on the stator at r/b = 0.993. The rotor inlet angle and velocity are β and V, respectively. At the *design condition*, $\beta = \beta_0$, though the rig (or engine) can be operated off design: $\beta - \beta_0 > 0$ is referred to as the under-speed case and $\beta - \beta_0 < 0$ the over-speed case. For the rig, β_0 = 56°, α = 73.5°, and Re_W / Re_Φ = 0.538. All rim-seal effectiveness data presented in this thesis are for the design condition, with similar velocity triangles at the three operating points listed in Table 5.2.

Calculated Parameter	**2000 rpm DP**	**3000 rpm DP**	**3500 rpm DP**
Axial-Flow Reynolds Number (Re_w)	2.86 x 10^5	4.40 x 10^5	5.21 x 10^5
Rotational Reynolds Number (Re_Φ)	5.32 x 10^5	8.17 x 10^5	9.68 x 10^5
Re_w/Re_Φ	0.538	0.538	0.538
Vane Exit Mach Number (M)	0.225	0.339	0.398

Table 5.2 Experimental operating points

5.2.2 Circumferential variation of pressure in the annulus

The time-average static pressure, p_2, in the annulus and the peak-to-trough pressure difference, Δp, are proportional to W^2, where W is the axial component of velocity in the annulus. From the definitions given in the Nomenclature, it follows that the pressure coefficient, C_p, and the non-dimensional pressure difference, ΔC_p, are therefore proportional to $(Re_w/Re_\Phi)^2$. As shown in Table 5.2, (Re_w/Re_Φ) = 0.538 at the design point.

The circumferential distribution of C_p is shown in Fig. 5.8 at locations A (vane platform) and B (on the outer casing at the axial location of the middle of the seal clearance). The definition of C_p is given as Eq. 5.1. The measurements were made at the design point for the case of no sealing flow, *i.e.* Φ_o = 0, and the results at location A are shown for three values of Re_Φ. It should be noted that the flow is over a small range of Mach numbers.

$$C_p = \frac{(p_2 - \overline{p_2})}{\frac{1}{2}\rho\Omega^2 b^2} \quad \text{(Equation 5.1)}$$

where:
- p_2 is the local static pressure in the annulus
- $\overline{p_2}$ is the average static pressure in the annulus over one vane pitch
- Ω is the angular speed of the disc
- b is blade platform inner-radius
- ρ is the density of air on the stator wall at r/b = 0.993

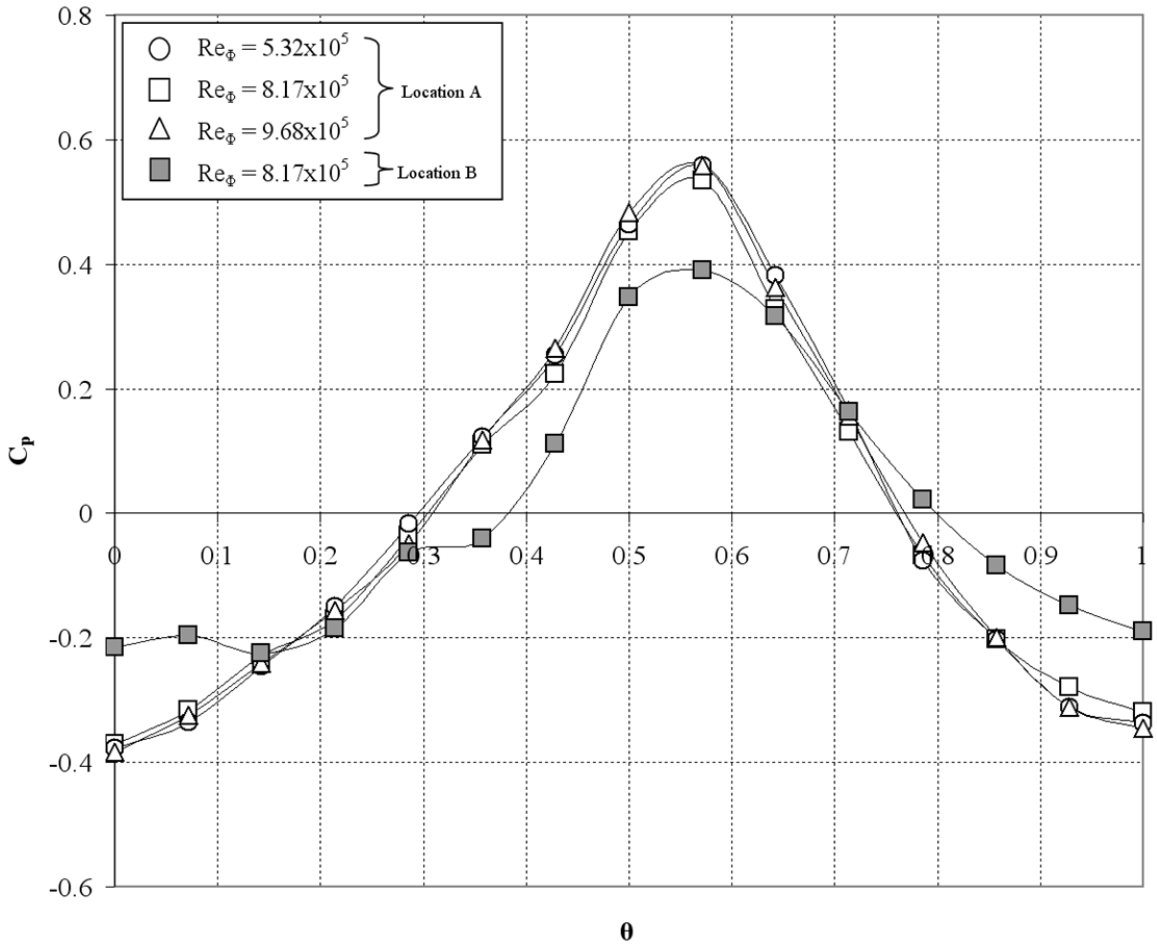

Figure 5.8 Effect of Re_Φ on circumferential distribution of C_p over non-dimensional vane pitch. (Re_w/ Re_Φ) = 0.538

It can be seen in Fig. 5.8 that, as Re_w/Re_Φ is constant, the three distributions at location A are virtually independent of Re_Φ. However, they differ significantly from the distribution at location B, and the non-dimensional peak-to-trough pressure difference, ΔC_p, at A is greater than that at B. Swirl causes a radial pressure gradient so that the pressure will increase in the radial direction. The pressure asymmetry is expected to decrease with axial distance from the vane; the

axial decrease evidently dominates causing the observed reduction at location B. It should be noted that ΔC_p depends on where it is measured.

Figure 5.9 illustrates the measured circumferential distribution of C_p for $Re_\Phi = 8.17\text{x}10^5$ at the design point at location A for three different values of $\Phi_0 / \Phi_{min,EI}$. The peak-to-trough pressure difference decreases slightly as Φ_0 increases. This decrease, which is attributed to the 'spoiling effect' of the egress as it interacts with the main flow in the annulus, is consistent with findings of Bohn *et al.* (2006). In the results presented here onwards, ΔC_p is given for $\Phi_0 = 0$, which is the case used by most experimentalists.

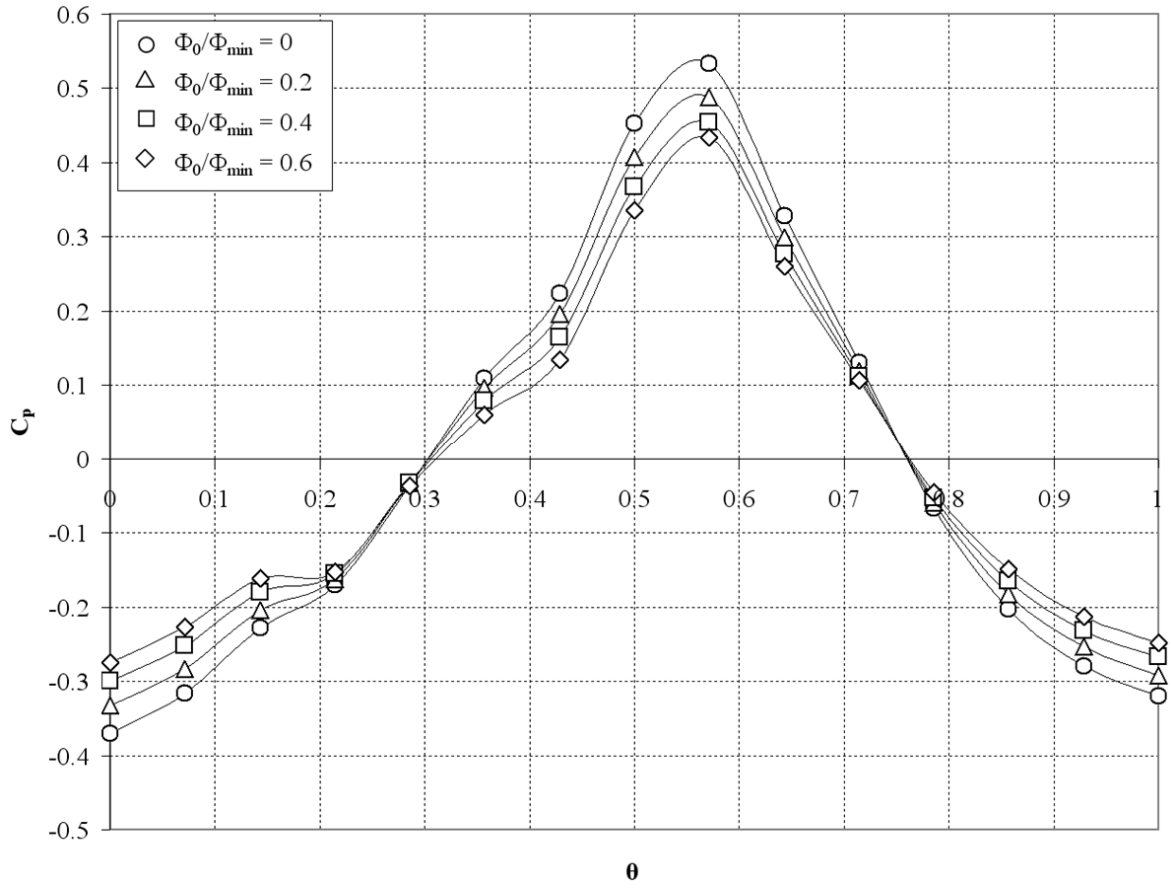

Figure 5.9 Effect of $\Phi_0 / \Phi_{min,EI}$ on circumferential distribution of C_p over non-dimensional vane pitch. $Re_\Phi = 8.17\text{x}10^5$ $(Re_w / Re_\Phi) = 0.538$

Figure 5.10 shows the expected linear variation of $\Delta C_p^{1/2}$ with Re_w/Re_Φ at the two locations (A and B) in the annulus. The data was collected for $Re_\Phi = 5.32\text{x}10^5$ and $8.17\text{x}10^5$ over the range $0 < Re_w < 4.9\text{x}10^5$. For the given vane and blade geometry, the ratio Re_w/Re_Φ uniquely determines the stage velocity triangles and, as stated above, ΔC_p. The angle $\beta - \beta_0$ is plotted on the upper axis and at the design condition, $\beta - \beta_0 = 0$ and $Re_w/Re_\Phi = 0.538$. As $|\beta - \beta_0|$ increases, the rig operates further from the design point and $\Delta C_p^{1/2}$ increases and decreases linearly with Re_w/Re_Φ for $\beta - \beta_0 >$

0 and $\beta - \beta_0 < 0$ respectively. In this thesis only the design point has been used for rim-seal effectiveness measurements.

Phadke and Owen (1988a) and Bohn and Wolff (2003) used the constant K defined by Eqs 2.7 and 2.8. It is useful to express this constant in terms of $\Phi_{min,EI}$ and ΔC_p.

$$\Phi_{min,EI} = \frac{2}{3} C_{d,e} \Delta C_p^{\frac{1}{2}} = K \sqrt{\frac{\Delta C_p}{2}} \qquad \text{(Equation 5.2)}$$

Figure 5.10 clearly illustrates that (for a given rim seal and turbine-stage geometry) the value of $C_{d,e}$ determined from Eq. 3.33, or the value of K from Eq. 5.2, will depend on where in the annulus ΔC_p is measured. It is therefore difficult to compare the values of $C_{d,e}$ and K obtained in one set of experiments or computations with another. Fortunately, these 'secondary parameters' are unnecessary in the determination of $\Phi_{min,EI}$, which is the principal empirical characteristic of the rim seal for a prescribed set of velocity triangles and fluid-dynamic conditions and in the annulus.

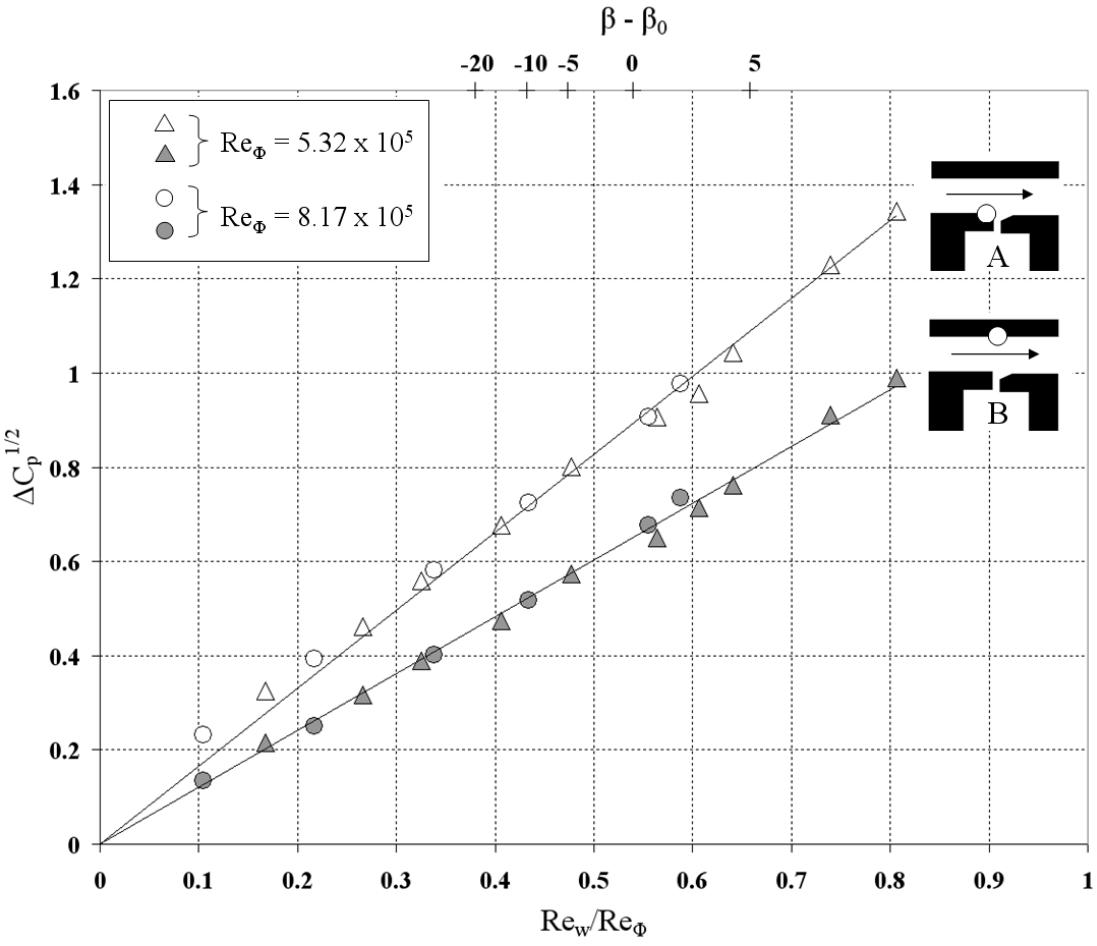

Figure 5.10 Effect of Re_Φ on variation of $\Delta C_p^{1/2}$ with Re_w / Re_Φ at locations A and B in the annulus

5.2.3 Rim seal displacements under experimental conditions

As stated in Section 4.7.3, eddy-current transducers were used to monitor the axial displacement and radial growths of the rotor under rotation in order to ensure the safe operation of the facility. A laser transducer was also used to monitor the radial seal tip growths as documented in Section 5.2.1 so that accurate values of $G_{c,rad}$ could used in the formulation of the Φ_0 parameter.

This same instrumentation was used to measure the centrifugal growth of the rotor hub, to ensure that there was a radial step-down from the stator during experiment. As discussed in Section 4.2.1, a theoretical disc-matching calculation estimated the centrifugal growth of the rotor platform to be 0.33 mm at the 6000 rpm upper bound on the motor. A laser transducer was positioned facing radially down on to the rotor platform, downstream of the blades and used to record the radial growth as a function of the disc speed. The radial growth is shown to be a linear function of the square of the disc speed in Fig. 5.11; an FEA calculation is included to show agreement between experiment and theory.

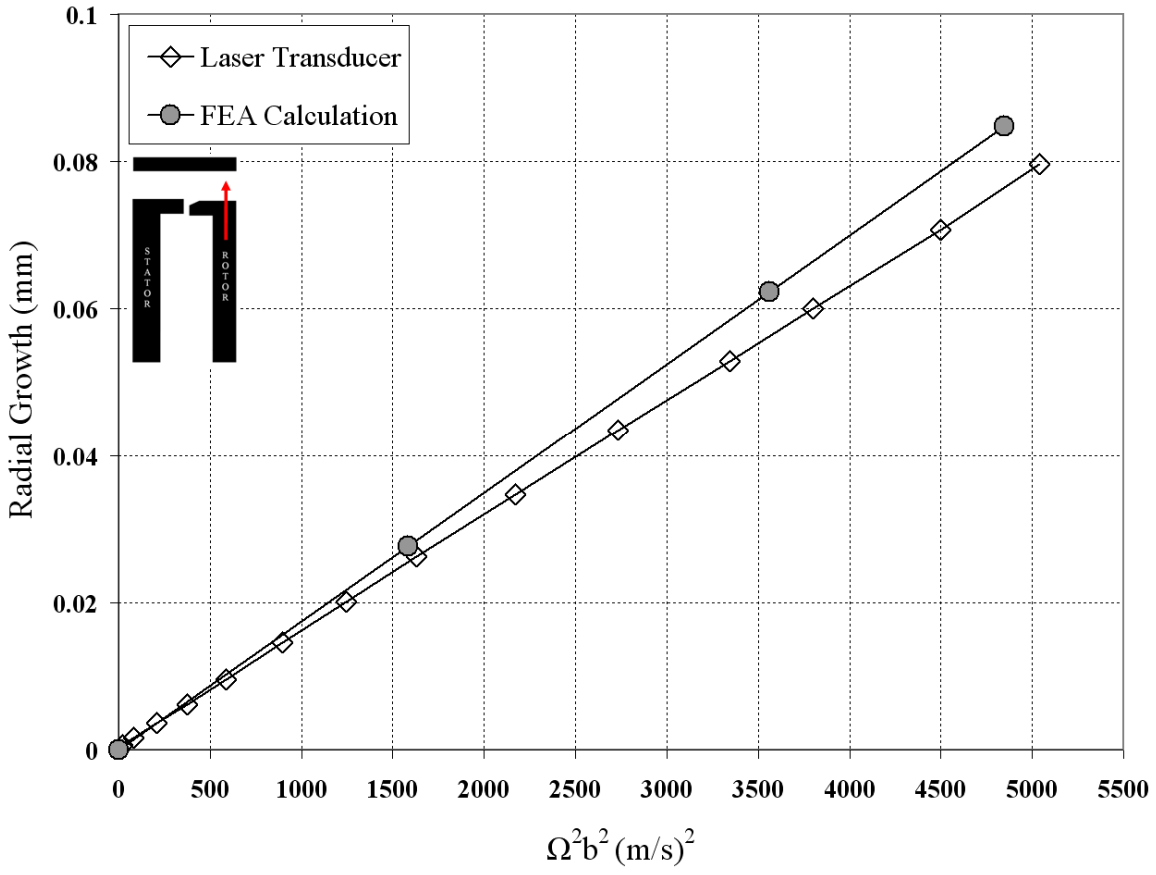

Figure 5.11 Radial displacement of rotor platform measured downstream of the blades

The radial growth at the upper design point is shown to be 0.08 mm, ensuring that a radial step-down indeed exists between stator and rotor platforms.If the linear fit is extrapolated to the 6000 rpm upper bound, a radial growth of 0.23 mm is predicted. This suggests that the estimated 0.33 mm growth from the disc matching theory was a conservative but nonetheless sufficient design criterion.

The axial displacement was also important, as this controlled the axial clearance for Generic Seals 1 and 4. It was expected that when the wheel-space was pressurised the rotor disc would deflect, causing an increase in the axial seal clearance. This was tested by simulating the cavity pressures experienced over the full testing range and monitoring the resulting axial deflection of the rotor platform. An eddy current transducer was pointed axially on to the downstream side of the rotor platform, with an assumption being that the displacement would be identical on the upstream side of the platform controlling the seal clearance. The axial deflection and its percentage of the seal clearance, $s_{c,ax}$, are shown as a function of the cavity gauge pressure in Fig. 5.12. The maximum expected experimental pressure rise is also shown. The maximum axial deflection has been measured to be 8% of $s_{c,ax}$.

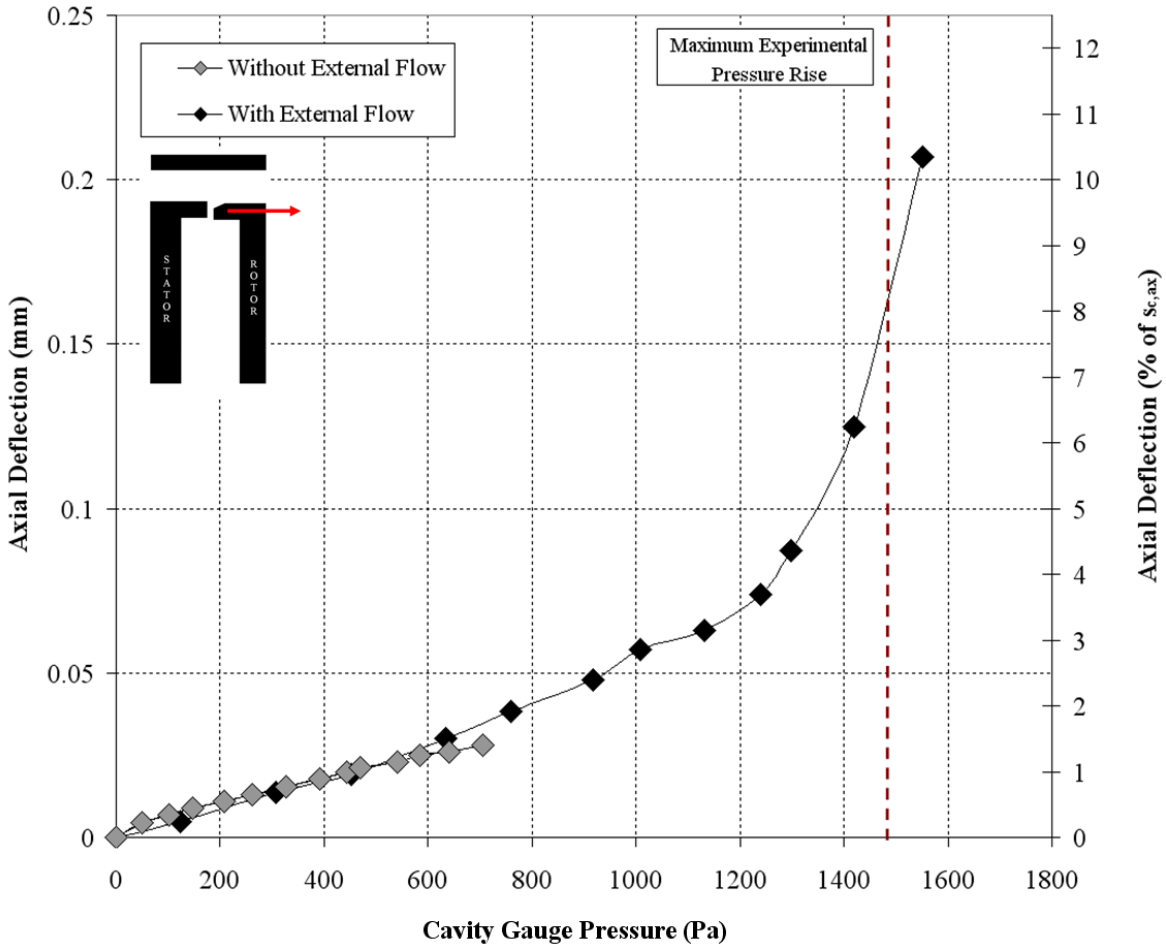

Figure 5.12 Axial displacement of rotor platform measured on downstream edge of rotor platform

5.3 Measurements of rim-seal effectiveness

In this section, experimental data collected using the generic axial- and radial-clearance seals shown in Fig. 5.5 are presented. The rim-seal effectiveness was measured using the concentration effectiveness, ε_c (defined by Eq. 3.44), collected on the stator at r/b = 0.958. The distribution of ε_c in the wheel-space, which is presented in Section 6.2, was found to be relatively insensitive to the radial location on the stator. Data is presented in terms of $C_{w,o}$, the widely used non-dimensional sealing flow rate, as well as Φ_0 , the non-dimensional flow parameter used in the orifice equations. The experimental data is compared with theoretical calculations from the orifice model using the EI effectiveness equations: Eqs 3.38 and 3.42.

5.3.1 Rim-seal effectiveness in terms of $C_{w,0}$

Figure 5.13 shows the variation of effectiveness with $C_{w,o}$, for the two rim seals. Measurements were made at three values of Re_Φ corresponding to the three operational points listed in Table 5.2 with Re_W / Re_Φ = 0.538. Thumb-nail sketches of the two seal configurations are shown on this and all following effectiveness figures, and it should be noted that the external flow is from left to right (*i.e.* from the stator towards the rotor).

The data illustrate that ε_c increases with increasing $C_{w,o}$, as the sealing flow pressurises the wheel-space and reduces ingestion of main-stream flow from the annulus. As Re_Φ (hence Re_W) increases, a larger $C_{w,o}$ is required to maintain a given level of effectiveness; $C_{w,min}$, the non-dimensional sealing flow required to seal the wheel-space correspondingly increases with Re_Φ and Re_W. The radial-clearance seal is shown to require a significantly smaller $C_{w,min}$ than the axial-clearance seal for the same Re_Φ, demonstrating the former to be a superior geometric design in terms of rim-seal effectiveness.

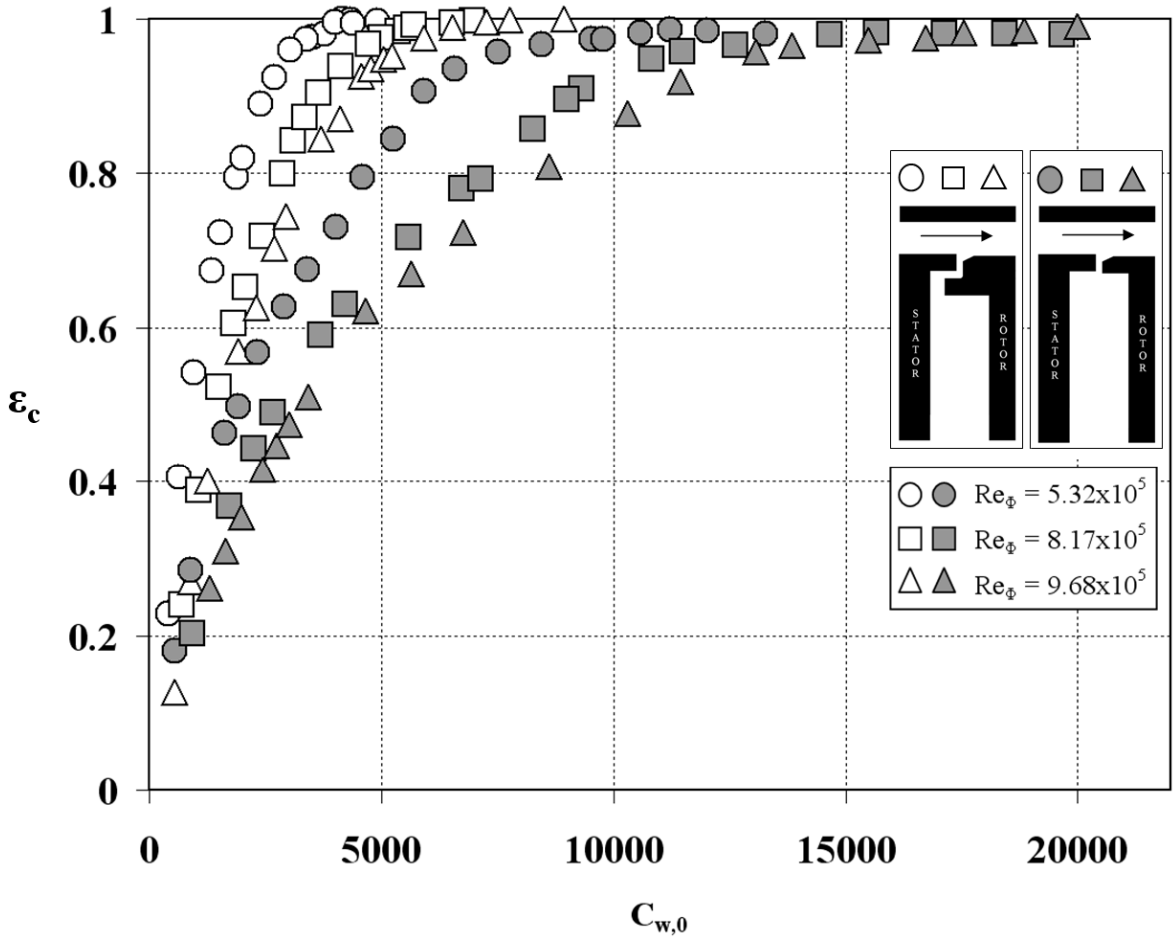

Figure 5.13 Effect of Re_Φ on measured variation of ε_c with $C_{w,o}$ for both tested rim seals. (Open symbols denote radial-clearance seal; solid symbols denote axial-clearance seal.)

Figure 5.14 shows the linear variation of $C_{w,min}$ with $C_{p,max}^{1/2}$ Re_W consistent with Eq. 2.7, and data presented by Phadke and Owen (1988a, b, c) and Bohn and Wolff (2003). Data for both the axial- and radial-clearance seals are shown for $C_{p,max}$ based on the peak-to-trough difference in static pressure obtained at the two measurement positions (A and B) in the annulus.

K, which is defined by Eq. 5.2, is a parameter commonly used for ranking the relative performance of different rim-seal geometries. The value of K, which is shown in Fig. 5.14, depends upon the measurement location of $C_{p,max}$. Phadke and Owen correlated their data with $K = 0.6$, and Bohn and Wolff correlated their data for a similar axial-clearance seal and a radial-clearance seal with $K = 0.46$ and 0.20, respectively. In light of the discussion in Section 5.2.2, it is surprising and perhaps fortuitous that these values of K are as close as they are to those obtained here.

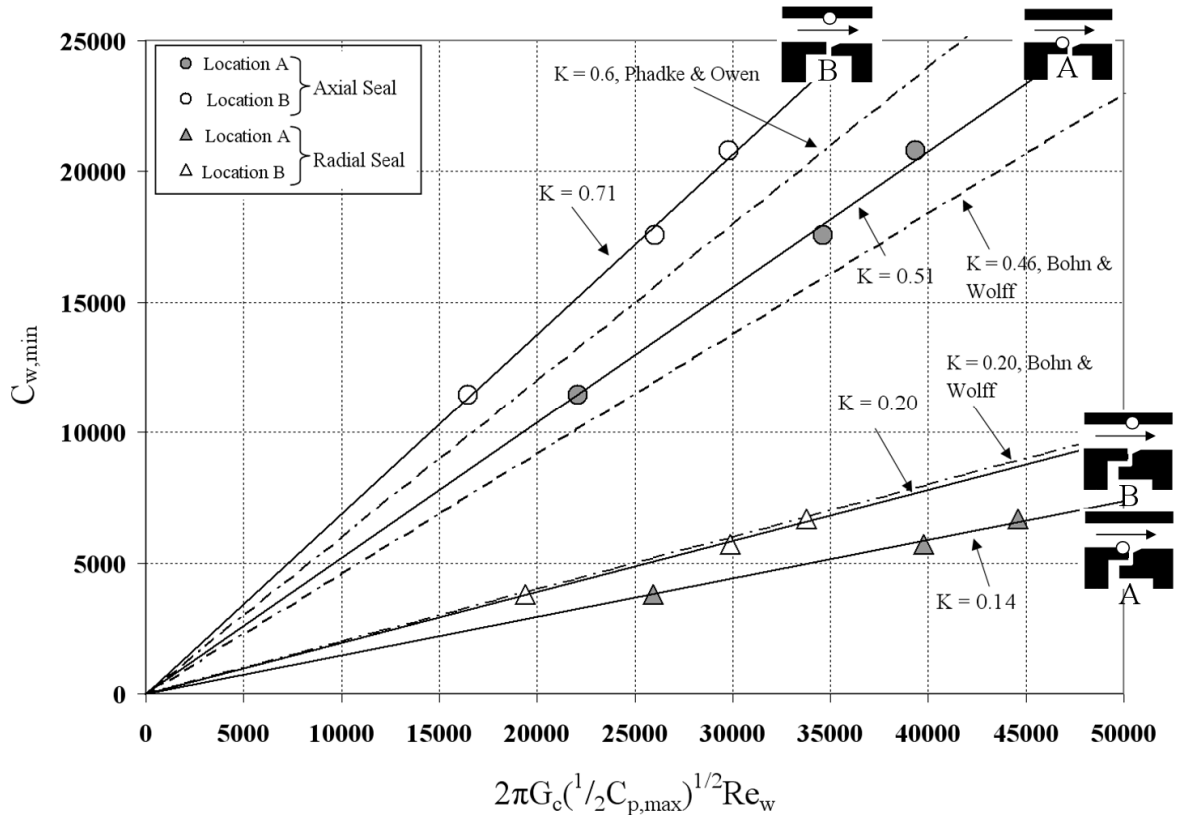

Figure 5.14 Variation of $C_{w,min}$ with $C_{p,max}^{½}\, Re_W$, highlighting seal comparisons using K

5.3.2 Rim-seal effectiveness in terms of Φ_0

The data in Fig. 5.13 have been re-plotted versus Φ_o in Fig. 5.15. Note that the radial-clearance seal has slightly varying values of G_c at different Re_Φ, as shown in Table 5.1. Instead of having to use separate correlations for the effects of G_c and Re_Φ on ε, Φ_o combines $C_{w,o}$, G_c and Re_Φ into a single flow parameter. For the design condition (for which the ratio $Re_W / Re_\Phi = 0.538$), the rim seals are shown to be characterised by $\Phi_{min,EI}$, which is independent of Re_Φ.

Eqs 3.38 and 3.42, the EI effectiveness equations derived from the orifice model, include the two parameters, $\Phi_{min,EI}$ and Γ_c. Figure 5.16 shows a comparison between the experimental data and the theoretical variation of effectiveness according to these equations for the axial-clearance seal, and Fig. 5.17 shows results for the radial-clearance seal. The ingested flow rate, not shown in Fig. 5.13, is presented as the non-dimensional parameter $\Phi_{i,EI}$, which was obtained from Eq. 3.45.

The fit between these equations and the measured variation of ε_c with Φ_o was optimised, in terms of $\Phi_{min,EI}$ and Γ_c, using a statistical model featuring maximum likelihood estimates described by Zhou *et al.* (2011a). Figures 5.16 and 5.17 show that the agreement between the optimum theoretical curves and the experimental data is very good.

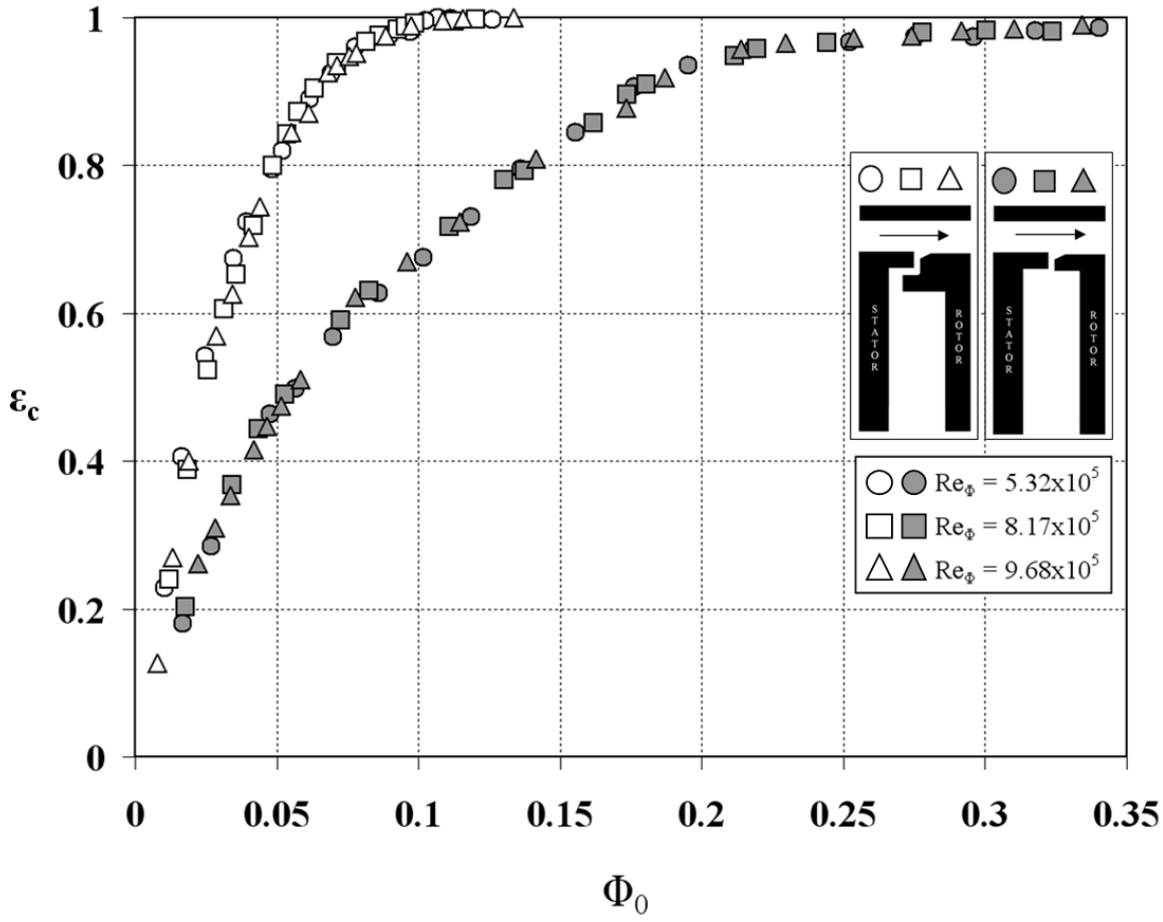

Figure 5.15 Measured variation of sealing effectiveness with Φ_0 for EI ingress for $(Re_w/Re_\Phi) = 0.538$
(Open symbols denote radial-clearance seal; solid symbols denote axial-clearance seal.)

The values of $\Phi_{min,EI}$ and Γ_c, as well as the standard deviation σ between the equation and the data, for the two seals are shown in Table 5.3. The table includes the values of $\Phi_{i,EI}^*$ calculated from Eq. 3.43. $\Phi_{i,EI}^*$ is the maximum value of $\Phi_{i,EI}$, which occurs when $\Phi_o = 0$; this theoretical value cannot be easily determined from the concentration measurements. Zhou *et al.* recommended that at least 16 data points are needed to produce accurate estimates, and the values of n shown in Table 5.3 are well in excess of this number.

Table 5.3 also shows that, for EI ingress, the ratio of Φ_{min} for the radial-clearance seal to that required for the axial-clearance seal is around 26%. The radial-clearance seal is significantly more effective that the axial-clearance seal. This result is consistent with the experiments of Bohn and Wolff (2003).

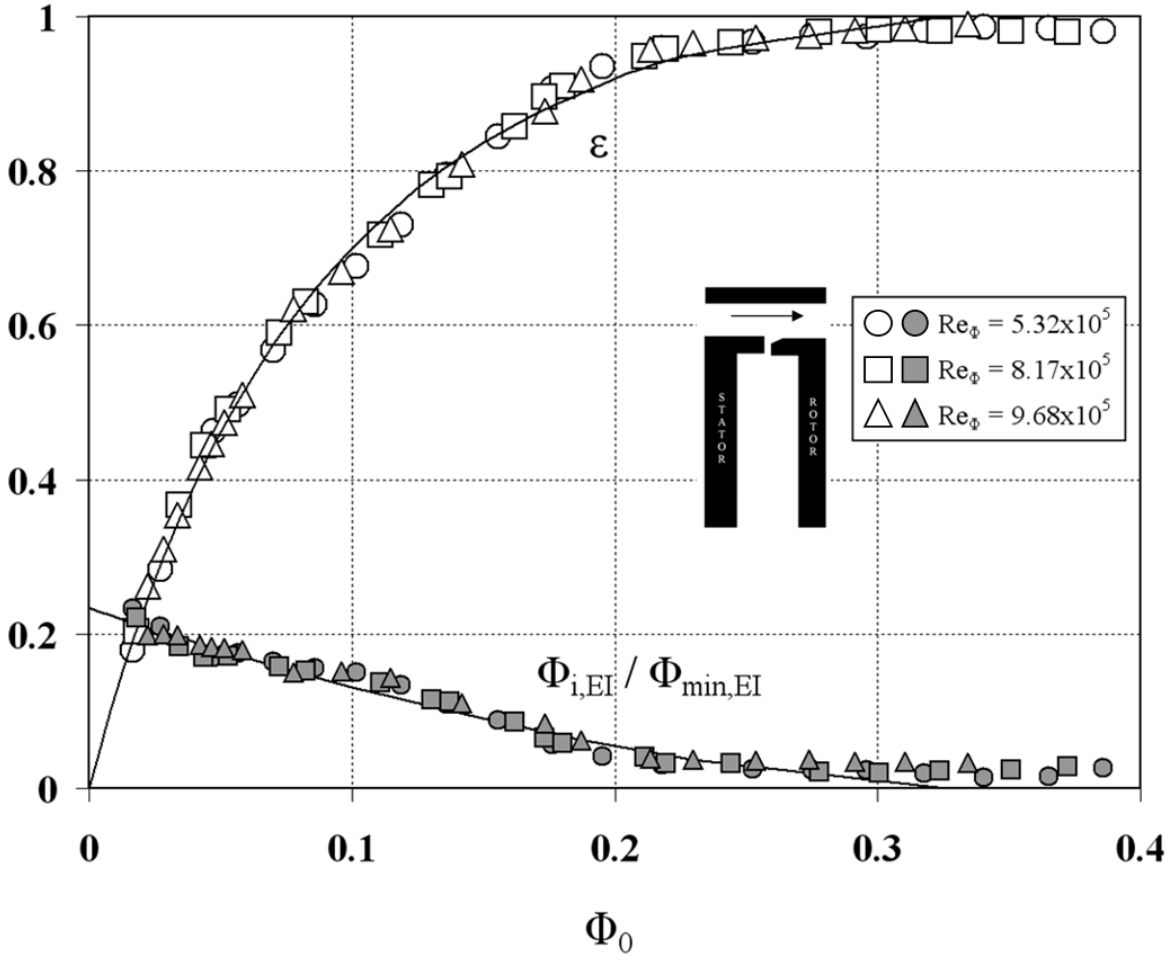

Figure 5.16 Comparison between theoretical effectiveness curves and experimental data for axial-clearance seal with EI ingress for (Re_w/Re_Φ) = 0.538
(Open symbols denote ε data; closed symbols denote $\Phi_{i,EI}/\Phi_{min,EI}$ data; solid lines are theoretical curves.)

Seal	Axial-Clearance	Radial-Clearance
$\hat{\Phi}_{min}$	0.326	0.0915
$\hat{\Phi}_{min}^{-}$	0.309	0.0869
$\hat{\Phi}_{min}^{+}$	0.344	0.0962
$\Phi_{i,EI}^{*}$	0.0764	0.0371
$\hat{\Gamma}_c$	0.476	1.32
$\hat{\Gamma}_c^{-}$	0.421	1.09
$\hat{\Gamma}_c^{+}$	0.545	1.63
n	60	54
σ	0.0146	0.0184

Table 5.3 Parameters for axial-clearance and radial-clearance seals, determined using method of Zhou *et al.* (2011) for the n data points. (^ denotes estimated value from the theory, and + - denote upper and lower bounds of 95% confidence intervals.)

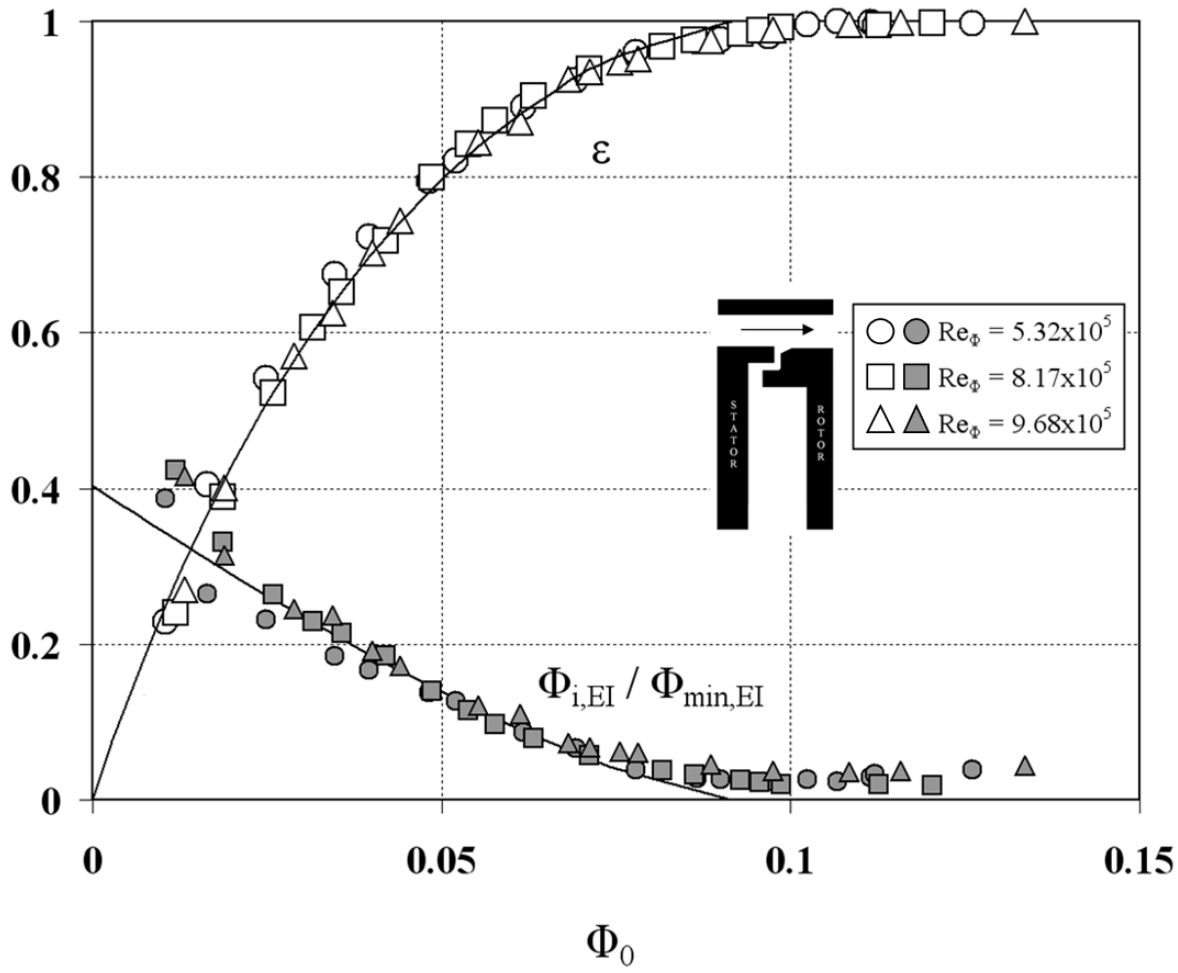

Figure 5.17 Comparison between theoretical effectiveness curves and experimental data for radial-clearance seal with EI ingress for $(Re_w/Re_\Phi) = 0.538$
(Open symbols denote ε data; closed symbols denote $\Phi_{i,EI}/\Phi_{min,EI}$ data; solid lines are theoretical curves.)

5.3.3 Rim-seal discharge coefficients

Table 5.4 shows the values of $C_{d,e}$, $C_{d,i}$ and K for the two seals. The $C_{d,e}$ were calculated from Eq. 3.33 and the values of $C_{d,i}$ were found from the corresponding value of Γ_c; K was calculated from Eq. 5.2. For each seal, the values of these three constants depends on where (*e.g.* location A or B) in the annulus ΔC_p was determined. Regardless of location, the value of $C_{d,e}$ for the radial-clearance seal is approximately 28% of that for the axial-clearance seal; the corresponding ratio for the $C_{d,i}$ values is approximately 78%.

The reduction in the amount of sealing air required to prevent ingestion for the radial-clearance seal is a direct consequence of the small value of $C_{d,e}$ for this seal, caused perhaps by the 'impinging jet phenomenon' (Owen and Rogers (1989)). This phenomenon occurs for overlapping radial-clearance seals in which the rotating disc creates an unstable radial wall jet that impinges on

the stationary part of the seal. If this is the case then this phenomenon causes a much larger reduction of $C_{d,e}$ than it does of $C_{d,i}$.

Seal	ΔC_p	Φ_{min}	Γ_c	$C_{d,e}$	$C_{d,i}$	K
Axial 'A'	0.82	0.326	0.48	0.54	0.26	0.51
Radial 'A'	0.82	0.092	1.32	0.15	0.20	0.14
Axial 'B'	0.42	0.326	0.48	0.75	0.36	0.71
Radial 'B;	0.42	0.092	1.32	0.21	0.28	0.20

Table 5.4 Discharge coefficients and K values for both seal configurations

5.4 Fluid-dynamics of the wheel-space

The fluid dynamics in the rotor-stator wheel-space can be described in terms of the radial distribution of swirl. A series of seven static pressure taps were placed along a single radial plane, with a complimentary pitot tube aligned with the static tap and situated at position z/S = 0.25 outside the stator boundary layer. The instrumentation discussed is shown schematically as Fig. 5.18 from a plan view of the stator.

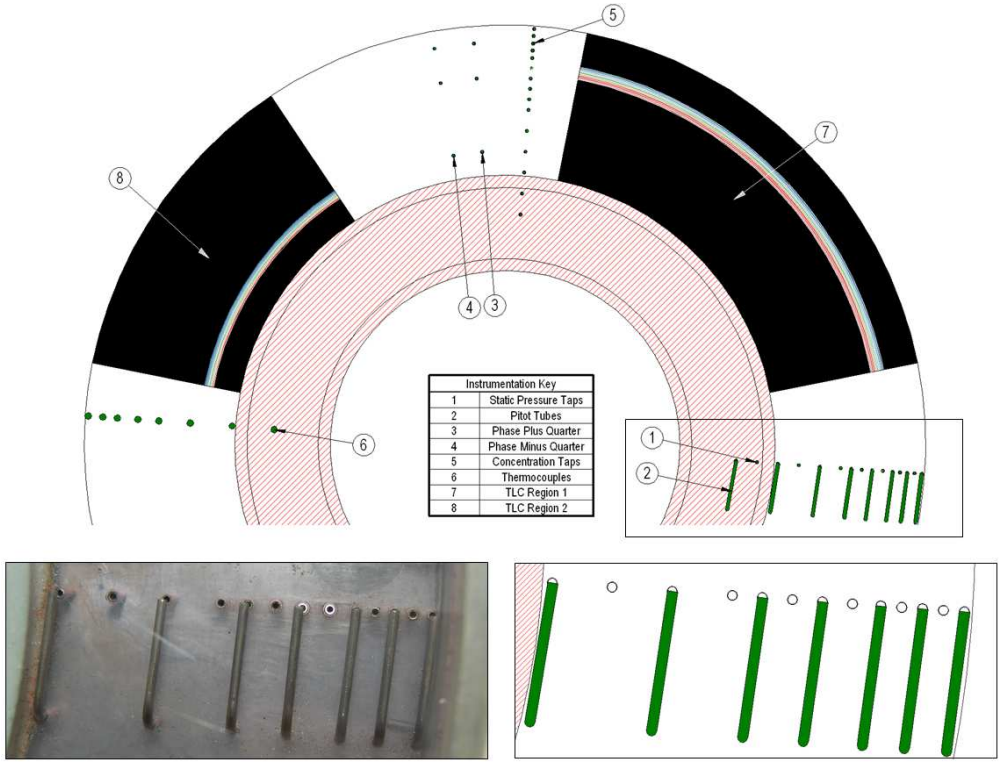

Figure 5.18 Swirl-ratio instrumentation

The core rotation speed, V_ϕ, is typically approximately 40% of the rotor disc speed for the case of turbulent flow (Childs (2010)), characterized by the swirl ratio, β

$$\beta = \frac{V_\phi}{\Omega b} \quad \text{(Equation 5.3)}$$

It is a common assumption that the swirl ratio will be decreased with the introduction of a sealing flow-rate, and increased with ingestion of usually highly swirling air from the annulus.

The swirl ratio for an inviscid core in a rotor-stator system was characterised empirically by Daily *et al.* (1964) who produced the following correlation (Eq. 5.4) based on the aspect ratio of the wheel-space. In the case of the current test facility, the core swirl ratio is thus predicted as 0.43, with the gap ratio *G* defined as *S/b*.

$$\beta = 0.49 - 0.57G \quad \text{(Equation 5.4)}$$

An alternate method described in Owen and Rogers (1989) and based on the work of Owen (1988) is to use the free-disc assumptions of von Kármán (1921). Solving the Ekman-layer equations for turbulent flow, a system with no sealant flow rate (hence $\lambda_T = 0$) also gives $\beta = 0.43$ in the inviscid core.

The turbulent flow parameter is defined below:

$$\lambda_T = \frac{C_w}{Re_\Phi^{0.8}} \quad \text{(Equation 5.5)}$$

As the sealant flow-rate and hence λ_T are increased, the rotating core is suppressed radially outwards as discussed in Section. 5.1. It is assumed that once the superposed sealant flow reaches the level of the free-disc entrainment rate (corresponding to $\lambda_{T,crit}$), the core rotation will reduce to zero. That is, once the critical value of λ_T is surpassed, the core rotation breaks down and $\beta \rightarrow 0$. Owen and Rogers (1989) calculated this critical value for turbulent flow over a free-disc, $\lambda_{T,crit} = 0.22$.

Figure 5.19 illustrates the swirl ratio distribution for the axial clearance seal (Generic # 1), shown for a number of different sealant flow-rates at the $Re_\Phi = 8.17 \times 10^5$ design point. The core rotation $\beta = 0.44$ is observed for $r/b < 0.8$, in agreement with Daily *et al.* (1964). The swirl ratio outside of the core region increases radially outward to $\beta = 0.9$ at the wheel-space periphery with the influence of highly swirling ingested flow.

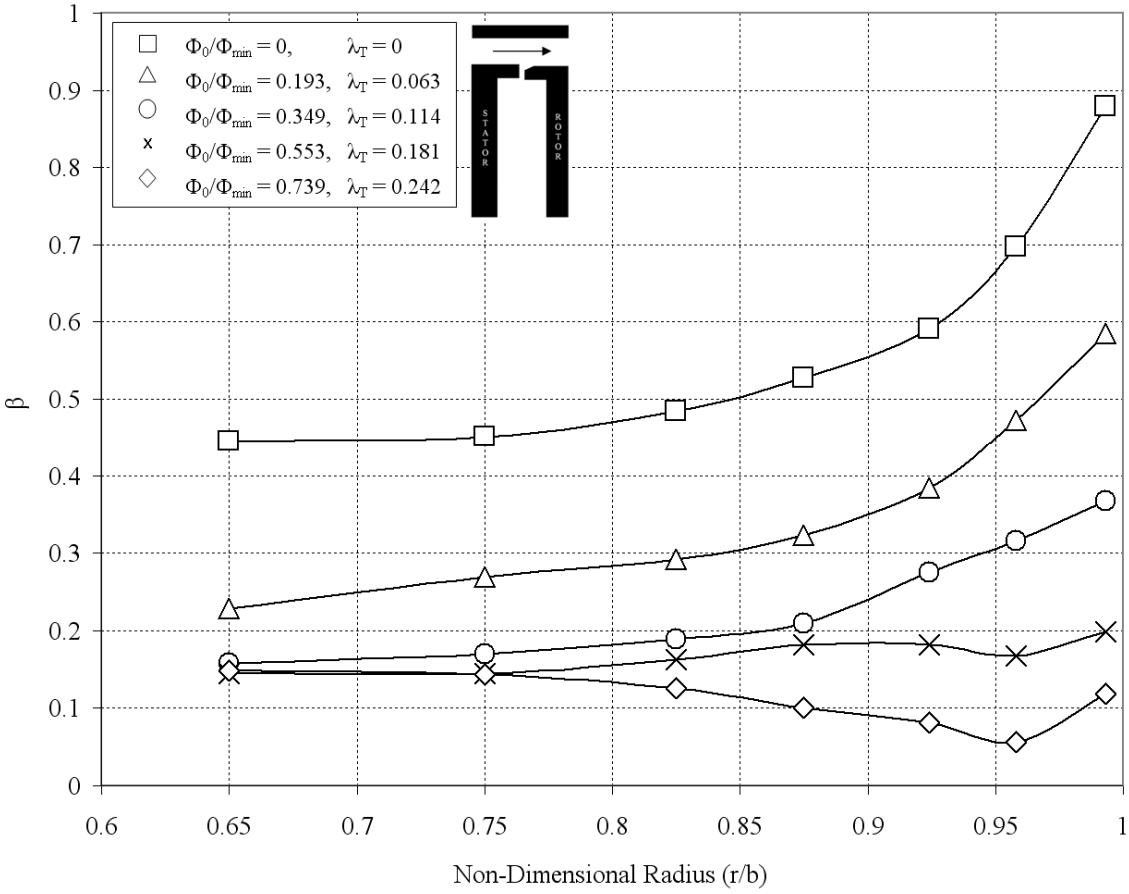

Figure 5.19 Swirl ratio distribution for axial clearance seal and different sealing flow-rates. (Lines are included for reader's convenience only.)

Increasing the sealant flow rate incrementally up to 74% of Φ_{min} caused the core rotation to diminish as the wheel-space was pressurised. The external influence at the wheel-space periphery also waned as the ingestion from the mainstream flow reduced accordingly as the sealant flow began to seal the system. As discussed, once the sealant flow is increased so that $\lambda_{T,} > 0.22$, the core rotation is seen to breakdown as $\beta \rightarrow 0$, especially at the outer radius.

Similar fluid-dynamic interpretations apply for the swirl distributions measured using the radial clearance seal (Generic # 2), shown in Fig. 5.20 for the $Re_{\Phi} = 8.17 \times 10^5$ design point. The core swirl-ratio is again seen to be approximately 0.44, in-line with the theoretical approximations, along with an external influence near the wheel-space periphery. The key difference between the two seals is that the sealant flow levels required to seal the wheel-space for the radial clearance seal are lower than the axial clearance seal. The λ_T values were therefore smaller for the radial clearance seal and therefore the rotating core did not diminish to as great an extent.

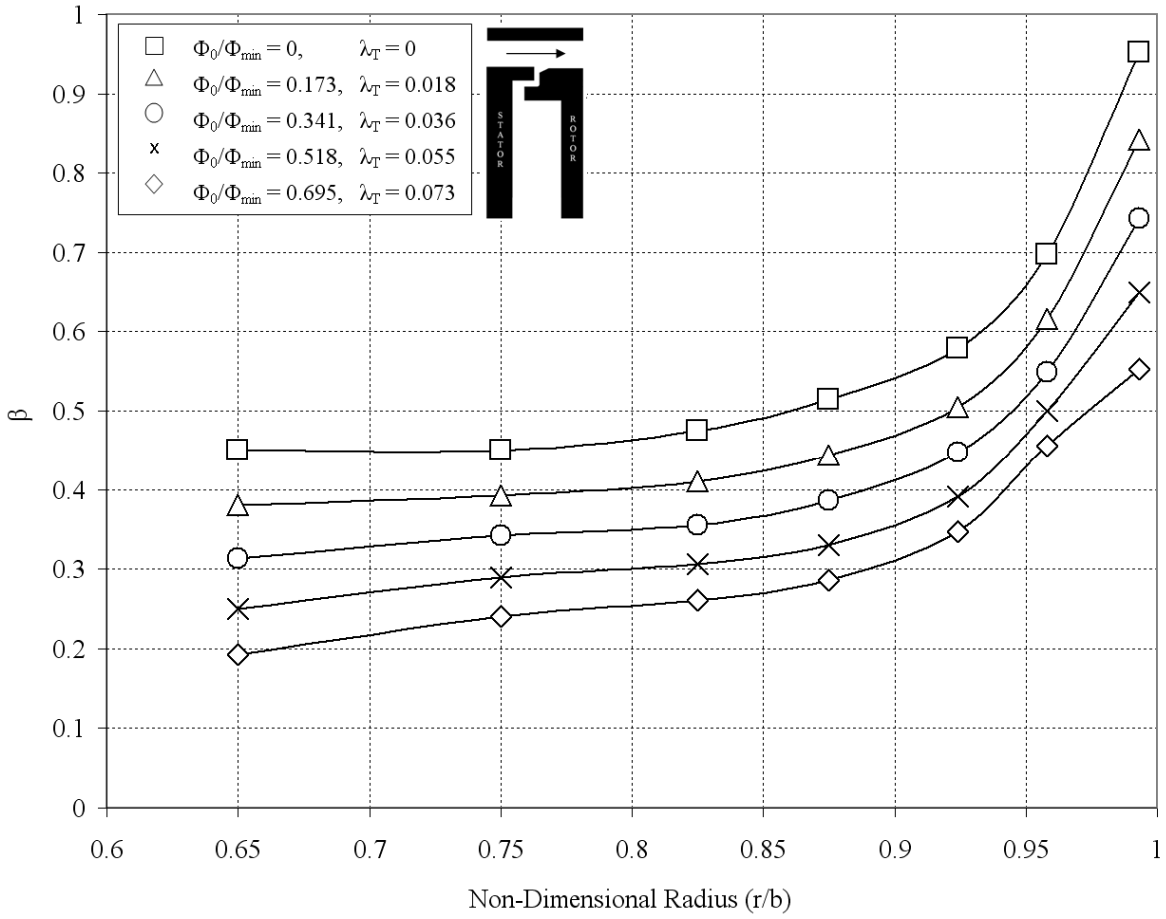

Figure 5.20 Swirl ratio distribution for radial clearance seal and different sealing flow-rates. (Lines are included for reader's convenience only.)

5.5 Practical implications

The object of this section is to suggest how the engine designer might use the experimental results presented here in conjunction with the theoretical orifice model discussed in Section 3. The model has been successful in interpreting and calculating mechanisms for EI ingress. The question arises: how could the designer estimate the sealing effectiveness in an engine?

As demonstrated here, concentration measurements made on an experimental rig can be used to determine $\Phi_{min,EI}$ and Γ_c for a particular value of ΔC_p. In principle, and within the limits of dimensional similitude, these values should apply to a geometrically-similar engine at the same operating conditions. It is often the case that, even if the geometric conditions are satisfied, the operating conditions (particularly Re_Φ and M) for the engine will differ from those for the rig. Eq 3.33 shows that, for EI ingress, $\Phi_{min,EI}$ is proportional to $\Delta C_p^{1/2}$, and it is tentatively suggested that this relationship could be used to extrapolate the results from a rig to an engine. At the design point

(Re_w/Re_Φ = 0.538), and at a fixed location in the annulus, ΔC_p, is independent of Re_Φ. At off-design conditions, $\Delta C_p \propto (Re_w/Re_\Phi)^2$. Rigs operating under quasi-incompressible fluid-dynamic conditions, as was the case here, may require compressibility corrections for ΔC_p.

Assuming that Γ_c is the same for rig and engine, Eqs 3.38 and 3.42 could then be used for design purposes. The new rig described in this thesis has been specifically designed to test this hypothesis. Future tests will determine the effect of ingress on the temperatures of the rotating and stationary surfaces in the wheel-space with the acid test being whether these rig-based results can be applied to an engine.

One final caveat relates to the importance of RI ingress, the subject of Chapter 6. Unlike EI ingress, where the pressure differences in the main gas path are dominant, RI ingress occurs when the effects of rotation in the wheel-space are dominant. Combined ingress (CI) occurs where the effects of both rotational speed and external flow are significant. If data obtained from an experimental rig are to be extrapolated to an engine then it is important to know that they are both operating in the same part of the CI domain. It has been shown in Owen *et al.* (2010a) that EI ingress cannot be assumed to occur unless $\Phi_{min,CI} / \Phi_{min,RI} > 2$.

Chapter 6: Rotationally-induced ingress

As explained in Chapter 5, hot-gas ingestion through turbine rim seals is caused principally by the circumferential variation of pressure in the external annulus. There is, however, another cause of ingress, which can occur even when the external flow is axisymmetric. The rotating fluid in the wheel-space creates a centripetal acceleration and a consequential radial gradient of pressure. The resulting pressure in the wheel-space increases with increasing radius, which means that the internal pressure can be less than that in the fluid outside the wheel-space. This pressure difference creates ingress through the seal clearance, and the 'disc-pumping effect' creates egress near the rotating turbine disc. This type of ingestion is referred to as *rotationally-induced* (RI) ingress, which is the subject of this chapter.

In many practical cases, RI ingress is negligible. However, there are some cases where its magnitude is similar to that of EI ingress; these cases are referred to as combined ingress. As stated by Owen *et al.* (2010b), it is quite probable that some previously published ingress experiments which were thought to have been conducted in the EI regime may well have been in the combined-ingress regime. More importantly, combined ingress can occur in double seals, like those illustrated in Fig. 6.1. Here the pressure asymmetries created in the external annulus are attenuated in the annular space between the inner and outer seals: EI ingress occurs through the outer seal and combined (or in the limit RI) ingress occurs through the inner seal. RI ingress is therefore not of academic interest alone, it is also of practical importance for the seal designer.

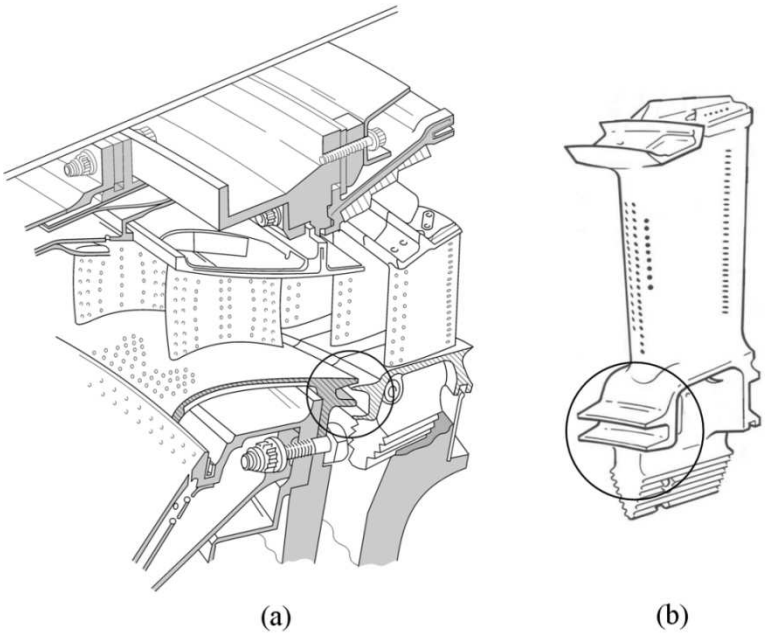

Figure 6.1 (a) Cooled turbine stage; (b) Double seal on blade

6.1 Experimental configuration

The new research facility which experimentally simulates hot gas ingestion into the wheel space of an axial turbine stage using CO_2 tracer gas, was described in Chapters 4 and 5. The test section of the facility, shown in Fig. 6.2, featured a turbine stage with 32 vanes and 41 blades.

For the RI ingestion experiments presented here, the inlet to the annulus was closed but the outlet was open to the atmosphere. As the stationary vanes and rotating blades were still present in the annulus, rotation of the disc would have created swirl in the external fluid. However, as found by Graber *et al.* (1987), the external swirl did not appear to affect RI ingress. This is shown in the experimental results presented in Section 6.3.2 where the measured value of $\Phi_{min,RI}$ for the axial-clearance seal is unaffected by rotational speed and its value is close to that of Bayley and Owen for RI ingress.

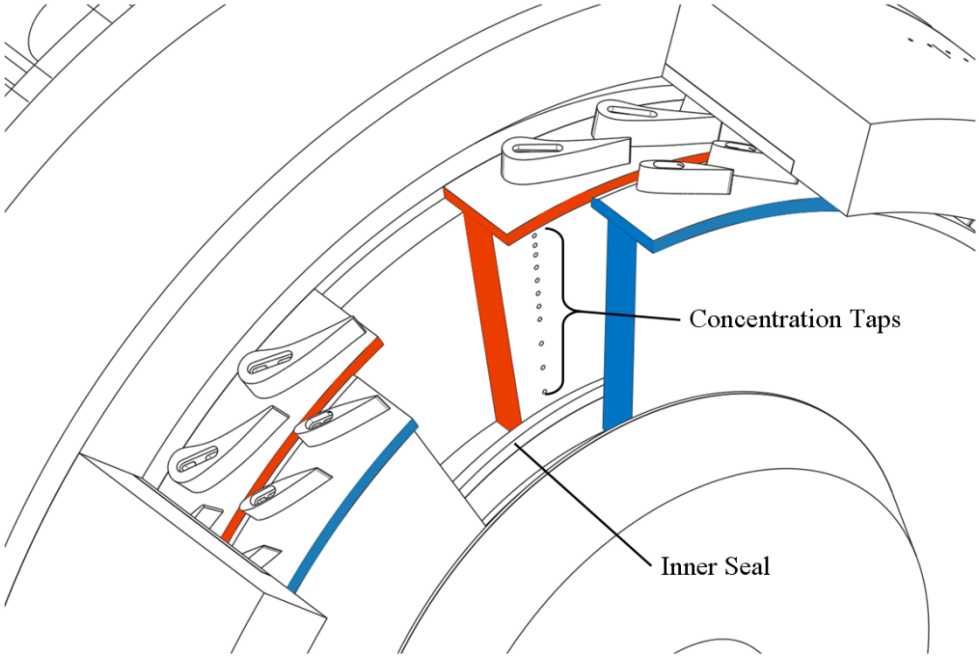

Figure 6.2 Experimental test section

Rotating fluid in the wheel-space created a radial gradient of pressure, so that the pressure inside the cavity was sub-atmospheric. The pumping action of the rotating disc caused a radial outflow of fluid, or egress, in the disc boundary layer, and the low pressure in the wheel-space caused ingress of external fluid through the rim seal into the cavity. Sealing air was introduced into the wheel-space at low radius through an inner seal. Increasing this superposed radial flow rate increased the relative pressure inside the wheel-space and consequently reduced the amount of ingested air. At sufficiently high superposed flow rates ingress did not occur.

To measure the degree of ingestion, this sealing flow was seeded with a carbon dioxide tracer gas. The variation of CO_2 gas concentration with radius ($0.55 < r/b < 0.993$) along the stator in the wheel-space was determined by sampling at 15 radial locations as illustrated in Fig. 6.1. As in Chapter 5, these measurements were used to determine the variation of ε_c (the effectiveness based on concentration on the stator at $r/b = 0.958$) with sealing flow rate. The effectiveness data is again presented in terms of $C_{w,o}$, the non-dimensional sealing flow rate, as well as Φ_0, the sealing parameter. The experimental data is compared with the RI effectiveness equations, Eqs 3.27 and 3.31, and the fitting method of Zhou *et al.* (2011a).

The two single-clearance rim seals investigated in the RI ingress experiments are the same as those described and used in Chapter 5. The stationary values of G_c were 0.0105 and 0.126 for the axial- and radial-clearance seals respectively; for the radial-clearance seal, G_c decreased to 0.119 at $Re_\Phi \sim 10^6$.

6.2 Radial variation of effectiveness on stator surface

The flow structure in a rotating-disc system depends on the value of λ_T, the turbulent flow parameter (Owen and Rogers (1989)). A value of $\lambda_T = 0.22$ is associated with the flow rate entrained by a free disc and, depending on the radius ratio of the wheel-space, values above this level are expected to suppress the core rotation in the wheel-space.

In the experiments conducted here, where $\lambda_T < 0.22$, the flow structure is expected to be similar to that shown in Fig. 6.3a. There are separate boundary layers on the rotating and stationary discs with a rotating core of inviscid fluid between the layers. Radial inflow occurs inside the boundary layer on the stator and outflow occurs inside that on the rotor; fluid migrates axially across the core from the stator to the rotor.

As discussed in Owen and Rogers (1989) and Childs (2010), the flow in an inviscid rotating fluid is governed by Coriolis forces. For rotating flow over a stationary disc, the fluid flows radially inward in the boundary layer and there is an axial flow away from the disc into the rotating core; for rotating flow over a rotating disc, where $V_\phi < \Omega r$, the fluid flows radially outward and there is an axial flow through the core towards the rotating disc.

Ingress affects this flow structure. The ingested fluid mixes with the sealing flow in a small mixing region near the rim seal. The mixed fluid then flows radially inward in the stator boundary layer, from where it is progressively entrained into the boundary layer on the rotor. If the flow is completely mixed in the outer mixing region then the concentration on the stator wall will be

invariant with radius. (For an adiabatic stator with negligible frictional heating, the wall temperature would also be invariant with radius.)

The core region is diminished in size and pushed to slightly higher radius (see Fig. 6.3b), as the wheel-space is pressurised and the superimposed sealing flow rate increased to $\Phi_{min,RI}$.

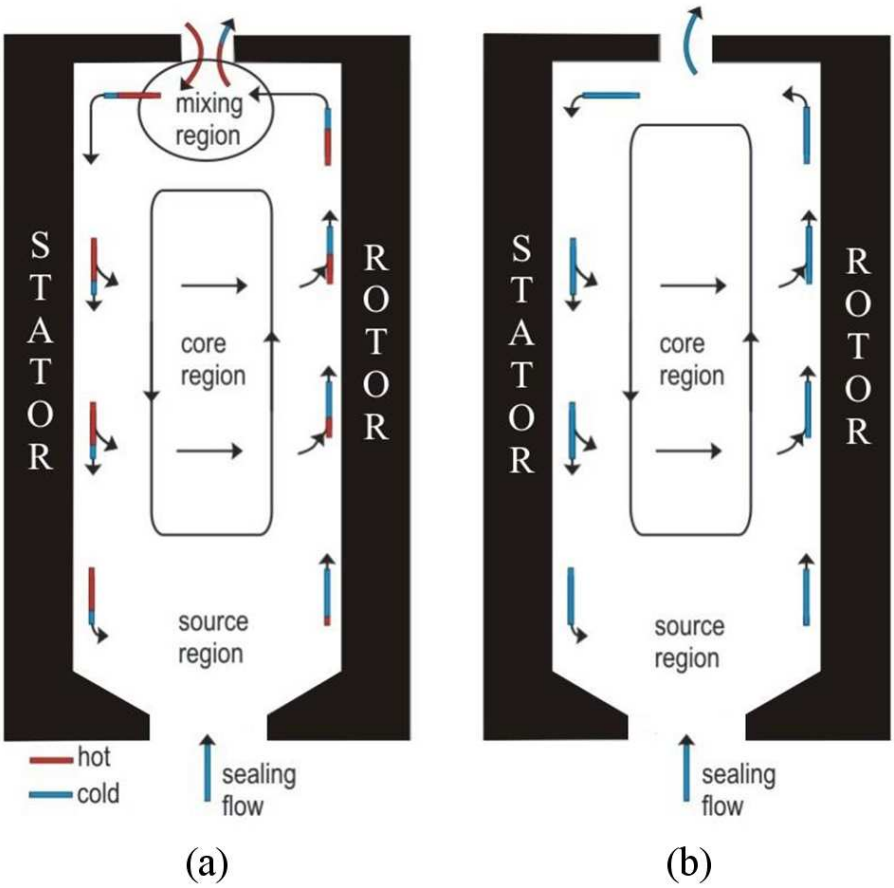

Figure 6.3 Simplified diagram of RI ingress and egress
(a) $\Phi_0 < \Phi_{min}$ (b) $\Phi_0 = \Phi_{min}$

Figure 6.4 shows the radial variation of ε_c on the stator surface for tests at $Re_\Phi = 5.3 \times 10^5$ for the axial-clearance seal; results for a test with EI ingress are shown for comparison. The tests were conducted for several values of Φ_0 / Φ_{min} and λ_T ; in all cases ingress occurred. As expected, ε_c increases as Φ_0 / Φ_{min} increases. For the RI tests, the effectiveness is virtually invariant with radius for $r/b > 0.65$, which suggests that complete mixing has occurred in a region very close to the rim seal. (The rapid increase in ε_c at the smaller radii is caused by the presence of the inner seal, which prevents, or strongly reduces, the ingestion of fluid into the 'inner wheel-space' where the sealing flow is introduced.)

EI ingress was discussed in detail in Chapter 5 but it is useful to compare the effectiveness distributions for EI with those for RI ingress. This comparison can be seen in Fig. 6.4 for λ_T = 0.020, which corresponds to the same value of Φ_0 for both cases. The sealing effectiveness for the RI case is significantly greater than that for the EI case: for the same sealing flow rates, EI ingress causes much more ingestion.

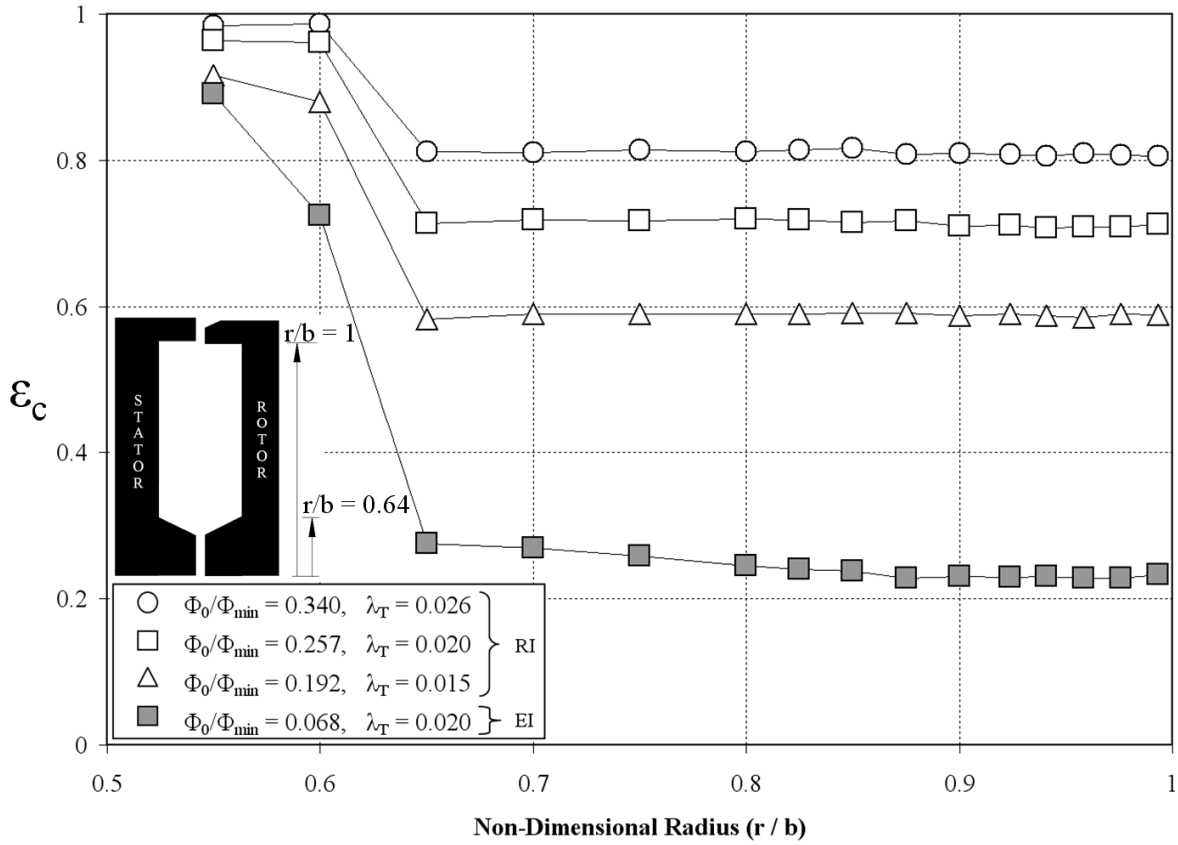

Figure 6.4 Effect of sealing flow rate on measured radial variation of effectiveness on stator surface for axial-clearance seal. (Open symbols denote RI ingress; solid symbols denote EI ingress. Lines are included for reader's convenience only.)

A similar analysis was conducted for the radial-clearance seal, where the radial variation of ε_c on the stator surface for tests at Re_Φ = 5.3 x 10^5 are shown for both RI and EI test cases in Fig. 6.5. For the both RI and EI tests, the effectiveness is virtually invariant with radius for $r/b > 0.65$, suggesting that the flow is fully mixed out in all cases. This differs from the EI results for the axial-clearance seal, possibly down to the radial seal lip pushing and compressing the mixing region towards the stator and thus promoting fully mixed out flow down the stator wall. There is thus no increase in ε_c at the lower radii as with the axial-clearance case.

The RI and EI comparison in Fig. 6.5 is for different values of λ_T, and so no flow-structure comparisons can be drawn, however the triangular data symbols are for conditions of $\Phi_0 / \Phi_{min} \approx$ 0.3 for both ingestion cases and allow for the relative performance to be considered. It can be seen

that the sealing effectiveness for the RI case is significantly greater than that for the EI case at the same Φ_0 / Φ_{min} ratio. This relative performance increase is owing to the shape and steeper gradient of the sealing effectiveness versus Φ_0 curve for RI relative to EI, discussed in Section. 6.33.

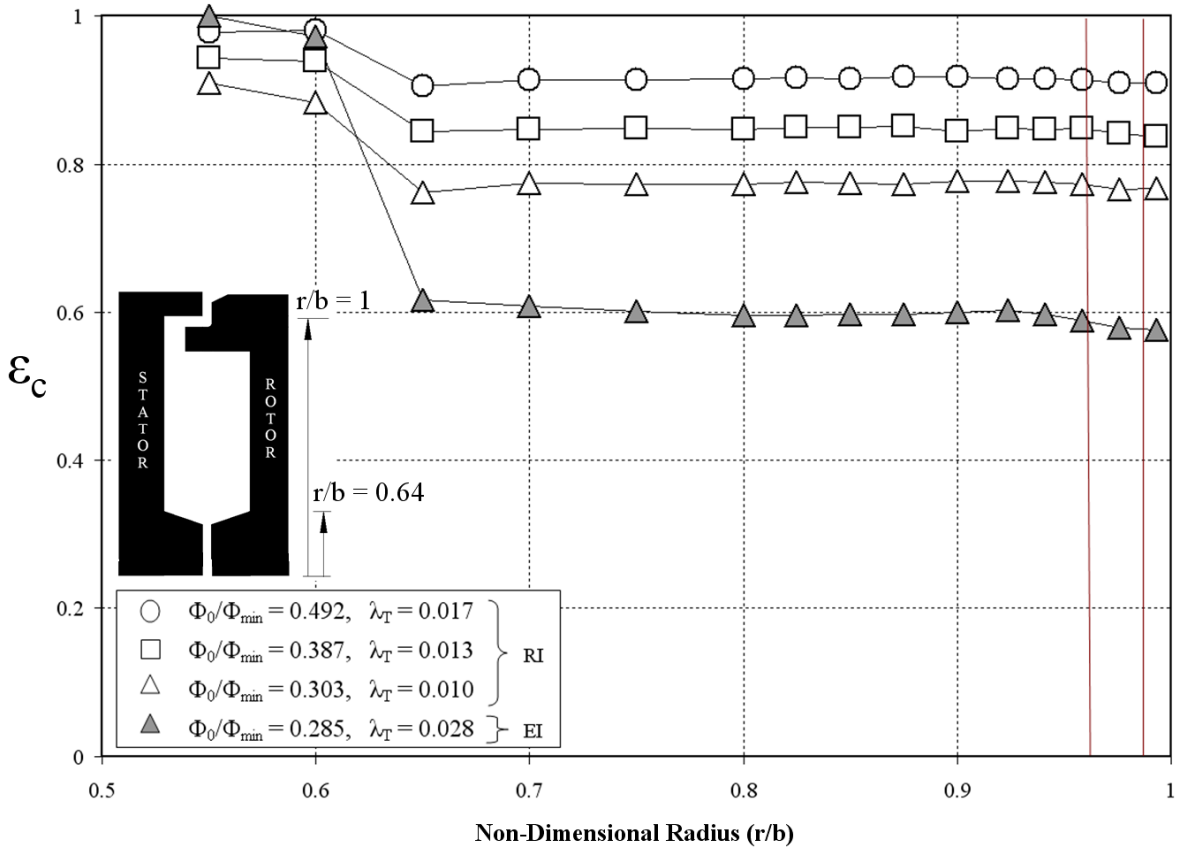

Figure 6.5 Effect of sealing flow rate on measured radial variation of effectiveness on stator surface for radial-clearance seal. (Open symbols denote RI ingress; solid symbols denote EI ingress, seal lip radius shown between vertical lines. Lines are included for reader's convenience only.)

For the results presented below, the effectiveness values were based on the concentration measurements on the stator surface at r/b = 0.958. The point r/b = 0.958 for both RI and EI and both seal configurations was deemed to be an appropriate sampling point where a constant concentration effectiveness was seen with radius for r/b > 0.85 in Figs 6.4 and 6.5.

6.3 Measurement of rim-seal effectiveness

In this section, experimental data collected using the generic axial- and radial-clearance seals shown in Fig. 5.5 are presented for the RI ingress case. The rim-seal effectiveness is measured using the concentration effectiveness, ε_c, which is defined by Eq. 3.44, collected on the stator at r/b

= 0.958. Data is presented in terms of $C_{w,o}$, the widely used non-dimensional sealing flow rate, as well as Φ_0 , the non-dimensional flow parameter used in the orifice equations. The experimental data is compared with the RI effectiveness equations, Eqs 3.27 and 3.31.

6.3.1 Rim-seal effectiveness in terms of $C_{w,0}$

Figure 6.6 shows the effect of Re_Φ on the variation of effectiveness with $C_{w,o}$, the nondimensional sealing flow rate, for the two rim seals with RI ingress. A thumb-nail sketch of the seal geometries is shown on this and all following figures. The figure illustrates that ε_c increases with increasing $C_{w,o}$, as the sealing flow pressurises the wheel-space and reduces ingestion through the rim-seal. Even allowing for the small difference between the values of G_c for the two seals, the radial-clearance seal is the more effective one. For both seals, ε_c decreases as Re_Φ increases.

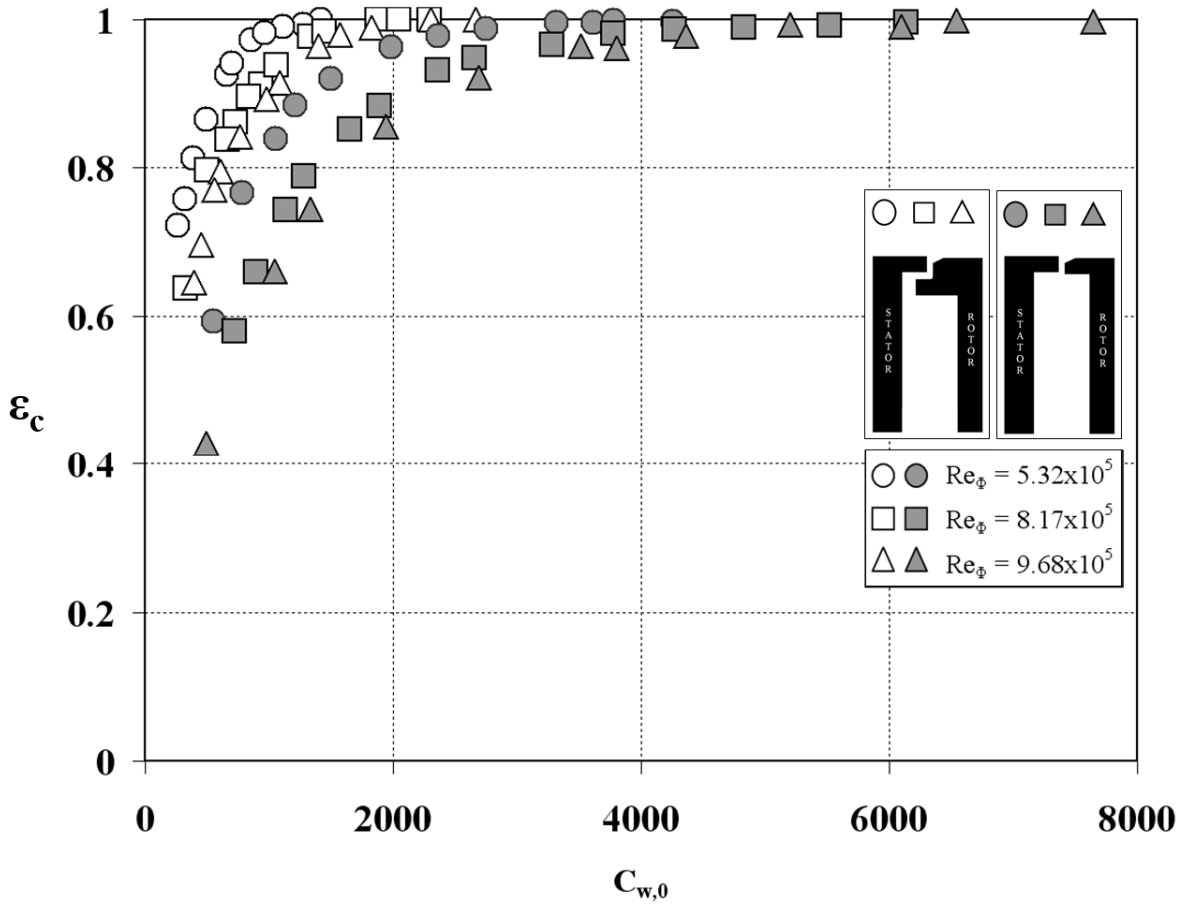

Figure 6.6 Effect of Re_Φ on measured variation of ε_c with $C_{w,o}$ for RI ingress. (Open symbols denote radial-clearance seal; solid symbols denote axial-clearance seal.)

6.3.2 Rim-seal effectiveness in terms of Φ_0

In Fig. 6.7, the data shown in Fig. 6.6 have been re-plotted versus Φ_0. Instead of having to use separate correlations for the effects of G_c and Re_Φ on ε, Φ_0 combines $C_{w,o}$, G_c and Re_Φ into a single flow parameter and collapses all the data. (As previously stated, the radial-clearance seal has slightly varying values of G_c at different Re_Φ.)

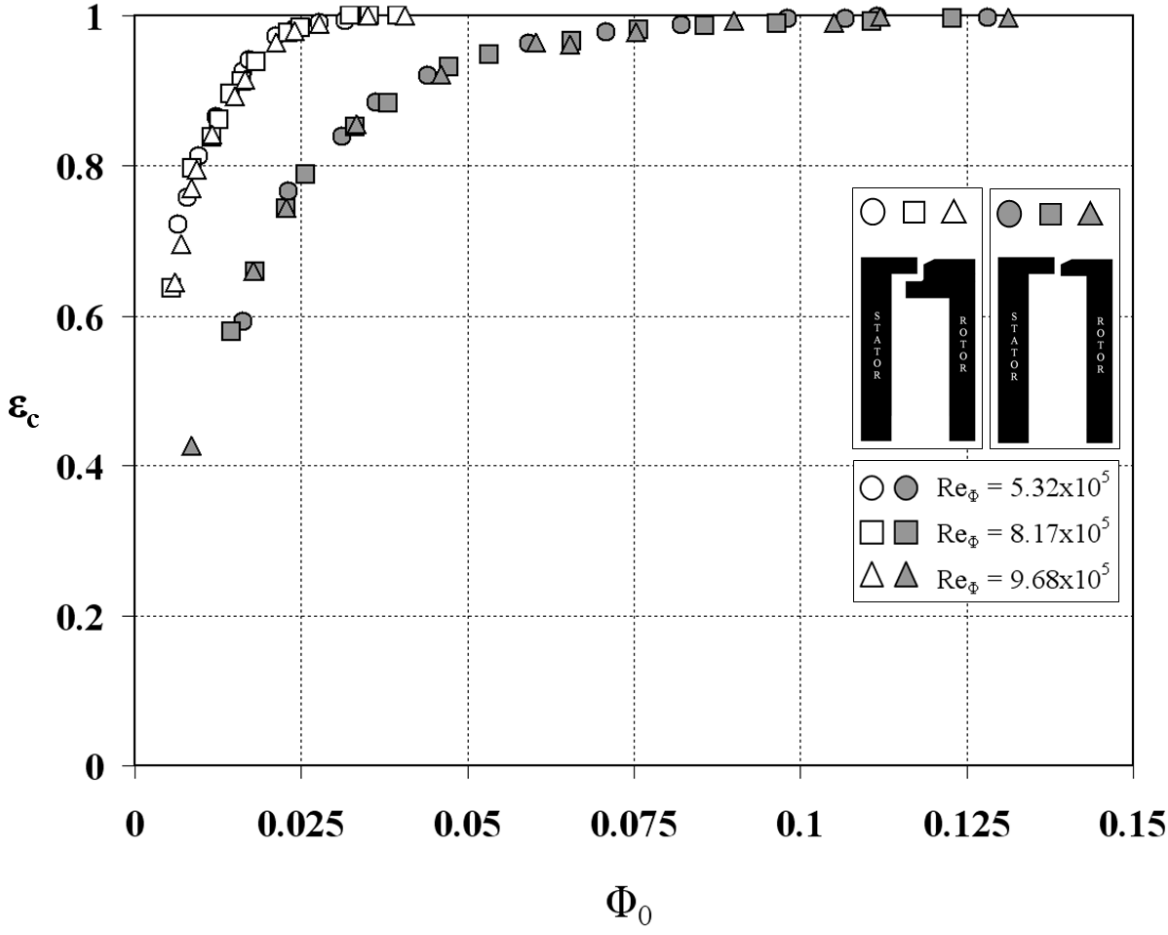

Figure 6.7 Measured variation of sealing effectiveness with Φ_0 for RI ingress. (Open symbols denote radial-clearance seal; solid symbols denote axial-clearance seal.)

Figures 6.8 and 6.9 show comparisons between the theoretical effectiveness curves and the experimental data for the two seals. The curves were based on Eqs 3.27 and 3.31, which were fitted to the data using the method of Zhou *et al*. (2011). The estimated values of $\Phi_{min,RI}$ and Γ_c and their 95% confidence intervals are shown in Table 6.1 together with the values for EI ingress from Chapter 5. The values of n, the number of data points used in the fits, and σ, the standard deviation between the data and the fitted curves, are also shown in the table. (Zhou *et al*. suggest that there should be at least 16 data points for an accurate estimate of Φ_{min}, a condition that is satisfied here.)

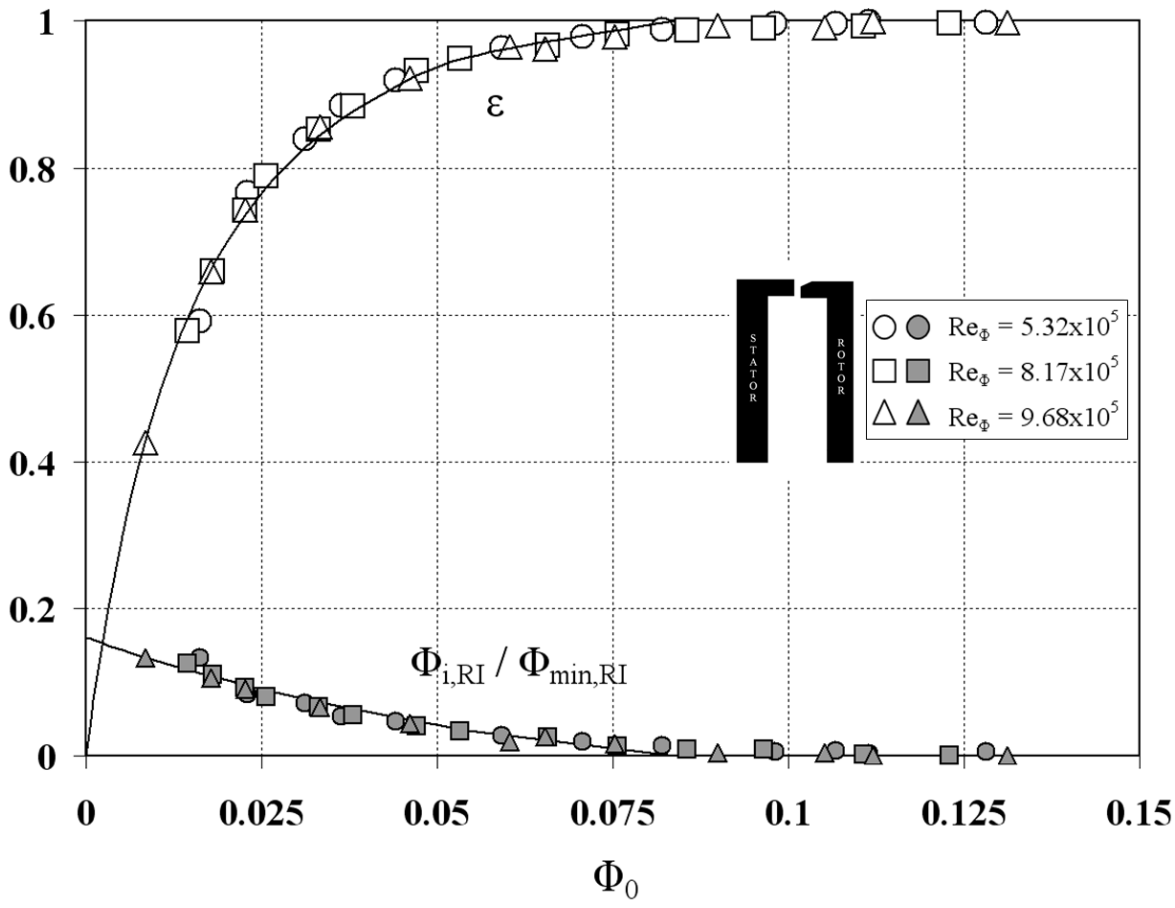

Figure 6.8 Comparison between theoretical effectiveness curves and experimental data for axial-clearance seal with RI ingress. (Open symbols denote ε data; closed symbols denote $\Phi_{i,RI}/\Phi_{min,RI}$ data; solid lines are theoretical curves.)

From the Bayley-Owen criterion for an axial-clearance seal, $\Phi_{min,RI} = 0.097$; this is around 13% larger than the value shown in Table 6.1. However, Bayley and Owen used pressure and not concentration measurements to determine their correlation. It can also be seen from Table 6.1 that the confidence intervals are around 10% of the estimated value of $\Phi_{min,RI}$. As Fig. 6.8 shows, it is very difficult to determine the precise value of Φ_0 when ε first equals unity, and consequentially there is uncertainty in the determination of $\Phi_{min,RI}$. (The value of Φ_0 at $\varepsilon = 0.95$ has a smaller uncertainty, and there is a case for using this, rather than Φ_{min}, as a design criterion for ingress.)

Both Figures 6.8 and 6.9 show very good agreement between the theoretical curves and the data; the good agreement is confirmed by the relatively small values of σ in Table 6.1. The estimated values of $\Phi_{min,RI}$ are 0.0838 and 0.0317 for the axial-clearance and radial-clearance seals, respectively. This shows that, to prevent ingestion for RI ingress, the radial-clearance seal requires approximately 38% of the air required for the axial-clearance seal.

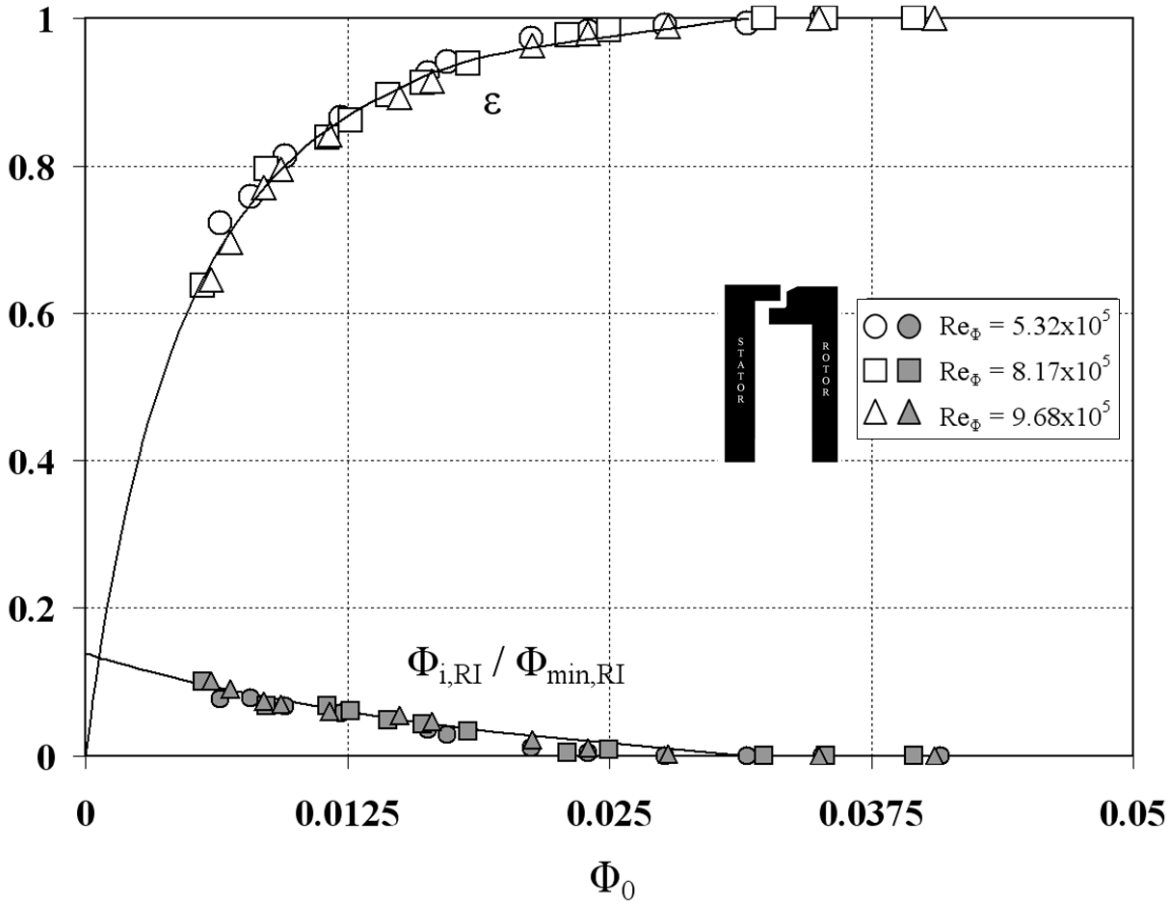

Figure 6.9 Comparison between theoretical effectiveness curves and experimental data for radial-clearance seal with RI ingress. (Open symbols denote ε data; closed symbols denote $\Phi_{i,RI}/\Phi_{min,RI}$ data; solid lines are theoretical curves.)

	RI Ingress		EI Ingress	
Seal	**Axial Clearance**	**Radial Clearance**	**Axial Clearance**	**Radial Clearance**
$\hat{\Phi}_{min}$	0.0838	0.0317	0.326	0.0915
$\hat{\Phi}_{min}^{-}$	0.0773	0.0296	0.309	0.0869
$\hat{\Phi}_{min}^{+}$	0.0921	0.0342	0.344	0.0962
$\Phi_{i,RI}^{*}$	0.0135	0.00446	0.0764	0.0371
$\hat{\Gamma}_c$	0.342	0.288	0.476	1.32
$\hat{\Gamma}_c^{-}$	0.297	0.257	0.421	1.09
$\hat{\Gamma}_c^{+}$	0.390	0.320	0.545	1.63
n	38	36	60	54
σ	0.0121	0.00986	0.0146	0.0184

Table 6.1 Parameters for axial-clearance and radial-clearance seals for RI and EI ingress. (^ denotes estimated value from the theoretical curve, and + - denote upper and lower bounds of 95% confidence intervals.)

Figures 6.8 and 6.9 also show the variation of $\Phi_{i,RI} / \Phi_{min,RI}$ with Φ_0 according to Eq. 3.31. This variation is of importance to the seal designer as it shows how much ingested flow enters the wheel-space when $\varepsilon < 1$. Table 6.1 includes values of $\Phi_{i,RI}^*$; this is the maximum value of $\Phi_{i,RI}$, which occurs when $\Phi_0 = 0$. It follows from the values in the table that $\Phi_{i,RI}^* / \Phi_{min,RI} = 0.17$ for the axial-clearance seal and 0.14 for the radial-clearance seal. That is, for either seal, the maximum ingress is only a relatively small fraction of the flow rate needed to prevent ingestion.

6.3.3 Comparison of seal performance for EI and RI ingress

Figure 6.10 shows the effectiveness data and theoretical curves for both seals with EI and RI ingress; the EI results were presented previously in Chapter 5.

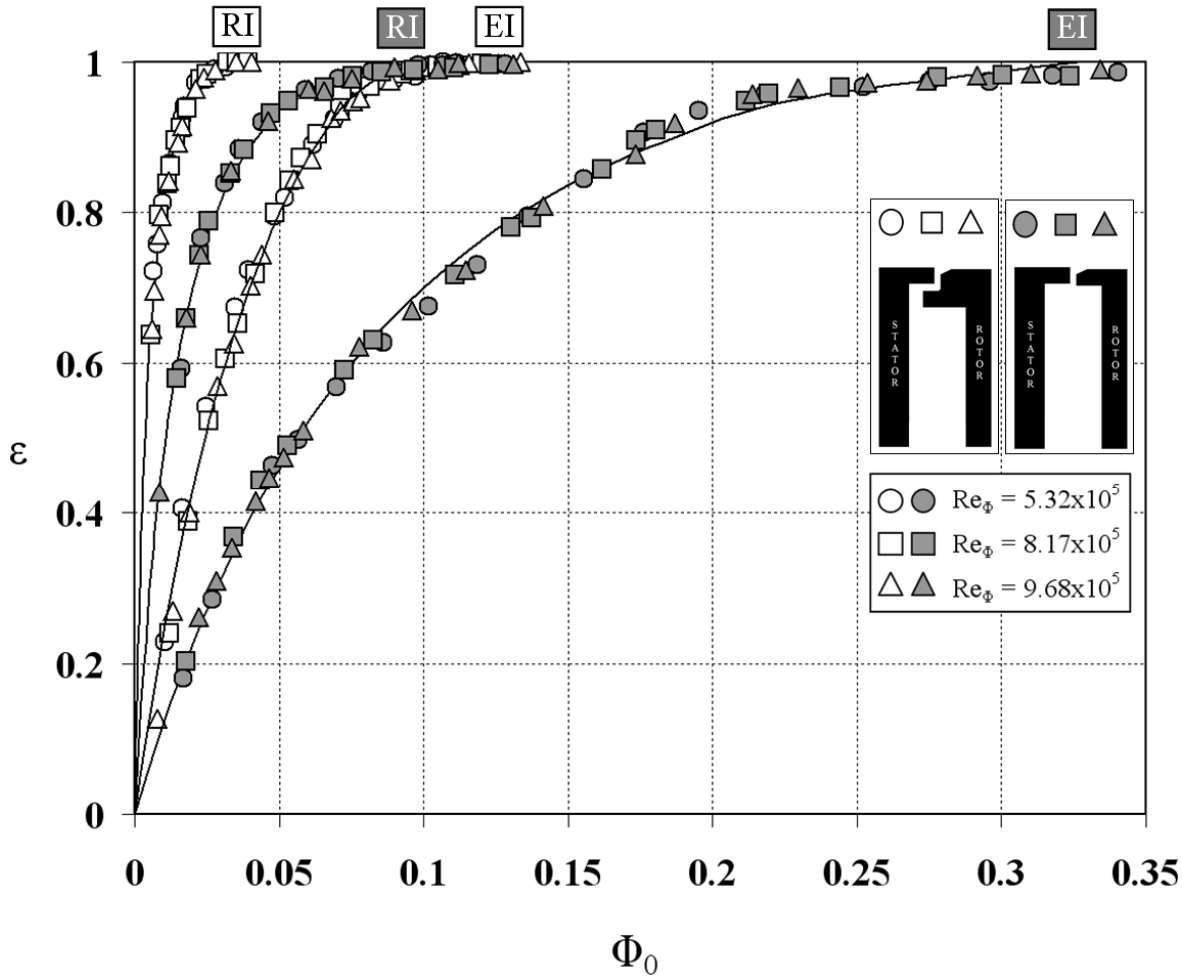

Figure 6.10 Comparison of sealing effectiveness for EI and RI ingress. (Open symbols denote radial-clearance seal; solid symbols denote axial-clearance seal; solid lines are theoretical curves.)

It can be seen from Table 6.1 that, for RI ingress, the ratio of Φ_{min} for the radial-clearance seal to that required for the axial-clearance seal is around 38%; for EI ingress, the ratio is around 26%. That is, for both EI and RI ingress, the radial-clearance seal is significantly more effective that the axial-clearance seal. This result is consistent with the experiments of Phadke and Owen (1988a) for RI ingress and Bohn and Wolff (2003) for EI ingress. It can also be seen from Table 6.1 that the value of Φ_{min} for an axial-clearance seal for RI ingress is similar to that for a radial-clearance seal for EI ingress.

Owen *et al.* (2010b) suggested that EI ingress only occurs when $\Phi_{min} > 2\ \Phi_{min,RI}$ and combined ingress occurs below this limit. In the experiments conducted here, the ratio of EI to RI ingress was 3.9 and 2.9 for the axial- and radial-clearance seals, respectively. These values confirm that the EI tests were outside the combined-ingress region.

6.4 Practical implications

The results presented in Chapters 5 and 6 address important design questions: how much sealing air is required to prevent ingestion and when ingress occurs how much gas enters the wheel-space? The experiments, the orifice model and the statistical technique used to fit the theoretical curves to the data provide a powerful method of quantifying the answers to both these questions. The combined techniques of experiment and theory are valuable tools which, used carefully, should be of value to the designer.

There are, however, some important questions that remain unaddressed. What is the effect of ingested hot gas on the heat transfer to the metal surfaces in the turbine wheel-space? Can the results obtained from an experimental rig operating at incompressible-flow conditions (which was the case for most of the experiments described here) be extrapolated to engine conditions? What happens to the sealing effectiveness at off-design conditions? Can the methods used here for simple single rim seals be used to optimise complex double seals?

Chapter 7: Performance characteristics of double seals

A typical turbine stage is shown in Fig. 7.1 featuring a double-clearance rim-seal geometry. Here the circumferential variation in pressure is attenuated in the annular space between the two seals. If the annular space is large enough to damp out the pressure asymmetry, EI ingress can dominate for the outer seal and RI ingress can dominate for the inner one. This optimum condition will form the *ultimate* double seal (discussed in Section 7.6). When the external pressure asymmetry is not completely attenuated in the intermediate annulus the inner seal will likely operate in the *combined ingress* (CI) regime.

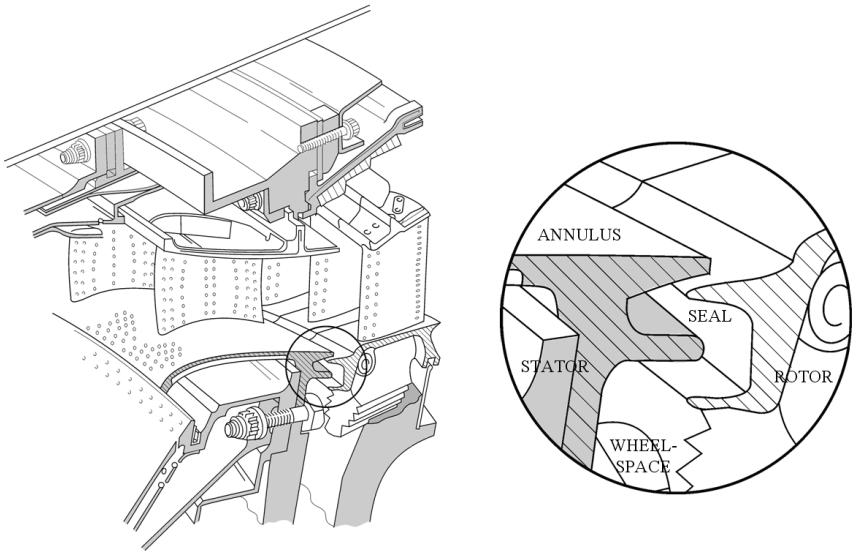

Figure 7.1: (a) Typical high-pressure gas-turbine stage; (b) detail of rim seal

7.1 Experimental configuration

The research facility which experimentally simulates hot gas ingestion into the wheel space of an axial turbine stage using CO_2 tracer gas, is again used, as was described in Chapters 4 and 5, but this time in a double seal configuration. In order to fully understand the performance characteristics of double seals, it was essential to test all seals under both EI and RI conditions.

For the RI ingestion tests presented here, the inlet to the annulus was closed but the outlet was open to the atmosphere. As explained in Chapter 6, the stationary vanes and rotating blades were still present in the annulus, and although the rotation of the blades would have created swirl in

the external fluid, it was appropriate to assume that these RI tests used a quiescent atmosphere. The EI tests were conducted at the three design point conditions discussed in Section 4.1.1. The theoretical effectiveness equations (Section 3.1) were fitted to the experimental data to produce estimates of Γ_c and Φ_{min} for each case.

Two different double-clearance rim seals were investigated. These are shown diagrammatically in Fig. 7.2, with geometric details (static and under rotation) given in Table 7.1. Generic # 3 seal features a radial-clearance outer and an axial-clearance inner seal. Generic # 4 seal features axial-clearance inner and outer seals.

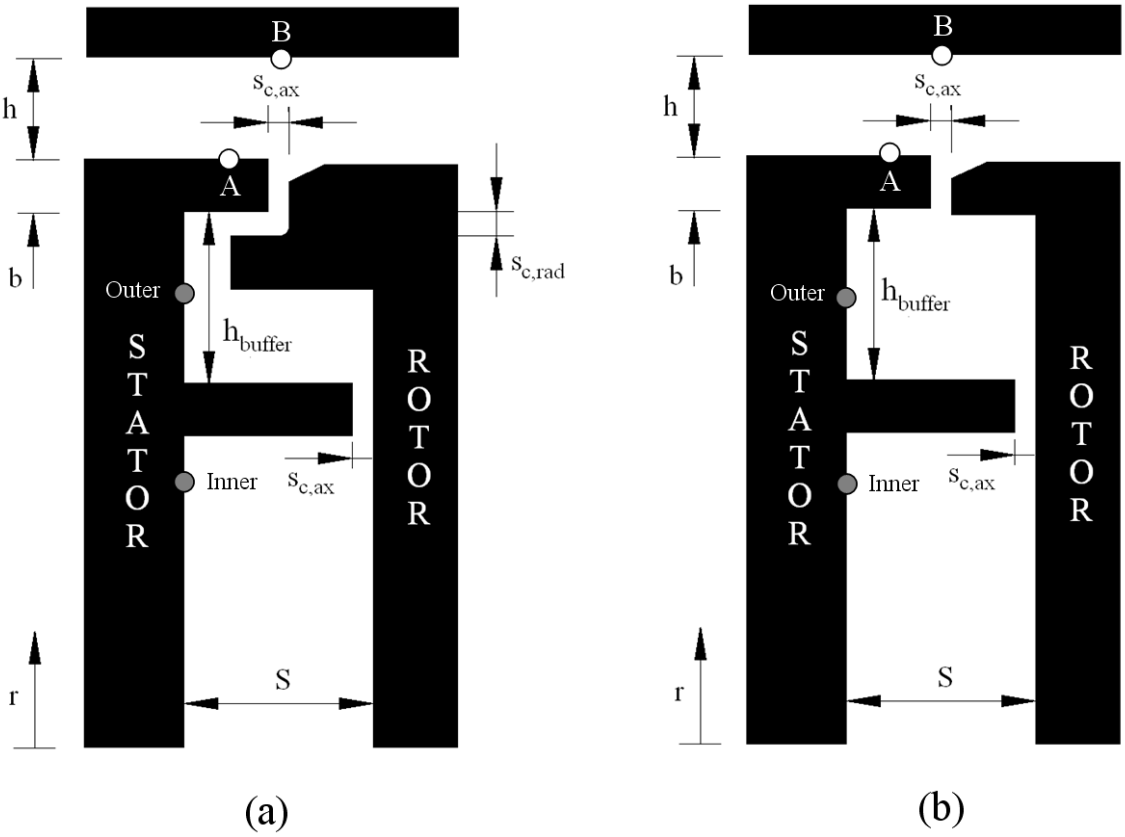

Figure 7.2: (a) Generic # 3 – Radial, axial clearance combination seal,
(b) Generic # 4 – Double axial-clearance seal

The circumferential variation of static pressure in the annulus was measured from 15 taps (each 0.5 mm diameter) arranged across one vane pitch, as described in Chapter 5; these taps were located in the vane platform 2.5 mm downstream of the vane trailing edge (location A) and in the outer casing above the centre-line of the seal clearance (location B), as marked in Fig. 7.2.

Displacement transducers were used to measure the radial growth of the radial-clearance seal under rotation, from which the operating seal clearances were determined. As the outer clearance seal from Generic # 3 is the same radial clearance seal insert featured in Chapter 4 and 5, the running clearances were hence the same.

Geometric Symbol	Radial-Axial Clearance Seal "Generic # 3"	Double-Axial Clearance Seal "Generic # 4"
h	10.0 mm	
b	190 mm	
S	20.0 mm	
h_{buffer}	16.5 mm	
$s_{c,ax}$	2.00 mm	
$G_{c,ax}$	0.0105	
$s_{overlap}$	3.70 mm	-
$s_{c,rad,0}$ (0 rpm)	2.40 mm	-
$G_{c,rad,0}$ (0 rpm)	0.0126	-
$G_{c,rad}$ (2000 rpm)	0.0124	-
$G_{c,rad}$ (3000 rpm)	0.0121	-
$G_{c,rad}$ (3500 rpm)	0.0119	-

Table 7.1 Geometric properties for the double seal configurations

Sealing air was introduced into the wheel-space at a low radius through an inner seal. Increasing this superposed radial flow rate increased the relative pressure inside the wheel-space and consequently reduced the amount of ingested air. At sufficiently high superposed flow rates ingress did not occur.

To measure the degree of ingestion, this sealing flow was seeded with a carbon dioxide tracer gas. The variation of CO_2 gas concentration with radius ($0.55 < r/b < 0.875$ and $0.924 < r/b < 0.993$) along the stator in the wheel-space was determined by sampling at 14 radial locations as discussed in Section 7.4. The 15th tap at $r/b = 0.9$ was covered by the stator seal lip and hence decommissioned.

As in Chapter 5, these measurements were used to determine the variation of ε_c with sealing flow rate. With the double seals however, two appropriate sampling points were chosen at r/b values of 0.958 and 0.85, corresponding to the intermediate annulus and inner wheel-space, respectively. These were termed the outer and inner sampling points and are highlighted in Fig. 7.2. The nomenclature associated with ε_c measured at the two sampling points is discussed in Section 7.2, along with the reasons for choosing dual sampling points. The effectiveness data is presented in terms of Φ_0, the sealing parameter, and compared with the effectiveness equations derived in Section 3.1 and the fitting method of Zhou *et al.* (2011a).

7.2 Appropriate sealing effectiveness for double seals

To be meaningful, all definitions of sealing effectiveness should equal unity when the ingress is zero and should equal zero when there is no sealing flow. In order to explain the double-seal variant, it is necessary to re-visit the definition of sealing effectiveness, both theoretically and experimentally for single seals.

7.2.1 Definition of sealing effectiveness for single seals

The effectiveness used in the orifice model is based on the ratio of the isentropic mass flow rates of ingress and egress, and the model ignores the friction, diffusion, heat transfer and mixing that occurs in the physical situation. The term *theoretical effectiveness* is used here for ε, which is defined as

$$\varepsilon = 1 - \frac{\dot{m}_i}{\dot{m}_e} = \frac{\dot{m}_o}{\dot{m}_o + \dot{m}_i} \quad \text{(Equation 7.1)}$$

where the subscripts *e*, *i* and *o,* respectively denote the egress, ingress and sealing flows. Expressed in terms of the sealing parameter Φ, Eq. 7.1 becomes

$$\varepsilon = 1 - \frac{\Phi_i}{\Phi_e} = \frac{\Phi_0}{\Phi_e} = \frac{\Phi_0}{\Phi_0 + \Phi_i} \quad \text{(Equation 7.2)}$$

It follows that

$$\frac{\Phi_i}{\Phi_0} = \varepsilon^{-1} - 1 \quad \text{(Equation 7.3)}$$

It is difficult (and unnecessary) to determine ε experimentally, and instead concentration measurements are used to determine the concentration effectiveness, ε_c. This is defined for single clearance rim-seals as

$$\varepsilon_c = \frac{c_s - c_a}{c_0 - c_a} \quad \text{(Equation 7.4)}$$

where the subscripts *a*, *o* and *s*, respectively denote the air in the annulus, the sealing air at inlet, and the surface of the stationary disc. In particular, $\varepsilon = 1$ when $c_s = c_o$ (zero ingress) and $\varepsilon_c = 0$ when $c_s = c_a$ (zero sealing flow).

The effectiveness equations (Section 3.1), which are derived from the orifice model and which express the theoretical relationship between ε and Φ_0, include two unknown parameters, Γ_c and Φ_{min}. These two parameters, which replace the two unknown discharge coefficients in the orifice model, are respectively the ratio of the discharge coefficients (for ingress and egress) and the minimum value of Φ_0 necessary to prevent ingress.

The effectiveness equations can be fitted to the values of ε_c and Φ_0, measured in the concentration tests, and the optimum values of Γ_c and Φ_{min} can then be estimated. *In effect, these optimum values of Γ_c and Φ_{min} transform the theoretical effectiveness (based on isentropic mass flow rates) into a concentration effectiveness (including viscous, diffusion and mixing effects).*

7.2.2 Definition of sealing effectiveness for double seals

Consider a double seal with inner and outer radii b' and b and clearances s_c' and s_c, respectively. (Note: primes are used to denote the inner seal.) As shown in Fig. 7.3, locations 1, 2 and 3 refer respectively to the wheel-space radially-inward of the inner seal, the annulus between the seals, and inside the outer annulus radially-outward of the outer seal. The subscripts 0, 1, 2 and 3 for the concentration refer respectively to the sealing flow at inlet, the stator at location 1, the stator at location 2 and the annulus.

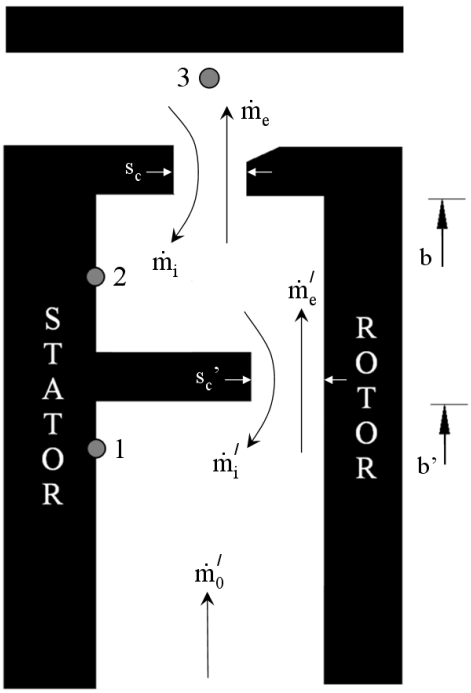

Figure 7.3 Simplified diagram of double seal

There are several ways of defining the concentration effectiveness for the double seal. For example, for the inner seal with a concentration effectiveness $\varepsilon_{c,12}$, it could be assumed that $\varepsilon_{c,12} = 0$ when $c_1 = c_2$ and that $\varepsilon_{c,12} = 1$ when $c_1 = c_0$. Hence, *for the inner seal*,

$$\varepsilon_{c,12} = \frac{c_1 - c_2}{c_0 - c_2} \qquad \text{(Equation 7.5)}$$

For the outer seal, it could be assumed that $\varepsilon_{c,23} = 0$ when $c_2 = c_3$ and that $\varepsilon_{c,23} = 1$ when $c_2 = c_0$. Hence, *for the outer seal*,

$$\varepsilon_{c,23} = \frac{c_2 - c_3}{c_0 - c_3} \qquad \text{(Equation 7.6)}$$

For the combined seals, it could be assumed that $\varepsilon_{c,13} = 0$ when $c_1 = c_3$ and that $\varepsilon_{c,13} = 1$ when $c_1 = c_0$. Hence, *for the combined seals*,

$$\varepsilon_{c,13} = \frac{c_1 - c_3}{c_0 - c_3} \qquad \text{(Equation 7.7)}$$

However, if we consider the theoretical effectiveness based on mass flow rates, as shown in Eqs 7.1 and 7.2 for a single seal, there are only *two* appropriate definitions of effectiveness:

$$\varepsilon_{23} = \frac{\Phi_0}{\Phi_0 + \Phi_i} \qquad \text{(Equation 7.8)}$$

$$\varepsilon_{13} = \frac{\Phi_0}{\Phi_0 + \Phi_i'} \qquad \text{(Equation 7.9)}$$

where Φ_i and Φ_i' are the respective nondimensional ingress parameters for the outer and inner seals. This creates a paradox: why should there be more definitions for ε_c than for ε ?

To understand this paradox, it can be shown from Eqs 7.5 to 7.7 that

$$\varepsilon_{c,12} = \frac{\varepsilon_{c,13} - \varepsilon_{c,23}}{1 - \varepsilon_{c,23}} \qquad \text{(Equation 7.10)}$$

For $\Phi_0 < \Phi_{min}$, Eq. 7.10 implies that $\varepsilon_{c,12} \neq \varepsilon_{c,13}$. This in turn means that these definitions produce two different values of Φ_i', the ingress parameter for the inner seal. This is physically impossible: Eqs 7.5 and 7.7 are therefore inconsistent.

There is another factor. Although c_2 might be the correct concentration to determine ingress through the outer seal, there is no reason to believe that it is the appropriate value for ingress through the inner one. In fact, it is shown in Section.7.5 that the measured effectiveness for the outer seal does not equal that for the equivalent single seal. This raises doubts about whether c_2 is the appropriate value for either the inner or the outer seal. *For these reason, it is suggested that only Eq. 7.7 should be used for comparison between different double seals*. However, for tentative comparison of the outer seal with that of a appropriate single seal alternative, data for $\varepsilon_{c,23}$, with

the concentration data recorded at the "outer wheel-space" sample point designated '2' and in the external annulus designated '3' will also be presented.

7.3 Rim-seal effectiveness in terms of Φ_0

In this section, experimental data collected for both double seal configurations shown in Fig. 7.2 are presented for both the EI and RI ingress cases. The rim-seal effectiveness is measured using two definitions of concentration effectiveness: $\varepsilon_{c,23}$, which is defined by Eq. 7.6 and collected on the stator at r/b = 0.958, and $\varepsilon_{c,13}$ which is defined by Eq. 7.7 and collected on the stator wall at r/b = 0.850. Data is presented in terms of Φ_0 , and is compared with the appropriate effectiveness equations for EI and RI ingress.

7.3.1 Axial-radial double-clearance seal

Figures 7.4 and 7.5 show comparisons between the theoretical curves and the experimental data for the axial-radial double-clearance seal (Generic # 3, Fig. 7.2) under the EI testing conditions specified in Section 7.1. Note that the outer radial-clearance seal has slightly varying values of G_c at different Re_Φ, as shown in Table 7.1. The outer clearance seal is used to define G_c and used in the formulation of Φ_0. For the design condition (for which the ratio Re_W / Re_Φ = 0.538), the rim seals are shown to be characterised by $\Phi_{min,EI}$, which is independent of Re_Φ.

The estimated values of $\Phi_{min,EI}$ and Γ_c and their 95% confidence intervals are shown in Table 7.2. The number of data points n used in the fits, and σ, the standard deviation between the data and the fitted curves, are also shown in the table. (Zhou *et al*. suggest that there should be at least 16 data points for an accurate estimate of Φ_{min}, a condition that is again satisfied here.)

Figures 7.4 and 7.5 show good agreement between the theoretical curves and the data; the good agreement is confirmed by the relatively small values of σ in Table 7.2. The estimated values of $\Phi_{min,EI}$ are 0.103 and 0.0822 using the definition of concentration effectiveness as $\varepsilon_{c,23}$ and $\varepsilon_{c,13}$, respectively. This shows that, to prevent ingestion into the inner wheel-space under EI conditions, approximately 80% of the air required to seal the outer seal is required. The data are shown on the same plot in Section 7.3.3.

Figures 7.4 and 7.5 also show the variation of $\Phi_{i,EI}$ / $\Phi_{min,EI}$ with Φ_0 according to Eq. 3.42. This variation is of importance to the seal designer as it shows how much ingested flow enters the wheel-space when ε < 1. Table 7.2 includes values of $\Phi_{i,EI}^*$; this is the maximum value of $\Phi_{i,EI}$, which occurs when Φ_0 = 0. It follows from the values in the table that $\Phi_{i,EI}^*$ / $\Phi_{min,EI}$ = 0.571 and 0.160 using the definition of concentration effectiveness as $\varepsilon_{c,23}$ and $\varepsilon_{c,13}$, respectively. That is, for

either cavity, the maximum ingress is no more than 60% of the flow rate needed to prevent ingestion.

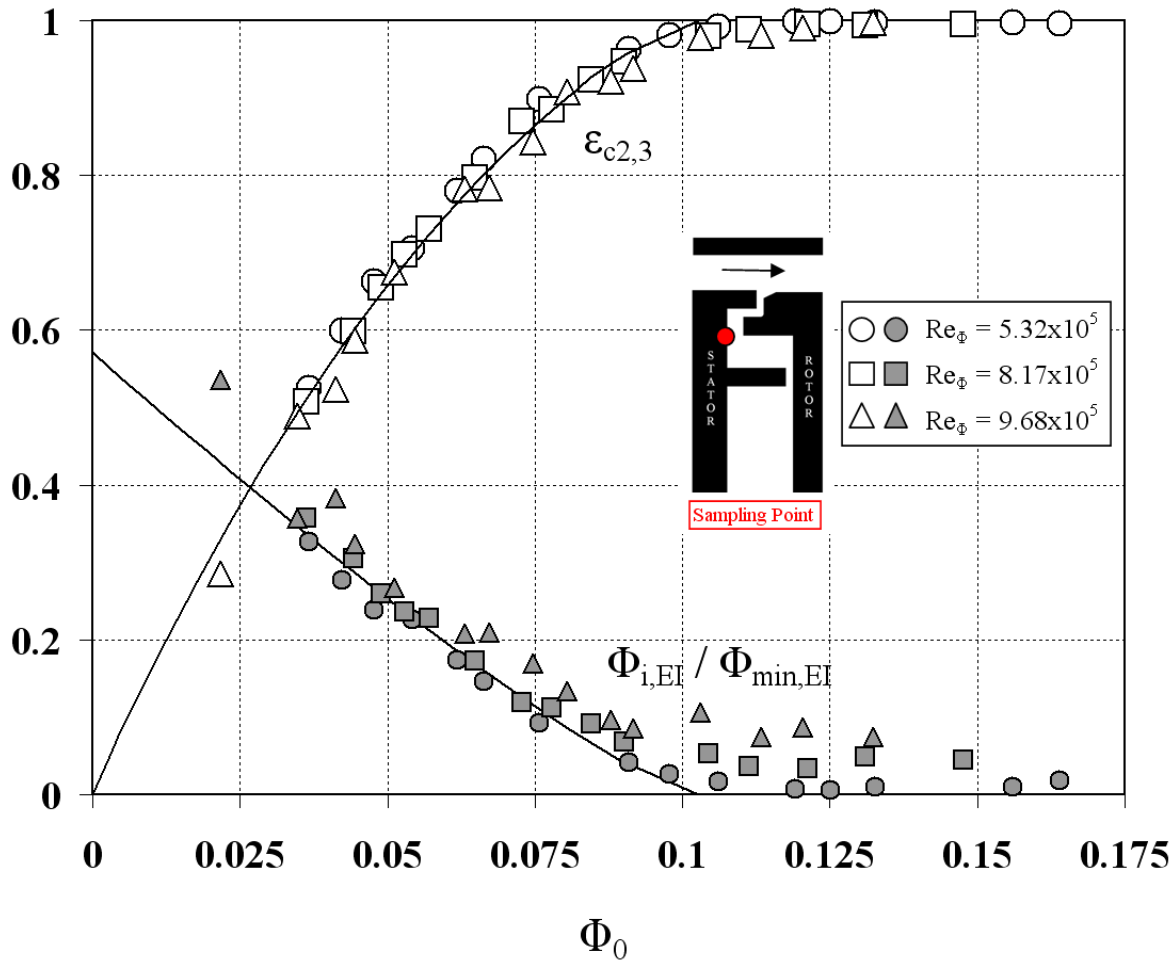

Figure 7.4 Comparison between theoretical effectiveness curves and experimental data ($\varepsilon_{c,23}$) for radial-axial double seal (Generic # 3) with EI ingress for outer sampling point, ($Re_w/Re_\Phi = 0.538$).
(Open symbols denote $\varepsilon_{c,23}$ data; closed symbols denote $\Phi_{i,EI}/\Phi_{min,EI}$ data; solid lines are theoretical curves.)

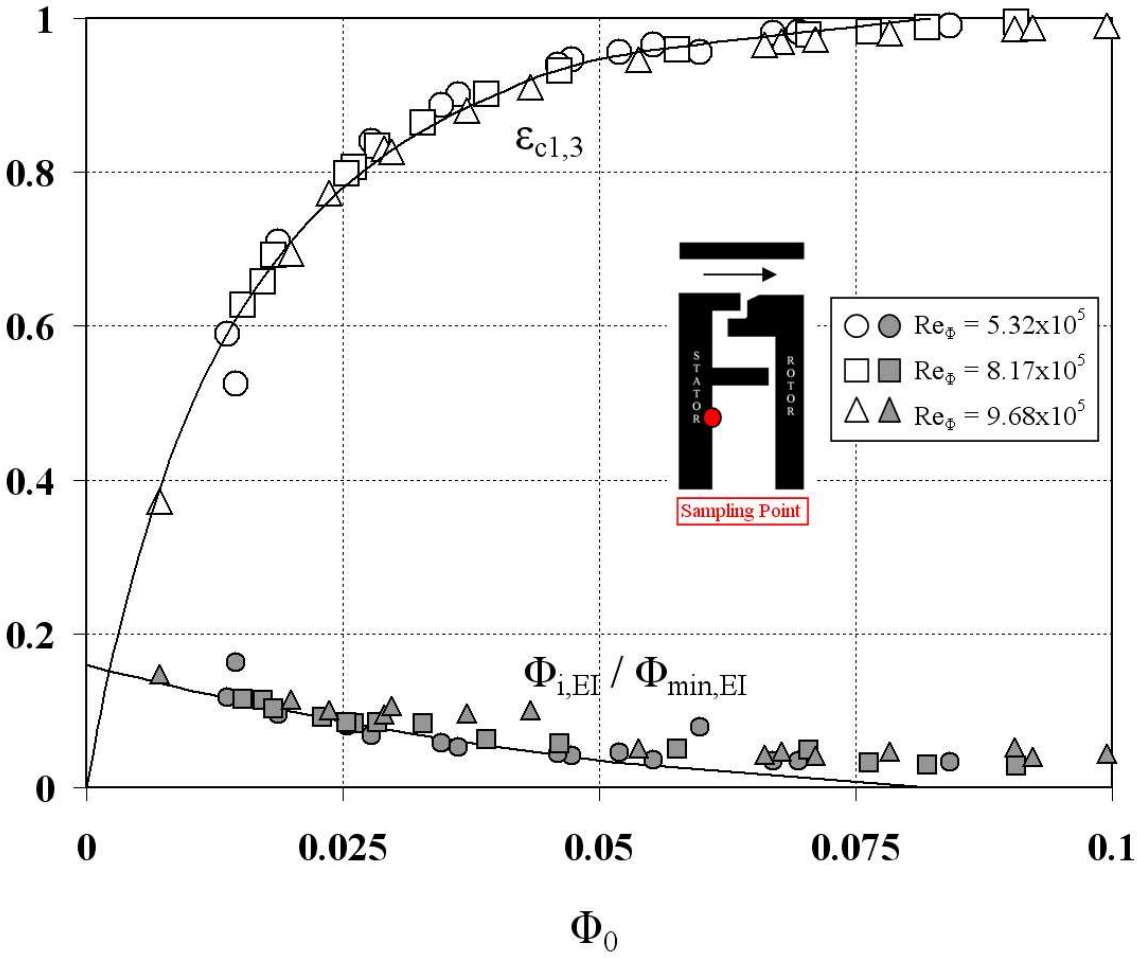

Figure 7.5 Comparison between theoretical effectiveness curves and experimental data ($\varepsilon_{c,13}$) for radial-axial double seal (Generic # 3) with EI ingress for inner sampling point, (Re_w/Re_Φ = 0.538).
(Open symbols denote $\varepsilon_{c,13}$ data; closed symbols denote $\Phi_{i,EI}/\Phi_{min,EI}$ data; solid lines are theoretical curves.)

Figures 7.6 and 7.7 show comparisons between the theoretical curves and the experimental data for the axial-radial double-clearance seal (Generic # 3, Fig. 7.2) under the RI testing conditions specified in Section 7.1. The estimated values of $\Phi_{min,RI}$ and Γ_c and their 95% confidence intervals are shown in Table 7.2, along with the number of data points n used in the fits, and σ, the standard deviation between the data and the fitted curves.

The estimated values of $\Phi_{min,RI}$ are 0.0278 and 0.0284 using the definition of concentration effectiveness as $\varepsilon_{c,23}$ and $\varepsilon_{c,13}$, respectively. This shows that approximately the same amount of air will seal both the inner cavity and the outer cavity at the same instance. Although it is physically impossible to require more air to seal the inner cavity compared to the outer one, the estimates of $\Phi_{min,RI}$ both fall within the 95% confidence interval of each seal. In order to be consistent with the data presented for other seals, the estimates of $\Phi_{min,RI}$ are still given to 3 significant figures.

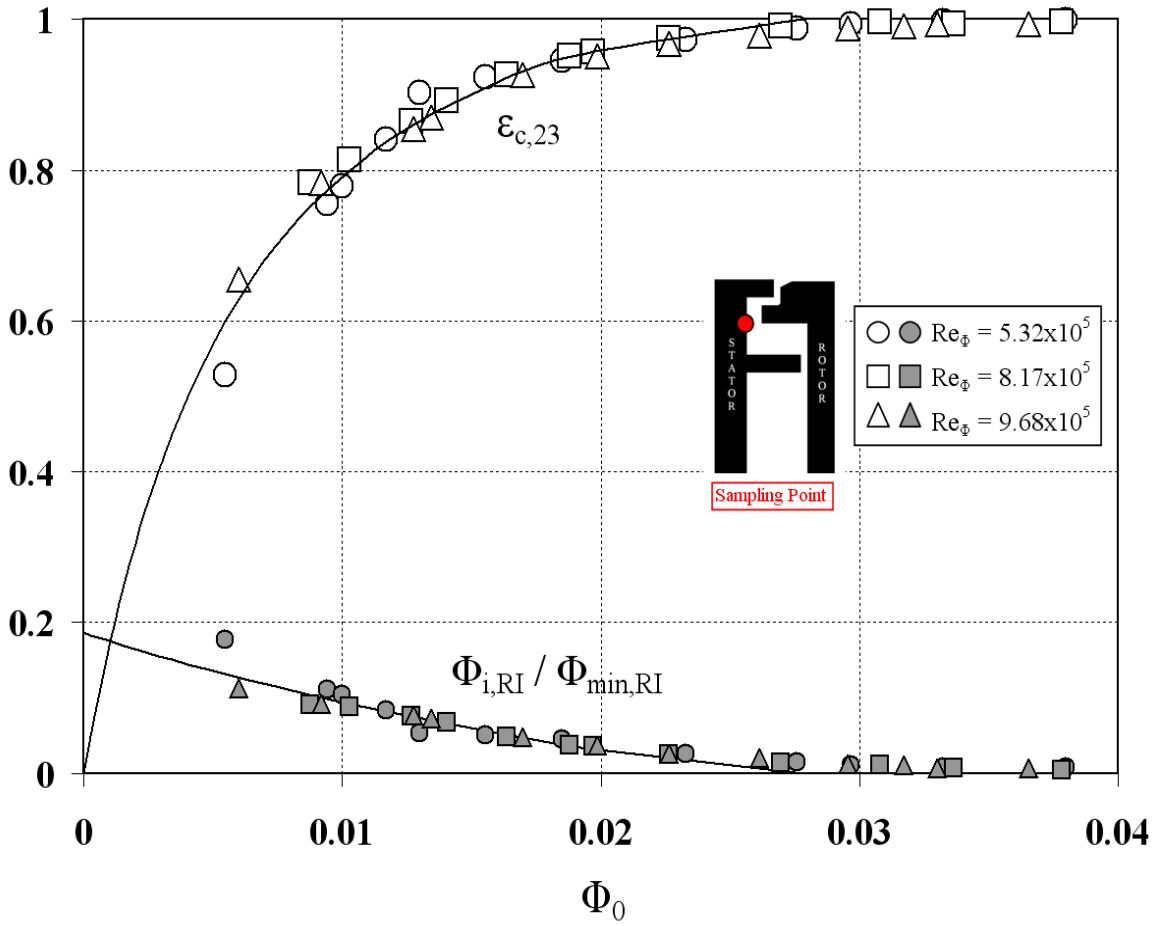

Figure 7.6 Comparison between theoretical effectiveness curves and experimental data ($\varepsilon_{c,23}$) for radial-axial double seal (Generic # 3) with RI ingress for outer sampling point.
(Open symbols denote $\varepsilon_{c,23}$ data; closed symbols denote $\Phi_{i,RI}/\Phi_{min,RI}$ data; solid lines are theoretical curves.)

	EI Ingress		RI Ingress	
Seal	$\varepsilon_{c,13}$	$\varepsilon_{c,23}$	$\varepsilon_{c,13}$	$\varepsilon_{c,23}$
$\hat{\Phi}_{min}$	0.0822	0.103	0.0284	0.0278
$\hat{\Phi}_{min}^{-}$	0.0736	0.0994	0.0251	0.0253
$\hat{\Phi}_{min}^{+}$	0.0922	0.107	0.0336	0.0314
$\Phi_{i,EI}^{*}$	0.0131	0.0586	-	-
$\Phi_{i,RI}^{*}$	-	-	0.00343	0.00517
$\hat{\Gamma}_c$	0.269	3.28	0.249	0.401
$\hat{\Gamma}_c^{-}$	0.213	2.52	0.198	0.324
$\hat{\Gamma}_c^{+}$	0.345	4.13	0.301	0.493
n	45	45	33	36
σ	0.0179	0.0161	0.0136	0.0174

Table 7.2 Parameters for radial-axial clearance seal (Generic # 3) for RI and EI ingress using both definitions of sealing effectiveness. (^ denotes estimated value from the theoretical curve, and + - denote upper and lower bounds of 95% confidence intervals.)

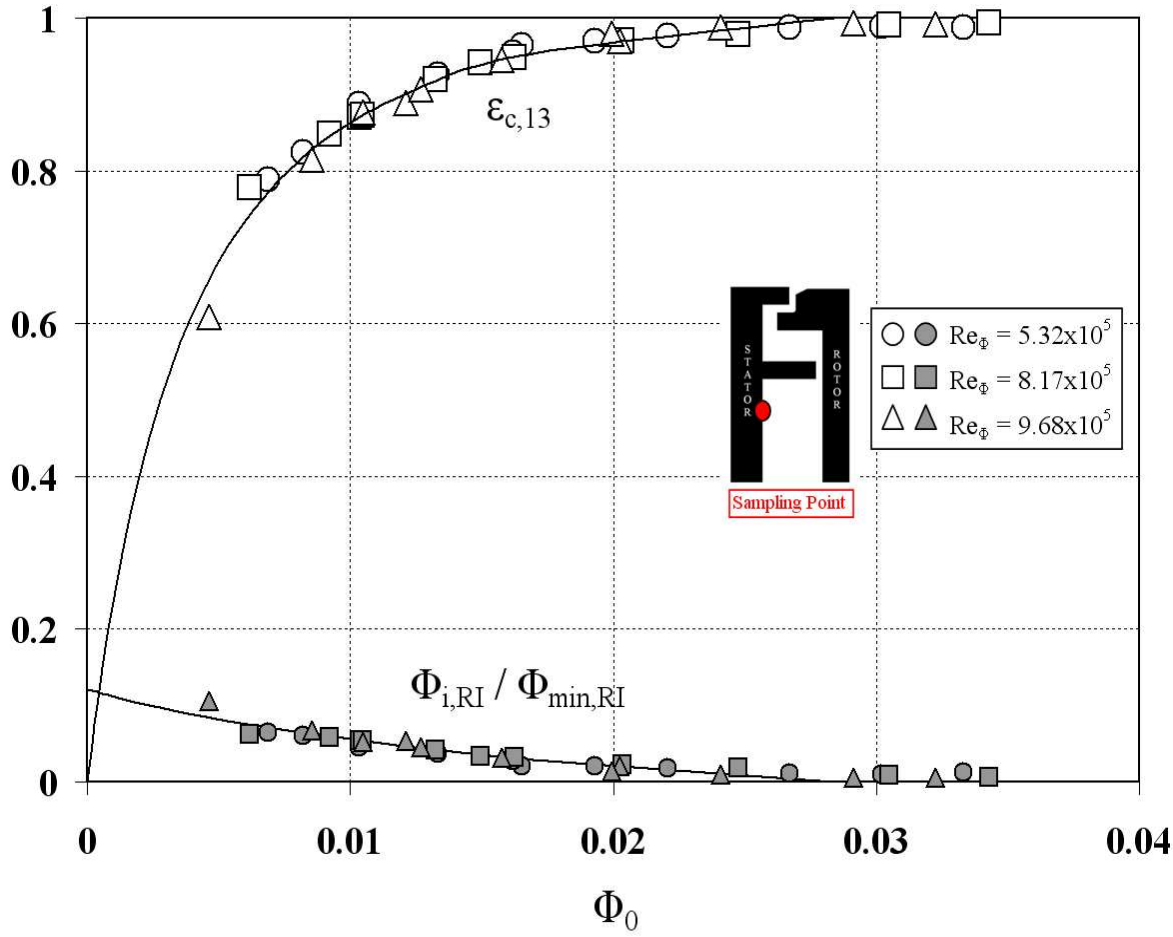

Figure 7.7 Comparison between theoretical effectiveness curves and experimental data ($\varepsilon_{c,13}$) for radial-axial double seal (Generic # 3) with RI ingress for inner sampling point.
(Open symbols denote $\varepsilon_{c,13}$ data; closed symbols denote $\Phi_{i,RI}/\Phi_{min,RI}$ data; solid lines are theoretical curves.)

Figures 7.6 and 7.7 also show the variation of $\Phi_{i,RI} / \Phi_{min,RI}$ with Φ_0 according to Eq. 3.31. Table 7.2 includes values of $\Phi_{i,RI}^*$; this is the maximum value of $\Phi_{i,RI}$, which occurs when $\Phi_0 = 0$. It follows from the values in the table that $\Phi_{i,RI}^* / \Phi_{min,RI} = 0.186$ and 0.121 using the definition of concentration effectiveness as $\varepsilon_{c,23}$ and $\varepsilon_{c,13}$, respectively.

7.3.2 Double-axial clearance seal

Figures 7.8 and 7.9 show comparisons between the theoretical curves and the experimental data for the double axial-clearance seal (Generic # 4, Fig. 7.2) under the EI testing conditions specified in Section 7.1. The rim-seal is shown to be characterised by $\Phi_{min,EI}$, which is independent of Re_Φ.

The estimated values of $\Phi_{min,EI}$ and Γ_c and their 95% confidence intervals are shown in Table 7.3. The number of data points n used in the fits, and σ, the standard deviation between the data and the fitted curves, are also shown in the table.

Figures 7.8 and 7.9 show good agreement between the theoretical curves and the data; the good agreement is confirmed by the relatively small values of σ in Table 7.3. The estimated values of $\Phi_{min,EI}$ are 0.265 and 0.156 using the definition of concentration effectiveness as $\varepsilon_{c,23}$ and $\varepsilon_{c,13}$, respectively. This shows that, to prevent ingestion into the inner wheel-space under EI conditions, approximately 60% of the air required to seal the outer seal is required. The data are shown on the same plot in Section 7.3.3.

Figures 7.8 and 7.9 also show the variation of $\Phi_{i,EI} / \Phi_{min,EI}$ with Φ_0 according to Eq. 3.42. Table 7.3 includes values of $\Phi_{i,EI}^*$; this is the maximum value of $\Phi_{i,EI}$, which occurs when $\Phi_0 = 0$. It follows from the values in the table that $\Phi_{i,EI}^* / \Phi_{min,EI} = 0.327$ and 0.137 using the definition of concentration effectiveness as $\varepsilon_{c,23}$ and $\varepsilon_{c,13}$, respectively. That is, for either cavity, the maximum ingress is no more than 33% of the flow rate needed to prevent ingestion under EI conditions.

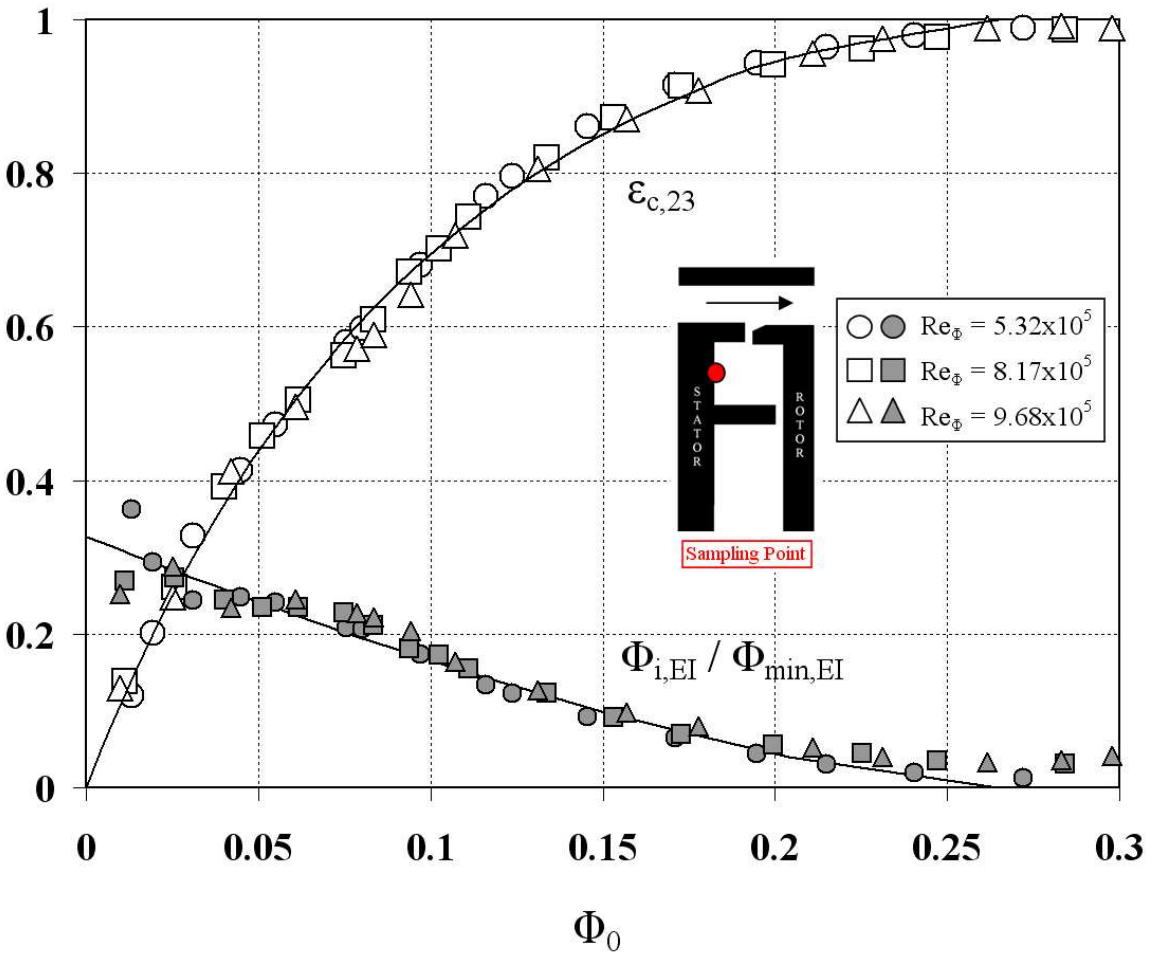

Figure 7.8 Comparison between theoretical effectiveness curves and experimental data ($\varepsilon_{c,23}$) for double-axial seal (Generic # 4) with EI ingress for outer sampling point, ($Re_w/Re_\Phi = 0.538$).
(Open symbols denote $\varepsilon_{c,23}$ data; closed symbols denote $\Phi_{i,EI}/\Phi_{min,EI}$ data; solid lines are theoretical curves.)

Figures 7.10 and 7.11 show comparisons between the theoretical curves and the experimental data for the double-axial clearance seal (Generic # 4, Fig. 7.2) under the RI testing

conditions specified in Section 7.1. The estimated values of $\Phi_{min,RI}$ and Γ_c and their 95% confidence intervals are shown in Table 7.3, along with the number of data points n used in the fits, and σ, the standard deviation between the data and the fitted curves.

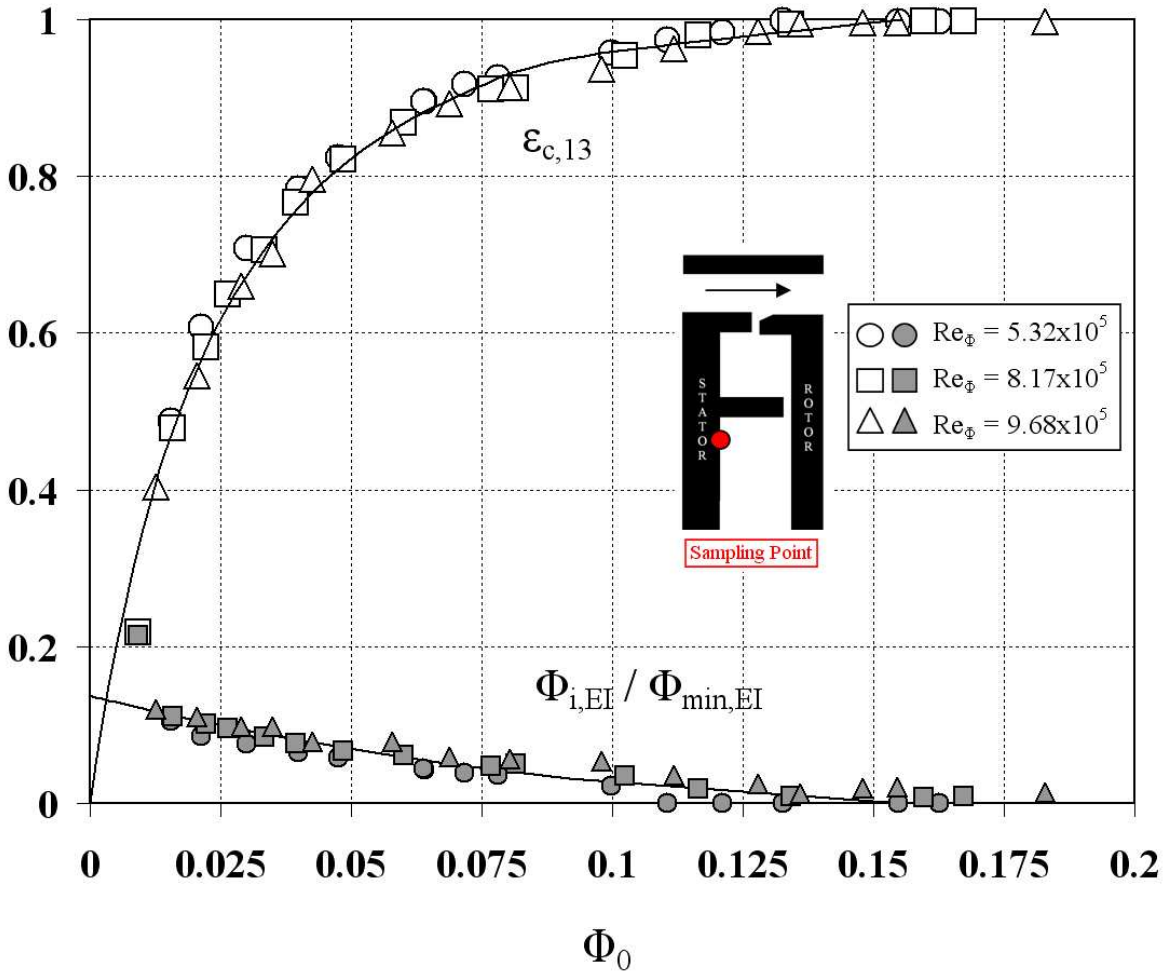

Figure 7.9 Comparison between theoretical effectiveness curves and experimental data ($\varepsilon_{c,13}$) for double-axial seal (Generic # 4) with EI ingress for inner sampling point, (Re_w/Re_Φ = 0.538).
(Open symbols denote $\varepsilon_{c,13}$ data; closed symbols denote $\Phi_{i,EI}/\Phi_{min,EI}$ data; solid lines are theoretical curves.)

The estimated values of $\Phi_{min,RI}$ are 0.0630 and 0.0544 using the definition of concentration effectiveness as $\varepsilon_{c,23}$ and $\varepsilon_{c,13}$, respectively. This shows that, for RI ingestion, approximately 87% of the sealant air required to purge the outer cavity is required to seal the inner wheel-space.

Figures 7.10 and 7.11 also show the variation of $\Phi_{i,RI} / \Phi_{min,RI}$ with Φ_0 according to Eq. 3.31. Table 7.3 includes values of $\Phi_{i,RI}^*$; this is the maximum value of $\Phi_{i,RI}$, which occurs when Φ_0 = 0. It follows from the values in the table that $\Phi_{i,RI}^* / \Phi_{min,RI}$ = 0.269 and 0.149 using the definition of concentration effectiveness as $\varepsilon_{c,23}$ and $\varepsilon_{c,13}$, respectively. That is, for either cavity, the maximum ingress is no more than 27% of the flow rate needed to prevent ingestion under RI conditions.

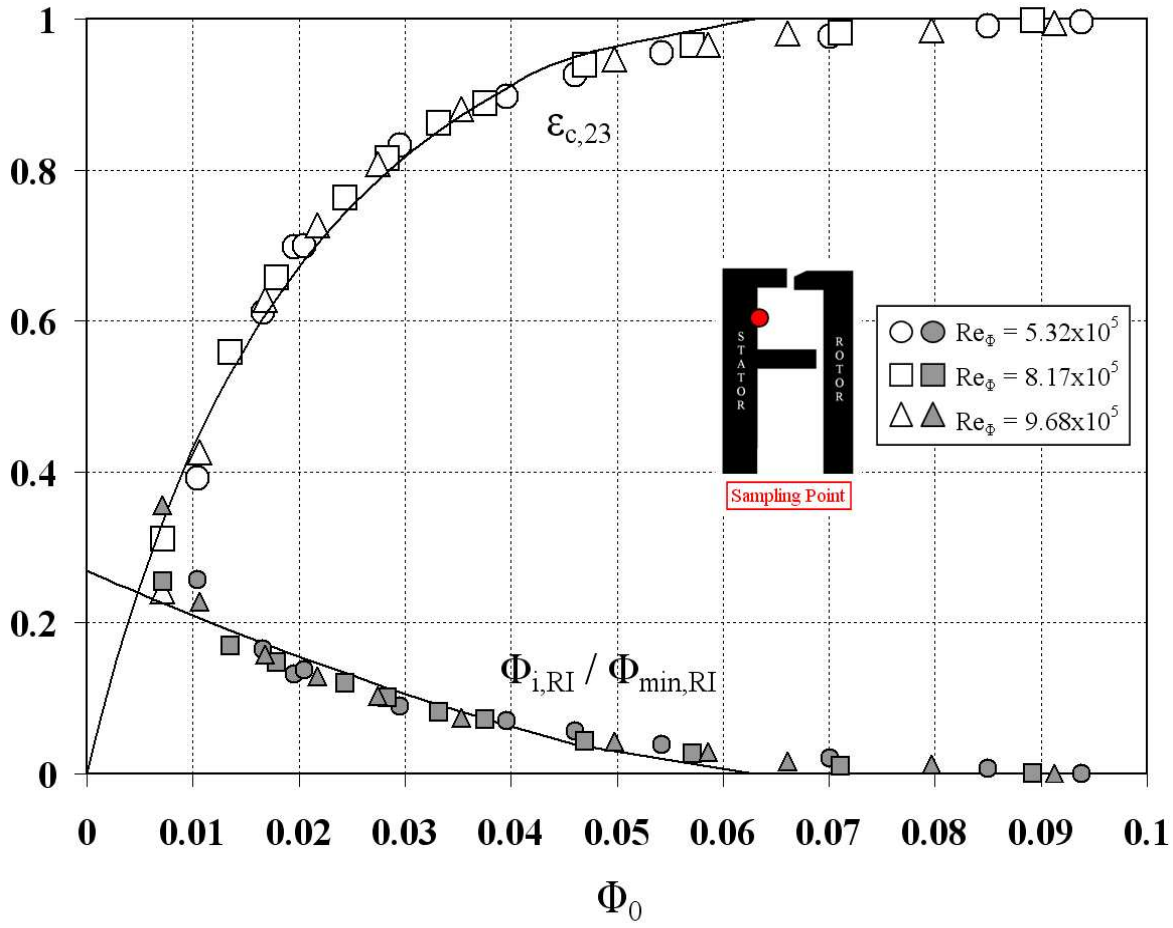

Figure 7.10 Comparison between theoretical effectiveness curves and experimental data ($\varepsilon_{c,23}$) for double-axial seal (Generic # 4) with RI ingress for outer sampling point.
(Open symbols denote $\varepsilon_{c,23}$ data; closed symbols denote $\Phi_{i,RI}/\Phi_{min,RI}$ data; solid lines are theoretical curves.)

	EI Ingress		**RI Ingress**	
Seal	$\varepsilon_{c,13}$	$\varepsilon_{c,23}$	$\varepsilon_{c,13}$	$\varepsilon_{c,23}$
$\hat{\Phi}_{min}$	0.156	0.265	0.0544	0.0630
$\hat{\Phi}_{min}^{-}$	0.138	0.253	0.0500	0.0563
$\hat{\Phi}_{min}^{+}$	0.177	0.277	0.0600	0.0710
$\Phi_{i,EI}^{*}$	0.0214	0.0867	-	-
$\Phi_{i,RI}^{*}$	-	-	0.00810	0.0169
$\hat{\Gamma}_c$	0.218	0.859	0.312	0.638
$\hat{\Gamma}_c^{-}$	0.173	0.751	0.270	0.498
$\hat{\Gamma}_c^{+}$	0.274	0.987	0.355	0.870
n	45	53	36	36
σ	0.208	0.014	0.0117	0.026

Table 7.3 Parameters for double-axial clearance seal (Generic # 4) for RI and EI ingress using both definitions of sealing effectiveness. (^ denotes estimated value from the theoretical curve, and + - denote upper and lower bounds of 95% confidence intervals.)

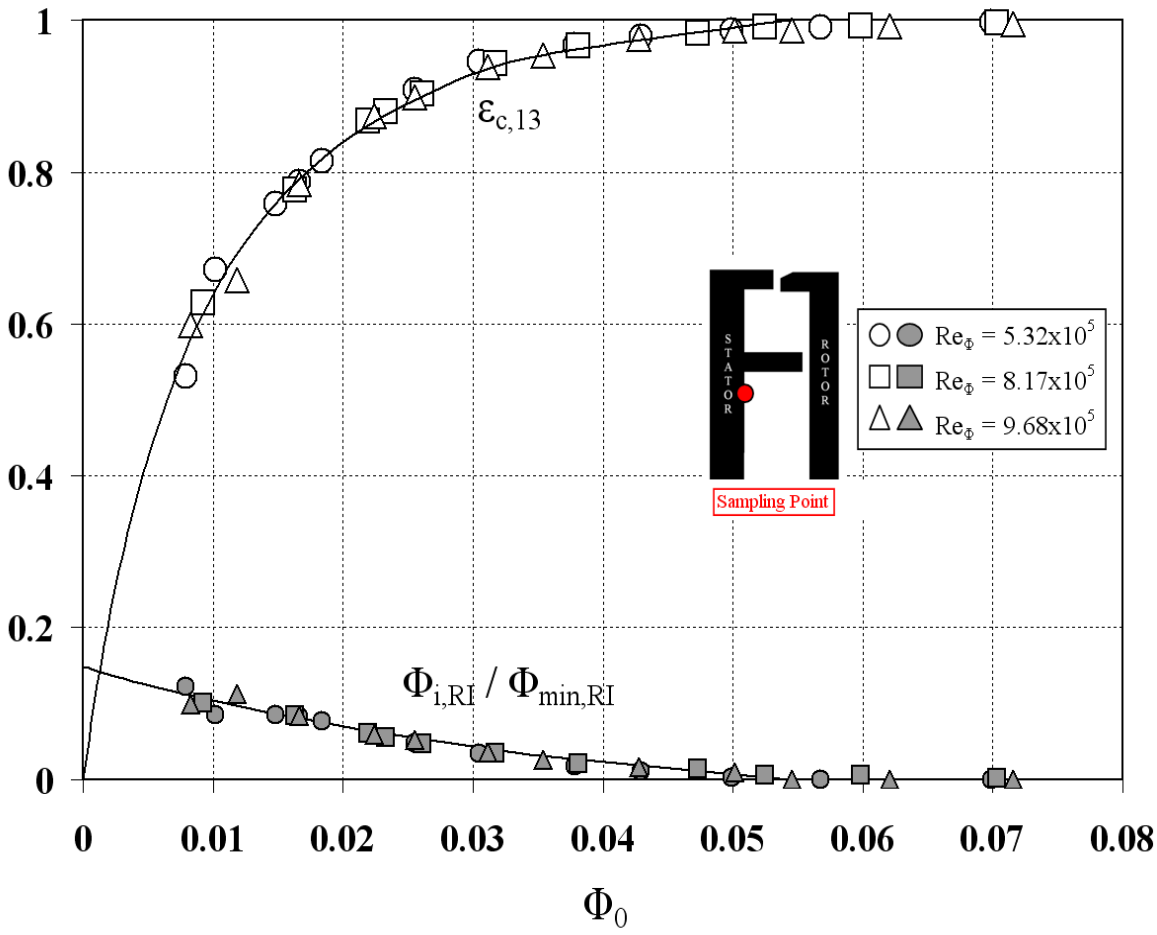

Figure 7.11 Comparison between theoretical effectiveness curves and experimental data ($\varepsilon_{c,13}$) for double-axial seal (Generic # 4) with RI ingress for inner sampling point.
(Open symbols denote $\varepsilon_{c,13}$ data; closed symbols denote $\Phi_{i,RI}/\Phi_{min,RI}$ data; solid lines are theoretical curves.)

7.3.3 Rim-seal effectiveness comparisons

Figure 7.12 shows a comparison of the effectiveness data and theoretical curves for both double seal configurations under conditions of EI ingress. It can be seen from Tables 7.2 and 7.3 that, for EI ingress, the ratio of Φ_{min} for the radial-axial double clearance seal to that required for the double-axial clearance seal is approximately 52% for $\varepsilon_{c,13}$; for $\varepsilon_{c,23}$, the ratio is 38%.

Figure 7.13 shows the effectiveness data and theoretical curves for both double seal configurations under RI ingress conditions. It can be seen from Tables 7.2 and 7.3 that, for RI ingress, the ratio of Φ_{min} for the radial-axial double clearance seal to that required for the double-axial clearance seal is approximately 52% for $\varepsilon_{c,13}$; for $\varepsilon_{c,23}$, the ratio is 44%.

Thus, for both EI and RI ingress, the radial-axial double clearance seal is significantly more effective that the double-axial clearance seal. This result is consistent with the findings of Chapters

5 and 6, in which a radial-clearance seal was shown to be significantly more effective that an axial-clearance seal.

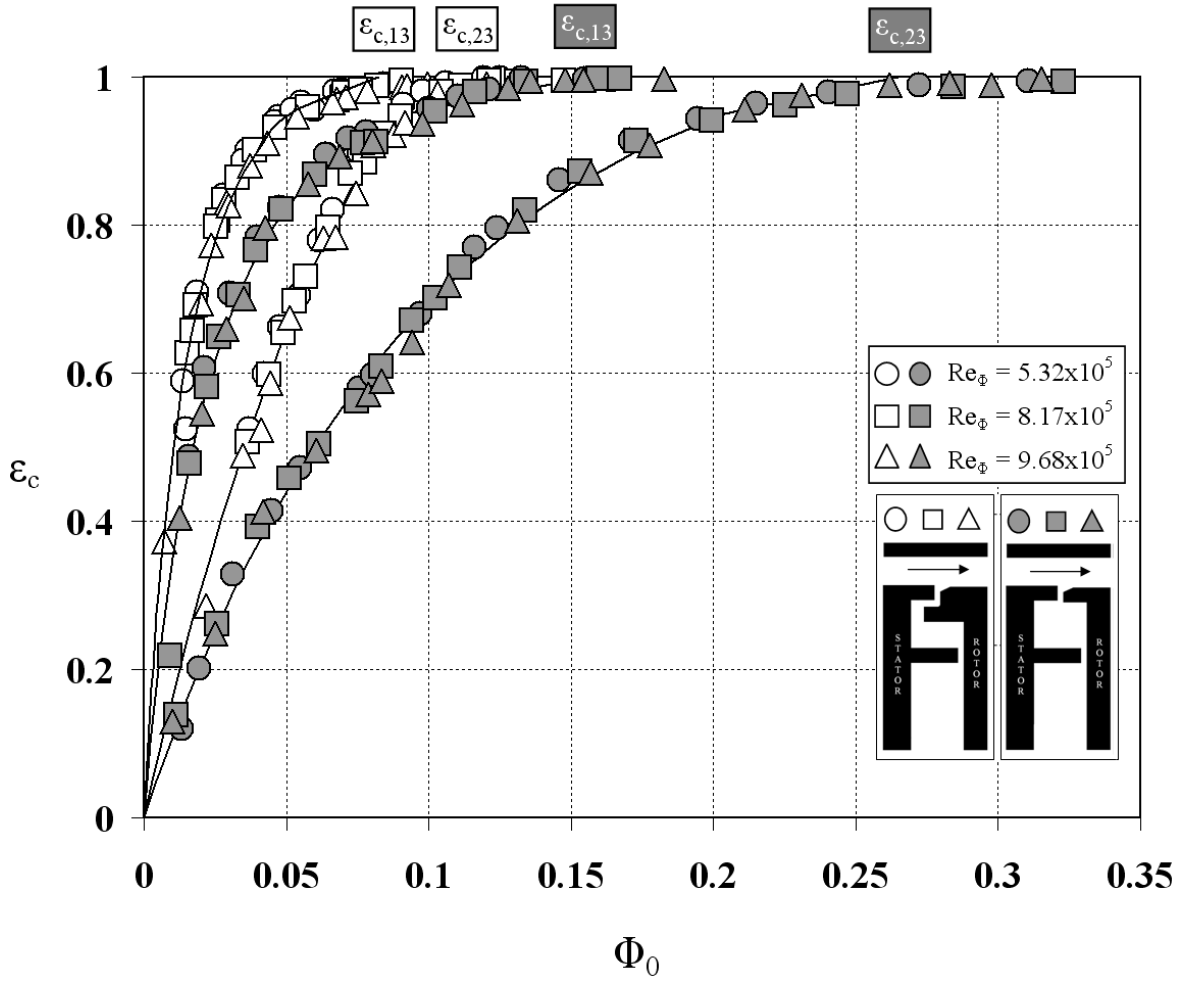

Figure 7.12 Comparison of sealing effectiveness characteristics of both double seals for EI ingress. (Open symbols denote radial-axial double seal; solid symbols denote double-axial seal; solid lines are theoretical curves.)

Importantly, the experiments using double seal configurations reveal the improved sealing effectiveness of the inner wheel-space when a secondary, inner axial-clearance seal is present. Figures 7.12 and 7.13 show that for the same Φ_0 value, $\varepsilon_{c,13} > \varepsilon_{c,23}$ for both seals in both the EI and RI ingress regimes. The *shielding* effect of these inner clearance-seals is revealed clearly in the concentration distribution with radius ($0.55 < r/b < 0.875$ and $0.924 < r/b < 0.993$) along the stator wall in the wheel-space, as discussed in Section 7.4.

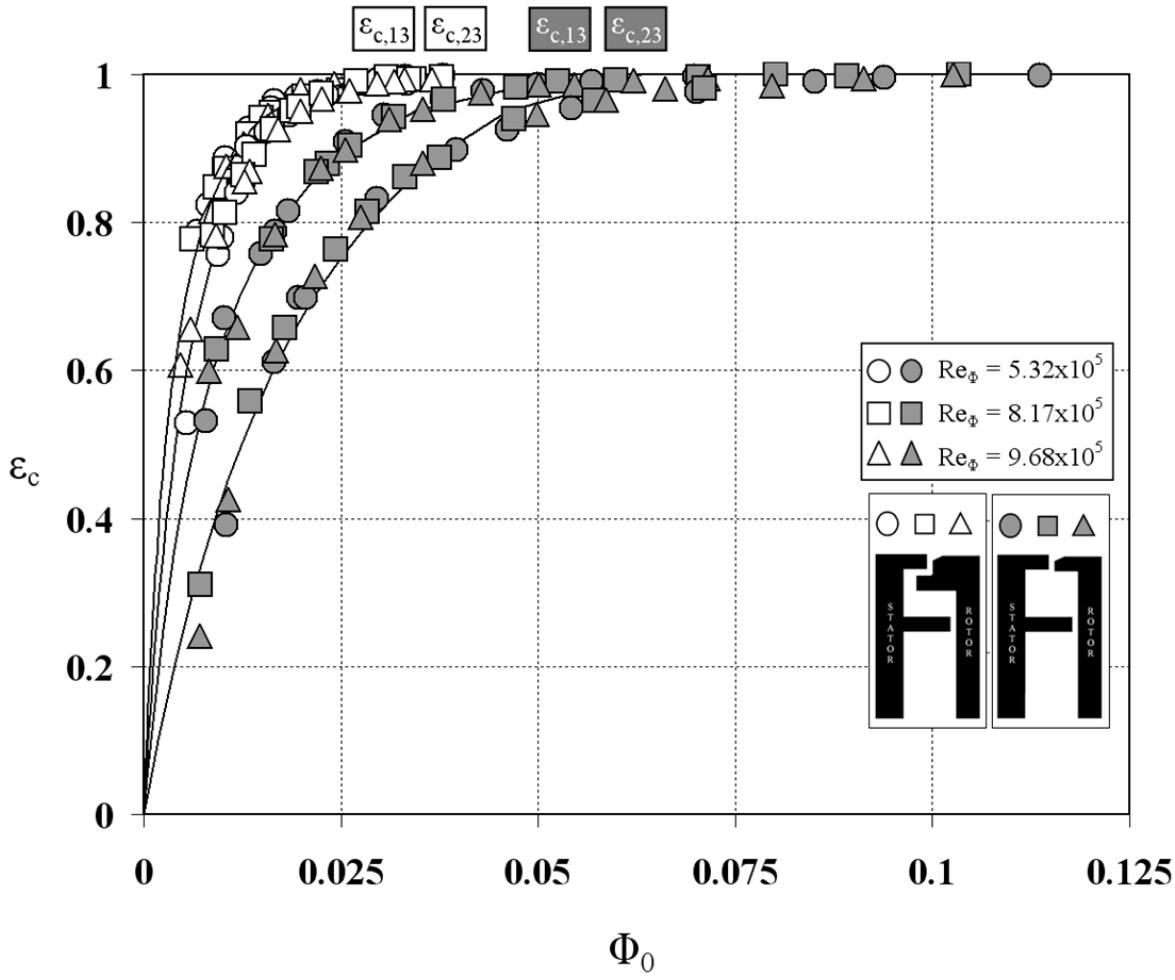

Figure 7.13 Comparison of sealing effectiveness characteristics of both double seals for RI ingress. (Open symbols denote radial-axial double seal; solid symbols denote double-axial seal; solid lines are theoretical curves.)

7.4 Radial variation of effectiveness on stator surface

Figures 7.14 and 7.16 show the radial variation of ε_c on the stator surface at $Re_\Phi = 5.3 \times 10^5$ for the radial-axial double clearance seal under both EI and RI conditions respectively; results for the single radial-clearance seal under similar test conditions are shown for comparison in each case. The tests were conducted for several values of Φ_0 / Φ_{min} and λ_T ; in all cases ingress occurred.

The radial position of the seals are shown within figures as vertical red lines. A significant increase in sealing effectiveness is observed across the inner seal clearance. For all cases, the effectiveness is essentially constant for $0.65 < r/b < 0.85$ with a decrease near the inner seal-clearance, possibly indicating a mixing region just inboard of the seal. The concentration within the intermediate annulus decreases with increasing radius, suggesting the flow here has not mixed fully. An increase in effectiveness of up to 44% can be seen across the inner seal of the radial-axial double-clearance seal in Fig. 7.14 for a sealant flow level of $\Phi_0 / \Phi_{min} = 0.251$, with increases seen

across the seal clearance for all tested purge flow rates. A similar, but reduced, effect is seen in Fig. 7.16 for the RI test cases, with an effectiveness increase of up to 7% across the inner seal for a sealant flow level $\Phi_0 / \Phi_{min} = 0.325$.

This shielding effect experienced by the inner cavity is of great importance to the gas turbine designer. If the inner-wheel-space is sufficiently protected, then more expensive, high-temperature alloys can be reserved for use in the intermediate annulus, with cheaper alternatives employed inward of the inner seal clearance.

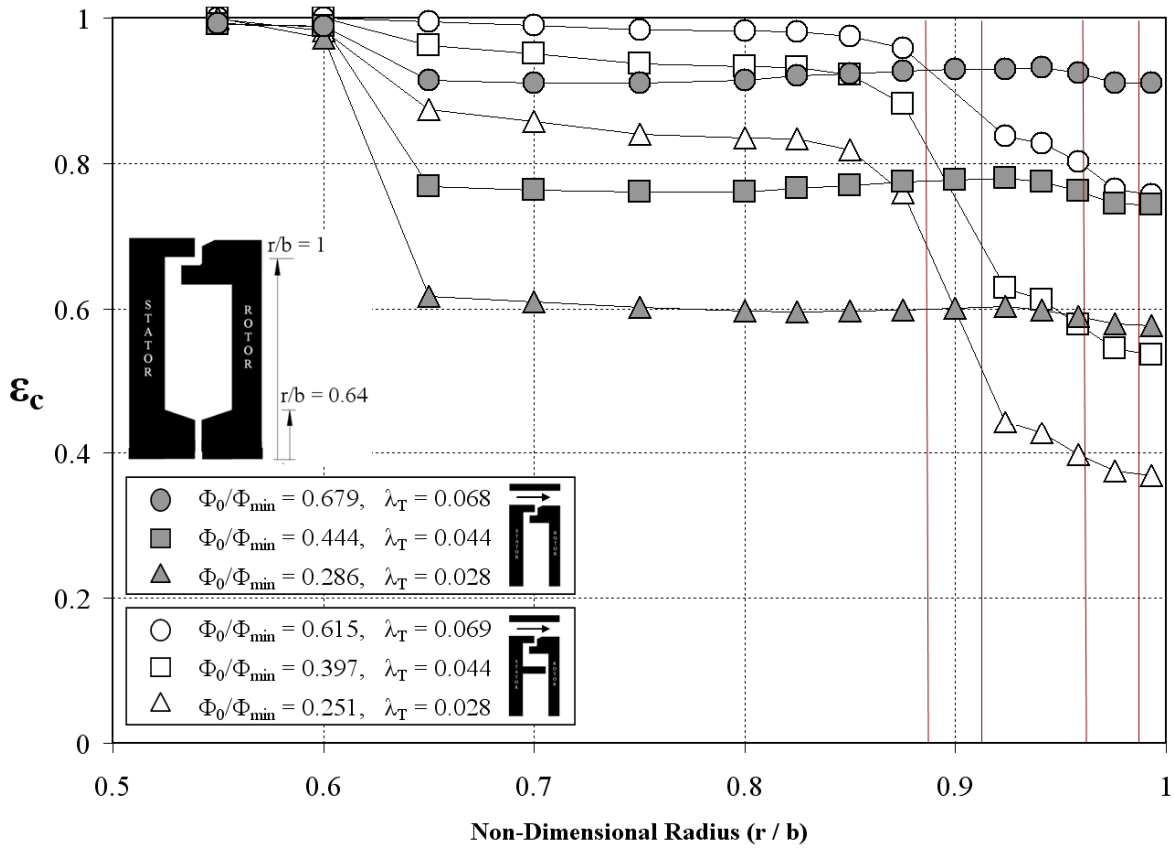

Figure 7.14 Comparison of the effect of sealing flow rate on measured radial variation of effectiveness on stator surface for radial-clearance seal and radial-axial double clearance seal, for EI ingress. (Open symbols denote radial-axial double clearance seal; solid symbols denote single radial-clearance seal. Lines are included for reader's convenience only.)

One possible deterrent from employing such a double seal configuration is the potential decrease in sealing effectiveness experienced in the intermediate annulus as a result of the inner wheel-space being protected. Figure 7.14 shows that an effectiveness reduction is seen radially outward of the inner seal ($r/b > 0.9$) for the radial-axial double seal compared with that of the single radial equivalent for the same internal fluid dynamic conditions. This effectiveness reduction is seen to be as high as 20%; that is, a proportion of the hot gas ingress is contained inside the formed intermediate annulus to potentially detrimental effect. The effect of this effectiveness

reduction on the heat transfer to the stator and rotor discs inside the intermediate annulus is beyond the scope of this thesis.

The radial stator-wall variation of ε_c, radially outward of the inner seal clearance ($r/b > 0.9$) is not of constant magnitude in Fig. 7.14 for the radial-axial double clearance seal, implying that the flow is not fully mixed out in this region. The expected flow-streams for this seal configuration are shown in Fig. 7.15; this highlights the existence of a mixing region in the intermediate annulus, adjacent to the stator wall.

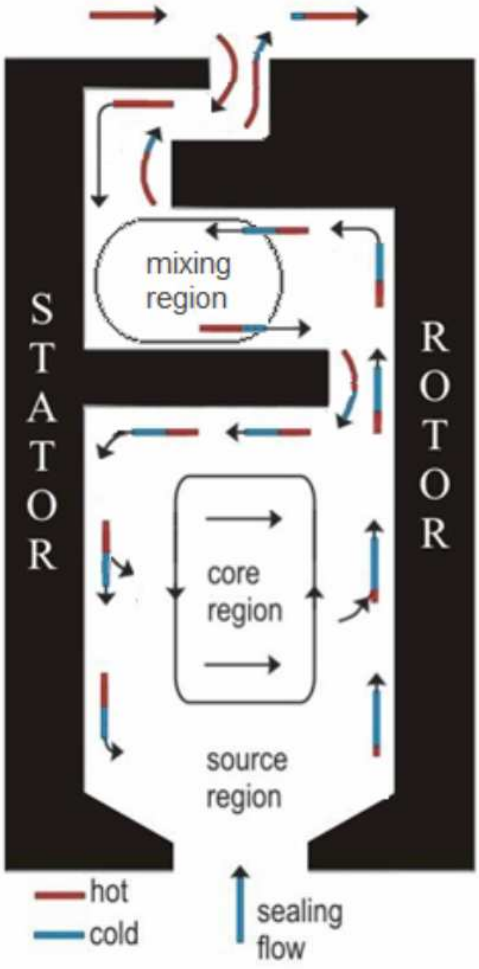

Figure 7.15 Expected flow-streams occurring in radial-axial double-clearance seal for $\Phi_0 < \Phi_{min}$.

This brings the applicability of the outer sampling point into question; the sealing effectiveness is seen to vary by approximately 7% over radial locations $0.993 > r/b > 0.9$. It is a matter of conjecture as to whether the sampling point selected at $r/b = 0.958$ is truly representative of the intermediate annulus in this case – in Section 7.2.2 it was suggested that the sample point at $r/b = 0.85$ (corresponding to $\varepsilon_{c,13}$) might be better suited to rank double-seal performance.

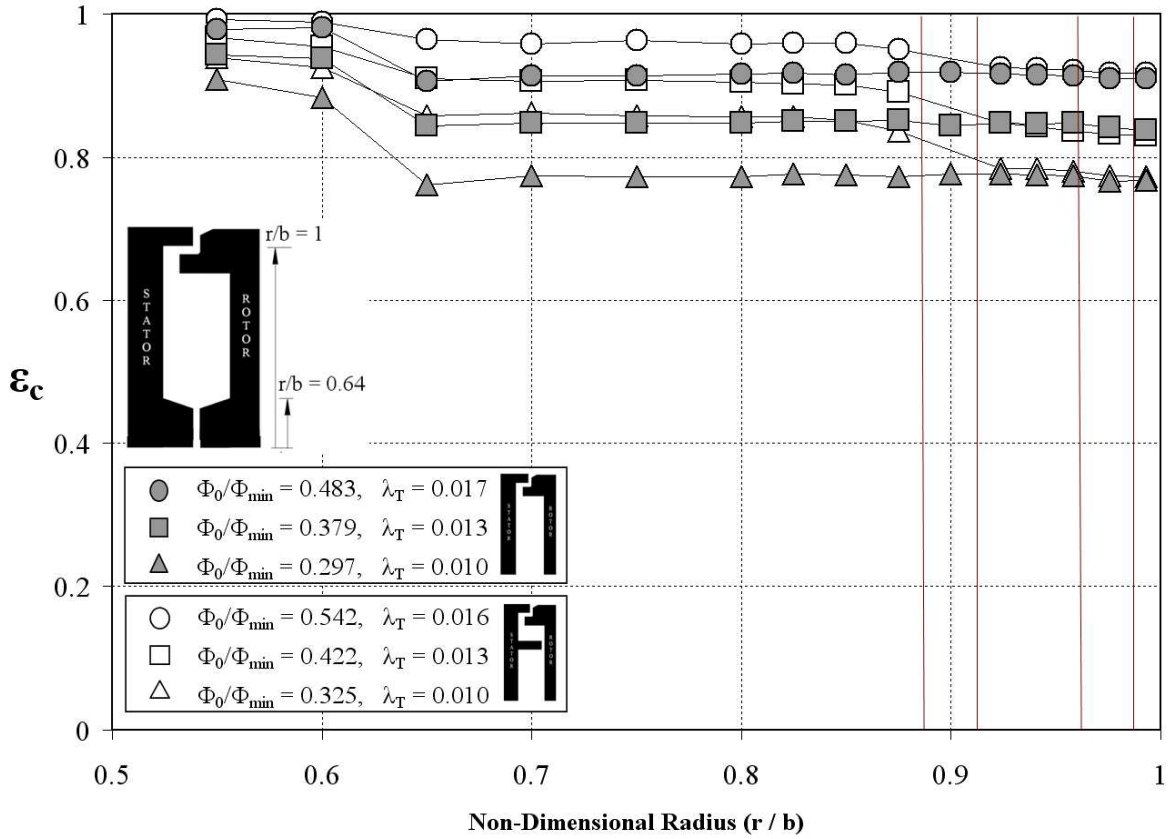

Figure 7.16 Comparison of the effect of sealing flow rate on measured radial variation of effectiveness on stator surface for radial-clearance seal and radial-axial double clearance seal, for RI ingress. (Open symbols denote radial-axial double clearance seal; solid symbols denote single radial-clearance seal. Lines are included for reader's convenience only.)

Figure 7.17 shows the core swirl ratio (β) distribution for the radial-axial double clearance seal (Generic # 3) for a number of different purge flow levels all at the Re_Φ = 8.17 x 10^5 design point (EI test conditions). For $r/b < 0.88$, $\beta \approx 0.44$ for the case of $\Phi_0 = 0$, in agreement with Daily *et al.* (1964). Interestingly, the swirl ratio is approximately constant throughout the whole inner-wheel-space ($0.65 < r/b < 0.88$) where there is a limited influence of the external swirl and the system retains a rotating core up till the maximum tested flow-rate, $\Phi_0/\Phi_{min} = 0.68$. Note that the swirl ratio in the external annulus is $\beta \approx 1.8$ – see Fig. 4.14.

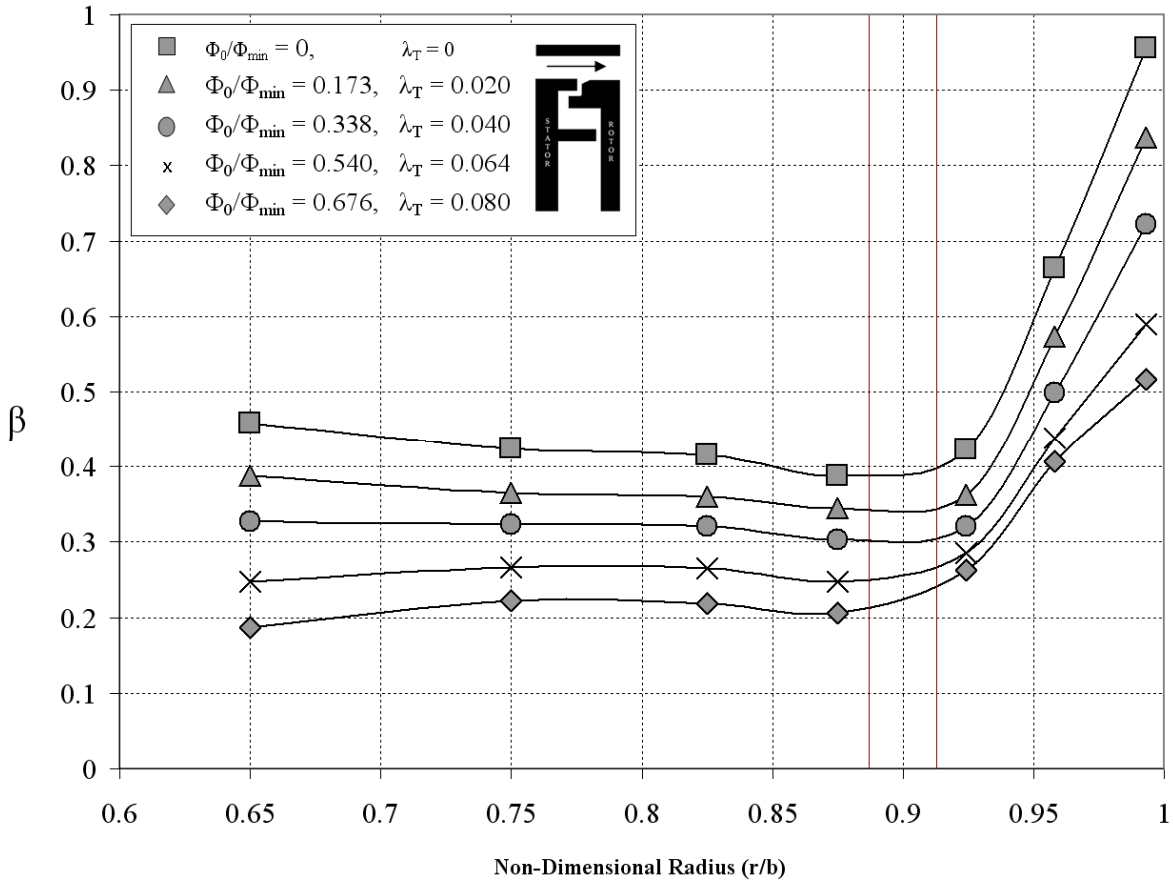

Figure 7.17 Swirl ratio distribution for radial-axial double clearance seal and different purge flow-rates, for EI ingress. (Lines are included for reader's convenience only.)

For the case $\Phi_0 = 0$, the swirl in the intermediate annulus ($0.924 < r/b < 0.993$) is seen to increase rapidly from $\beta \approx 0.44$ to $\beta = 0.96$ under the influence of highly-swirling ingested flow; this may explain the lack of fully mixed-out flow seen in Fig. 7.14. The inner seal constrains the ingested flow with high swirl in the intermediate annulus. Figure 7.18 highlights the containment of this high swirling fluid by showing a comparison of the swirl ratio distributions for the single radial-clearance seal and the radial-axial double clearance seal at multiple purge flow-rates. It can be seen that the swirl effects of the ingested flow are experienced at $r/b > 0.75$ for the single radial-clearance seal, whereas the radial-axial double clearance seal is relatively unaffected until $r/b > 0.924$. The containment of highly swirling flow in the intermediate annulus may create high levels of local heat transfer.

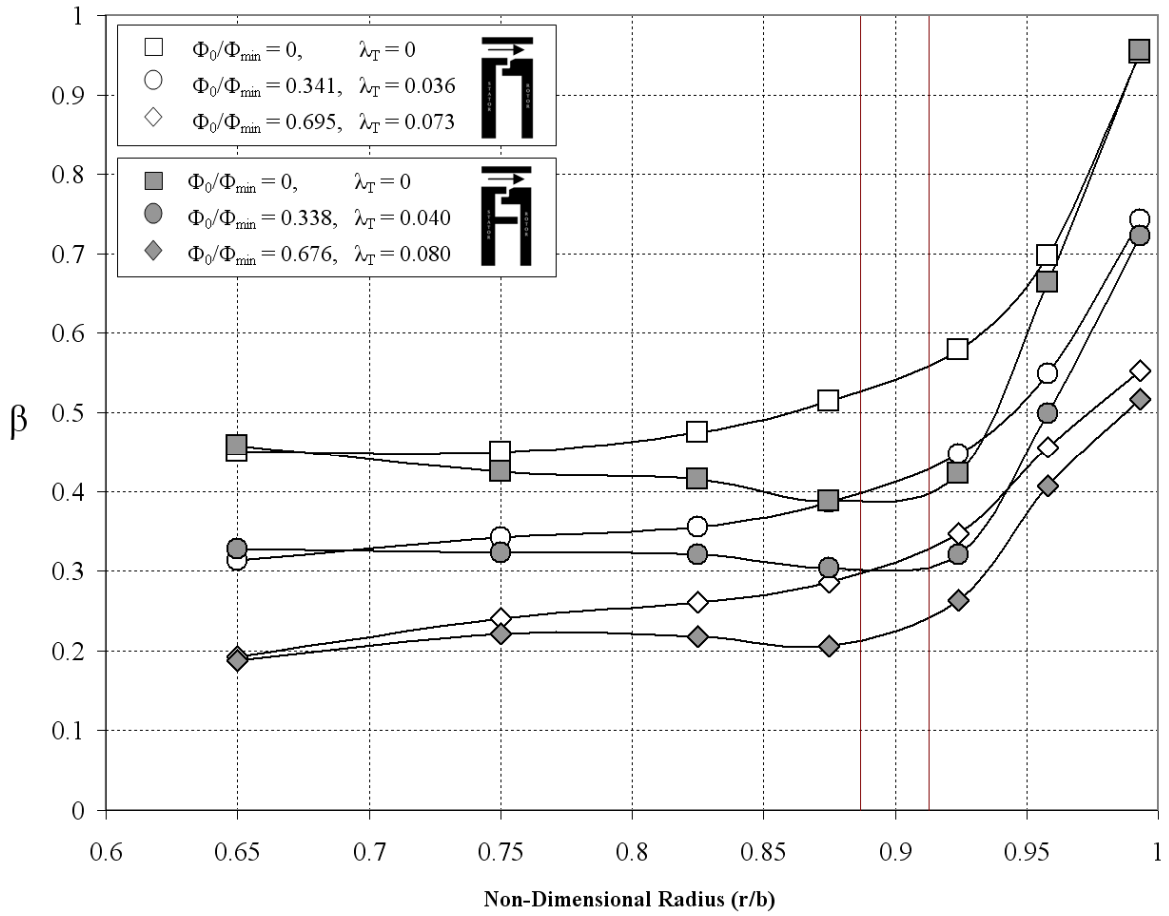

Figure 7.18 Comparison of swirl ratio distributions for radial-clearance seal and radial-axial double clearance seal and different purge flow-rates, for EI ingress. (Lines are included for reader's convenience only.)

Figures 7.19 and 7.20 show the radial variation of ε_c on the stator surface at Re_Φ = 5.3 x 10^5 for the double-axial clearance seal under both EI and RI conditions respectively; results for the single axial seal under similar test conditions are shown for comparison in each case. The tests were conducted for several values of Φ_0 / Φ_{min} and λ_T ; in all cases ingress occurred.

The radial position of the stator seal is shown between vertical lines. A significant increase in sealing effectiveness is observed across the inner seal clearance. An increase in effectiveness of up to 34% can be seen across the inner seal of the double-axial seal in Fig. 7.19 for a sealant flow level of Φ_0 / Φ_{min} = 0.083, with increases seen across the seal clearance for all tested purge flow rates. A similar, but reduced, effect is seen in Fig. 7.20 for the RI test case, with an effectiveness increase of up to 18% across the inner seal for a sealant flow level Φ_0 / Φ_{min} = 0.260.

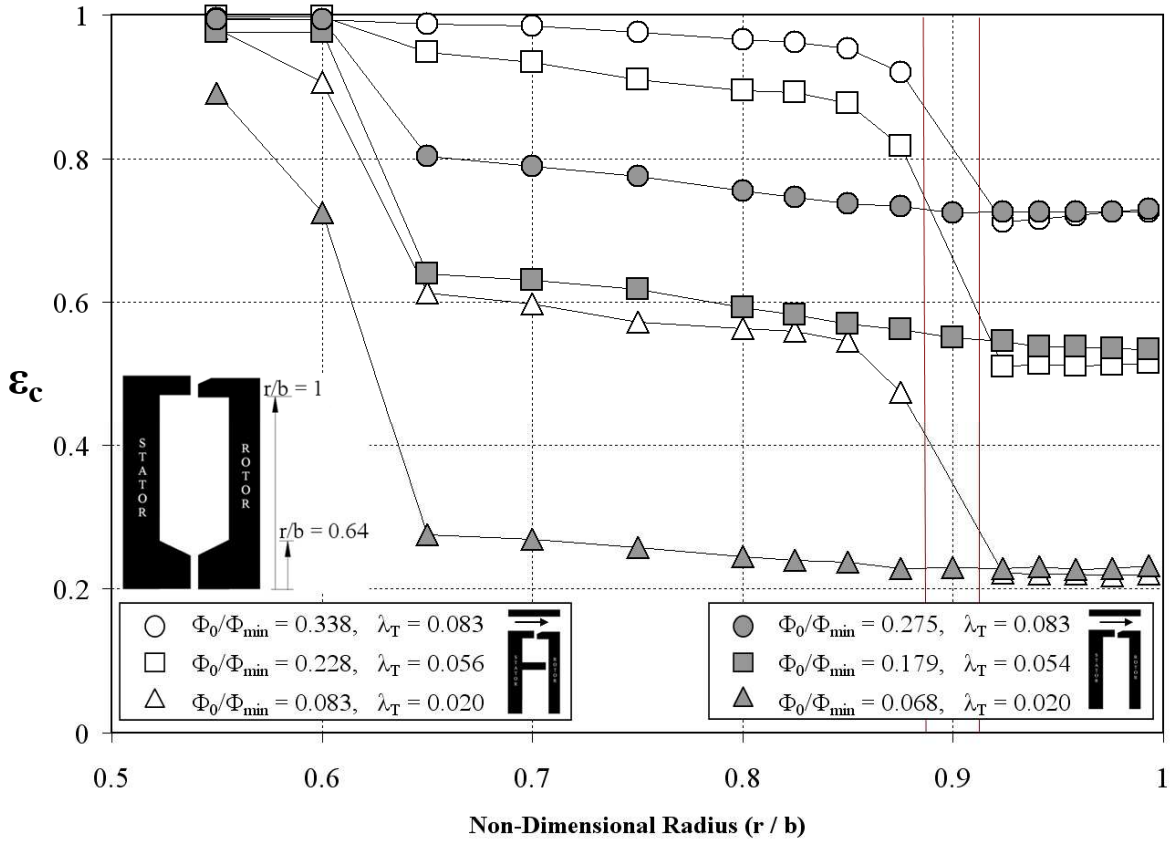

Figure 7.19 Comparison of the effect of sealing flow rate on measured radial variation of effectiveness on stator surface for axial-clearance seal and double-axial clearance seal, for EI ingress. (Open symbols denote double-axial clearance seal; solid symbols denote single axial-clearance seal. Lines are included for reader's convenience only.)

The shielding effect experienced by the double axial-clearance seal comes with no reduction in effectiveness in the intermediate annulus. This is encouraging in terms of the potential of double seals in gas turbine design as the swirl contained in the intermediate annulus observed with the radial-axial double seal may be geometry specific and not a universal trend with double seal configurations. Figure 7.21 shows a comparison of the radial distribution of swirl ratio for the axial-clearance seal and the double-axial clearance seal for multiple purge flow-rates at the Re_Φ = 8.17 x 10^5 design point (EI test conditions). No alteration to the swirl at outer radius (r/b > 0.875) is apparent between the seal geometries, with only a slight and temporary reduction in swirl shown directly radially inward of the seal insert (r/b = 0.9) for the double seal variant.

The addition of a second inner clearance to form a double axial-clearance seal configuration was a beneficial and protective measure, with sealing effectiveness improvements observed under both EI and RI ingress conditions. In order to understand the full effects of a double seal configuration, a thorough local heat transfer study is recommended to build upon these highly encouraging findings.

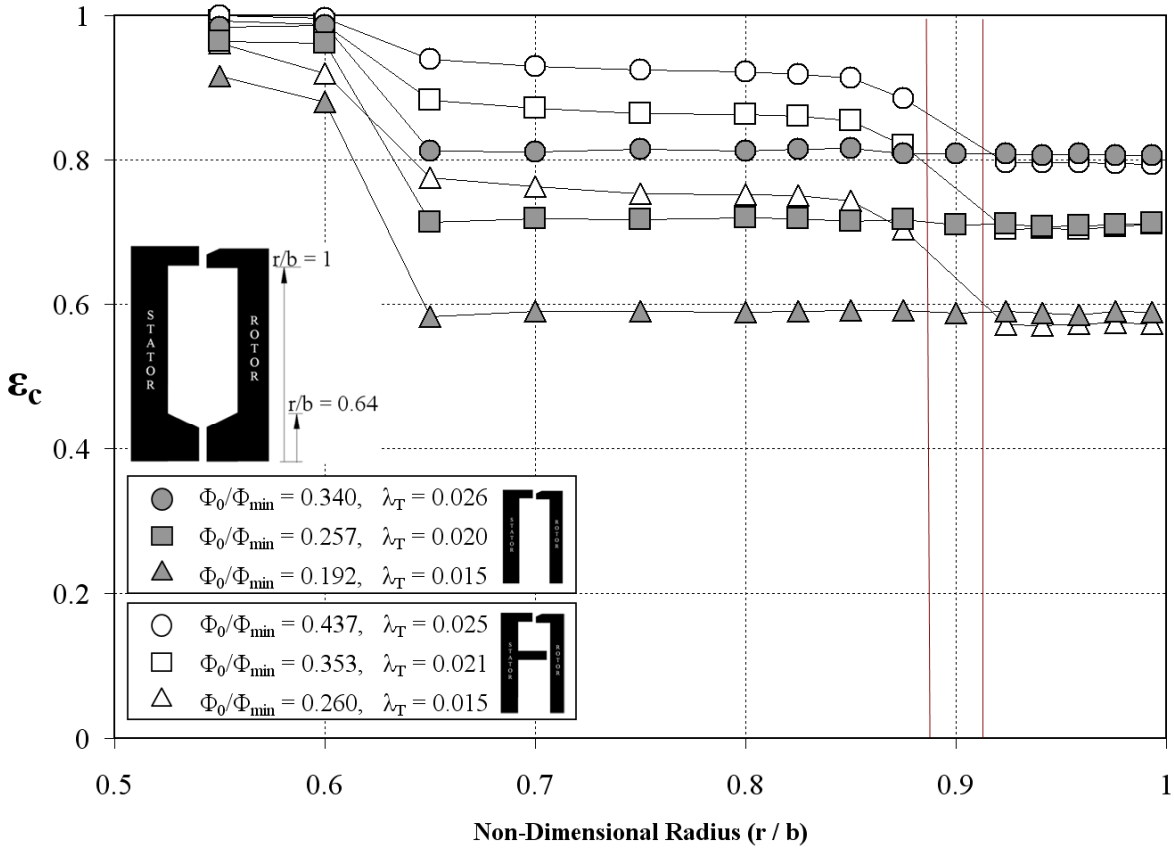

Figure 7.20 Comparison of the effect of sealing flow rate on measured radial variation of effectiveness on stator surface for axial-clearance seal and double-axial clearance seal, for RI ingress. (Open symbols denote double-axial seal; solid symbols denote single axial-clearance seal. Lines are included for reader's convenience only.)

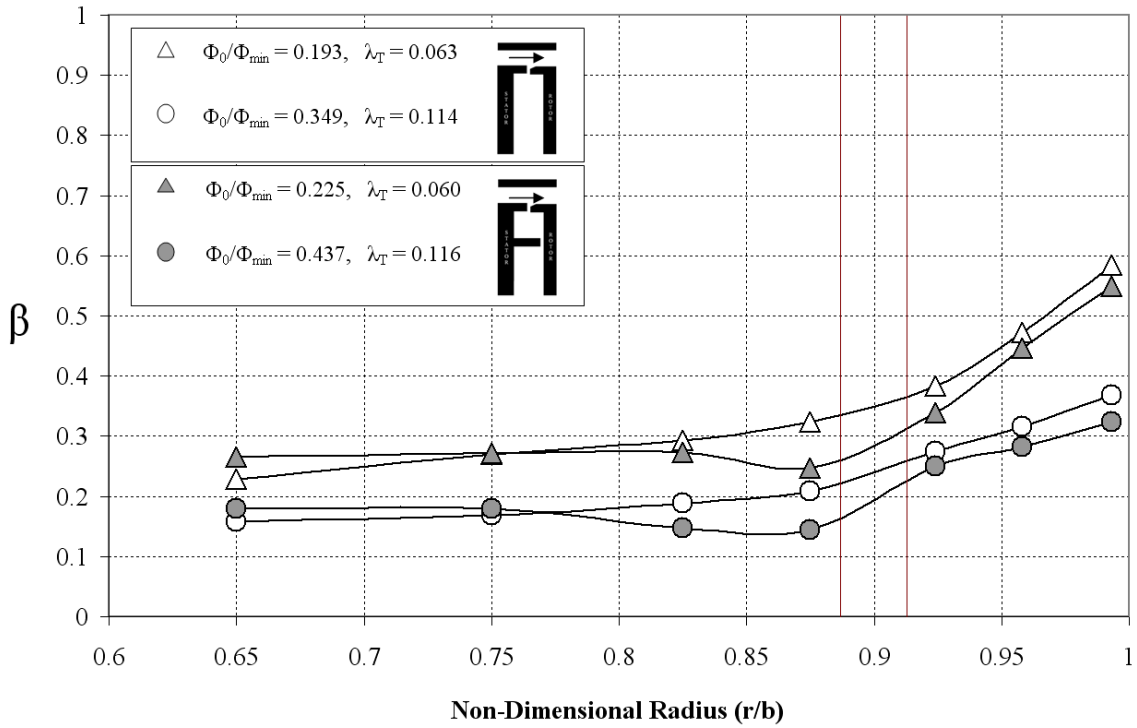

Figure 7.21 Comparison of swirl ratio distributions for axial-clearance seal and double-axial clearance seal and different purge flow-rates, for EI ingress. (Lines are included for reader's convenience only.)

7.5 Rim-seal discharge coefficients

Table 7.4 shows the values of $C_{d,e}$, $C_{d,i}$ and K for the double seal configurations, with the single seal variants included for comparison. The values of $C_{d,e}$ were calculated from Eq. 3.33 and the values of $C_{d,i}$ were found from the corresponding value of Γ_c; K was calculated from Eq. 5.2. For each seal, these three constants depend on where (location A or B) in the annulus ΔC_p was determined. The double seal variants are shown for both the inner and outer seal clearance with Φ_{min} determined using $\varepsilon_{c,13}$ and $\varepsilon_{c,23}$, respectively.

Regardless of location, the value of $C_{d,e}$ for the radial-axial double clearance seal compared to that for the double-axial clearance seal, is approximately 39% for the outer seal-clearance and 53% for the inner seal-clearance; the corresponding ratios for the $C_{d,i}$ values are approximately 147% and 62-66%, respectively. Although the radial-axial double-clearance seal out performs the double-axial counterpart in terms of sealing effectiveness, the larger $C_{d,i}$ values for the outer seal clearance could explain the large effect of external swirl in the intermediate annulus present for Generic # 3 but not Generic # 4 (Section 7.4).

ΔC_p Location	Seal Type	Configuration Geometry	ΔC_p	Φ_{min}	Γ_c	$C_{d,e}$	$C_{d,i}$	K
'A'	Generic Single Seal # 1	Axial Clearance	0.82	0.326	0.48	0.54	0.26	0.51
	Generic Single Seal # 2	Radial Clearance	0.82	0.092	1.32	0.15	0.20	0.14
	Generic Double Seal # 3	Radial Clearance Outer	0.82	0.103	3.28	0.17	0.56	0.16
		Axial Clearance Inner	0.82	0.082	0.27	0.14	0.04	0.13
	Generic Double Seal # 4	Axial Clearance Outer	0.82	0.265	0.86	0.44	0.38	0.41
		Axial Clearance Inner	0.82	0.156	0.22	0.26	0.06	0.24
'B'	Generic Single Seal # 1	Axial Clearance	0.42	0.326	0.48	0.75	0.36	0.71
	Generic Single Seal # 2	Radial Clearance	0.42	0.092	1.32	0.21	0.28	0.20
	Generic Double Seal # 3	Radial Clearance Outer	0.42	0.103	3.28	0.24	0.78	0.22
		Axial Clearance Inner	0.42	0.082	0.27	0.19	0.05	0.18
	Generic Double Seal # 4	Axial Clearance Outer	0.42	0.265	0.86	0.61	0.53	0.58
		Axial Clearance Inner	0.42	0.156	0.22	0.36	0.08	0.34

Table 7.4 Discharge coefficients and K values for all tested seal configurations

The reduction in the amount of sealing air required to prevent ingestion for the rim-seals featuring a radial-clearance (Generics 2 and 3) is a direct consequence of the small values of $C_{d,e}$ for these seals compared to the axial outer-seal configurations. As explained in Section 5.3.3, this is caused perhaps by the 'impinging jet phenomenon' resulting in a much larger reduction of $C_{d,e}$ than $C_{d,i}$.

Generic Double Seal # 3 is similar in geometry to the data collected for Configuration # 4 used by Bohn and Wolff (2003) which was correlated with $K = 0.12$. Although perhaps fortuitous this compares well with the value of $K = 0.13$ calculated in Table 7.4 for the inner seal-clearance, with ΔC_p measured at a similar though not geometrically identical position in the annulus.

7.6 Ultimate double-seal concept

The ultimate double seal concept is one in which the circumferential distribution of pressure is damped out in the annular space between the two seal clearances; this space is referred to below as the *intermediate annulus*. Under these conditions, the inner seal experiences RI ingress. That is,

$$\hat{\Phi}'_{min} = \Phi'_{min,RI} \qquad \text{(Equation 7.11)}$$

where ^ denotes the ultimate seal and the prime denotes the inner seal.

In the concentration experiments, Φ_0 is based on the outer radius b, where

$$\Phi_0 = \frac{C_{w,0}}{2\pi G_c Re_\Phi} \qquad \text{(Equation 7.12)}$$

and

$$C_{w,0} = \frac{\dot{m}_0}{\mu b}, \qquad G_c = \frac{s_c}{b}, \qquad Re_\Phi = \frac{\rho \Omega b^2}{\mu} \qquad \text{(Equation 7.13)}$$

For the inner seal,

$$\Phi_0' = \frac{C_{w,0}'}{2\pi G_c' Re_\Phi'} \qquad \text{(Equation 7.14)}$$

where

$$C_{w,0}' = \frac{\dot{m}_0}{\mu b'}, \qquad G_c' = \frac{s_c'}{b'}, \qquad Re_\Phi' = \frac{\rho \Omega b'^2}{\mu} \qquad \text{(Equation 7.15)}$$

It follows that

$$\frac{\Phi_0{}'}{\Phi_0} = \frac{s_c}{s_c{}'}\left(\frac{b}{b'}\right)^2 \qquad \text{(Equation 7.16)}$$

Equation 7.16 should be used to convert the sealing flow parameter calculated for the outer seal to one appropriate for the inner seal. The performance of the ultimate inner seal is given by Eq. 7.11, and performance of actual seals could be compared with this.

7.6.1 Double-seal performance factor

Table 7.5 shows the values of Φ_{min} obtained by concentration measurements for the two single and two double seals tested. For the double seals, Φ_{min} corresponds to $\varepsilon_{c,23}$ = 1 for the outer seal and to $\varepsilon_{c,13}$ = 1 for the inner seal.

It can be seen from the table that, apart from the radial-clearance outer seal for EI ingress, the values of Φ_{min} for the outer seals are less than those for the corresponding single seals. The reason for the differences between the performance of the single and outer seals is discussed in Section 7.6.2.

Seal Type	Configuration Geometry	$\Phi_{min,RI}$	$\Phi_{min,EI}$
Generic Single Seal # 1	Axial Clearance	0.0838	0.326
Generic Single Seal # 2	Radial Clearance	0.0317	0.0915
Generic Double Seal # 3	Radial Clearance Outer	0.0278	0.103
	Axial Clearance Inner	0.0284	0.0822
Generic Double Seal # 4	Axial Clearance Outer	0.0630	0.265
	Axial Clearance Inner	0.0544	0.156

Table 7.5 Values of Φ_{min} from concentration measurements

It is useful to rank double seals on their performance relative to the ultimate variant described in Section 7.6. The value of Φ_{min} for any single seal is independent of the dimensions of that seal, which means that, for any seal geometry, $\Phi'_{min,EI} = \Phi_{min,EI}$ and $\Phi'_{min,RI} = \Phi_{min,RI}$. The definition for the *performance factor*, η, for a double seal is that it should equal unity when all the pressure asymmetry has been damped out, so that $\Phi'_{min} = \Phi_{min,RI}$, and that it should equal zero when there is no damping, so that $\Phi'_{min} = \Phi_{min,EI}$. The appropriate definition for the performance factor is therefore

$$\eta = \frac{\Phi_{min,EI} - \Phi'_{min}}{\Phi_{min,EI} - \Phi_{min,RI}} \quad \text{(Equation 7.17)}$$

where Φ'_{min} for the double seal can be determined from Eq. 7.7 with $\varepsilon_{c,13} = 1$, and $\Phi_{min,EI}$ and $\Phi_{min,RI}$ are the values for a single seal of the same type as the inner seal (e.g. axial-clearance).

For the Generic # 3 seal, with a radial-clearance outer and an axial-clearance inner seal, for EI ingress $\varepsilon_{c,13} = 1$ when $\Phi_0 = 0.082$. For this seal, $s_c = 2.4$ mm, $s_c' = 2$ mm, $b'/b = 0.9$. Hence, from Eq. 7.16, $\Phi_0' / \Phi_0 = 1.48$ and therefore $\Phi'_{min} = 0.122$. For a single axial-clearance seal, $\Phi_{min,RI} = 0.0838$ and $\Phi_{min,EI} = 0.326$, and it follows from Eq. 7.17 that $\eta = 0.84$.

For the Generic # 4 seal, with axial-clearance inner and outer seals, for EI ingress $\varepsilon_{c,13} = 1$ when $\Phi_0 = 0.156$. For this seal, $s_c = 2$ mm, $s_c' = 2$ mm, $b'/b = 0.9$. Hence, from Eq. 7.16, $\Phi_0' / \Phi_0 = 1.23$ and therefore $\Phi'_{min} = 0.192$. For a single axial-clearance seal, $\Phi_{min,RI} = 0.0838$ and $\Phi_{min,EI} = 0.326$, as above, and it follows from Eq. 7.17 that $\eta = 0.55$.

It is apparent when using the derived *performance factor*, η, which compares double seal configurations to the ultimate seal concept, that the radial-axial combination seal provides a 50% performance improvement over its double axial-clearance counterpart. The increased performance of the outer radial-clearance seal present in Generic # 3, but not in # 4, is expected to be a strong contributor to this.

In order to improve the design of the intermediate annulus between the two rim seals and achieve $\eta = 1$ in the optimal case, it is important that the intermediate annulus should be a very effective damping chamber. As a rotating disc tends to produce axisymmetric flow, it would seem that the intermediate annulus should have as much rotating surface area as practical.

7.6.2 Further investigation

The rim-seal effectiveness comparisons between the single and double seal configurations shown in Table 7.5 highlight inconsistencies between the concentration effectiveness of the outer seals with that of the equivalent single seal. The radial-clearance rim-seal seems to work less effectively when combined with an inner axial-clearance seal, however the axial-clearance rim-seal works in the opposite way and demonstrates improved performance with the inner seal addition. Additional investigation is therefore required, possibly with the use of CFD, to uncover the fluid dynamics creating this scenario.

7.7 Practical implications

Effectiveness results have been presented showing the improved performance of double clearance rim-seals. An inner axial-clearance seal was seen to substantially increase the sealing effectiveness radially inward of its location, whilst containing much of the ingestion to the intermediate annulus. With gas turbine designers eager to reduce the amount of purge air required to seal a gas turbine wheels-space, it is encouraging to see that with the addition of a simple inner seal, much of the turbine discs can be protected with relatively minimal sealant flow-rates. In a commercial environment dominated by cost, it is pertinent to suggest that the use of expensive high-temperature alloys needs to be minimised in modern engine design. The double seal configurations discussed would allow for these expensive alloys to be reserved for use in the intermediate annulus, with more modest materials forming the inner-wheel-space.

The concept of an "*ultimate* double seal" is proposed where the outer seal works in the EI regime, however the intermediate annulus formed between the seals attenuates the circumferential pressure difference, allowing the inner seal to work in the RI regime. In this limiting case, the seal cannot be improved further. A double-seal performance ranking is derived, where it may be possible to optimise the geometry of such an intermediate annulus to approach the ultimate case.

An invention disclosure was submitted to Siemens detailing the design of an optimised intermediate annulus with the use of radial fins on the rotor disc. It is hoped that this concept will offer improved sealing characteristics over other double seal configurations and approach the *ultimate* seal case. This document will form the basis of a patent application.

Chapter 8: Conclusions

A new experimental facility has been commissioned at the University of Bath to investigate the fluid dynamics and heat transfer effects of hot gas ingestion through turbine rim seals. The rig was constructed as an engine representative model of a gas turbine stage and wheel-space, from which data could be scaled and applied to an engine design. The rig design has evolved from a concept sketch with preliminary calculations, right through to a fully operational test facility. The rig is able to measure the effectiveness of generic and engine-specific rim seal geometries as well as investigating the thermal effects of hot gas ingress, providing insight never before achieved. An extensive commissioning process was undertaken to ensure that the correct, albeit benign, fluid-dynamic conditions were created inside the single stage turbine rig, before an extensive experimental program was conducted.

This programme is ongoing and has led to plans for a new facility with 1.5 stages. The thermal effects of hot gas ingress have also been successfully studied and is the subject of an ASME paper planned for ASME 2012 (Pountney *et al.* (2012)), as well as a PhD thesis (Pountney (2012)).

8.1 Design of the testing facility

The main conclusions from the design of the rig are as follows:

- The capability to investigate the thermal effects of hot gas ingestion was a high priority. Throughout the rig development, care was always taken to ensure there was full optical access to the wheel-space for TLC measurements. This involved unrestricted frontal access through the volute and housing, which dominated the design process from the start.

- Turbine stage velocity triangles were used to create design points for the flow in the external annulus. This led to a series of calculations governing the flow characteristics through each section of the rig, and allowed geometric CAD models to be created, which provided dimensions of the rig as it evolved.

- It was decided to design the rig based on three design points at disc speeds of 2000, 3000 and 3500 rpm; effectiveness tests would be conducted at all speeds. The rig featured a 10 mm annulus height, a vane with a 73.5^{o} turning angle and a symmetric blade angled at 56.7^{o} to

the axial. These angles ensured that the blade remained unloaded; a dynamometer was not available and so turned blades could not be used.

- Two mainstream feed systems were designed with a 'cold main annulus' design going into immediate fabrication and a 'hot main annulus' design being held back for future work. The rig had to be put into production by strict time schedules for Siemens and the early effectiveness tests did not require a heated external flow. The CMA (cold main annulus) design featured thirty-two inlet pipes, each feeding a vane with unheated air, aimed at producing a high level of pressure axisymmetry.

- A series of seal geometries were finalised, featuring a set of interchangeable generic seals which could reproduce the appropriate fluid dynamics inside the cavity. It was hoped that the fundamental knowledge acquired from the generic tests would allow Siemens to optimise more company proprietary seals that could be potentially tested in the future. This has indeed been the case and seals have been tested which could not be published in the open domain.

- In terms of the orifice model, development continued in parallel to the rig design, with mathematical analysis of both rotationally-induced and externally-induced ingress producing agreeable results with published literature. Most recently, the explicit effectiveness equations have been derived, which provide the theoretical fits to the experimental data.

- Much work was conducted into achieving a sufficient pressure asymmetry in the external annulus, which was required to generate externally-induced ingress. A series of static pressure taps inside the annulus was used to record this cyclical pressure distribution. Other instrumentation implemented in the rig included radial and axial displacement transducers to monitor seal and running clearances, thermocouple probes, pitot tubes, pressure tapings and concentration probes, all which have been used extensively to great success.

- In terms of material selection, work was undertaken into structural testing to determine appropriate materials for the rig. For optical access, the discs were manufactured from polycarbonate, with an aluminium-alloy containment ring used to restrict the internal stresses and growth caused by rotation.

It is pertinent to end the design conclusions with a series of CAD projections and photographic images of the rig in its commissioned state, as shown in Appendix D.

8.2 Externally-induced ingress research

Measurements of CO_2 gas concentration in the rim-seal region inside the cavity were used to assess the performance of two generic (though engine-representative) rim-seal geometries in terms of the concentration effectiveness, ε_c, under externally-induced ingress conditions. Instead of having to use separate correlations for the effects of G_c and Re_Φ on ε_c, Φ_o (the sealing parameter) combines $C_{w,o}$, G_c and Re_Φ into a single parameter, and the variation for ε_c and $\Phi_{i,EI}$ is presented against Φ_o. It should also be noted that the flow, which was over a small range of Mach numbers, was virtually incompressible (M< 0.4).

The circumferential variation of the non-dimensional peak-to-trough pressure difference, ΔC_p, in the turbine annulus, which governs this externally-induced (EI) ingestion, was obtained from steady pressure measurements downstream of the vanes and near the rim seal upstream of the rotating blades. At the design point (Re_w/Re_Φ = 0.538), and at a fixed location in the annulus, ΔC_p, is independent of Re_Φ. At off-design conditions, $\Delta C_p \propto (Re_w/Re_\Phi)^2$.

An orifice model was used to provide simple effectiveness equations that express the variation of ε and $\Phi_{i,EI}$ with Φ_o. The effectiveness equations were able to estimate $\Phi_{min,EI}$, the minimum non-dimensional sealing flow rate to prevent ingress, from the (ε_c, Φ_o) data points without any knowledge of the pressure distribution in the annulus or any associated rim-seal discharge coefficients; this makes the model a powerful tool for rim-seal design.

The ingestion through the rim seal is a consequence of an unsteady, three-dimensional flow field; the cause-effect relationship between pressure and effectiveness is complex and it may not be possible for an experiment to isolate the many intertwined mechanisms which govern ingress. Despite this, the steady-state experimental data presented here is shown to be successfully correlated by the simple effectiveness equations developed from the orifice model. The data (and model) illustrate that for similar turbine-stage velocity triangles, a rim seal geometry can be characterised principally by the parameter $\Phi_{min,EI}$ which, at the design point, is independent of Re_Φ.

A statistical model featuring maximum-likelihood estimates was used to fit the effectiveness equations to the experimental data for the two seals. In both cases, the agreement between the fitted curves and the data was very good. Using the statistical model, the ratio of the sealing flow rate required to prevent ingress for the radial-clearance seal to that required for the axial-clearance seal was found to be around 26%.

In principle, and within the limits of dimensional similitude, $\Phi_{min,EI}$ should apply to a geometrically-similar engine operating at the same fluid-dynamic conditions. The orifice model shows that, for EI ingress, $\Phi_{min,EI}$ is proportional to $\Delta C_p^{1/2}$, and it is tentatively suggested that this relationship could be used to extrapolate the results from an experimental rig to an engine.

8.3 Rotationally-induced ingress research

Further experiments to determine the sealing effectiveness, were conducted for the rotationally-induced (RI) regime. Two different seals were again tested, and RI ingress was achieved by running the rig at different rotational speeds with no axial flow through the external annulus. Using, Φ_o the nondimensional sealing parameter, the effectiveness data obtained at different rotational speeds was collapsed onto a single curve, similar to the case for EI ingress.
There was again, very good agreement between the experimental measurements and the theoretical effectiveness curves (and with the theoretical ingress curves) obtained from the RI orifice model.

For RI ingress, the ratio of the sealing flow rate required to prevent ingress for the radial-clearance seal to that required for the axial-clearance seal was around 38%. For the axial-clearance seal, the ratio of the sealing flow rate required to prevent ingress for the RI case to that required for the EI case was around 26%; for the radial-clearance seal, the ratio was around 35%.

8.4 Implication of double seal configurations

Effectiveness results were presented showing the improved performance of double clearance seals over their single-clearance counterparts. An inner axial-clearance seal was seen to substantially increase the sealing effectiveness radially inward of its location, whilst containing much of the hot gas ingestion to the so-formed intermediate annulus between the two seal clearances in a double rim-seal configuration. With gas turbine designers eager to reduce the amount of purge air, it was encouraging to measure the improved protection provided by a single inner seal. In fact when considering the radial-outer and axial-inner seal combination, up to a 44% increase in sealing effectiveness was measured across the inner seal when compared to a single radial outer-clearance seal at a sealant flow level of $\Phi_0/\Phi_{min} = 0.251$.

The concept of an "*ultimate* double seal" was discussed as a limiting case. Here the outer seal works in the EI regime, however the intermediate annulus formed between the seals attenuates the circumferential pressure variation, allowing the inner seal to work in the RI regime. A double-seal performance ranking, η, was derived, where it may be possible to optimise the geometry of an intermediate annulus to approach the ultimate case.

The double seal geometries tested here fall short of the *ultimate* double seal; the radial-outer and axial-inner combination produced a performance factor of 84%, with the double axial-clearance performance at 55%. An invention disclosure was submitted to Siemens detailing the design of an optimised intermediate annulus with the use of radial fins on the rotor disc. It is hoped

that this concept will offer improved sealing characteristics over other double seal configurations and approach the *ultimate* seal case. This document will form the basis of a patent application.

8.5 Future work

With the orifice model shown to successfully predict experimental data in the RI and EI regimes, it seems only natural that the work must be extended to envelope the CI regime; where most non-optimal double seal configurations would work. In order to test the single clearance-seals in the CI regime, a series of "*off-design*" tests would be desirable. This would be achieved by holding the rotor at a fixed rotational speed and incrementally increasing the external flow from the quiescent case, where the conditions would be RI dominated, up to the balanced conditions for unloaded blades, where EI would dominate, before venturing beyond to the so called *'under-speed'* conditions. This would allow the rim-seal to work in this transitional regime and for effectiveness data to be recorded that would take the theoretical orifice model into a new validation program as started by Owen *et al.* (2010b). It is suggested that the blade effects may be pronounced as the rig is operated '*under-speed*' and '*over-speed*,' and that blade *shielding* functions may be required to take this into account. Work has already begun on the development of a theoretical fitting process for off-design work by extending the orifice model to include such functions.

Such is the performance benefit of well-configured double seal geometries that further work is essential to optimise their designs. Buffer cavity volume is a key driver for onward research, whereby it is expected that this will be key to damping out the external pressure asymmetry; potentially by increasing the exposure to rotating surfaces. Other optimisation possibilities include the effect of the radial-overlap dimension upon the sealing effectiveness of the seal. With Φ_0 taking G_c into account it would be interesting to see if the $s_{overlap}$ parameter; not included in the model, could be varied to beneficial effect. Extension and reduction of the single radial-clearance seal lips would be desired to investigate this effect; with any potential improvement being carried over to the design of an optimised double seal. It has become increasingly apparent from technical liaison with industrial sponsors that the quest to approach the *ultimate* double seal is high on the agenda of any future test programmes.

References

Abe, T., Kikuchi, J. and Takeuchi, H. (1979). "An Investigation of Turbine Disk Cooling (Experimental investigation and Observation of Hot Gas Flow into a Wheel Space)." CIMAG - 13th International Congress on Combustion Engines.

Anderson, M. R. and Baughn, J. W. (2004). "Hysteresis in Liquid Crystal Thermography." J. Heat Transf. **126**(3): pp. 339-346.

Batchelor, G. K. (1951). "Note on a Class of Solutions of the Navier-Stokes Equations Representing Steady Rotationally-Symmentric Flow." Quart. J. Mech Appl. Math. **4**: pp. 29-41.

Bayley, F. J. and Owen, J. M. (1969). "Flow Between a Rotating and a Stationary Disc." Aeronautical Quarterly **20**: pp. 333 -354.

Bayley, F. J. and Owen, J. M. (1970). " Fluid Dynamics of a Shrouded Disk System with a Radial Outflow of Coolant." Journal of Engineering for Power **92**(3): pp. 335-.

Bohn, D., Johann, E. and Krueger, U. (1995). Experimental and Numerical Investigations of Aerodynamic Aspects of Hot Gas Ingestion in Rotor-Stator Systems with Superimposed Cooling Mass Flow. Gas turbine and aeroengine 95-GT-143

Bohn, D. and Wolff, M. (2003). Improved Formulation to Determine Minimum Sealing Flow: Cw, min - for Different Sealing Configurations. ASME Paper GT2003-38465

Bohn, D. E., Decker, A., Ma, H. and Wolff, M. (2003). Influence of Sealing Air Mass Flow on the Velocity Distribution in and Inside the Rim of the Upstream Cavity of a 1.5-Stage Turbine. ASME Paper GT2003-38459

Bohn, D. E., Decker, A., Ohlendorf, N. and Jakoby, R. (2006). Influence of an Axial and Radial Rim Seal Geometry on Hot Gas Ingestion Into the Upstream Cavity of a 1.5-Stage Turbine. ASME Paper GT2006-90453

Bunker, R. S., Metzger, D. E. and Wittig, S. (1992a). "Local Heat Transfer in Turbine Disk Cavities: Part I---Rotor and Stator Cooling With Hub Injection of Coolant." ASME J. Turbomach. **114**(1): pp. 211-220.

Bunker, R. S., Metzger, D. E. and Wittig, S. (1992b). "Local Heat Transfer in Turbine Disk Cavities: Part II---Rotor Cooling With Radial Location Injection of Coolant." ASME J. Turbomach. **114**(1): pp. 221-228.

Cao, C., Chew, J. W., Millington, P. R. and Hogg, S. I. (2004). "Interaction of Rim Seal and Annulus Flows in an Axial Flow Turbine." J. Eng. Gas Turb. Power **126**(4): pp. 786-793.

Cengel, Y. A. and Boles, M. A. (2002). Thermodynamics: An Engineering Approach; Fourth Edition, McGraw-Hill International. ISBN 007121688x

Chen, J. X., Gan, X. and Owen, J. M. (1996). "Heat Transfer in an Air-Cooled Rotor-Stator System." ASME J. Turbomach. **118**(3): pp. 444-451.

Chew, J. W. (1991). "A Theoretical Study of Ingress for Shrouded Rotating Disk Systems With Radial Outflow." ASME J. Turbomach. **113**(1): pp. 91-97.

Chew, J. W., Dadkhah, S. and Turner, A. B. (1992). "Rim Sealing of Rotor--Stator Wheelspaces in the Absence of External Flow." ASME J. Turbomach. **114**(2): pp. 433-438.

Chew, J. W., Green, T. and Turner, A. B. (1994). Rim Sealing of Rotor-Stator Wheelspaces in the Presence of External Flow. Gas turbine and aeroengine 94-GT-126

Childs, P. R. N. (2010). Rotating Flow, Butterworth-Heinemann. ISBN 0123820987

Cumpsty, N. (1997). Jet Propulsion, University Press, Cambridge. ISBN 0521596742

Dadkhah, S., Turner, A. B. and Chew, J. W. (1992). "Performance of Radial Clearance Rim Seals in Upstream and Downstream Rotor--Stator Wheelspaces." ASME J. Turbomach. **114**(2): pp. 439-445.

Daily, J. W. and Nece, R. E. (1960). "Chamber Dimension Effects on Induced Flow and Frictional Resistance of Enclosed Disks." ASME J. Basic Eng. **82**: pp. 217-232.

Daily, J. W., Ernst, W. D. and Asbendian, V. V. (1964). Enclosed rotating discs with superposed through-flow: Mean steady and periodic unsteady characteristics of induced flow, MIT Department of Civil Engineering. **Hydrodynamics Laboratory Report No.64**.

Daniels, W. A., Johnson, B. V., Graber, D. J. and Martin, R. J. (1992). "Rim Seal Experiments and Analysis for Turbine Applications." ASME J. Turbomach. **114**(2): pp. 426-432.

Dring, R. P., Joslyn, H. D., Hardin, L. W. and Wagner, J. H. (1982). "Turbine Rotor-Stator Interaction." Journal of Engineering for Power-Transactions of the Asme **104**(4): pp. 729-742.

Gentilhomme, O., Hills, N. J., Turner, A. B. and Chew, J. W. (2003). "Measurement and Analysis of Ingestion Through a Turbine Rim Seal." ASME J. Turbomach. **125**(3): pp. 505-512.

Graber, D. J., Daniels, W. A. and Johnson, B. V. (1987). "Disk Pumping Test." Pratt and Whitney West Palm Beach, FL Government Products Division.

Green, T. and Turner, A. B. (1994). "Ingestion Into the Upstream Wheelspace of an Axial Turbine Stage." ASME J. Turbomach. **116**(2): pp. 327-332.

Hamabe, K. and Ishida, K. (1991). A Simplified Model for Estimating Ingress of Gas-Turbine Rotor-Stator Systems. Yokohama International Gas Turbine Congress IGTC-19

Hamabe, K. and Ishida, K. (1992). Rim Seal Experiments and Analysis of a Rotor-Stator System with Nonaxisymmetric Main Flow. ASME Paper 92-GT-160

Ireland, P. T., Gillespie, D. R. H. and Wang, Z. (1996). Heating Element. E. P. Specification. **EP 0 847 679 B1**.

Johnson, B. V., Jakoby, R., Bohn, D. E. and Cunat, D. (2006). A Method for Estimating the Influence of Time-Dependent Vane and Blade Pressure Fields on Turbine Rim Seal Ingestion. ASME Paper GT2006-90853

Johnson, B. V., Wang, C. Z. and Roy, R. P. (2008). A Rim Seal Orifice Model with 2 Cd s and Effects of Swirl in Seals. ASME Paper GT2008-50650

Kakade, V. U., Lock, G. D., Wilson, M., Owen, J. M. and Mayhew, J. E. (2009a). "Accurate heat transfer measurements using thermochromic liquid crystal. Part 1: Calibration and characteristics of crystals." Int. J. Heat Fluid Flow **30**(5): pp. 939-949.

Kakade, V. U., Lock, G. D., Wilson, M., Owen, J. M. and Mayhew, J. E. (2009b). "Accurate heat transfer measurements using thermochromic liquid crystal. Part 2: Application to a rotating disc." Int. J. Heat Fluid Flow **30**(5): pp. 950-959.

Kakade, V. U., Lock, G. D., Wilson, M., Owen, J. M. and Mayhew, J. E. (2011). "Effect of Radial Location of Nozzles on Heat Transfer in Preswirl Cooling Systems." ASME J. Turbomach. **133**.

Kármán, T. v. (1921). "Uber laminare und turbulente reibung [On laminar and turbulent friction]." Zeitschrift fur angewandte Mathematik Mechanik **1**: pp. 223-252.

Khilnani, V. I. and Bhavnani, S. H. (2001). "Sealing of gas turbine disk cavities operating in the presence of mainstream external flow." Experimental Thermal and Fluid Science **25**(3-4): pp. 163-173.

Kingsley-Rowe, J. R., Lock, G. D. and Michael Owen, J. (2005). "Transient heat transfer measurements using thermochromic liquid crystal: lateral-conduction error." Int. J. Heat Fluid Flow **26**(2): pp. 256-263.

Klein, E. J. (1968). Application of Liquid Crystal to Boundary Layer Flow Visualisation. AIAA Paper 68-376

Lock, G. D. (2007). Aircraft Propulsion - Lecture Course Notes.

Meher-Homji, C. B. (1997). "The Development of the Junkers Jumo 004B---The World's First Production Turbojet." J. Eng. Gas Turb. Power **119**(4): pp. 783-789.

Meher-Homji, C. B. (1998). "The Development of the Whittle Turbojet." J. Eng. Gas Turb. Power **120**(2): pp. 249-256.

Meher-Homji, C. B. and Prisell, E. (2000). "Pioneering Turbojet Developments of Dr. Hans Von Ohain---From the HeS 1 to the HeS 011." J. Eng. Gas Turb. Power **122**(2): pp. 191-201.

Morley, A. (1954). Strength of Materials, Longmans, Green and Co. Ltd. ISBN 144462749X

Newton, P. J., Yan, Y., Stevens, N. E., Evatt, S. T., Lock, G. D. and Owen, J. M. (2003). "Transient heat transfer measurements using thermochromic liquid crystal. Part 1: An improved technique." Int. J. Heat Fluid Flow **24**(1): pp. 14-22.

Owen, J. M., Haynes, C. M. and Bayley, F. J. (1974). "Heat Transfer from an Air-Cooled Rotating Disk." Proceedings of the Royal Society of London. Series A, Mathematical and Physical Sciences **336**(1607): pp. 453-473.

Owen, J. M. (1988). An Approximate Solution for the Flow Between a Rotating and a Stationary Disc. ASME Paper 88-GT-293

Owen, J. M. and Rogers, R. H. (1989). Flow and Heat Transfer in Rotating-Disc Systems, Volume 1 - Rotor Stator Systems. ISBN 0863800904

Owen, J. M. and Rogers, R. H. (1995). Flow and Heat Transfer in Rotating-Disc Systems, Volume 2 - Rotating Cavities. ISBN 086380179X

Owen, J. M., Newton, P. J. and Lock, G. D. (2003). "Transient heat transfer measurements using thermochromic liquid crystal. Part 2: Experimental uncertainties." Int. J. Heat Fluid Flow **24**(1): pp. 23-28.

Owen, J. M. (2009a). Prediction of Ingestion through Turbine Rim Seals. Part 1: Rotationally-Induced Ingress. ASME Paper GT2009-59121

Owen, J. M. (2009b). Prediction of Ingestion through Turbine Rim Seals. Part 2: Externally-Induced and Combined Ingress. ASME Paper GT2009-59122

Owen, J. M., Pountney, O. J., Zhou, K., Wilson, M. and Lock, G. D. (2010a). Prediction of Ingress Through Turbine Rim Seals. Part 1: Externally-Induced Ingress. ASME Paper GT2010-23346

Owen, J. M., Pountney, O. J. and Lock, G. D. (2010b). Prediction of Ingress Through Turbine Rim Seals. Part 2: Combined Ingress. ASME Paper GT2010-23349

Owen, J. M. (2010). Theoretical Modelling of Hot Gas Ingestion through Gas Turbine Rim Seals. 3rd International Symposium on Jet Propulsion and Power Engineering

Owen, J. M., Lock, G. D., Sangan, C. M., Tham, K.-M., Lee, C.-P. and Laurello, V. P. (2011). Finned Rim Seal for Gas Turbine. S. I. Disclosure. **2011E10442US**.

Phadke, U. P. (1982). Aerodynamic Aspects of the Sealing of Rotor-Stator Systems in Gas Turbines, Univeristy of Sussex, United Kingdom. **D.Phil Thesis**.

Phadke, U. P. and Owen, J. M. (1983). "An Invesigation Of Ingress For An Air-Cooled Shrouded Rotating-Disk System With Radial-Clearance Seals." Journal of Engineering for Power-Transactions of the Asme **105**(1): pp. 178-183.

Phadke, U. P. and Owen, J. M. (1988a). "Aerodynamic Aspects of the Sealing of Gas-Turbine Rotor-Stator Systems : Part 1: The Behavior of Simple Shrouded Rotating-Disk Systems in a Quiescent Environment." Int. J. Heat Fluid Flow **9**(2): pp. 98-105.

Phadke, U. P. and Owen, J. M. (1988b). "Aerodynamic Aspects of the Sealing of Gas-Turbine Rotor-Stator Systems : Part 2: The Performance of Simple Seals in a Quasi-Axisymmetric External Flow." Int. J. Heat Fluid Flow **9**(2): pp. 106-112.

Phadke, U. P. and Owen, J. M. (1988c). "Aerodynamic Aspects of the Sealing of Gas-Turbine Rotor-Stator Systems : Part 3: The Effect of Nonaxisymmetric External Flow on Seal Performance." Int. J. Heat Fluid Flow **9**(2): pp. 113-117.

Picha, K. G. and Eckert, E. R. G. (1958). "Study of Air Between Coaxial Discs Rotating with Arbitrary Velocities in an Open or Enclosed Space." Proc. 3rd U.S. Nat. Cong. Appl. Mech.: pp. 791-798.

Pountney, O. J. (2012). PhD Thesis.

Pountney, O. J., Sangan, C. M., Owen, J. M. and Lock, G. D. (2012). Measurements of the thermal effects of hot gas ingestion through turbine rim seals. ASME Paper GT2012 pp.

Rolls-Royce (1996). The Jet Engine, Rolls-Royce PLC. ISBN 0902121235

Roth, T. B. and Anderson, A. M. (2007). "The Effects of Film Thickness, Light Polarization, and Light Intensity on the Light Transmission Characteristics of Thermochromic Liquid Crystals." J. Heat Transf. **129**(3): pp. 372-378.

Roy, R. P., Xu, G. and Feng, J. (2001). "A Study of Convective Heat Transfer in a Model Rotor--Stator Disk Cavity." ASME J. Turbomach. **123**(3): pp. 621-632.

Sangan, C. M., Pountney, O. J., Zhou, K., Wilson, M., Owen, J. M. and Lock, G. D. (2011a). Experimental Measurements of Ingestion through Turbine Rim Seals. Part 1: Externally-Induced Ingress. ASME Paper GT2011-45310

Sangan, C. M., Pountney, O. J., Zhou, K., Wilson, M., Owen, J. M. and Lock, G. D. (2011b). Experimental Measurements of Ingestion through Turbine Rim Seals. Part 2: Rotationally-Induced Ingress. ASME Paper GT2011-45313

Sangan, C. M., Zhou, K., Litherland, K., Lam, R. and Lock, G. D. (2011c). "Thermal imaging as flow visualization for gas-turbine film cooling." Proceedings of the Institution of Mechanical Engineers, Part G: Journal of Aerospace Engineering **225**(4): pp 417-431.

Smith, C. R., Sabatino, D. R. and Praisner, T. J. (2001). "Temperature sensing with thermochromic liquid crystals." Experiments in Fluids **30**(2): pp. 190-201.

Standard, E. (2003). Measurement of Fluid Flow by Means of Pressure Differential Devices Inserted in Circular Cross-Section Conduits Running Full -. Part 2: Orifice Plates (ISO 5167-2:2003), European Commity for Standardisation.

Stewartson, K. (1953). "On the Flow Betwwen Two Rotating Coaxial Discs." Proc. Camb. Phil Soc. **49**: pp. 333-341.

Theodorsen, T. and Regier, A. (1944). "Experiments on drag of revolving discs, cylinders and streamline rods at high speeds." NACA Report **793**.

Wang, C. Z., Johnson, B. V., Cloud, D. F., Paolillo, R. E., Vashist, T. K. and Roy, R. P. (2006). Rim Seal Ingestion Characteristics for Axial Gap Rim Seals in a Closely-Spaced Turbine Stage From a Numerical Simulation. ASME Paper GT2006-90965

White, F. M. (1994). Fluid Mechanics, McGraw-Hill, Inc. ISBN 0-07-113765-3

Wiberg, R. and Lior, N. (2004). "Errors in thermochromic liquid crystal thermometry." Review of Scientific Instruments **75**(9): pp. 2985-2994.

Wood, S. N. (2006). Generalized Additive Models: An Introduction with R, Boca Raton: Chapman and Hall/CRC. ISBN 9781584884743

Yan, Y. and Owen, J. M. (2002). "Uncertainties in transient heat transfer measurements with liquid crystal." Int. J. Heat Fluid Flow **23**(1): pp. 29-35.

Zhou, K., Wood, S. N. and Owen, J. M. (2011a). Analysis of Data for Ingestion through Turbine Rim Seals. ASME Paper GT2011-45139

Zhou, K., Wilson, M., Lock, G. D. and Owen, J. M. (2011b). Computation of Ingestion through Gas Turbine Rim Seals. ASME Paper GT2011-45314

Appendix A: Estimation of technical design specifications

The external-flow temperature rise required by the HMA design is considered, along with assessment of the rotor power requirements and sealant flow quantities required.

Temperature rise and required power supply for HMA:

It was possible to size the power required to heat the external flow-rate by the desired amount. Assuming a 50°C temperature rise across the heaters, the approximate power required can be calculated using Eq.A1 (Cengel and Boles (2002)):

$$Q = \dot{m}\, c_p\, \Delta T \qquad \text{(Equation.A1)}$$

where:
- $\dot{m}$ is the external mass flow-rate through the four mesh heaters
- Q is the power required
- c_p is the specific heat capacity of air
- ΔT is the temperature rise across the heaters

Calculation of entrainment coefficient and power to drive disc (Owen *et al.* (1974)):

Definition of useful coefficients:

i) Free Disc Moment Coefficient: $C_m = \frac{M}{\frac{1}{2}\rho\Omega^2 b^5}$ (Equation. A2)

ii) Non-Dimensional Entrained Flow-rate: $C_w = \frac{\dot{m}}{\mu b}$ (Equation. A3)

where:
- $\dot{m}$ is the entrained mass flow-rate
- ρ is the density
- b is the stator platform inner-radius
- μ is the dynamic viscosity
- Ω is the angular disc speed

Using the theory presented by von Kármán (1921) and an updated correlation from Bayley and Owen (1969), estimates of the two coefficients can be made directly from the rotational Reynolds number for turbulent flow over a single disc:

$$C_m = 0.0655\, Re_{\Phi}^{-0.186} \quad \text{(Equation. A4)}$$

$$C_w = 0.22\, Re_{\Phi}^{0.8} \quad \text{(Equation. A5)}$$

Rearrangement of Eqs A2 and A4 can be used to formulate the disc moment:

$$M = 0.03275\rho\Omega^2 b^5 Re_{\Phi}^{-0.186}$$

Rearrangement of Eqs A3 and A5 can be used to estimate entrainment flow rate:

$$\dot{m} = 0.22\mu b Re_{\Phi}^{0.8}$$

It is then possible to calculate the power required to drive the disc from the moment on it:

$$P = M\Omega \quad \text{(Equation. A6)}$$

Note: this is a minimum power required to run the disc.

Appendix B: Construction of the new gas dynamics laboratory

Figure B.1 Electrical re-fit of the test facility

Figure B.2 Construction of the remote running annexe

Figure B.3 Completion of the two adjacent rooms to house the new rig

Figure B.4 Fitting of the test cell with pipe-work, electrics and bed-plate

Figure B.5 Installation of Kinetrol valves to electrically control the flows to and from the test facility

Appendix C: Mesh heater design calculations

In order to avoiding extreme bowing of the mesh, it was proposed to take the maximum flow velocity from past experience using a pre-swirl rig (Kakade *et al.* (2011)). The mesh heater used there had dimensions of 120 mm by 60 mm with experimental flow-rates of approximately 0.15 kg/s, corresponding to a maximum flow velocity of 17.3 m/s.

Knowing that the mesh bowed extremely or broke at higher flow velocities, the required mesh area for the new ingestion rig was calculated using Eq. C1:

$$\dot{m} = \rho V A \qquad \text{(Equation.C1)}$$

where:
- $\dot{m}$ is the external mass flow-rate through the four mesh heaters
- ρ is the density
- V is flow velocity
- A is the mesh area

In order to keep the distance between the electrodes constant with the previous design, the proposed area was 120 mm by 112 mm, providing the calculated area required. The power required to give a 50°C temperature rise was calculated using Eq. C2:

$$Q_{total} = \dot{m} c_p \Delta T \qquad \text{(Equation.C2)}$$

where:
- $\dot{m}$ is the external mass flow-rate through the four mesh heaters
- Q_{total} is the total power required
- c_p is the specific heat capacity of air
- ΔT is the temperature rise across the heaters

Due to the four external flow paths, the mass-flow through each heater was a quarter of the total flow-rate

$$Q_{each\ heater} = \frac{Q_{total}}{4} \qquad \text{(Equation.C3)}$$

The wire mesh resistance was calculated from the manufacturer stated value of resistance (given in Ω/square) using Eq. C4:

$$R = R_s \left(\frac{L}{W}\right) \qquad \text{(Equation.C4)}$$

where:
- R is the wire mesh resistance
- R_s is the manufacturers stated wire resistance per square
- L and W are the wire mesh dimensions

The power source required for the heaters was given by Equation C5:

$$P = i^2 R \qquad \text{(Equation.C5)}$$

where:
- R is the wire mesh resistance
- i is the current source required
- P is the electrical power required

Appendix D: Photographs of the gas turbine test facility

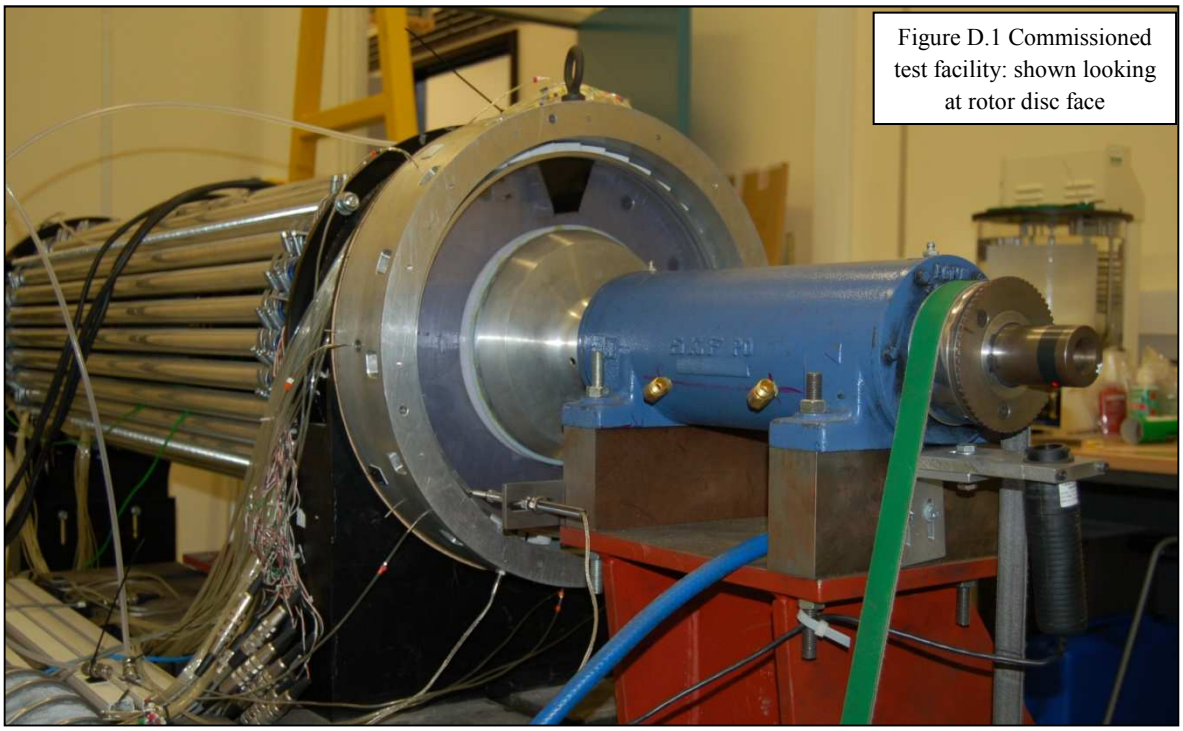

Figure D.1 Commissioned test facility: shown looking at rotor disc face

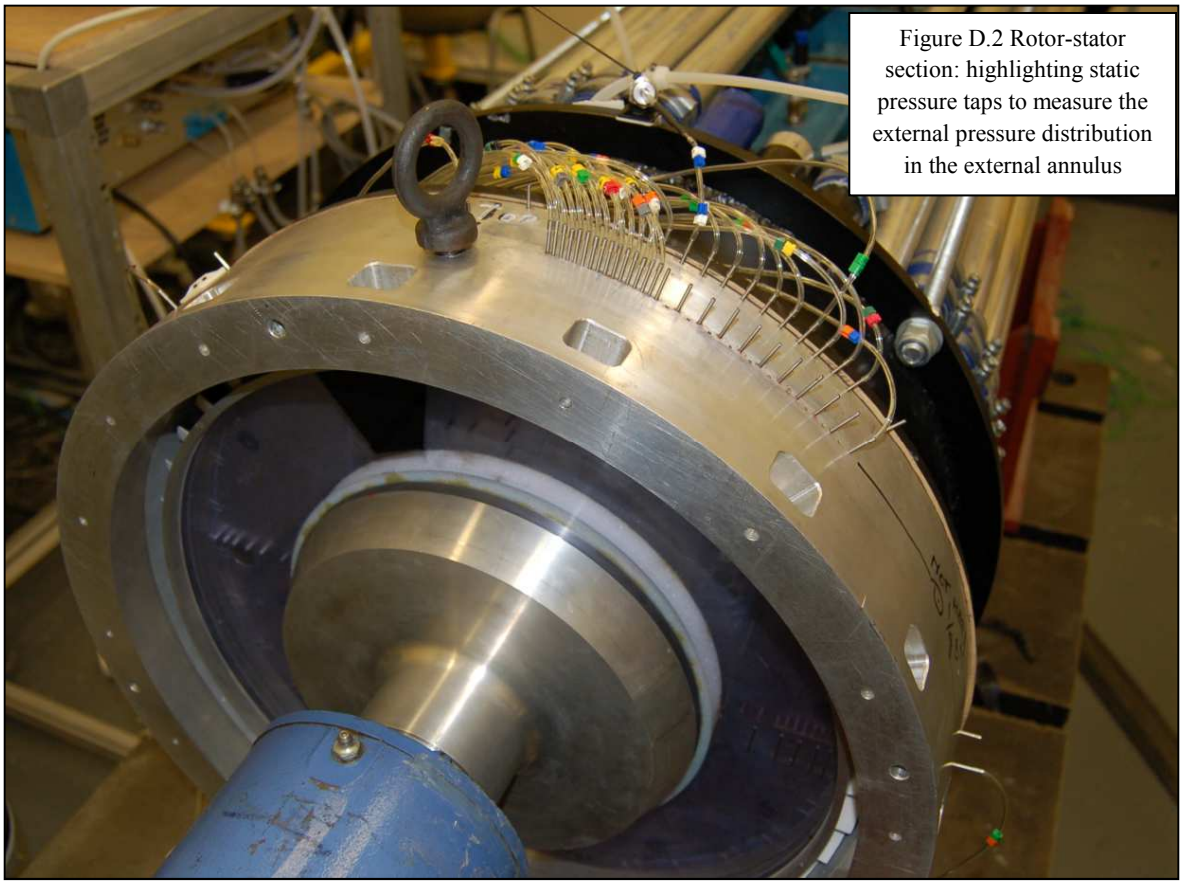

Figure D.2 Rotor-stator section: highlighting static pressure taps to measure the external pressure distribution in the external annulus

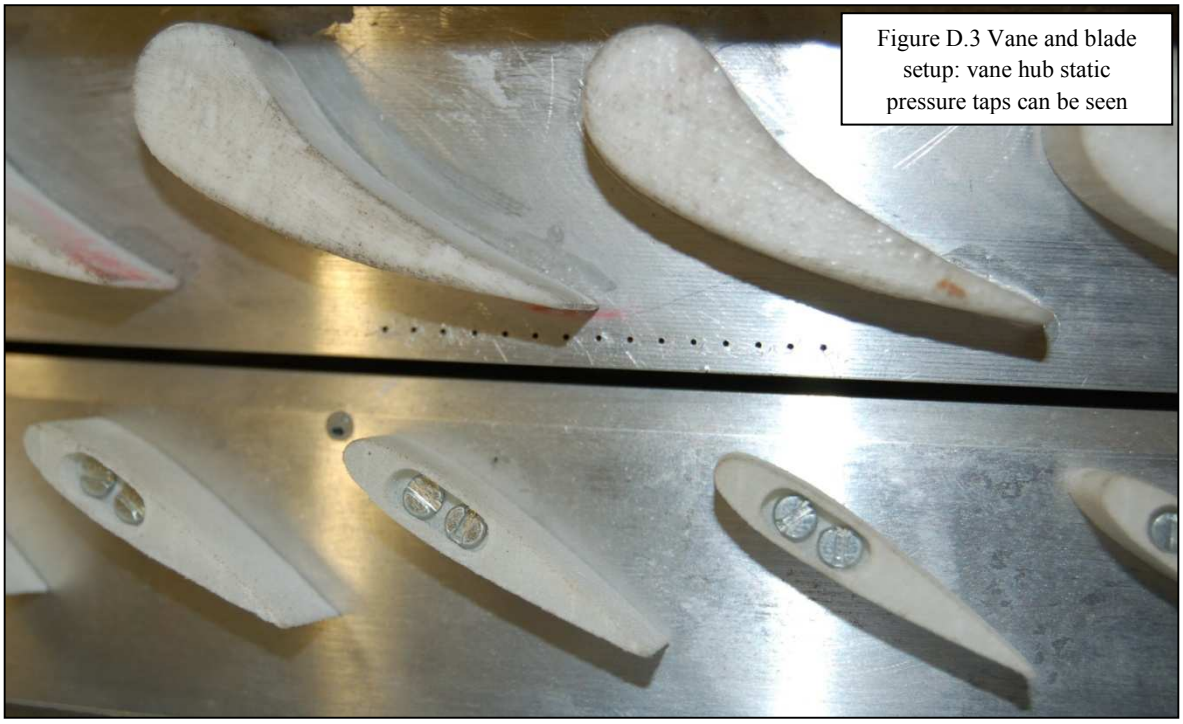

Figure D.3 Vane and blade setup: vane hub static pressure taps can be seen

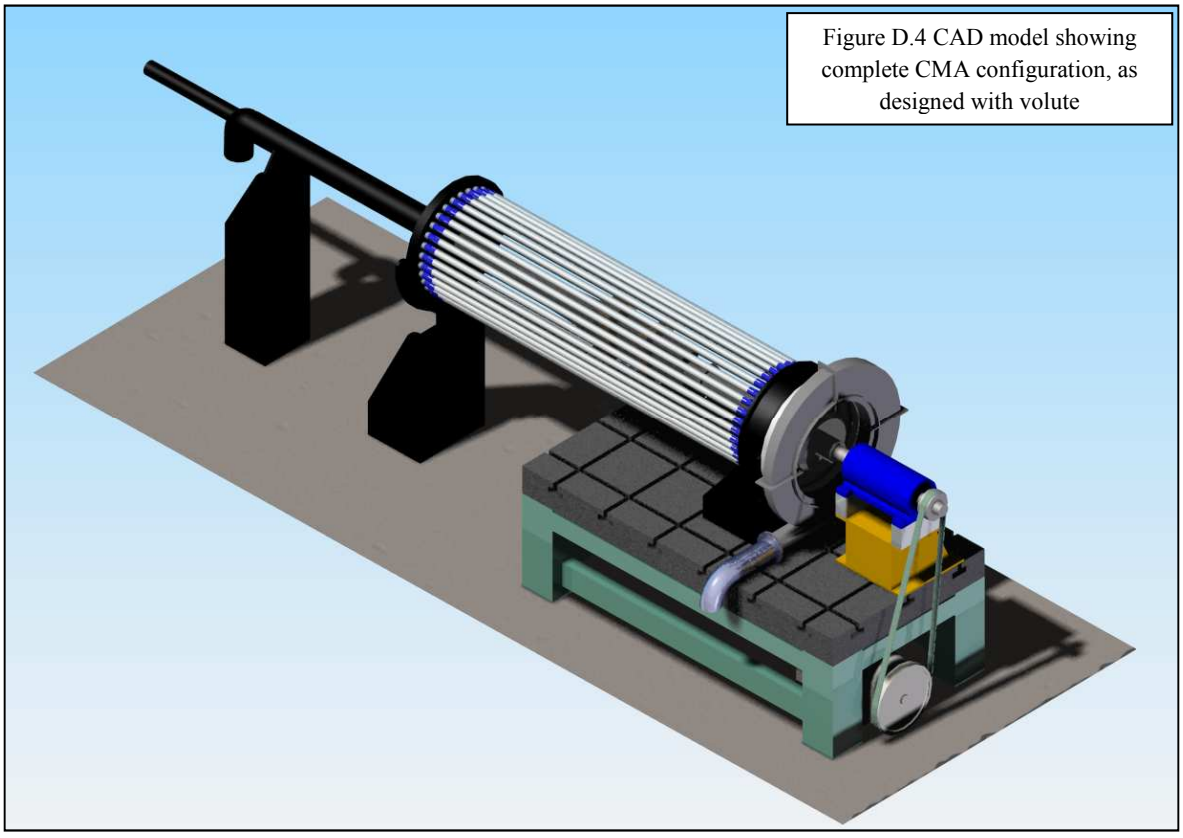

Figure D.4 CAD model showing complete CMA configuration, as designed with volute

Appendix E: Journal of Aerospace Engineering publication

Sangan, C. M., Zhou, K., Litherland, K., Lam, R. and Lock, G. D. (2011c). "Thermal imaging as flow visualization for gas-turbine film cooling." Proceedings of the Institution of Mechanical Engineers, Part G: Journal of Aerospace Engineering **225**(4): pp 417-431.